

INFORMATION TO USERS

This manuscript has been reproduced from the microfilm master. UMI films the text directly from the original or copy submitted. Thus, some thesis and dissertation copies are in typewriter face, while others may be from any type of computer printer.

The quality of this reproduction is dependent upon the quality of the copy submitted. Broken or indistinct print, colored or poor quality illustrations and photographs, print bleedthrough, substandard margins, and improper alignment can adversely affect reproduction.

In the unlikely event that the author did not send UMI a complete manuscript and there are missing pages, these will be noted. Also, if unauthorized copyright material had to be removed, a note will indicate the deletion.

Oversize materials (e.g., maps, drawings, charts) are reproduced by sectioning the original, beginning at the upper left-hand corner and continuing from left to right in equal sections with small overlaps.

Photographs included in the original manuscript have been reproduced xerographically in this copy. Higher quality 6" x 9" black and white photographic prints are available for any photographs or illustrations appearing in this copy for an additional charge. Contact UMI directly to order.

**ProQuest Information and Learning
300 North Zeeb Road, Ann Arbor, MI 48106-1346 USA
800-521-0600**

UMI[®]

Optical mapping of pacemaker interactions

Gil Bub, Physiology Department, McGill University, Montreal.

November 5, 1999.

A thesis submitted to the Faculty of Graduate Studies and Research in partial fulfilment of the requirements of the degree of Doctor of Philosophy.

©Gil Bub, 1999.



**National Library
of Canada**

**Acquisitions and
Bibliographic Services**

**395 Wellington Street
Ottawa ON K1A 0N4
Canada**

**Bibliothèque nationale
du Canada**

**Acquisitions et
services bibliographiques**

**395, rue Wellington
Ottawa ON K1A 0N4
Canada**

Your file Votre référence

Our file Notre référence

The author has granted a non-exclusive licence allowing the National Library of Canada to reproduce, loan, distribute or sell copies of this thesis in microform, paper or electronic formats.

The author retains ownership of the copyright in this thesis. Neither the thesis nor substantial extracts from it may be printed or otherwise reproduced without the author's permission.

L'auteur a accordé une licence non exclusive permettant à la Bibliothèque nationale du Canada de reproduire, prêter, distribuer ou vendre des copies de cette thèse sous la forme de microfiche/film, de reproduction sur papier ou sur format électronique.

L'auteur conserve la propriété du droit d'auteur qui protège cette thèse. Ni la thèse ni des extraits substantiels de celle-ci ne doivent être imprimés ou autrement reproduits sans son autorisation.

0-612-64526-6

Canada

Abstract

Under normal conditions the sinoatrial node serves as the pacemaker of the heart. However, under disease states other pacemaker sites can emerge which compete with the sinoatrial node or with each other. This thesis describes theoretical and experimental studies of pacemaker initiation and interaction. The first aspect of this thesis deals with an arrhythmia called modulated parasystole, which is generated by the interaction between the sinus pacemaker and an ectopic pacemaking focus. A mathematical model was developed to study the dynamics of modulated parasystole using discontinuous circle maps. The mathematical model displayed banded chaos, characterized by zero rotation interval width in the presence of a positive Lyapunov exponent. Banded chaos in the parasystole map produces rhythms characteristic of those found clinically. The second aspect of the thesis deals with spontaneous pacemaker activity and interaction using optical mapping techniques and mathematical models. A macroscopic imaging system was designed and constructed that records fluorescent signals from thin preparations over large areas (1 cm^2) for long time periods (> 30 minutes). Rotating waves (rotors) of cellular activity were observed by mapping calcium in nonconfluent cultures of embryonic chick heart cells. Unlike previous observations of rotors or spiral waves in other systems, the rotors did not persist but exhibited a repetitive pattern of spontaneous onset and offset leading to a bursting rhythm. Similar dynamics were observed in simple excitable media models that incorporated spontaneous initiation of activity and a decrease of excitability as a consequence of rapid activity (fatigue). These results provide a mechanism for bursting dynamics in normal and pathological processes. Activation maps were also obtained from the rabbit atrioventricular (AV) node, a small region of the heart with specialized pacemaking and conducting properties. This work determined sites of delay and spontaneous activity within the AV node.

Résumé

Dans des conditions normales, le battement régulier du coeur est coordonné par quelques cellules stimulatrices dites "pacemakers" formant le noeud sinoatrial. Cependant, dans certaines arythmies cardiaques, d'autres sites pacemakers peuvent apparaître et entrer en compétition avec le noeud sinoatrial ou entre eux. Cette thèse décrit les modèles théoriques et expérimentaux de l'initiation de ces sites et de leur interaction. En premier lieu, nous avons étudié la parasystole modulée, une arythmie générée par l'interaction entre un stimulateur normal (sinus) et un autre anormal (ectopique). Un modèle mathématique a été développé pour étudier la dynamique de cette parasystole en utilisant des cartes de cercles discontinus. Il a montré un chaos bandé caractérisé par une largeur nulle d'intervalle de rotation en présence d'un exposant de Lyapunoff positif. La carte de chaos bandé de la parasystole a ainsi produit des rythmes avec des configurations sinusales et des battements ectopiques semblables à ceux mesurés en recherche clinique. En second lieu, nous nous sommes intéressés aux activités stimulatrices spontanées et leurs interactions en nous servant de techniques de cartographie optique et de modèles mathématiques. Un système d'imagerie macroscopique a été conçu et réalisé pour enregistrer des signaux fluorescents provenant de surfaces relativement importantes (1 cm^2) de préparations minces et ce, sur de longues périodes de temps ($> 30 \text{ min}$). Nous avons donc visualisé les taux de calcium dans des monocouches de cellules embryonnaires de coeur de poussin. Nous avons ainsi observé des vagues tournantes ("rotors") d'activité cellulaire. Contrairement à ce qui avait déjà été observé sur des rotors ou des vagues en spirale dans d'autres systèmes, ces rotors ne sont pas maintenus de façon continue: leur activité va et vient de manière répétitive donnant naissance à un rythme de bouffées. Des résultats semblables ont été observés dans des modèles d'excitabilité simples qui incluent la génération spontanée d'activité et la diminution de l'excitabilité suite à une activité très rapide (fatigue). Ces résultats fournissent un mécanisme pour les bouffées d'activité dans des processus normaux et pathologiques. Des cartes d'activation ont également été obtenues pour le noeud atrioventriculaire (AV), une petite région du coeur aux propriétés de stimulation et de conduction spécialisées. Ce travail détermine des sites de délais et d'activité spontanée dans le noeud AV.

Contributions to original knowledge

Contributions

Chapter 2 has been published[26]. The paper was co-authored by Dr. Leon Glass. I was responsible for the simulations and analytical proofs in the paper. Dr. Glass supervised the project and determined which directions it would take, as well as giving necessary and expert advice on the many technical aspects of the work.

Chapter 4 has been presented as a poster and published as an abstract[199]. Andrew Munk was first author for this study, as he was responsible for the AV node preparation and interpretation of the data. I was responsible for all aspects of the optical imaging and data analysis, including construction of the bath to house the preparation.

Sections of chapter 5 have been published[27]. Dr. Leon Glass and Dr. Alvin Shrier supervised the theoretical and experimental work, and Nelson Publicover was involved in the pilot studies preceding the work. I was responsible for preparing cell cultures, all optical mapping and analysis, and generation of mathematical models.

I was primarily responsible for all aspects of designing and building the optical mapping system that produced the data in this thesis. I also wrote all the software for data analysis, image processing, and control of A-D boards. The design and construction of the optical mapping system is detailed in Chapter 3.

Contributions to Original knowledge

The bifurcation structure of a discontinuous piecewise monotonically increasing noninvertible map was studied in the context of an arrhythmia called modulated parasystole. We found that these maps display banded chaos, and analytically determined conditions for its existence. We developed analytical methods for determining the bifurcation structure and the location of locking zones in parameter space, and proved the structure to be fractal. We related these findings to a clinically relevant model of modulated parasystole, showing that banded chaotic behaviour can give patterns of beats characteristic of those found clinically.

We developed an optical mapping system which uses photodiodes and a CCD camera attached to a microscope and specially constructed macroscope. The optical path is a unique design which allows microscopic and macroscopic monitoring of the same preparation. We also developed an original computer controlled second stage offset and gain control circuit for conditioning signals from the photodiode array. We wrote software for viewing and image processing raw data, constructing and viewing isochronal maps as movie sequences, and generating fluorescence intensity plots were developed.

We mapped activation of the atrioventricular (AV) node using the optical mapping system. Activation maps of escape beats coming from the AV node were also recorded. These were the first optically recorded maps of conduction through the AV node.

We used the optical mapping system to show, for the first time, the presence of spiral waves in monolayers of excitable tissue. We also showed that spiral waves are linked to bursting behaviour in the monolayer. This discovery is the first indication that bursting dynamics may be driven by spatial patterns of activation in the form of spiral waves. Spiral wave initiation and termination is also atypical in this preparation; spiral waves form from spontaneously formed broken wavefronts, and terminate by slowing down and blocking due to fatigue. Mathematical models were developed that mimic these behaviours using a few simple assumptions.

Acknowledgements

I would like to thank both Leon Glass and Alvin Shrier for tremendous amount of help and guidance they have given to me over the years. Their patience and intelligence has been inspirational, and the advice they have given has always been very valuable. I could not imagine finishing any of this work without them. Thanks!

I would also like to express my sincere thanks for the fantastic technical assistance of Johanne Ouellette, John Knowles, and Steve Kekani. Each was essential for an aspect of the project, and their enthusiasm and expertise has been invaluable. Thanks for all the cell cultures, electrical circuits and hardware!

Some people in the department have also been a tremendous help... Michael Mackey and Michael Guevara both have given great advice when needed. Thanks!

I would like to thank all my lab friends over the years... Arkady, Andrew, Adam, Kosta, Andrew, Harald, Caroline, Tiger, Hortensia, Dermot, and Kevin. Its been great! And thanks, Isabelle, for translating the abstract, and thank you, Siobhan, for editing!

And all my other friends and family, who I doubt will read this... Ron, Jeff, Tanya, Percy, Danny, Michele, Naomi, Julian, Yoni, Michali, Carrie and David, as well as Katie, thanks for being so patient.

Contents

1	Introduction	1
1.1	Nonlinear Dynamics	2
1.2	Pacemakers	4
1.2.1	Patterns of Behaviour of Coupled Oscillators	5
1.2.2	Circle Maps	5
1.2.3	Multiple Pacemaker Interaction	6
1.3	Excitable Media	7
1.3.1	Two Pacemaker Interaction via an Excitable Medium: Parasys- tole	10
1.3.2	Mathematical Models of Excitable Media	11
1.3.3	Reentry in Excitable Media: Spiral Waves	18
1.4	Bursting	22
1.4.1	Conceptual Models of Bursting Behaviour	22
1.4.2	Endogenous Bursters - Mechanisms	23
1.4.3	Aplysia Models	24
1.4.4	Single β -Cell Models	25
1.4.5	Coupled β -cell models	26
1.4.6	Network Bursters	26
1.4.7	Reentrant Bursting Models	27
1.5	The Heart as an Excitable Medium	28
1.5.1	Conduction in Healthy Hearts	29
1.5.2	Anisotropy	30

1.5.3	Propagation in 3D	31
1.5.4	Local Heterogeneity	31
1.5.5	Overdrive Suppression and Fatigue	32
1.5.6	Conduction in Diseased Heart: Reentry	33
1.5.7	Changes in Refractory and Excitability Properties in Diseased Hearts	35
1.5.8	Spontaneous Activity in Diseased Heart: Focal Mechanisms .	35
1.5.9	Cultured Monolayers as Models for Cardiac Conduction	36
1.6	Mapping Techniques	37
1.7	Oscillators and Excitable Media, Experiments and Theory	39
2	Pacemaker Interactions: A Mathematical Model for Parasystole	42
2.1	Introduction	42
2.2	Circle Maps	43
2.3	The Dynamics of Discontinuous Maps	47
2.3.1	Banded Chaos	47
2.4	Conditions for Banded Chaos	48
2.4.1	Rotation Interval for Banded Chaotic Maps	51
2.4.2	Bifurcation Structure of Discontinuous Maps	52
2.5	A Theoretical Model for Parasystole	55
2.6	The Dynamics of Parasystole	58
2.7	Discussion	64
3	Activation Mapping	66
3.1	Introduction to Optical Recording	66
3.1.1	Activation Mapping: Electrodes vs. Optical Techniques	67
3.1.2	Extrinsic vs. Intrinsic Signals	68
3.1.3	Fluorescence vs. Absorption Dyes	69
3.1.4	Slow vs. Fast Fluorescent Dyes	71
3.1.5	Ion Sensitive Dyes	72
3.1.6	Dye Choice	73

3.1.7	Detection Systems	73
3.1.8	Photomultiplier Tubes	74
3.1.9	Photodiodes	74
3.1.10	Video tubes	75
3.1.11	Charged Coupled Devices	76
3.1.12	Detector Choice	76
3.1.13	Light Collection and Data Acquisition	77
3.2	Optical Mapping System Design and Construction	77
3.2.1	Theory	77
3.2.2	Design	81
3.2.3	Macroscopic Construction	84
3.2.4	Optical Components	84
3.2.5	Mechanical Components	86
3.2.6	Illumination	86
3.2.7	Performance	87
3.3	Camera Theory	87
3.3.1	Choosing an Appropriate System:	93
3.4	Data Analysis	96
3.4.1	Pixel and Frame Transformations	96
3.4.2	Data Analysis within Gview.exe	98
3.4.3	Additional Output Modes	102
3.5	Photodiode Array Construction	102
3.5.1	The Photodiode Array	103
3.5.2	Second Stage Circuitry	110
4	Optical Mapping of the Atrioventricular Node.	119
4.1	Introduction	119
4.1.1	Background	120
4.2	Atrioventricular Node Preparation	122
4.3	AV Node Results	122

4.4	Discussion	124
5	Bursting Behaviour in Cardiac Monolayer Preparations	127
5.1	Introduction	127
5.2	Methods	127
5.2.1	Monolayer Cell Culture	128
5.2.2	Electrophysiology	129
5.2.3	Optical Mapping	129
5.3	Preliminary Experiments	129
5.3.1	Potential Mapping	130
5.3.2	Calcium Mapping	132
5.4	Optical Mapping of Bursting Behaviour	135
5.4.1	Bursting Dynamics: Experimental Results	138
5.4.2	Bursting Dynamics: Modeling	150
5.5	Discussion	170
5.5.1	Mechanisms for Bursting in Other Systems	170
5.5.2	Rotor Initiation in Other Systems	171
5.5.3	Rotor Annihilation in Other Systems.	173
5.5.4	Continuum Considerations	174
5.5.5	Conclusion	178
6	Conclusions	180

Chapter 1

Introduction

The interaction of pacemakers is a broad area of study with applications in a variety of disciplines[102, 264, 287]. Coupled oscillators are investigated in pure and applied mathematics[158, 203]. Autocatalytic reaction diffusion systems are studied in chemistry[89]. Dynamics of oscillating circuits are of interest to electrical engineers[79]. Biologists study entrainment in firefly populations[287], physiologists study coupled cardiac cells[71, 278], and neurologists study the interaction of spontaneously firing neurons[131]. Pacemakers are of primary importance in the field of cardiology; hearts can be considered as a group of connected cells beating at a rhythm determined by a few spontaneous pacemakers. Arrhythmias can result when normal pacemaker interactions break down. Nonentrained pacemakers give rise to relatively benign arrhythmias such as parasystole[195], or potentially life threatening conditions such as multifocal atrial tachycardia[176].

The dynamics of pacemakers under conditions of periodic forcing and as globally and locally coupled populations has been the subject of extensive theoretical investigation. In general pacemakers do not interact directly in cardiac preparations, but through a medium with its own dynamic properties¹. The present work investigates two cases in which pacemakers interact with a conductive excitable medium.

We study cardiac pacemaker/excitable media interactions in model systems using nonlinear mathematics and optical mapping techniques. This introductory chapter

¹Pacemaker cells interact with each other within pacemaking regions such as the sinoatrial and atrioventricular nodes.

provides a background to theoretical and experimental work on pacemakers and excitable media. The dynamics of two pacemakers coupled via a simplified excitable media is discussed in the context of a theoretical model for parasystole in Chapter 2. The assumptions introduced by the addition of an excitable medium dramatically alter the behaviour of the two oscillator system. Experimental investigation of coupled pacemaking systems and excitable media in cardiac preparations requires observing the behaviour of the system at many points in space simultaneously. Optical techniques for mapping activity in cardiac preparations are introduced in this chapter and discussed in detail in Chapter 3. Preliminary results and pilot studies using optical mapping techniques are presented in Chapter 4. The dynamics of a large number of interconnected oscillators is investigated in an experimental and theoretical model in Chapter 5. Here, the dynamics can be primarily driven not by the pacemakers themselves but by the properties of the underlying excitable media.

1.1 Nonlinear Dynamics

A discussion of pacemaker interaction requires some familiarity with a field of mathematics called non-linear dynamics. This section informally introduces concepts discussed later in this chapter. More rigorous definitions are given in subsequent chapters when needed.

Mathematical models can be formulated as differential equations or finite difference equations. *Differential equations* are equations of the form $\frac{dx}{dt} = f(x)$, where $f(x)$ defines the rate of change of variable x over time t . The above equation is one dimensional in the sense that the rate of change of x depends only on itself. Mathematical models of biological systems are often multidimensional, with several interacting variables varying continuously over time. *Finite difference equations* have the form $x_{t+1} = f(x_t)$. Here the value of variable x is determined at some time in the future ($t + 1$) by the function f and the state of the variable at time t . A finite difference equation is *iterated* over time by repeatedly substituting x_{t+1} for x_t . Despite their apparent simplicity, one dimensional difference equations (like

the equation above) are capable of displaying a wide range of qualitatively different dynamics. For clarity, the remainder of the discussion in this section considers one dimensional difference equations; however the concepts can be applied to the study of differential equations as well.

An equation is considered *linear* if the right side of the equation describes a line $ax_t + b$, where a and b are constants. One dimensional linear equations have a limited range of behaviours. They either reach a *steady state*, a *cycle* or approach positive or negative infinity. A steady state is a solution where $x_{t+1} = x_t$. A period P cycle occurs when $x_{t+P} = x_t$, where $x_{t+N} \neq x_t$ for $N < P$. Finite difference equations are *non-linear* if the right side of the equation describes a form other than a line. Non-linear finite difference equations can display *chaos* and *quasiperiodicity* in addition to the behaviours described above. Both chaos and quasiperiodicity are aperiodic ($x_{t+P} \neq x_t$ for all P .) In quasiperiodicity, two initial conditions initially close together stay close as time evolves. An example of quasiperiodic behaviour is two uncoupled clocks, running at slightly different speeds. The difference in phases (here the time read by the clock) changes slowly over time, and a small change of phase of one clock does not change the overall behaviour of the system. Chaotic dynamics, on the other hand, are sensitive to small changes in initial conditions. In chaotic dynamics, two initial conditions that are close together will diverge after several iterations. Chaos is usually characterized by dynamics that appear random at first glance.

The *trajectory* of an equation refers to the sequence of values obtained by repeatedly iterating $f(x_t)$. Nonlinear finite difference equations undergo a large change in dynamics when their parameters are slowly varied under certain conditions. Such a change is referred to as a *bifurcation*. An example of a bifurcation is when a trajectory moves from a steady state solution to a cycle. Chapter 2 investigates the bifurcation structure of a finite difference equation formulated as a circle map. Circle maps are addressed later in this chapter and are discussed in detail in Chapter 2.

1.2 Pacemakers

Pacemaking activity is seen in many biological systems. Cells with pacemaking activity produce periodic signals. Some well-known examples are the circadian rhythm, which controls the 24 hour cycle in animals[177], islet cells in the pancreas, which give periodic bursts of activity releasing insulin[53], and cardiac sinus[278] and atrioventricular (AV) node cells, which control the periodic rhythm of the heart[102].

Mechanisms of pacemaking activity have been extensively studied. Theoretical studies involving ionic mechanisms have been used to give detailed analyses of sinus node[71], AV node, β -pancreas cells[32] and other systems[212]. These models use differential equations to describe a slow current that causes membrane voltage to rise to threshold initiating an action potential. Such models have been used to study the effects of external stimulation on single or small groups of cells, and have been used to study the interaction of large numbers pacemaking cells[188]. As these models are complex, simple models of pacemakers are used as tools to develop a theoretical basis for pacemaker behaviour. These simple models use equations that do not represent ionic currents directly, but rather the qualitative characteristics of oscillators.

Any system that exhibits a periodic behaviour is called an oscillator. Mathematical models of oscillators are typically formulated as differential equations, in which the variables represent the key components needed to describe the oscillator. For example, for the ideal pendulum, the phase space consists of position and velocity and the trajectory is approximately elliptical for small amplitude oscillation.

Biological oscillators differ from the pendulum in that they tend to have a characteristic period and amplitude, to which they return following perturbations. Oscillators that return to a set trajectory are called *limit cycle oscillators*. A simple limit cycle oscillator, called the Poincaré oscillator[102] can be given by:

$$\begin{aligned}d\theta/dt &= 2\pi \bmod(2\pi) \\ dr/dt &= Kr(1-r)\end{aligned}\tag{1.1}$$

where θ gives the rotation angle and r gives its distance from the origin. K is a

positive parameter that regulates the rate at which the value of r approaches 1. Equation (1.1) has an unstable steady state at $r = 0$ and a stable limit cycle at $r = 1$. Any perturbation results in a spiraling of the trajectory back to $r = 1$. Despite its simplicity, this model has been used to characterize the behaviour of paced cardiac oscillators[115].

1.2.1 Patterns of Behaviour of Coupled Oscillators

Despite the simplicity of limit cycle oscillators like the Poincaré oscillator, the range of observed behaviours under periodic forcing from another oscillator is complex. *Phase locking* occurs when periodic rhythms arise from the interaction of two oscillators. Phase locked rhythms are characterized by giving the ratio of frequencies of the two oscillators. For example, in 2:1 phase locking one oscillator undergoes two cycles while the other oscillator goes through one cycle. Phase locked patterns change as intrinsic frequencies and coupling strengths of the oscillators are varied. A regions in the frequency/coupling strength parameter space in which a certain rhythm is maintained is called a *phase locking zone*. Coupled oscillators can also display chaos and quasiperiodicity. The organization of phase locking zones in parameter space has been extensively studied and is discussed in Chapter 2.

1.2.2 Circle Maps

Periodic stimulation of simple limit cycle oscillators can often be represented by difference equations. Here, the oscillator's phase just before a stimulus cycle is written as a function of the previous phase, $\theta_t = F(\theta_{t-1})$. $F(\theta)$ is called a circle map as it can be thought of as giving the rotation of $F(\theta)$ around a unit circle. A circle map maps points on the circumference of a circle to different points on that circle. Circle maps have been extensively used to analyze pacemaker and oscillator dynamics[15, 16, 10, 44].

Circle maps are reviewed in detail in Chapter 2. Briefly, circle maps can be characterized by their topological degree. The topological degree of $F(\theta)$ counts the number of times F traverses the unit circle as θ traverses the circle once. For exam-

ple, $F(\theta) = M\theta + b \pmod{1}$, where M is an integer, has topological degree M . The dynamics of circle maps can be quantified by their *rotation number*, which gives the average change in $F(\theta)$ over many iterations. For example, 2:1 phase locking results in a rotation number of $1/2$. Rational rotation numbers are associated with periodic dynamics, while irrational rotation numbers are hallmarks of quasiperiodicity and chaos. The class of circle maps investigated in Chapter 2, however, display chaotic dynamics while having rational rotation numbers. This results in surprisingly regular chaotic trajectory called ‘banded chaos’. This unusual behaviour is a result of fractional topological degree caused by a jump discontinuity in the circle map.

1.2.3 Multiple Pacemaker Interaction

The dynamics become more complex when more than one pacemaker is involved. Each oscillator can be coupled to its nearest neighbours or to all the oscillators in a large population. Global coupling interactions are observed in firefly populations[264], and synchronization of women’s menstrual cycles[182]. Nearest neighbour interactions in multiple oscillator systems are studied in biological contexts with neuromuscular oscillators in the intestine[49], pacemaker neurons in the eye[131], spinal cord[37, 279], and in culture[198].

Computer simulations and mathematical analysis demonstrated that globally coupled pacemakers necessarily synchronize or their phases remain evenly scattered if the oscillators have identical intrinsic cycle lengths and the coupling is weak[264]. Under some coupling rules, the population of oscillators breaks down into subpopulations of synchronous oscillators called ‘clusters’. The number of clusters depends on the nature of coupling between oscillators[203]. Winfree[284] showed that coupled oscillators with different frequencies can still synchronize if their intrinsic frequencies are not far from a global mean value. Synchrony can persist even when some stochasticity is included in the form of random external forcing[203].

Locally coupled systems add a level of complexity by allowing the formation of spatial structures. Clustering still exists in locally coupled systems with identical frequencies [204], but the stability of the clusters depend on the conduction delay be-

tween oscillators. Simulations and analysis with one-dimensional chains[158, 279, 37] of weakly coupled oscillators with different intrinsic frequencies have been conducted in the context of studying conduction in the lamprey spinal cord[37]. Frequency differences cause phase lags in conduction and can cause a loss of entrainment if the differences in intrinsic frequencies are too great. Phase lags can be lengthened or shortened depending on the distribution of coupling strengths in the chain[37].

The above analyses on globally and locally coupled oscillators assume that coupling is extremely weak. This assumption ensures that oscillator timing maintains a relative order: an oscillator with phase lagging behind other oscillators can never overtake them. Under conditions of strong coupling, oscillators can change their order, resulting in mixing of their phases. Strongly coupled oscillator systems can display changes in the collective frequency and exhibit chaos[203].

1.3 Excitable Media

Excitable media are spatially distributed systems which have the ability to propagate signals without damping. For example, a forest fire travels as a wave from its initiation point, and regenerates with every tree it ignites. This is in contrast to passive wave propagation, which is characterized by a gradual damping of signal amplitude due to friction. An example of passive wave propagation is sound waves passing through air. The interaction of waves in active media also differs from waves in passive media: waves in a pond from two thrown rocks sum when they collide while forest fires started from two sources cancel. An active medium also has to reconstitute after a wave passes through it (for example, trees must regrow after they burn down) while a passive medium can transmit signals without a delay.

Travelling waves in excitable media have been observed in many contexts. Travelling regenerative waves are observed in chemical systems, the most well studied being the Belousov-Zhabotinskii (BZ) reaction[80]. Other examples of waves in excitable media include autocatalysis reactions on metal surfaces[94], and propagation of forest fires[11]. In biological contexts propagating waves are used for communica-

tion within and across nerves, to generate contraction in an ordered fashion in the heart and to organize slime mold[217] in response to starvation. Despite the obvious differences in the above systems, propagation in all excitable media share many characteristics. The following briefly discusses features common to all excitable media systems.

An excitable medium system can be considered as a group of individual elements coupled to each other. Each element can pass information to its neighbors. In physical systems signals can pass by diffusion; in the case of the BZ reaction chemical species (HBrO_2 and Fe^{3+}) diffuse to neighbouring regions; in cardiac muscle current carried by sodium and potassium ions moves to neighboring cells. Each (coupled) point in the excitable medium is characterized by a *rest state* that is it stable for small perturbations. An impulse with strength greater than a certain *threshold* can cause that point to undergo a large excursion from, and eventually return to, its rest state value. The time required to return close to the steady state value is a factor that determines the refractory time of that point; a *refractory* point cannot easily undergo another cycle until it recovers.

An impulse over a certain threshold initiates a wave of activity moving across the excitable medium. As each element undergoes an excursion from steady state, it causes its neighbors to move over threshold at a rate determined by the diffusion coefficient (a 'passive' property of the medium), and the rate of rise of the diffused species of the excited element (a 'active' property of the medium.) A wave of activity propagates with a speed controlled by how fast elements ahead of the wave are induced to cross the threshold. For planar waves, wave speed is only a function of the active and passive properties of the medium. However, a wavefront's curvature can affect the speed of the wave. The reason for this is that diffusion to points ahead of a curved wavefront distribute over an area that depends on the wavefront shape. For example, convex (curving outward) waves must drive a greater area of excitable media over threshold than concave waves do. Wave speed (c) for excitable media can be approximated by the following relation:

$$c = c_0 + D\rho, \tag{1.2}$$

where the curvature ρ is defined as the negative reciprocal of the local radius of curvature, D is the diffusion coefficient, and c_0 is the planar wave speed. Equation (1.2) is an approximation valid for ρ close to zero. Derivation of an exact relation depends on the system being studied. However Equation (1.2) has been verified experimentally for many physical and theoretical systems[89, 90]. Equation (1.2) is a good first approximation over a large range of curvatures in these systems.

Since conduction velocity decreases as wavefront curvature becomes more negative, Equation (1.2) shows that velocity drops to zero for a critical radius of curvature (ρ_c):

$$\rho_c = -c_0/D. \quad (1.3)$$

assuming that Equation (1.2) is valid at high ρ . It also follows that a circular nucleus of excitation does not result in outward propagation if $\rho \leq \rho_c$.

A point seldom addressed in the study of excitable media is the effect of curvature on wavefront stability in heterogeneous media. Heterogeneities are more likely to prevent propagation at highly curved fronts than at wave fronts with shallow curves. Consider a case where small areas ahead of a target wave are refractory. The target wave with refractory holes is generated as the excited wave moves around refractory regions. This resulting patchy wave is less able to drive media ahead of it over threshold than a fully active wave, so a wave may not propagate even if $\rho \geq \rho_c$. Decreasing ρ lowers the relative contribution of refractory regions, allowing propagation. This mechanism is investigated in more detail in Chapter 5.

Another feature common to excitable media is dispersion[89, 91, 95, 258]. Dispersion refers to the dependence of wave speed on recovery time of the medium. During periodic signaling at high rates, the medium does not have enough time to fully return to its rest state between waves. Consequently, the threshold increases as more excitation is required to trigger the next wave. If D is constant, it takes longer for a region ahead of the wavefront to reach threshold, resulting in slower wave speed. The dependence on conduction velocity c on recovery time T_{rec} can

usually be fitted by an exponential function for diverse systems[95, 130]:

$$c = 1/\alpha \exp(-T_{rec}/\beta) + \gamma, \quad \text{for } T_{rec} \geq \text{refractory time} \quad (1.4)$$

where α , β and γ are positive constants.

1.3.1 Two Pacemaker Interaction via an Excitable Medium: Parasystole

In the healthy heart, the cardiac rhythm is set by a single pacemaking site called the sinoatrial node (see Section 1.5.1 for background information on cardiac conduction.) Occasionally, there can be pacemakers in abnormal locations that generate rhythms that compete with the normal sinus rhythm. The interaction between the ectopic pacemaking sites and the sinus pacemaker generate an arrhythmia called parasystole.

Parasystolic rhythms can be pure or modulated. In pure parasystole, the sinus and ectopic pacemakers do not phase reset each other. In modulated parasystole, the sinus rhythm acts to phase reset the ectopic focus. This introductory section discusses the dynamics of pure parasystole. Chapter 2 gives a detailed analysis of modulated parasystole.

The ectopic and sinus pacemakers interact via excitable cardiac tissue between them. An ectopic beat results if the ectopic focus depolarizes outside the refractory period of the surrounding tissue, otherwise it is blocked. The sinus beat following an expressed ectopic beat is usually blocked due to refractoriness of the ventricles. In pure parasystole, the time intervals between ectopic beats are multiples of a common divisor, and the time interval between sinus and ectopic beats is variable.

The above observations on the mechanism of parasystole allow the excitable media between the pacemakers to be modeled by a simple equation. More complex models of excitable media are considered in the next section. A model for pure parasystole can be formulated as a circle map[43, 101] (see Section 1.2.2). The sinus cycle is represented by a circle and the hearts refractory period is a segment of this circle. The ectopic pacemaker produces impulses that land within the sinus cycles

phase. The ectopic beat is blocked if it occurs within the refractory period, and is expressed otherwise. Mathematically, this is formulated as a map of a circle into itself, $\phi_{t+1} = f(\phi_t) \bmod 1$, where ϕ is the phase of the sinus cycle when the ectopic beat occurs. Glass *et al.*[101] looked at the number of sinus beats between ectopic beats obtained by iterating the circle map. Iterating the map results in a sequence of values that represent the number of interpolated sinus beats (NIBs) between each ectopic beat. Glass *et al.*[101] proved that the following four rules govern the NIB sequence: 1) there are three or fewer NIB values in a sequence of NIBs, 2) if there are three NIB values, the sum of the two smaller values is one less than the larger one, 3) only one of the values is odd, 4) only one of the allowed values can succeed itself in the sequence. The above rules hold only when the mathematical model of parasystole can be represented by an invertible circle map. If the sinus node resets the ectopic focus, this condition no longer holds. Chapter 2 investigates the dynamics of discontinuous noninvertible circle maps, and applies these results to a mathematical model of modulated parasystole.

1.3.2 Mathematical Models of Excitable Media

Excitable media are most naturally represented as partial differential equations. Here the excitable medium is divided up into individual cells, where each cell is modeled by differential equations. The number of differential equations required to represent a cell in the system may be large. For example, the DiFrancesco-Noble model of Purkinje fibers[65] has 14 variables and over a hundred parameters. The rationale for developing such complicated theoretical models is the assumption that inclusion of all known components is needed to achieve an accurate simulation of the behaviour. Although this modeling approach may be justified in some situations (where the effects of altering a specific variable are to be tested, for example), the high dimensionality of such models hinders intuitive understanding of the underlying dynamics.

An excitable medium model can be represented in a simplified form by the interaction of two variables: an excitation variable (u) and a recovery variable

(v). The variables interact locally according to the ordinary differential equations $du/dt = f(u, v)$, $dv/dt = g(u, v)$, where the nullclines for functions f and g have a characteristic shape shown in Figure 1.1. In this model there is a rest state where the nullclines intersect. A small perturbation is damped out but a perturbation over a certain threshold triggers a long excursion.

The excitation variable u increases rapidly until the trajectory approaches the rightmost arm of $f(u, v) = 0$. At this point the trajectory moves slowly up the nullcline as the recovery variable increases. When the trajectory reaches the top of the right arm of $f(u, v) = 0$, the trajectory moves to the leftmost arm as variable u rapidly decreases, which is followed by a slow decrease of v back to the rest state.

A simple mathematical model that behaves as described above is the FitzHugh-Nagumo[82] model of excitation in nerve and muscle tissue:

$$\begin{aligned} du/dt &= f(u, v) = u - u^3/3 - v \\ dv/dt &= g(u, v) = E(u + a - bg) \end{aligned} \quad (1.5)$$

where u is membrane potential and v approximates a slow current (when $0 < E \ll 1$). The excursion that u takes in response to a supra-threshold stimulus is similar in appearance to voltage changes called action potentials (APs) produced in nerve and muscle tissue. Although the model is unable to reproduce the detailed characteristics of APs in nerve and muscle fibers, it successfully encompasses many characteristics of excitable tissue including threshold behaviour, a refractory period, and dispersion effects.

Modeling wave propagation in two dimensions with a model similar to Equation (1.5) involves having several equations coupled to each other by diffusion:

$$\frac{\partial u}{\partial t} = f(u, v) + D_x \frac{\partial^2 u}{\partial x^2} + D_y \frac{\partial^2 u}{\partial y^2} \quad (1.6)$$

$$\frac{\partial v}{\partial t} = g(u, v) + D_x \frac{\partial^2 v}{\partial x^2} + D_y \frac{\partial^2 v}{\partial y^2} \quad (1.7)$$

where D_x and D_y are diffusion constants in the x and y directions. More complex coupling relations can simulate preferential propagation in one axis[234, 292] or take

into account different diffusion rates for substances in different compartments (for example, the bidomain model of cardiac conduction uses different conductances for substances inside and outside cells[292].)

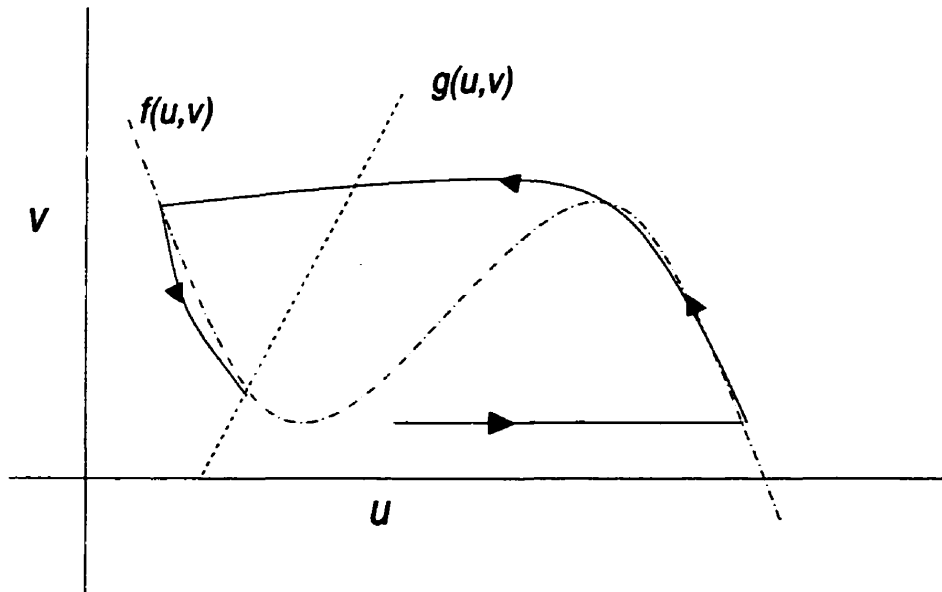


Figure 1.1: The FitzHugh-Nagumo excitable medium model. The nullclines for $f(u, v)$ and $g(u, v)$ are shown. The trajectory takes a path discussed in text.

Much effort has been expended in creating different coupled differential equation models for different biological and physical systems. For example, the Hodgkin-Huxley model[120] and FitzHugh-Nagumo equations[83, 202] model nerve tissue specifically, the Beeler-Reuter model[14] models heart tissue, the Oregonator model[80] models the BZ reaction, and the Martiel-Goldbeter equations[183] model slime mold aggregation. All differential equation models represent known microscopic quantities (such as the movement of a particular current) with equations. The different underlying mechanisms result in models with few obvious mathematical similarities.

Accurate simulation of travelling waves becomes computationally expensive as the complexity of the underlying model increases. Investigating the dynamics of

travelling waves where the wavefront is involved in subtle changes requires integration of 'stiff' equations which can result in thousands of iterations for each wave of excitation. If a large number of spatially discrete points is required, simulations may require a large amount of computer time[95]. In addition, changing one variable can change more than one characteristic of the model. For example, lowering the refractory period (by decreasing the slope of $g(u, v)$) in Equation (1.5) also decreases upstroke velocity. This problem is exacerbated with higher dimensional models, and it becomes increasingly difficult to ask simple functional questions. Simulations in the Beeler-Reuter[14] model could easily determine what changes a 10 percent increase in extracellular sodium would cause, but cannot answer how a 10 percent increase in refractory period alone would change its dynamics. Complex models are therefore not appropriate for generating general results applicable to all excitable media.

Another approach for modeling excitable media that has recently been explored is the use of diffusively coupled difference equations. The coupled map lattice is a discrete time (as each point in the lattice is a difference equation), continuous state model[13, 140, 257]. Each point is diffusively coupled to its neighbours and the lattice is updated using small time steps, making it continuous in space in the same sense as is a coupled differential equation model. A coupled map lattice may be appropriate when each point in the physical system is well defined by a map and spatial averaging of the difference equation variable can be used to model diffusion.

Excitable media can also be simulated using discrete time models with simple update rules. These models consist of a grid of points where each point takes on any of a small set of discrete states and there is set of rules that determine future states of points in the grid based on the present state of the grid. Discrete models, also called cellular automata[201], have been applied to a variety of physical processes. It is important to note that all simulations, including that of coupled differential equations, necessarily update in discrete time due to limitations inherent in the way computers integrate the models[245]. Coupled differential equation models are continuous in the sense that the underlying equations are continuous in time.

Cellular automaton models simplify the dynamic description of a system by mapping the system's behaviour onto a few discrete states. The states have values that reflect each grid point's functional characteristic (such as an excitable or refractory state) as opposed to the value of particular state variables (such as voltage or ion concentration.) Space is discretized by mapping the continuous effects of diffusion to simple rules based on neighbourhood interaction. The discrete approach was first investigated in a biological context by Wiener and Rosenblueth[277], who modeled waves rotating around an obstacle in models of excitable cardiac muscle.

Cellular automata models can be labelled as first generation or second generation for the purposes of this discussion. First generation cellular automata are characterized by cell-cell interaction limited to adjacent neighbours, a small number of update states and cell spacing on a regular grid. First generation cellular automata have several shortcomings that are addressed by more complex second generation cellular automata models. First generation and second generation cellular automata are discussed below.

First generation cellular automata models usually have elements existing in one of three states, resting, excited or refractory. A resting cell updates its state based on the activity of its neighbours, while excited and refractory cells update their state based on the cells history. A resting cell remains at rest until a certain number of its neighbours are excited, at which point it becomes excited in the next time step. Excited cells become refractory and refractory cells return to rest.

A given cell has a number of neighbours which depend on the radius of interaction and the shape of the neighbourhood. Most first generation cellular automata use either a Neuman or Moore neighbourhood geometry with radius equal to one. A Neuman neighbourhood consists of the 4 cells on each of the cell's edges. A Moore neighbourhood of radius N includes all cells encompassed by a square of side length $2N+1$.

First generation cellular automata models of excitable media have two advantages over differential equation models; they are more intuitively transparent and computer simulations run significantly faster. Their simplicity comes at a price,

however. Radius of curvature and dispersion effects, which are common to all excitable media in nature, are absent in these models. Another problem encountered in first generation cellular automata models is that wave propagation direction is influenced by the underlying lattice. In contrast to the homogeneous system modeled by differential equations, waves in cellular automata models often have sharp edges not found in nature. The shape of the grid results in preferred conduction in the horizontal and vertical directions, while diagonal speed is reduced. This can result in pronounced artifacts that can affect dynamics as parameters are changed. For example, Weimar *et al.*[275] investigated wave speed in simple threshold cellular automata models with an extended Moore neighbourhood. They found that horizontal and vertical speed differ from diagonal speed in a manner strongly dependent on threshold.

Second generation models are a response to the shortcomings of first generation models. Models with thresholds greater than one (more than one neighbour must be active to induce a resting cell to the excited state) generate curvature effects if neighbourhood size or the number of excited states is greater than one[95]. Fast and Efimov[78] add dispersion effects by adding a weighing function (where a cell's relative contribution to excitability decreases as a function of distance from the wavefront) and another state called the relative refractory period (where cells have a higher threshold than resting cells but can still be excited). Gerhardt *et al.*[95] add dispersion by making threshold a decreasing function of time. Several methods have been proposed to remove anisotropic effects. Marcus and Hess[181] randomize the grid by leaving many (random) grid points empty in circular neighbourhoods. Kurrer and Shulten[165] select a random subset of a square neighbourhood as the active grid. Several second generation models define diffusion coefficients[97, 275] and use cellular automata models to simulate continuous differential equation models.

Cellular automata models offer a level of abstraction over differential equations as a number of underlying variables are encompassed in a single state. For example, the refractory period is not directly represented by differential equations but is a function of the interaction of several differential equations. In a cellular automaton

model, the refractoriness of a modeled cell is simply one of several states of that cell. This allows construction of models which encompass many different natural systems. Models by Gerhardt *et al.*[95], and Fast and Efimov[78], were designed as general models of excitable media that can be applied to specific systems by fitting parameters.

Ito[129] introduced a different approach, called mesoscopic modeling, for formulating general models of excitable media. Coupled differential equation, coupled map lattice and cellular automata models divide excitable media into a large number of cells, where each cell encompasses the microscopic characteristic of the system. Parameter fitting is difficult if the microscopic behaviour of the system is unknown. Dispersion and curvature relationships cannot be used directly to fit parameters in these models as they are macroscopic features caused by the interaction of many cells. Mesoscopic models [129, 130] model the functional behaviour of tissue on a larger space scale. Here, each cell is modeled by the dispersion relation directly. The mesoscopic model is similar to differential equation models in that its underlying dynamics are controlled by the continuous Equation (1.4), but it still models cell interaction using update rules as opposed to diffusion.

To summarize, several model types are available for modeling propagation in excitable media. Coupled differential equations can be considered continuous in time and space, because the equations that drive local dynamics and cell interaction are continuous even if the mechanism for integrating them (discretely on a computer) is not. Coupled map lattices are similar to differential equations but the local dynamics are driven by discrete time (difference equations) processes. First generation cellular automata models are discontinuous in time and space, because a small number of states define cell activity and diffusion is approximated by simple update rules for a small local neighbourhood. Although these cellular automata models are computationally efficient and can be generalized to encompass many systems, they do not display curvature or dispersion effects which are ubiquitous features of excitable media. Second generation models have managed to include these effects by increasing the complexity of the cellular automata in regard to local dynamics and update

rules.

Several models are addressed in this thesis. Chapter 2 looks at the interaction of two pacemaking sites coupled by excitable media. Here, dispersion and geometric effects are assumed to be unimportant, allowing the excitable media to be approximated by simple rules. Chapter 5 looks at cellular automata and differential equation models coupling excitable media and multiple pacemaking sites. Limitations of the specific modeling approaches used are discussed.

1.3.3 Reentry in Excitable Media: Spiral Waves

As discussed above, a suprathreshold stimulus on an excitable medium can elicit a wave of excitation travelling from the initiation site. In homogeneous isotropic media, the wave of excitation moves out as an expanding circle, called a target pattern. Initial conditions in the media can give rise to a different pattern of excitation called a spiral wave. Spiral waves form naturally when a wavefront travels around a pivot point repeatedly reexciting itself. A spiral is created as points further from the pivot have to travel farther to make a circuit, and therefore lag behind the wave at the center.

Spiral waves of excitation are observed in a wide variety of natural systems. Spirals have been observed in the BZ reaction[284], intact[50] and cultured (Chapter 5) cardiac tissue, retinal[106] and cortical[253] neural preparations, and aggregating slime mold [98]. The existence of spiral waves of excitation (also called vortices and rotors) is a general property of excitable media. The mechanisms of onset and stability of spirals are the subject of extensive ongoing investigation. This section reviews some basic results.

Initiation

Spiral wave formation involves generation of a wave of excitation with a free end. A wave of excitation with a free end is also called a broken wavefront. The free end curves inward to excite tissue previously excited to form a spiral. There are several mechanisms for generating wave fronts with a free end.

One mechanism was proposed by Krinsky in 1968[160], who studied propagation in a heterogeneous cellular automata model. He assumed a region D with a prolonged refractory period in the path of two closely spaced excitation fronts. After the first wave passes, region D remains refractory while surrounding tissue becomes excitable. Passage of the second wave results in a broken wave at the boundary of D . The wave front moves around D until it becomes excitable again, at which point it reexcites the region to form a spiral wave.

Rotor formation in homogeneous excitable media involves the creation of a heterogeneity in refractoriness in the medium with a stimulus followed by the creation of a wave break near the heterogeneity by a specially timed second stimulus. Winfree[283, 289] first demonstrated that spirals can be created in homogeneous media with a procedure called the 'pinwheel experiment'. It involves crossing a spatial gradient of phase with a spatial gradient of stimulus intensity. This mechanism creates a pair of mirror image rotors. A related mechanism is cross field stimulation[287]. A wave of excitation passes perpendicularly through a gradient of refractoriness created by a previous wavefront. The two waves are timed such that the second wave blocks close to the previous wave but can propagate further back. This results in a wave break and rotor formation. This mechanism has been used to generate spirals in cardiac slices[51, 92].

A third mechanism is thought to play a significant role in systems displaying spontaneous oscillations leading to frequent target excitation patterns. Here, a region in the wake of a travelling wave becomes excited, generating a wave moving outward from the excitation point. The excitation is blocked in the direction of the first wave, which results in a semicircular wavefront centered at the excitation point with two free ends. The free ends curve inward to generate a pair of mirror-image spiral waves. This mechanism has been observed in spontaneously oscillating BZ reactions and slime mould preparations[217].

A different mechanism of initiation in heterogeneous media with spontaneous oscillations is discussed in Chapter 5. Here, initiation sites have a high chance of generating a broken wavefront due to heterogeneities in the media. Radius of

curvature effects stabilize the wave front as it propagates outward, allowing it to pass through locally heterogeneous media and form a stable spiral wave.

Existence and Geometry

The geometry of and period of spiral waves are constrained by the ability of the free end, or *spiral tip*, to curve inward. Propagation speed near the spiral tip is influenced by the shape of the tip and excitability of the media. The tip can travel inward at a maximum angle set by Equation (1.2). As cell coupling (parameterized by diffusion coefficient D) increases the tip can move inward at a sharper angle provided it does not collide with refractory medium. The circular region circumscribed by the travelling tip is called the core of the spiral. The spiral core remains unexcited despite rapid periodic activity in surrounding regions.

Tyson and Keener analytically determined the relationship between core size and period for stationary spirals[269]. Rotating spiral waves generate (approximately) planar waves far from the core. As these waves follow each other periodically, their dynamics are governed only by the dispersion relation: Equation (1.4). Close to the core, where wave front curvature is high, Tyson and Keener used the curvature relation to derive a second constraint between wave speed and period based on the size of the core. The intersection of this new constraint and the dispersion relation gives unique values of planar wave speed and period in terms of core size. The spiral solution derived in reference [269] assumes that excitation occurs much (infinitely) faster than recovery, which is not valid in real systems[95].

The stability and shape of the spiral depend on the relative size of the core and refractory period of the tissue. If the refractory period is small relative to the period of the spiral wave, then the media ahead of the wave is always excitable, and the path of the wave tip is not affected by refractoriness of tissue. If the inward rotation angle of the tip is large then the core collapses, and the tip's trajectory is controlled by the refractory medium directly ahead of it. In this case, the period of the spiral is simply equal to the refractory period of the medium. Collapsed cores are always seen in first generation cellular automata models because radius of curvature

effects are not present. There is some evidence that reentry in intact cardiac tissue follows this regime[92, 78]. Finally, intermediate states exist, where the core follows a trajectory primarily limited by radius of curvature effects but interacts with the partially refractory medium ahead of it. This results in a ‘flower-petal’ shaped trajectory called meandering. Computer simulations have shown transitions between circular cores, meandering, and collapsed linear cores as a function of threshold in second generation cellular automata models[78, 95] and coupled differential equation models[289, 298].

Spiral Instability

A rotating spiral can undergo destabilizing changes that result in wave annihilation. The most studied form of spiral wave destabilization, often referred to as ‘spiral break up’ involves spontaneous wave breaking on the spiral arm. Spiral breakup results in multiple spirals which propagate in an erratic fashion through the medium. This transition is thought to occur in heart tissue, in the case where ventricular flutter (presumably caused by a single spiral wave[287]) degenerates into fibrillation. The breakup process is poorly understood and is under investigation, but is partly due to the interaction of the wavefront and the repolarizing medium ahead of or behind it. Simulations show that wave breaks are related to variability in period[142], a slowing of the repolarization wave front and collisions with the subsequent excitation wave[46, 170] (see also [272] for similar behaviour in a ring), or a slowing of the excitation wave front leading to collision with the repolarization wave[95].

Spiral wave break up does not result in annihilation of activity, but multiplies the number of cores resulting in disorganized activity[12]. Two mechanisms of spiral wave annihilation have been studied: meandering of the wave tip in homogeneous media can cause the wave to collide with a boundary[78], and spirals can drift to the boundary in heterogeneous media[222].

A different form of spiral wave annihilation is discussed in Chapter 5. Here, wave propagation is inhibited by a gradual decrease in the excitability of the cells. A cellular automaton model with curvature effects is used to simulate the effects of

a gradual change in parameters of the system (in this case threshold). Spiral wave annihilation is preceded by a gradual increase in period and core size, which is also observed experimentally.

1.4 Bursting

Bursting behaviour refers to spontaneous activity in cells or groups of cells that is characterized by periods of rapid firing followed by periods of silence. Bursting is observed in diverse systems such as whole and cultured neuronal preparations[74, 198, 233, 253], and networks of pancreatic β -cells[32, 53, 252], as well as in disease states such as paroxysmal (reoccurring) reentrant tachycardias[224] and epilepsy[63]. The experiments in Chapter 5 demonstrate that bursting also occurs in dispersed monolayer cultures of embryonic heart cells.

Theoretical analyses of bursting have focused on cellular ionic models[29, 41, 274, 251] or small network models[38, 250]. In contrast, bursting in cultured cardiac monolayers is generated by large scale spatial patterns of activation. As this mechanism is different from those previously described, models of bursting behaviour are reviewed below.

1.4.1 Conceptual Models of Bursting Behaviour

There are two ways that bursts can be generated in groups of cells: one or more cells in a population have the property of endogenous bursting, or else the bursting arises from interactions between cells.

A cell can be considered a true endogenous burster if it produces bursting pacemaker potentials when completely isolated from its neighbours as well as from blood-borne substances[250]. The most important feature of these cells is that they contain intrinsic conductances that produce slow potential waves. Voltage-sensitive conductances necessary to generate spikes are activated by the slow potential waves to generate bursts[29, 30, 63, 145, 212, 233, 255].

Bursting activity can be generated in networks of cells without endogenous

bursters as a function of the connections between cells. Most network bursters depend on the activity of inhibitory connections on spontaneously firing cells: low frequency patterns are generated by alternate phases of rapid spontaneous firing and suppression of activity by activated neighbours. Other variants use networks to average ionic currents or rely on a fixed delay excitation mechanism to generate bursting. Examples of each class are given in the sections below.

1.4.2 Endogenous Bursters - Mechanisms

There are a large number of theoretical studies on endogenous bursting[30, 32, 191, 211, 212, 233, 252]. In general, these models have a spike generating mechanism of the Hodgkin-Huxley[120] type, and the slow process includes slow inward or outward currents which either activate currents which induce spiking or deactivate currents resulting in cessation of spiking[233, 252].

An illustrative example of the general form of these models is taken from[252]:

$$\frac{\partial v}{\partial t} = (-I_{fast}(v) - I_{K(V)}(v, n) - I_{slow}(v, S_l))/c_m \quad (1.8)$$

where c_m is membrane capacitance, I_{fast} is a voltage dependent inward current (usually sodium or calcium), $I_{K(V)}$ is a delayed rectifier potassium current, and I_{slow} is a slowly varying current. Variables for v (voltage) and n (the gating variable) are fast relative to the burst period, while S_l varies slowly with the burst period. The variables (v, n) generate the spikes within the bursts while changes in S_l cause the model to move from active to silent dynamics by activating an inhibitory outward current. The concentration of S_l gradually increases during the active phase, hyperpolarizing the cell. The downward shift in membrane potential raises the threshold for spiking, and firing stops. S_l returns to baseline during the silent phase and cell firing resumes.

Theoretical and experimental studies have generated several variations of the above equation with different dynamic properties. A classification scheme for the different mechanisms was constructed that groups models into three classes[233]. Classification is based on theoretical analysis of how the slow and fast subsystems

interact. In each case, fast variables can be considered at steady state (between bursts) or on a stable limit cycle (during bursts). The system of equations undergoes a bifurcation to switch between the two stable states as parameters controlled by slow changing variables are varied.

Class I models are bistable for a range of S_I , with a stable fixed point and stable periodic cycle. S_I increases during a burst until the trajectory undergoes a homoclinic bifurcation and moves to a stable fixed point. S_I then decreases until the trajectory jumps via a saddle node bifurcation back to the stable cycle. Class I models demonstrate an increasing period during each burst as the trajectory moves toward the homoclinic bifurcation. Class II models do not have bistability, but generate bursting via two slow variables with their own oscillation. A homoclinic bifurcation is crossed at the beginning and end of each burst, causing the period of oscillation to start high, decrease, and then increase with each burst. This characteristic change in period is called parabolic bursting. Class III systems are bistable like class I systems, but here S_I increases during a burst, causing the trajectory to lose stability via a Hopf bifurcation and leading to a stable cycle. S_I now decreases until the trajectory undergoes another bifurcation (a saddle node bifurcation of periodic orbits, in which one stable and one unstable limit cycle are created) and reaches a stable cycle. The period of oscillation during a burst is not determined by movement to this bifurcation point as it is with homoclinic (Class I and II) bifurcations.

1.4.3 Aplysia Models

A commonly studied endogenous bursting pacemaker is the R-15 cell in the abdominal ganglion of the mollusk *Aplysia*[29]. The general scheme for bursts in *Aplysia* is as follows: Calcium ions enter the cell with each action potential. During a burst, internal calcium accumulates at a rate faster than the cell can remove it. Eventually, internal calcium concentrations reach levels which both activate a calcium activated potassium outward current as well as reduce calcium current by calcium induced inactivation of calcium channels. These two effects hyperpolarize the cell, shutting off spiking activity. Inactivity halts calcium entry allowing the cell to slowly

lower internal calcium levels. The potassium channels shut when internal calcium concentration reaches baseline levels, and bursting resumes.

An *Aplysia* model was proposed by Plant[212]. Plant's scheme falls under the Type II class of parabolic bursting models. The fast variables are contained in sodium, potassium and leak currents, and the two slow variables are calcium current $I_{Ca^{++}}$ and a factor x that controls calcium activation. Slow oscillation in $I_{Ca^{++}}$ and x moves $I_{Ca^{++}}$ backward and forward through a homoclinic bifurcation. The rate of this oscillation is controlled by a time constant for activation of $I_{Ca^{++}}$; $I_{Ca^{++}}$ in the model activates and deactivates slowly in response to changes in voltage.

1.4.4 Single β -Cell Models

The pancreatic β -cell is also studied using the endogenous bursting framework. β -cells secrete insulin, which regulates use and uptake of glucose in target tissues. The character of electrical bursting in β -cells is in turn partially regulated by the glucose concentration surrounding the cells. The period of a burst monotonically increases during the burst. Models for β -cells follow a Class I scheme.

Early models for β -cell bursting were developed by Chay *et al.*[32, 33]. The proposed mechanisms are similar to those for *Aplysia*, but here Class I dynamics involving hysteresis and bistability are responsible for switching between silent and active states. Fast variables are controlled by voltage and calcium activated potassium currents. The early models have the internal calcium concentration $[Ca^{++}]_i$ as S_l and I_{slow} as either a calcium/potassium current[32] or a calcium inactivated calcium current[33].

The models proposed by Chay *et al.*[32, 33] have been challenged by experiments. The early models predict that I_{slow} varies with a slow sawtooth pattern (increasing slowly during a burst, and decreasing slowly between bursts). Direct measurements of $[Ca^{++}]_i$ showed that it varied as a square wave. This indicates that $[Ca^{++}]_i$ is fast, not slow, relative to the burst period, eliminating calcium as the slow variable. More recent models have set S_l to variables that could respond slowly to $[Ca^{++}]_i$. Satin and Cook[244] postulate that $[Ca^{++}]_i$ is slowly inactivated by voltage, however

Smolen and Kaizer[255] show this hypothesis is incompatible with voltage clamp data. Recently, Smolen and colleagues proposed $K(ATP)$ for I_{slow} and ATP for S_i [255], but these candidates have been ruled out by experiment[236, 254].

1.4.5 Coupled β -cell models

In addition to the uncertainty associated with the mechanisms of bursting, there is debate as to whether isolated β -cells burst at all. β -cells comprise the Islets of Langerhans, an organelle of 10^3 to 10^4 cells. Although bursting is a robust behaviour in whole islets, isolated β -cells spike erratically[252]. It has been proposed that electrical coupling between β -cells is necessary for bursting behaviour[256, 251].

One coupled cell model proposes that channel noise in individual β -cells is high, masking intrinsic bursting dynamics. Coupling cells acts to remove noise by averaging, allowing β -cells to burst[33, 251]. An alternate hypothesis is based on cell heterogeneity[256]. Bursting dynamics in most models occurs over a narrow range of parameters, with silence at one end of the range and continuous spiking at the other[252]. The heterogeneity hypothesis assumes that currents from different cells with non bursting modes of behaviour sum in such a way that the population as a whole bursts.

The coupled β -cell models depend on cell interactions to burst but they do so in a way different from other network models. The underlying assumption in both coupled β -cell models is that each individual cell bursts under the right (low noise or parametric) conditions.

1.4.6 Network Bursters

Bursting can be generated as a function of the connections between cells in the absence of endogenous bursting mechanisms. Network driven bursters are often studied in neuronal systems, where they are commonly referred to as central pattern generators (CPGs). Network bursters in these systems are characterized by a known set of neurons, with excitatory or inhibitory connections, which have well defined roles in generating bursting behaviour. Network bursters are well-studied in

invertebrate systems such as the lamprey pattern generator for locomotion[37], the *Tritonia* swim oscillator[280], and the locust flight motor pattern generator[281] but are also studied in vertebrates in the context of respiratory rhythm generation[216].

A simple example of a network burster is the sea slug *Tritonia* swim oscillator[280]. Here three groups of premotor interneurons are responsible for bursting. The principal synaptic mechanism underlying the swim oscillator is reciprocal inhibition with delayed excitation. Three broad groups of cells are involved in this system; dorsal swim interneurons (DSI), ventral swim interneurons (VSI) and a cerebral cell (C2). The swim cycle begins when the DSI depolarizes and begin to fire. These cells inhibit the VSI and excite C2. C2 fires synchronously with DSI, and stimulates VSI, which eventually start firing despite inhibition from DSI. The VSI acts to inhibit DSI and C2, terminating their bursts. VSI stops firing as stimulation via C2 is lacking, releasing DSI from inhibitory input, allowing the cycle to start again.

Inhibition of one group of neurons by activity of another is observed in complex networks. A mechanism similar to *Tritonia* is seen in the vertebrate respiratory rhythm generator, which involves six interconnected neuronal groups[216]. The lamprey swim pattern generator may involve chains of dozens of interconnected oscillators[37, 38]. The lamprey pattern generator consists of groups of endogenously bursting elements that use inhibition to synchronize dorsal and lateral elements 180° out of phase.

1.4.7 Reentrant Bursting Models

Bursting dynamics are sometimes a symptom of disease states. An example is repetitive paroxysmal tachycardia, which is characterized by the onset and offset of rapid cardiac activity. The mechanism of bursting in this system is not well understood. The tachycardia could be set by the rhythm of a spontaneously beating focus. Alternatively, the tachycardia could be caused by activation along a reentrant pathway. In this case, both termination and initiation could be caused by physiological properties of the conductive tissue itself.

A simple experimental model for paroxysmal tachycardias is presented in Kunysz

and associates[164]. The experimental model consists of spontaneously beating aggregates of chick embryonic atrial heart cells. A reentry loop is modeled by causing the aggregate to be excited a fixed time after it fires. The fixed delay is set so that the aggregate is forced to beat faster than its control cycle length. It is proposed that prolonged rapid activity results in the build-up of ion species which act to increase the cycle length of the aggregate (the increase in cycle length is called overdrive suppression[163]). The reexcitation pulse falls at progressively earlier times in the cycle of the aggregate until excitation fails. The aggregate beats again after a few seconds (its reset intrinsic cycle length) and the bursting pattern resumes.

The above model assumes the reentrant loop has properties that are invariant over time. Termination of reentry can occur due to changes in the conductive tissue itself. Dispersion effects as well as time-dependent changes in the refractory period and action potential duration can cause excitable tissue to block under rapid stimulation conditions. There is a large body of work discussing the dynamics of reentry and block on rings of cardiac tissue[227, 47, 272, 104]. Frame *et al.*[91, 20] conducted experiments on rings of cardiac tissue of fixed and variable (using a fixed delay protocol[91]) diameters. Reentry becomes unstable and eventually blocks for small rings.

1.5 The Heart as an Excitable Medium

The propagation of electrical activity in cardiac muscle involves the interaction of different ion species across a combination of active and passive ion channels and diffusion of charge through a heterogeneous substrate with dynamically changing conductances[77, 151]. Despite complexity inherent in conduction at microscopic scales, the heart has been approximated as a continuous excitable medium in many studies. A variety of cardiac tachycardias have been attributed to the formation of large scale patterns of excitation such as the interaction of several oscillators or the formation and break up of spiral waves. The following sections outline some of the differences between cardiac tissue and simple excitable media, and discuss reentry

and initiation of ectopic pacemaking activity in diseased heart tissue.

1.5.1 Conduction in Healthy Hearts

The mammalian heart is functionally organized into left and right sides. The right side of the heart circulates oxygen-depleted blood from the body to the lungs. Re-oxygenated blood flows from the lungs to the leftmost chambers and then is pumped to the rest of the body. The left and right sides of the heart each consist of two chambers. The lower two chambers of the heart (the *ventricles*) act as the main pumps while the top chambers (the *atria*) act to prime the lower chambers by filling them with blood prior to contraction.

The chambers of the heart contract in a precise sequence controlled by the oscillatory and conductive properties of a number of different cell types. All cardiac cells are excitable and some can sustain spontaneous oscillatory activity. In the healthy heart, the cardiac rhythm originates from a small area (3-8 mm²) called the sinoatrial (SA) node located in the upper right atrium. The spontaneous activity in the SA node acts to suppress the activity of other groups of slowly beating cells[271]. These latent pacemakers can drive the activity of the heart if the sinus node fails to beat.

The impulse originating from the SA node is conducted through the atria, which causes them to contract and move blood to the ventricles. The impulse then passes through the atrioventricular node, which is normally the sole conductive pathway connecting the atria and ventricles. The low electrical coupling and slow rise time of AV node cells impose a delay, which allows efficient filling of the ventricles. Once the impulse passes the AV node, it flows through rapidly conducting Purkinje fibers to the ventricles. The ventricles forcefully contract, completing the cycle.

There is strong spatial specialization in cells that constitute the myocardium. Action potential characteristics, such as duration, upstroke velocity, and threshold, change with anatomical location. Action potential duration is a factor controlling the refractory period and duration of contraction of cardiac cells[197]. The action potential duration is different for every cell type in the heart. The upstroke velocity

(which is a factor controlling conduction velocity) is fast in ventricular and atrial cells (300-400 V/s) and slow in AV and SA nodal cells (4 - 30 V/s)[199]. In addition, cells in different regions have different excitation thresholds and can display graded or partial excitation in response to suprathreshold stimuli[199].

There are several additional differences which distinguish the heart from the simple homogeneous excitable media, discussed in Section 1.3.2. Cardiac tissue has appreciable thickness, allowing for propagation in three dimensions, and cells are aligned in a preferred orientation. Conduction in cardiac tissue can also be affected by heterogeneities at the cellular level. Finally, cardiac tissue can display long term effects based on its stimulation history. These issues are discussed below.

1.5.2 Anisotropy

It is well established that conduction velocity is greater in the longitudinal direction than in the horizontal direction in cardiac tissue[77]. Adult cardiac ventricular cells have a tubular shape, with a length of approximately 100 μm and a width of 10-20 μm . Cells are aligned side to side in tissue. Conduction velocity is greater in the direction parallel to fiber orientation than in the direction perpendicular to the fiber axis[243]. The directional differences in velocity are believed to be due to higher resistivity in the transverse direction. This can be modeled in two-dimensional excitable media by using different diffusion coefficients in the x and y axes. Additional anisotropic effects are discussed in section 1.5.4 below.

Simulations with models with different diffusion coefficients give elliptical targets from point source excitation, and spirals 'stretched' in one axis. Patterns created by anisotropic simulations can be rescaled to have (approximately - see reference [292]) radial symmetry. Several interesting points relating to changes in conduction velocity along an elliptical target due to change in front shape are discussed in reference [292]. Anisotropy can give rise to subtle changes in regards to the direction of conduction, interaction of the wave with boundaries, and in the critical radius of curvature. The effects of anisotropy on conduction is an area of ongoing research [292, 170].

1.5.3 Propagation in 3D

Although cardiac systems are all three-dimensional, two-dimensional models can approximate many naturally occurring excitable media because they are too thin for the depth of the system to play an important role. A clear example of two-dimensional propagation can be seen in a monolayer of excitable tissue. Ventricular tissue can be over 1 cm thick, allowing formation of excitation patterns in three dimensions. Excitation patterns in three dimensions have been observed in the BZ reaction[285] and have been modeled numerically[286, 149, 221].

Spirals in three dimensions manifest as scroll waves. A simple scroll wave can be visualized as a loosely wound sheet with its ends connected. The spiral core becomes an elongated filament connected at both ends. A scroll wave has a circular filament. However, complex geometries with highly twisted filaments are possible. Simulations show that the filament follows a path that depends on both the curvature and the twist of the filament. In addition to moving through the medium, the filament can contract and expand in length. Scroll waves extinguish themselves if the filament collapses to a point or expands past the medium's boundaries[221, 149].

1.5.4 Local Heterogeneity

Propagation of activation partially depends on tissue microanatomy and the distribution and function of intracellular connections[77]. Anisotropic conduction can be partially modeled in continuous equations by assuming different diffusion equations in different directions (Section 1.3.2). However, the maximal upstroke velocity of cardiac cells also shows anisotropic effects. These local effects are not controlled by the diffusion coefficient, and therefore cannot be modeled by continuous equations such as Equation (1.6). Anisotropy in voltage implies that the discrete structure of cardiac muscle plays an important role in conduction[77, 292].

Discontinuities can be due to the distribution of gap junctions, and the presence of small clefts and anatomical boundaries such as blood vessels. The effects of heterogeneity on conduction have been investigated in models[238, 260] and in ex-

perisomal systems[77]. Experimental studies have shown that intracellular clefts (on the order of one cell in length) cause increases in the upstroke velocity at either side of the cleft and reductions of the upstroke velocity as the waves of excitation pass through narrow channels between clefts. Changes in the upstroke velocity are implicated as sites of reduced conduction velocity and unidirectional block.

The effect of small discontinuities is considered in greater detail in Chapter 5. An experimental system is presented which is highly heterogeneous at microscopic scales but appears to behave as a continuous (isotropic) medium at macroscopic scales. The relationship between discontinuous conduction and continuous theoretical models is unclear. Winfree[292] gives several ‘rules of thumb’ that test whether a continuous representation is valid at macroscopic scales (see Section 5.5.4). The continuity conditions are met in normal intact cardiac tissue and may hold for the model system under investigation as well. The distinction between continuous and discontinuous theoretical models is partially avoided by using a discontinuous cellular automaton model.

1.5.5 Overdrive Suppression and Fatigue

Periods of sustained rapid activity can affect conductive and oscillatory properties of cardiac tissue. These effects are thought to be due to the gradual build-up of ion species such as sodium, potassium or calcium[19, 39, 163, 271] which move across cell membranes during each action potential. Rapid activity overwhelms the cell’s ability to restore the ion concentrations to steady state levels. The resulting imbalances are indirectly responsible for secondary effects such as hyperpolarization or reduced cell coupling, which alter functional characteristics (such as period and conduction velocity) of the tissue. These long term effects are referred to as *fatigue* in conductive tissue[19] and *overdrive suppression* in pacemaking tissue[163].

Overdrive suppression has been studied in a variety of spontaneous cardiac tissue preparations. Overdrive suppression results in a gradual increase of the intrinsic cycle period in response to prolonged rapid pacing. Overdrive suppression has been modeled in heart cell aggregates[163] by assuming that each action potential (AP)

produces an outward (hyperpolarizing) current which decays exponentially with a long time constant.

Fatigue has been extensively studied in AV nodal preparations, where prolonged rapid stimulation produces pronounced effects. The dominant effect of fatigue on function is to shift the AV nodal recovery curve² upward, increasing the conduction time. Fatigue has been modeled by assuming that a fatigue term increases with each AP and decays away exponentially with a long (30 seconds) time constant[265]. The fatigue term is summed with the recovery curve, increasing conduction time. Fatigue is discussed in greater detail in Chapter 5.

1.5.6 Conduction in Diseased Heart: Reentry

A common cause of arrhythmias is reentrant excitation. Normal cardiac rhythm is a result of spontaneous pacemaking activity in the sinus node, which initiates travelling waves of excitation. Under some circumstances the travelling wave can circle back and reexcite cells that had recently fired, resulting in a spiral wave of excitation (Section 1.3.3), or circus motion reentry around an obstacle.

In healthy myocardium, rapid conduction velocity and long refractory periods protect the medium from reexcitation from the propagating wave front. For example, assuming a conduction velocity of 50 cm/s[154] the conduction time across the ventricle is 25-30 ms, which is 8 times shorter than the refractory period of the ventricles.

In the diseased heart, changes in conduction velocity and refractory period can result in conditions that allow reentry. The most common form, proposed by Mines[190] involves reentrant conduction around a non-excitabile obstacle. The conceptual model involves conduction along a one-dimensional ring of tissue. Reentrant excitation is possible because the tissue ahead of the exciting wavefront regains excitability. This can occur if the length of the refractory zone (sometimes called the

²The dispersion relation (Equation (1.4)) can be rewritten to give the dependence on the AV nodal conduction time on recovery time. This relation is known as the recovery curve. Fatigue would shift the dispersion relation downward, decreasing conduction velocity.

wavelength of excitation) is shorter than the circumference of the ring. Therefore, shorter refractory times, slower conduction velocities, and longer path lengths increase the ability of the circuit to support reentrant excitation. Mines's ring model may explain forms of reentry with distinct pathways such as Wolff-Parkinson-White syndrome[153], but is not easily applied to intact myocardium.

Allessie *et al.*[2, 3] showed that reentry is possible without an anatomical obstacle. Here, the mechanism of reexcitation is analogous to that of spiral waves as discussed in Section 1.3.3. The mechanism proposed by Allessie is called 'leading circle reentry' where a core region displays a slightly longer refractory period than the surrounding region. Partial excitation of the core result in increased refractoriness in these cells. This mechanism has the impulse circulating around the smallest possible pathway at the highest speed supported by the tissue. It is unclear whether the length of the reentrant pathway in this conceptual model is a function of the circumference of the functionally refractory core or is limited by refractory tissue directly in front of the excitation front.

Another related mechanism does not require heterogeneity of refractory times. The progress of a wave of excitation is only limited by refractory tissue directly ahead of it. The core (in this case a collapsed line) circumference is the minimum path length allowed by the refractory period. The period of rotation is therefore equal to or slightly greater than to the refractory time of the cells. As discussed above, the period of spiral wave rotation can also be a function of the excitability of (fully recovered) cells ahead of the wavefront. Here, the diameter of the core is determined by the curvature angle of the spiral tip, and is not limited by the refractoriness of the myocardium. Both leading circle and excitation limited reentry can in theory result in an *excitable gap*³[292]: a region of tissue ahead of the wavefront that is excitable. Excitable gaps have been observed experimentally in cardiac preparations[126].

³The 'leading circle reentry' model is commonly associated with having no excitable gap, as activations recur at the maximum rate allowed by the tissue. This conceptual model ignores curvature effects (which may not play a major role in defining rotor period in tissue as excitable as the heart) and dispersion effects. Dispersion effects predict that speed is inversely related to period. As there should be a gradient in wavefront speed near the reentry period[292], there should be a partially excitable gap.

1.5.7 Changes in Refractory and Excitability Properties in Diseased Hearts

Biological models for reentrant arrhythmias in intact hearts involve inducing ischemia (a reduction of blood flow.) Ischemic conditions can be produced by ligation of a coronary artery, reperfusion of acutely ischemic myocardium, or production of chronic infarction[153]. These models correspond to frequent clinical situations where tachyarrhythmias are encountered. Ischemic conditions alter ionic properties of cardiac cells and the functional properties of the tissue, allowing reentry.

Conduction velocity can be decreased by decreasing cell-cell coupling or by decreasing cell excitability. Decreased cell coupling is known to occur in ischemic tissue, and is probably due to an increase in intracellular Ca^{++} [153, 180]. Increases in Ca^{++} occur at later phases of ischemia (10-20 minutes after arrest of coronary flow[155]). Other changes occur earlier in ischemic models and are more likely to play important roles in induction of reentry. One of the first changes is an increase in excitability, brought on by a depolarization of the membrane and a decrease in the amplitude and duration of the action potential. Action potential shortening and membrane depolarization decreases the refractory period of cells, allowing reentry in ischemic tissue. On the other hand, infarction results in decreased cell coupling, while maintaining normal action potential shape[153]. This allows reentry to occur by decreasing conduction velocity.

1.5.8 Spontaneous Activity in Diseased Heart: Focal Mechanisms

Ischemic tissue can give rise to spontaneously beating foci that can result in a variety of arrhythmic conditions[153]. Experimental techniques for mapping waves originating from a small site are not precise enough to elucidate the exact origin of the waves. Five initiating mechanisms have been proposed[153]: microreentry, electrotonic reflection, delayed afterdepolarization (DAD), spontaneous activity, and excitation by injury currents. Microreentry and reflection have been shown to cause premature beats in small networks of cells[293, 133]. Two focal mechanisms which

have been extensively studied are excitation by injury currents and DADs.

Injury currents are due to local potential differences between ischemic and non ischemic cells (recall ischemia depolarizes cells and decreases action potential duration). If ischemic and healthy cells are electrically coupled the difference in membrane current produces local circuits that source excitation current to cells, inducing premature APs.

DADs are related to Ca^{++} overload which occurs late in ischemia. The cellular Ca^{++} overload causes a cyclic release of calcium from intracellular stores[153, 73]. Cyclic changes in calcium levels cause cyclic changes in membrane potential, as increased calcium levels cause inward movement of positive charge (electrogenic inward movement of sodium via the sodium/calcium exchanger and inward current through calcium activated cation channels are thought to play a role.)

1.5.9 Cultured Monolayers as Models for Cardiac Conduction

Heart cell monolayers are thin layers of tissue grown in culture dishes from embryonic or neonatal cardiac cells[56, 138, 173, 174]. Cardiac cells from very young animals have the capacity to easily form gap junctional connections with neighbouring cells in culture. After a few days in culture, embryonic cardiac cells are capable of supporting propagating waves of excitation over long distances. The availability of potential mapping techniques (See Chapter 3 and Section 1.6) has renewed interest in cultured monolayers, as they allow controlled environments for studying conduction on a microscopic scale[75, 127, 128, 151, 175, 230, 231, 232].

Israel *et al.*[127, 128] measured intercellular time delays in monolayers of 10-day chick embryo myocytes grown on a microelectrode array. Their aim was to test the theoretical model of Diaz *et al.*[61, 238] which indicated that conduction velocity within a cell is an order of magnitude higher than the average conduction velocity over many cells, and predicted delays of 0.45 ms between adjacent cells. Israel and coworkers found delays as long as 0.41 ms between adjacent cells under conditions of reduced cell-cell coupling.

Fast and Kleber[75] developed an experimental system that allows them to control the pattern of cell growth on a collagen substrate. The collagen substrate is brushed so that cells plated on the collagen align themselves in a parallel fashion. Impulses from the monolayers are recorded with a photodiode array. Their experimental system allows the study of anisotropy and heterogeneity in cell culture (see Sections 1.5.2, 1.5.4 and 5.5.4 for further discussion).

Fast and Kleber[76] calculated the minimum diameter of a strand of tissue necessary for conduction into a large area. Block of conduction during conduction from a small to large tissue volume occurs due to critical curvature beyond the point of expansion (see Equation (1.2)). Rhor and Salzberg[231] confirmed this theory with optical mapping studies of conduction in cultured neonatal rat myocytes. Rhor and colleagues developed a cell culture system that allows for patterns of cell adhesive collagen to be laid out using photolithographic techniques[230, 231, 232].

Rhor, Kleber *et al.*[232] altered cell-cell coupling and cell excitability on cultured strands of neonatal rat myocytes. The motivation for their study was to investigate slowed conduction, which is a contributing factor for the creation of reentrant arrhythmias. By lowering conductance the experimenters were able to slow conduction from 47 cm/s to less than one cm/s, a speed which would allow reentry in tissue areas of less than 1 mm².

The experimental work detailed in Chapter 5 investigates the effects of low coupling and heterogeneity on macroscopic conduction. Poorly coupled and spontaneously beating monolayers generate broken wave fronts which evolve to spiral waves. Heterogeneities in local cell-cell coupling may play an important role in generating unidirectional block at the site of initiation. Alternative theories are discussed in Chapter 5.

1.6 Mapping Techniques

Observing the phenomena in coupled oscillator and excitable media systems requires equipment that can simultaneously record signals from many spatial points

at one time. In some systems, such as the BZ reaction[88, 89] and slime mould aggregation[90, 217] wave propagation is visible to the naked eye and is slow enough to allow use of conventional camera equipment. Other systems, such as electrical propagation in cardiac and neural tissue, occur at fast time scales and are not directly visible by eye. The importance of spatio-temporal patterns in biology has driven development of sophisticated imaging techniques. This section is a brief introduction to propagation mapping in biological systems.

The electrical activity of interacting cells has been of interest to researchers for many years. The primary methods for detecting electrical activity have been extracellular electrodes that measure potential differences between different areas and intracellular microelectrodes that penetrate the cell and measure potential across the cell membrane. Arrays of extracellular electrodes remain popular for detecting patterns of propagation in whole[70] and cultured[127] cardiac preparations, and slices[105] and cultured neural[198] preparations.

Recently, optical methods have been developed that give direct information on membrane potential or the concentration of particular ion species without requiring cell penetration. A sample is stained with a voltage or ion sensitive dye whose fluorescence, absorption, or birefringence changes linearly with changes in the measured quantity in the cell. Over 1800 substances have been tested for optical responses, yielding 200 dyes with significant optical changes with acceptable levels of phototoxic damage and pharmacological side effects[246]. The mechanism producing optical changes controls the response time of the dyes. Dyes either act slowly, by diffusing in response to changes in the local environment, or act rapidly by changing orientation or conformation.

A number of fast responding dyes have been used to map potential changes in a variety of preparations. Early mapping studies were in giant squid axon[52, 266] and invertebrate central neurons[242, 241]. These techniques have more recently been applied to whole brain[111] and sections of the visual cortex[110] and olfactory system[215]. Intact[100, 168], sectioned[239, 50] and cultured[231, 77] cardiac preparations have also been studied. Reentry has been initiated and observed optically in

epicardial slices and whole heart[50, 100]. The effects of structural anisotropy and heterogeneity have also been studied using optical mapping techniques[77]. Propagation abnormalities due to extracellular stimulation have been investigated in intact heart[99]. The effect of geometry on block[231] has been investigated in cultured preparations, and measurements of the effects of wavefront curvature on conduction velocity and block[152, 28] have been investigated in intact and sectioned preparations. Optical mapping techniques have been used to track changes in individual ion species such as Ca^{++} [223, 72, 175] and metabolites (i.e. NADH[240]) in a variety of substrates.

All optical mapping studies involve specialized illumination and detection apparatus. In most studies, stained samples are illuminated over a relatively large area. Appropriate sources of illumination vary with the characteristics of the dye. Usually a tungsten halogen or mercury arc lamp fitted with appropriate filters to select optimal excitation wavelengths is used. Fluorescent light from the preparation is filtered to remove background reflected light. A detector with multiple elements, such as a photodiode array or CCD, is placed in the objective image plane and detects the signal of interest. The image is then processed and stored. Variations on this general scheme have used a single detector with a scanning excitation light source[196]. The specifics of the above schemes are discussed in detail in Chapter 3.

1.7 Oscillators and Excitable Media, Experiments and Theory

Oscillators' responses to periodic pacing have been studied extensively. An extension of these studies to intact cardiac preparations is limited to direct stimulation of pacemaking sites by extracellular electrodes. Simple interaction of two pacemaking sites located a distance from each other requires that the intervening excitable medium be considered. In some cases, theoretical understanding of the rhythms produced by a two oscillator system can be obtained by using gross approximations of the effect of the excitable medium on the interaction of the oscillators.

Chapter 2 investigates the two-way interaction of two pacemakers in an excitable media in the context of modulated parasystole. Parasystole is a generally benign arrhythmia caused by intermittent beats originating from an ectopic pacemaking site located some distance from the sinus node. In pure parasystole, the pacemakers do not phase reset each other, but the effects of either pacemaker can be masked if the surrounding excitable tissue is refractory. Modulated parasystole assumes the ectopic pacemaker can be reset by the sinus rhythm.

The modulated parasystole model is presented as a circle map which incorporates the Poincaré oscillator as the ectopic pacemaker. The Poincaré oscillator has well understood dynamics under conditions of direct forcing. Addition of assumptions associated with an excitable media introduces a discontinuity in the circle map which dramatically alters the dynamics. Investigations into the behaviour of the discontinuous parasystole map led to a general analysis of a broad class of discontinuous maps which have not previously been characterized. The class of maps investigated is chaotic but display a type of periodicity (called banded chaos) on a macroscopic scale. The analytic results from the chaotic maps are extended by carrying out simulations on the more complicated modulated parasystole map, which also displays quasiperiodic and periodic dynamics for certain parameters.

Experiments on oscillators coupled by an excitable substrate are performed using monolayer cultures of embryonic chick cardiac cells. The pacemaking behaviour of embryonic chick cells has been extensively documented. Aggregates of embryonic chick cardiac cells spontaneously beat and their dynamics under periodic forcing are relatively well understood. Aggregates are considered to be isopotential systems and therefore do not incorporate effects of conduction into their dynamics. However, conduction can be observed in spatially extended cultured monolayers of cardiac cells.

Here monolayers are used to investigate the interaction of many oscillators dispersed in space. Monolayers of coupled pacemaking cells can potentially provide insight into fundamental issues related to initiation and conduction in spontaneously active media. The behaviour of the model system may also help understand diseased

cardiac tissue, which can display spontaneous oscillations when ischemic[153].

Cultured cells couple to each other by forming gap junctions after they are plated. Microscopic examination of cultured cells suggests that functional connectivity increases over time. Older cultures (2-3 days) appear to fire in relative synchrony. A simple explanation is that a periodic target wave originating from one point in the culture acts to entrain the entire population. Younger cultures (1 day old) display complex dynamics. Cells occasionally synchronize, but often beat in a disorganized fashion. The dynamics of the entire system is impossible to characterize by eye as the field of view (where movement artifacts are visible) is only a few tenths of a millimeter in diameter. The dynamics of loosely coupled monolayer cultures is investigated using macroscopic mapping techniques and mathematical models in Chapter 5.

Chapter 2

Pacemaker Interactions: A Mathematical Model for Parasystole

2.1 Introduction

A circle map is a function that maps the circumference of a circle onto itself. A large body of work has investigated the dynamics of continuous circle maps for both their mathematical interest as well as their relevance to physical and biological problems[7, 10, 113]. Circle maps can also be discontinuous, but the bifurcations of these maps are not as well studied. One type of discontinuous circle map that has been investigated is the piecewise monotonically increasing noninvertible map as shown in Fig. 2.1. Keener[143] has considered maps for the case in which there is at least one fixed point. Such maps have long been considered by ergodic theorists [166], as interval maps. The dynamics of noninvertible discontinuous maps without fixed points have been studied for piecewise linear models in relation to the study of neuronal networks[23] and analog to digital converters[79]. Our present interest is in the application to modulated parasystole[43, 125, 134, 195].

Modulated parasystole is a cardiac arrhythmia caused by an abnormal (ectopic) pacemaking site located in the ventricles of the heart that competes with the normal rhythm generated in the sinus node[195, 43]. The two pacemakers do not fire independently of each other, but rather interact in a complicated fashion depending

on the electrophysiological properties of the cardiac tissue. Despite the apparent complexity of the problem, the reduction of the problem to mathematical questions involving circle maps has enabled one to make theoretical predictions, that in some cases can be confirmed in clinical studies. Previous theoretical studies of modulated parasystole employed discontinuous circle maps that for some parameter values displayed deterministic chaos[43, 118].

In this paper we consider the possible dynamics of a general class of discontinuous maps with no fixed points and apply our findings to a mathematical model for modulated parasystole. In Section 2.2, we review relevant terminology and definitions concerning circle maps. In Section 2.3, we consider the dynamics of a general class of discontinuous, noninvertible circle maps with slope greater than one and no fixed points. During the course of this investigation we became aware that some of the results in this section have already been presented using a different approach employing symbolic dynamics[79]. In Section 2.5 we describe a theoretical model for modulated parasystole using discontinuous circle maps without fixed points but with slope less than one for part of their domain. Results of simulation of the theoretical model are presented in Section 2.6. The results are discussed in Section 2.7.

2.2 Circle Maps

We consider circle maps, defined as follows. Consider the functions $f : [0, 1) \mapsto \mathbb{R}$, and $F = f(\text{mod } 1)$, where f is a single valued function. Then the map F is a circle map, $F : S^1 \mapsto S^1$. An example of a well studied class of circle maps is

$$\phi_{i+1} = M\phi_i + a + \frac{b}{2\pi} \sin(2\pi\phi_i) \pmod{1} \quad (2.1)$$

where M, a, b are constants. It is usual to assume that M is an integer, so that the circle map has topological degree M . The case $M = 1$ has been analyzed extensively [7, 113]. If M is not an integer the circle map will be discontinuous since $f(0) \neq f(1)$.

There are several important concepts that are necessary to characterize the dynamics of circle maps: periodicity, rotation number, resonance interval, Farey order

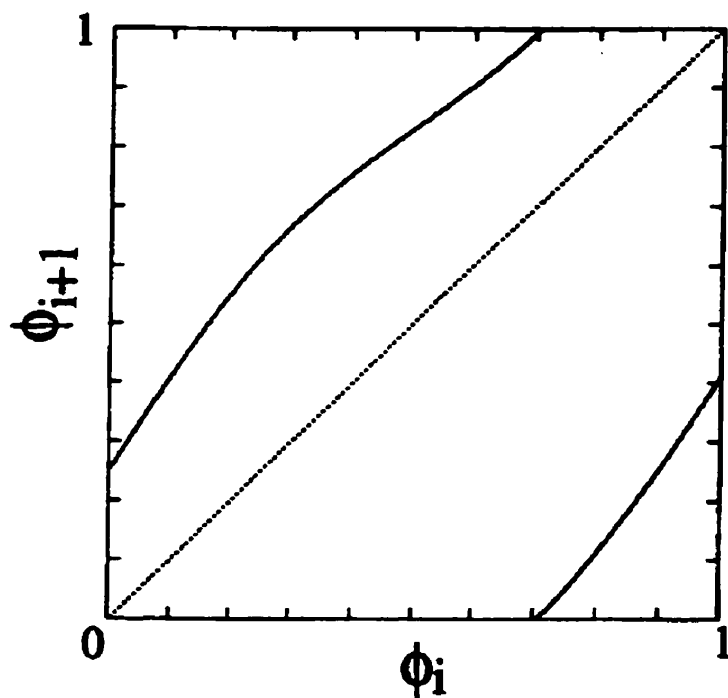


Figure 2.1: An example of a map in class F . The sine map, Eq. (2.1), with $M = 1.15$, $B = 0.4$, and $\alpha = 0.25$ has a discontinuity at $\phi = 0 = 1$, and is noninvertible since $F(0) < F(1)$.

and Lyapunov number.

Given an initial condition ϕ_0 , $\phi_{i+1} = F(\phi_i)$, $i = 0, 1, \dots$. Consider the sequence ϕ_0, ϕ_1, \dots , generated from iteration of F .

There is a periodic orbit of period n if $\phi_n = \phi_0$ and $\phi_j \neq \phi_0$ for $j = 1, 2, \dots, n-1$.

The *rotation number* $\rho(\phi_0)$, measures the average increase in ϕ per iteration of the circle map[6, 113]. For maps with discontinuities such as we have here there are several technical problems with applying the standard definitions, so we follow Bélair & Glass[16] and define

$$\rho(\phi_0) = \lim_{n \rightarrow \infty} \frac{1}{n} \sum_{i=0}^n [f(\phi_i) - \phi_i].$$

The rotation number is independent of the initial conditions for invertible circle maps, but may depend on initial conditions, for a noninvertible map[93, 143]. If ρ is sensitive to initial conditions $\rho(\phi)$, $\phi \in [0, 1)$, will span a non-zero interval $[\alpha, \beta]$, $\alpha \neq \beta$, called the *rotation interval* I [143].

Another concept associated with rotation number is the *resonance interval*, or mode-locking interval[7, 137]. The resonance interval is defined as the set of parameter values for which $\rho(\phi_0) = p/q$ for some $\phi_0 \in S$. For invertible circle maps, resonance intervals will have a *Farey order*; for two resonance intervals with rotation numbers $\frac{M}{N}$ and $\frac{M'}{N'}$ the most prominent resonance interval between them will have $\rho = \frac{M+M'}{N+N'}$.

The *Lyapunov number*, λ is defined

$$\lambda = \lim_{N \rightarrow \infty} \frac{1}{N} \sum_{i=1}^N \ln |F'(\phi_i)| \quad (2.2)$$

where negative values of the Lyapunov number indicate periodicity, zero indicates quasiperiodicity and a positive value reflects chaotic behavior. In this paper we take a positive Lyapunov number as a definition of deterministic chaos. Other studies define deterministic chaos based on a non zero rotation interval [93, 143], but as we show below, the two definitions are not equivalent.

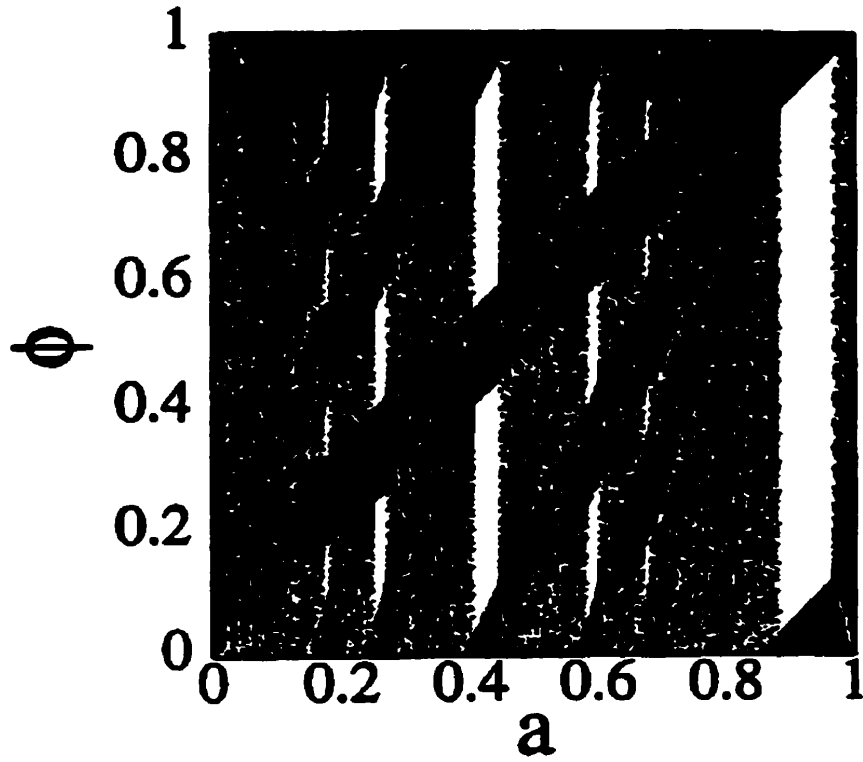


Figure 2.2: Bifurcation diagram for Eq. (2.1) with $b = 0.4$, $M = 1.15$. The first 500 different values of Φ are plotted after a transient of 1000 iterates, for 600 values of a evenly spaced on $[0,1)$.

2.3 The Dynamics of Discontinuous Maps

2.3.1 Banded Chaos

Figure 2 shows a bifurcation diagram for Eq. (2.1), where $M = 1.15$, $b = 0.4$, and a varies. The parameters are chosen so that the slope of the map is always greater than one, resulting in a positive Lyapunov number and chaotic dynamics. For each value of a , ϕ is plotted for 500 points following a transient of 1000 iterations. For some values of a and b , the trajectory is restricted to discrete bands on $[0,1]$. The trajectory moves in a periodic fashion between the bands, but the trajectory is chaotic within each band. This phenomenon was first observed in the logistic map and is called 'noisy periodicity'[178], or 'banded chaos'[116]. Banded chaos has been more formally investigated by ergodic theorists as asymptotic periodicity in the density evolution of maps[166, 167, 225].

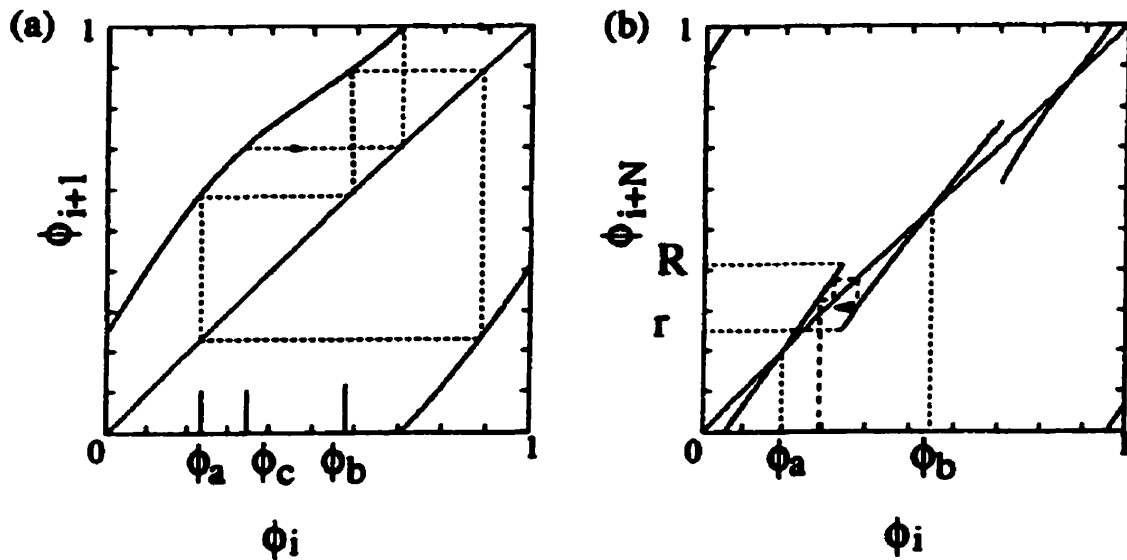


Figure 2.3: Fig. 3. Conditions for banded chaos illustrated for a period 3 orbit. (a) Between two unstable periodic points, ϕ_a and ϕ_b , there is a third point ϕ_c that maps to the discontinuity at $0(1)$. (b) ϕ_{i+N} ($N = 3$) is plotted against ϕ_i for a map where Eq. (2.4) holds. Here, $r = \lim_{\phi \rightarrow \phi_c^+} F^N(\phi)$ and $R = \lim_{\phi \rightarrow \phi_c^-} F^N(\phi)$ as described in the text.

Here we 1) describe conditions for banded chaotic behavior in discontinuous circle maps, and 2) argue that if the map displays banded chaos, then the rotation interval goes to a point and has a rational value.

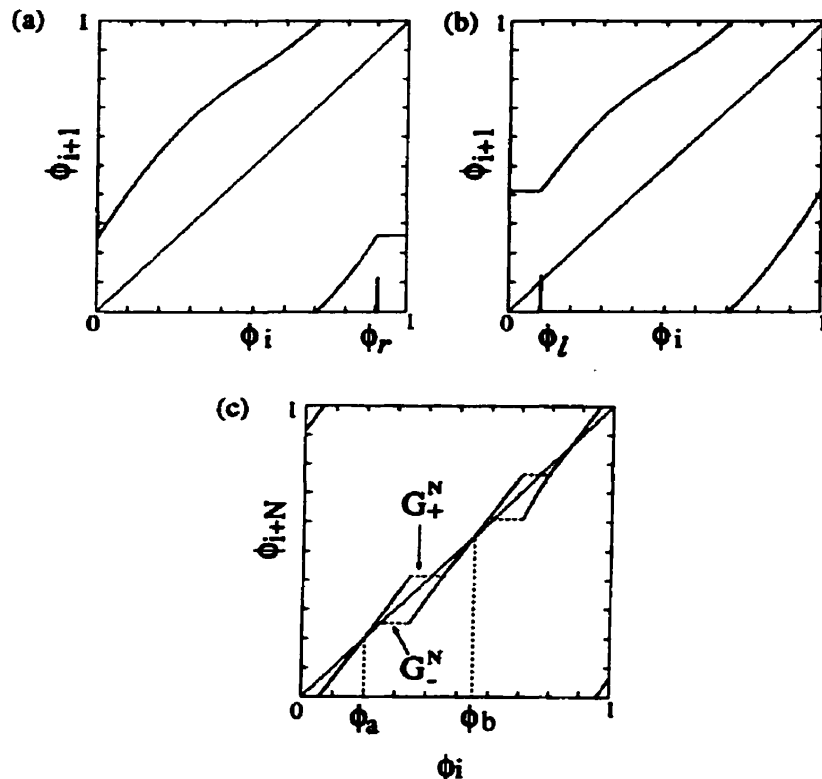


Figure 2.4: (a) G_+ and (b) G_- , as defined in the text. Both G_+ and G_- have a 'flat' region. (c) ϕ_{i+N} vs ϕ_i for G_+ and G_- where Eq. (2.4) is satisfied, $N = 3$. The flat regions of the third iterate of G_+ and G_- intersect the $\phi_{i+N} = \phi_i$ line. Also, G_+ and G_- share unstable periodic points ϕ_a and ϕ_b .

2.4 Conditions for Banded Chaos

We consider the following class of maps. If $F \in \mathcal{F}$, it is a circle map defined on $[0,1)$, with a discontinuity at $\phi = 0(1)$, such that:

1. $F(0) < F(1)$.
 2. $F'(\phi) > 1$, for all $\phi \in [0, 1)$.
 3. $F(\phi) \neq \phi$, for all $\phi \in [0, 1)$.
- (2.3)

An example of a map in class \mathcal{F} is shown in Fig. 2.1.

If $F \in \mathcal{F}$, $F'(\phi) > 1$ for all ϕ , the Lyapunov number of F will be positive. Although F has no stable periodic orbits, the density of the trajectory can have a regular structure.

Consider an unstable period N orbit of a function $F \in \mathcal{F}$. Assume that ϕ_a and ϕ_b are two periodic points of F with $\phi_b > \phi_a$, and that no other periodic points of F lie in the interval $[\phi_a, \phi_b]$, Fig. 2.3a.

The function F^N is shown in Fig. 2.3b. Since the slope of F is greater than 1, the slope of F^N is also greater than 1. Therefore, $F^N > 1$ at ϕ_a and ϕ_b . Since $F^N(\phi_a) = \phi_a$, F^N cannot be continuous in the interval $[\phi_a, \phi_b]$, since if it were this would imply that $F^N(\phi_b) > \phi_b$, which cannot be true. Therefore there is a point ϕ_c , $\phi_a < \phi_c < \phi_b$, such that F^N is discontinuous at ϕ_c . The point ϕ_c maps to the discontinuity in F at 0(1). As the function F^N has only N images of the discontinuity at 0(1), ϕ_c is the only discontinuity such that $\phi_a < \phi_c < \phi_b$.

Define

$$r = \lim_{\phi \rightarrow \phi_c^+} F^N(\phi), \quad R = \lim_{\phi \rightarrow \phi_c^-} F^N(\phi).$$

Provided that

$$R < \phi_b, \quad r > \phi_a, \quad (2.4)$$

then for any point $\phi \in [\phi_a, \phi_b]$, $F^N(\phi) \in [F^N(r), F^N(R)]$. Consequently, if conditions Eq. (2.4) hold, then for n a positive integer, for any point $\phi \in [\phi_a, \phi_b]$, $F^{nN}(\phi) \in [F^N(r), F^N(R)]$. Thus, though the trajectory is chaotic, it is confined to restricted regions on $[0, 1)$. This is what we call banded chaos.

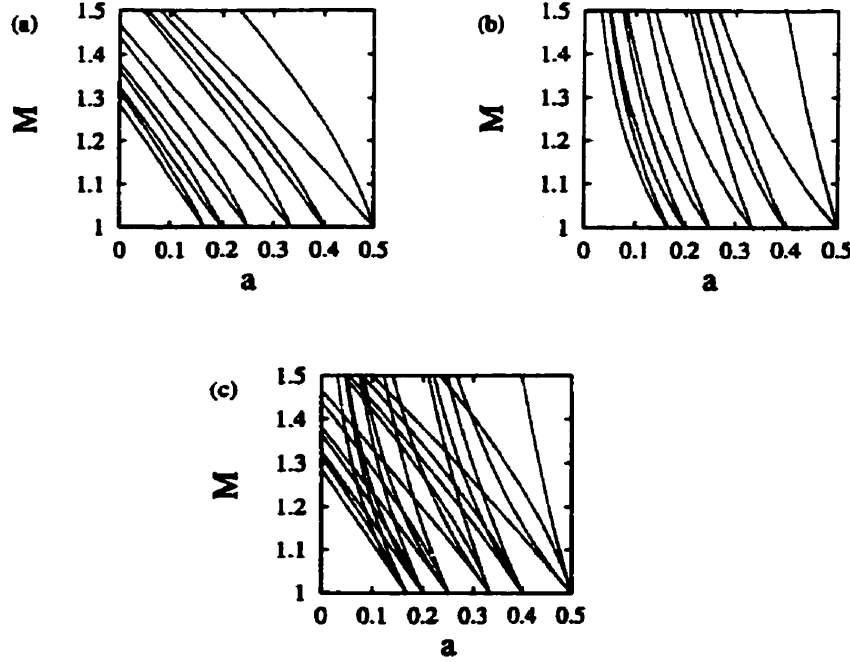


Figure 2.5: Resonance zones calculated for G_+ and G_- . All zones with period less than or equal to 6 were calculated. Here we give a sample calculation for determining the first order period 3 resonance zone for G_+ . The ‘flat’ of G_+ covers $[0, \phi_r)$ (see text). For a trajectory to have a stable period $N : 1$ orbit, the point ϕ_r must map in three iterates to $[0, \phi_r)$. If this is true then $\phi_r > F^3(\phi_r)$ and $0 < F^3(\phi_r)$. The point ϕ_r is equal to $(M - 1)/M$, and $F^3(\phi) = M^3(\phi) + a(M^2 + M + 1)$. The equations for the boundaries of the resonance zone are therefore $a = (M - 1)/(M^2 + M + 1)$ and $a = (\frac{M-1}{M} - M^3 + M^2 + 1)/(M^2 + M + 1)$. (a) Resonance zones for G_+ . (b) Resonance zones for G_- . The 6 resonance zones present in both Figs. 5a and 5b are ordered, from right to left, 1/2, 2/5, 1/3, 1/4, 1/5, and 1/6. (c) Resonance zones for both G_+ and G_- . The overlap corresponds to the banding zones for Eq. (2.6).

2.4.1 Rotation Interval for Banded Chaotic Maps

We now consider the rotation interval for maps that display banded chaos. Define ϕ_d as the point of discontinuity of the map F . The discontinuity separates the map into two branches, a left hand branch and a right hand branch. We call ϕ_l the preimage of $F(1)$ on the left hand branch, and ϕ_r the preimage of $F(0)$ on the right hand branch. We now construct two maps G_+ and G_- , that bound F ,

$$\begin{aligned} G_+(\phi) &= F(1) \text{ for } \phi \in [0, \phi_l) \\ G_+(\phi) &= F(\phi) \text{ for } \phi \in [\phi_l, 1) \\ G_-(\phi) &= F(\phi) \text{ for } \phi \in [0, \phi_r) \\ G_-(\phi) &= F(0) \text{ for } \phi \in [\phi_r, 1) \end{aligned} \tag{2.5}$$

As G_+ and G_- are continuous nondecreasing circle maps they each have a single ρ for all initial ϕ_0 [116]. Since G_+ and G_- have a region where the function is flat and are increasing functions with slope greater than one everywhere else, the rotation number assumes rational value[21]. Maps G_+ and G_- bound F so that $G_+(\phi) \geq F(\phi) \geq G_-(\phi)$ for all $\phi \in [0, 1)$. It follows[93, 116] that the rotation interval of F is bounded by $\rho(G_+)$ and $\rho(G_-)$ for all $\phi \in [0, 1)$.

Figure 2.4c shows G_+ and G_- , where ϕ_{i+N} is plotted against ϕ_i with $N = 3$. G_+ (or G_-) will have a stable period N orbit if the flat portion of the N^{th} iterate of $G_+(\phi)$ (or $G_-(\phi)$) intersects with the $\phi_i = \phi_{i+N}$ line, as shown. As the N^{th} iterate of G_+ and G_- share points R and r , respectively, with $F^N(\phi)$ (see Fig. 2.3b), the conditions for banded chaos (Eq. (2.4)) are the same as the conditions for G_+ and G_- to have stable period N orbits. In addition, Eq. (2.4) ensures that G_+ and G_- share unstable period N points ϕ_a and ϕ_b , as shown. As continuous nondecreasing circle maps of this class have a constant rotation number for all initial conditions[21], both G_+ and G_- will have the same rotation number as the unstable orbit including ϕ_a and ϕ_b . Therefore, the rotation interval assumes the rational value $\rho(F) = \rho(G_+) = \rho(G_-)$.

The above results allow us to determine whether a given map of class F will have a banded structure in the density of the trajectory over many iterates. If Eq.

(2.4) is satisfied, the trajectory will then be restricted to N discrete bands, on $[0,1)$. The existence and the number of bands as well as $\rho(F)$ depends on parameters of F . In the following we use G_+ and G_- to study the bifurcations of a simple two parameter discontinuous map of class F .

2.4.2 Bifurcation Structure of Discontinuous Maps

We now investigate the bifurcations of a simple equation in \mathcal{F} . We consider the map

$$\phi_{i+1} = M\phi_i + a \pmod{1}, \quad (2.6)$$

where $(1 < M < 2 - a)$ and $(0 < a < 1)$. The bifurcations of Eq. (2.6) have been investigated by Feely *et al.*[79] using a different approach employing symbolic dynamics.

For any values of a and M , we can define G_+ and G_- as in Section 2.4.1. Figure 2.5a and 2.5b show all resonance zones up to period 6 calculated for G_+ and G_- . Figure 2.5c shows the resonance zones of G_+ superimposed on those G_- . The regions where zones of the same rotation number overlap correspond to regions in the parameter space where Eq. (2.4) is satisfied for Eq. (2.6) and where the banding of the trajectory occurs.

We can state the following results for Eq. (2.6):

1. Parameters that result in banding are organized into discrete zones, which we call *banding zones*.
2. The rotation number within each banding zone is a constant rational value M/N , and the trajectory will be restricted to N bands on $[0,1)$.
3. The banding zones have a Farey ordering in the parameter space.
4. The banding zones cannot overlap.

The above results are a consequence of the structure of the resonance zones for the bounding maps G_+ and G_- . Banding occurs in regions in the parameter space

(M, a) where $\rho(G_+) = \rho(G_-)$. For constant M , this will occur only when equivalent resonance intervals of G_+ and G_- overlap. Therefore, a (M/N) banding zone will occur only on a subset of a that gives rise to a M/N resonance interval of G_+ . As G_+ has a Farey order with respect to ρ this will also be true for the banding zones for Eq. (2.6). For any value of M and a , G_+ is a non-decreasing map and therefore the resonance zones cannot overlap in the (M, a) plane. We conclude that the banding zones for Eq. (2.6) do not overlap in the parameter space.

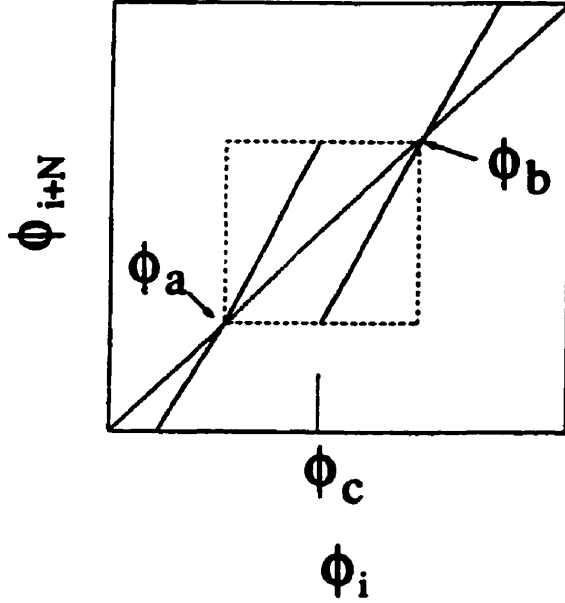


Figure 2.6: Schematic diagram for N bands in Eq. (2.6). The graph of ϕ_{i+N} vs. ϕ_i must be within the square. The line segments must have a maximum slope of 2, or else they fall outside the box. The line segments have slope M^N , and so if $M^N < 2$ banding with N bands will occur.

The above results are general in that they will hold for all maps of class \mathcal{F} . We now discuss the conditions for the existence of a given M/N banding zone for Eq. (2.6). Consider the diagram of ϕ^N vs ϕ shown in Fig. 2.6. Equation (2.4) will hold if $F^N(\phi)$, $\phi \in (\phi_a, \phi_b)$, falls within a square with corners at unstable fixed points ϕ_a and ϕ_b , as shown. As we are considering the upper and lower bounds of Eq. (2.4)

$(R \rightarrow \phi_b, r \rightarrow \phi_a)$, and both line segments within the square have equal slope, the discontinuity ϕ_c is located between the unstable fixed points at $(\phi_a + \phi_b)/2$. The slope of the line segments, which is equal to M^N , is therefore equal to two in this limiting case. Therefore, all N banded zones, with $\rho = p/N$, $p < N$, will first appear as M decreases below $\sqrt[N]{2}$, and disappear as M approaches 1. Also, for a given M , the highest order banding zone (N') is given by the integer part of $\log(2)/\log(M)$. As $M \rightarrow 1$, $N' \rightarrow \infty$, and as there are at least N' different banding zones, the number of different banding zones also goes to ∞ as M decreases to 1.

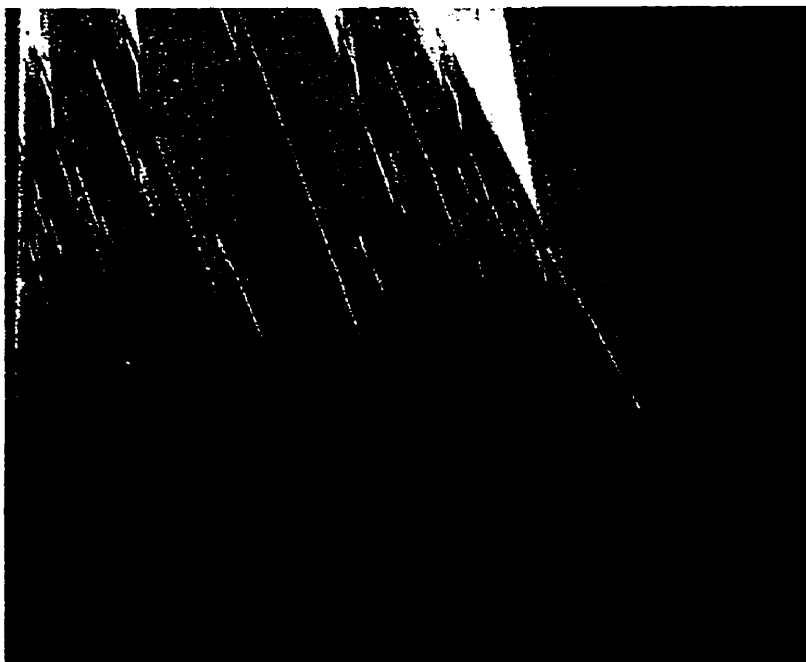


Figure 2.7: Colour representation of the bifurcation structure of Eq. (2.6). The rotation numbers of G_+ and G_- were calculated for 10^6 points in the (M, a) plane. For each point, the rotation numbers of G_+ and G_- were determined using 500 iterates. The colour represents the difference in rotation numbers of G_+ and G_- . At each point in the (M, a) plane. Zero rotation interval width corresponds to black. As the rotation interval width increases, the colours change from violet \rightarrow blue \rightarrow green \rightarrow red \rightarrow yellow.

Figure 2.7 is a plot created by determining the width of the rotation interval using G_+ and G_- for many values of M and a . Each point in Fig. 2.7 is a colour

representation of the difference in the rotation number for G_+ and G_- ($\Delta\rho[G_+, G_-]$). The intensity of the colour used is proportional to the magnitude of the rotation interval. If $\Delta\rho[G_+, G_-] = 0$ the colour is black. The banding zones are black.

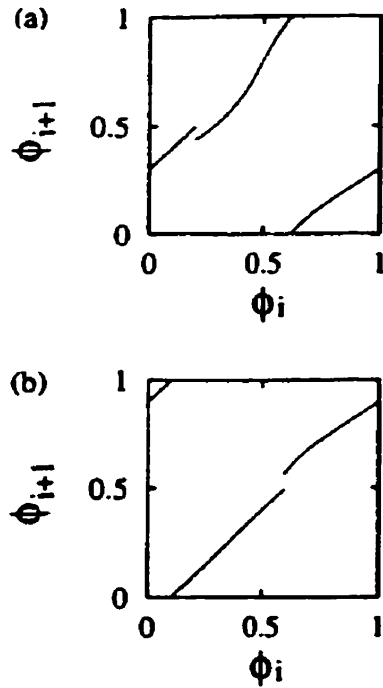


Figure 2.8: Equation (2.7) for (a) $\theta = 0.34$, $B = 0.5$, $\tau = 0.3$ and (b) $\theta = 0.34$, $B = 0.5$ and $\tau = 0.9$.

2.5 A Theoretical Model for Parasystole

A mathematical model for parasystole was proposed by Moe and co-workers [195], and several subsequent studies have proposed models in terms of nonlinear maps[43, 101, 118, 125, 134, 59, 273].

In this paper we follow the development of Courtemanche *et al.*[43]. The mathematical model of modulated parasystole used in this study is based on the following rules:

- The sinus and ectopic pacemakers each have their own intrinsic periods, designated t_S, t_E , respectively.
- A beat initiated by the sinus node may modulate the time when the ectopic pacemaker next fires;
- There is a refractory period (θ) after each sinus beat.
- After each ectopic beat the next sinus beat is blocked.

To express this model in mathematical terms, we call ϕ_i the phase of the sinus beat in the ectopic cycle. The i th sinus beat at phase ϕ_i leads to a phase resetting of the ectopic pacemaker so that immediately after the sinus beat the phase of the ectopic pacemaker is $g(\phi_i)$, where g is a function (sometimes called the phase transition curve) that is either measured experimentally or modelled in an approximate fashion. The model for modulated parasystole can be expressed in terms of the following difference equations:

$$\begin{aligned} \phi_{i+1} &= \alpha(\phi_i) \\ \begin{cases} \alpha(\phi_i) = \phi_i + \tau & \text{if } \phi_i \in [0, \tau - \frac{\theta}{T_E}] \\ \alpha(\phi_i) = G(\phi_i, B) + \tau & \text{if } \phi_i \in [\tau - \frac{\theta}{T_E}, 1] \end{cases} \end{aligned} \quad (2.7)$$

where $G(x, B)$ gives the degree of modulation. The general form of this model was first used by Courtemanche *et al.*[43], where phase resetting curves $G(x, B)$ were based on clinical data. In this study $G(x, B)$ is modelled by the Poincaré oscillator, which has been studied as a model for biological oscillators[103, 115, 144]. The Poincaré oscillator can be given by:

$$\cos(2\pi G(\phi, B)) = \frac{B + \cos 2\pi\phi}{(1 + 2B \cos 2\pi\phi + B^2)^{\frac{1}{2}}} \quad (2.8)$$

The Poincaré oscillator has been proposed as a model for phase resetting in parasystole[248]. The Poincaré oscillator may not provide phase resetting curves as realistic as those derived from clinical data. However, it allows constant changes in stimulation amplitude. The periodically stimulated Poincaré oscillator can display periodicity and

quasiperiodicity, as well as chaos, under different conditions. Chaotic dynamics are observed at high stimulation strengths ($B > 1$) in the periodically stimulated Poincaré oscillator.

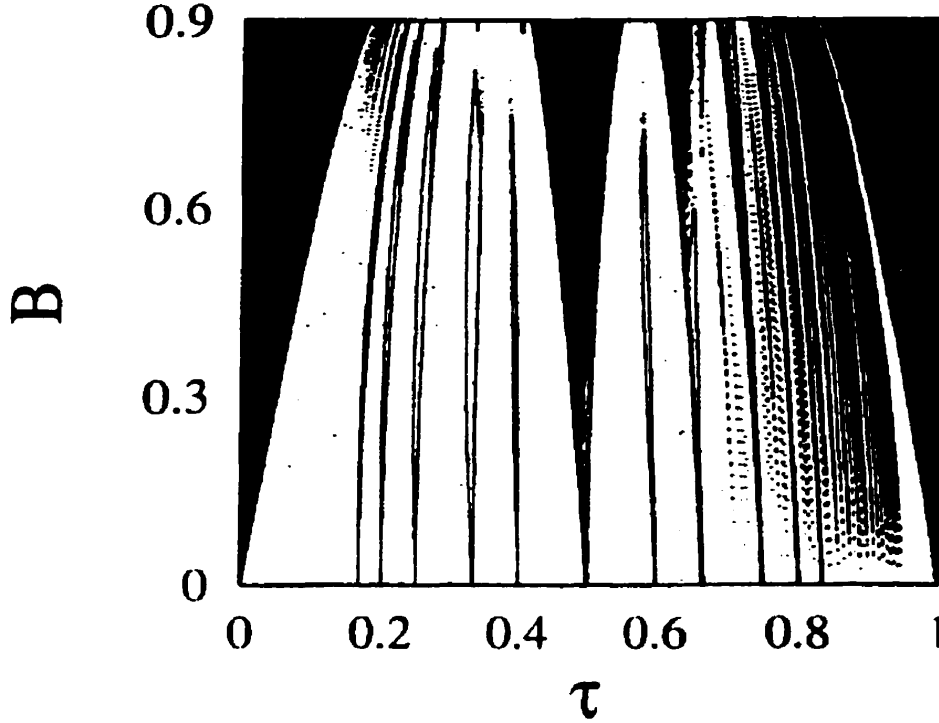


Figure 2.9: Representation of dynamics in Eq. (2.7) for constant $\theta = 0.34$. B was varied from 0 to 0.9 in increments of 0.001, and τ was varied from 0 to 1, in steps of 0.001. Periodicity was checked in the phases (ϕ) as well as from symbolic sequences \mathcal{M} collected by counting the number of iterates before $f(\phi) > 1$. Periodicity was determined by collecting 2000 values (after a 10000 transient) of \mathcal{M} and ϕ , and checking for periodicity of up to length 100. Values of B and τ that give rise to banding have periodic symbolic sequences with aperiodic sequences of phases. Parameters that give rise to banding are outlined (only parameters that give rise to 6 bands or less are shown). Regions that are periodic have both periodic phase and symbolic sequences (coloured black).

Equation (2.7) is shown in Fig. 2.8. It has a discontinuity at $\phi_\delta = \tau - \frac{\theta}{T_E}$. Equation (2.7) is piecewise monotonic if the stimulation strength B is less than one. The nature of Eq. (2.7) at the discontinuity depends on τ . If $\tau < \frac{1}{2(1-\theta)}$ the map

will step down at the discontinuity (this is the condition that allows banded chaos), whereas if $\tau > \frac{1}{2(1-\theta)}$ the map will step up at the discontinuity. In addition, the slope of the map is less than one for a large part of its domain.

Parasystole is frequently characterized in models and in clinical situations by counting the number of expressed sinus beats between each expressed ectopic beat (NIBs)[125, 101, 43, 59, 273]. Expressed ectopic beats occur in Eq. (2.7) when $\phi \in (0, \phi_\delta)$. A sequence of NIB values can be generated by counting the number of iterates minus one that fall in $[\phi_\delta, 1)$ for every iterate in $[0, \phi_\delta)$ [43].

2.6 The Dynamics of Parasystole

In order to test for banded chaotic behavior such as that seen in Eq. (2.6), we collected symbolic sequences as well as sequences of phases from continued iteration of the parasystole map. A symbolic sequence consists of a list of symbols representing a discrete region of the map. A symbolic sequence for maps like Eq. (2.7) would typically involve three or more symbols to represent the individual branches of the map. However, we collect a symbolic sequence $\mathcal{M} = m_1, m_2, m_3 \dots$ where m equals the number of iterates before the trajectory passes to the leftmost branch (Fig. 2.8) of the parasystole map. This is equivalent to counting NIBs. However here we count both expressed and suppressed beats. The symbolic sequence \mathcal{M} also gives information on the rotation number: if \mathcal{M} repeats every N symbol, then $\rho = N/(m_1 + m_2 + \dots m_N)$.

The N banded chaotic trajectory would appear the same as a period N trajectory when counted as symbolic sequence \mathcal{M} , as long as a chaotic band does not cover the origin. Values of B and θ that give rise to banding should then have periodic symbolic sequences with aperiodic sequences of phases. Regions where no banded chaos or periodicity exist should have aperiodic sequences in the phase and symbolic sequences. Regions that are periodic will have both periodic phase and symbolic sequences.

Equation (2.7) was iterated over a large range of values of B and τ . Periodicity

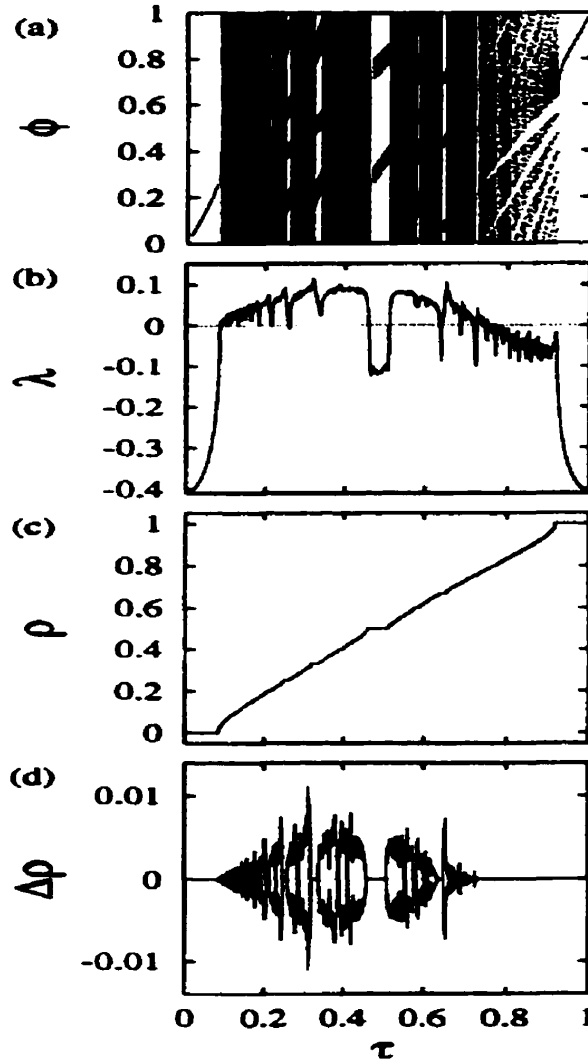


Figure 2.10: Characterization of dynamics in Eq. (2.7). with $B = 0.5$, $\theta = 0.3$ and τ varying. (a) The bifurcation diagram, (b) The Lyapunov number λ , (c) The rotation number ρ . Equation (2.7) was iterated 100000 times for each of 1000 values of τ and the first 20000 iterates were discarded. The bifurcation diagram was plotted using the first 500 different points after the transient. (d) Theoretical maximum for the rotation interval. This value is determined using a similar construct used to generate Figs. 4 and 5. Two continuous invertible maps are generated that closely bound Eq. (2.7). The rotation number is calculated for both maps, the results are averaged and subtracted from each original rotation number. The resulting two points are plotted against τ .

was determined for both symbolic sequences and phase sequences. The results are summarized in Fig. 2.9. In Fig. 2.9, black dots were plotted at points in the parameter space where periodicity was detected in the phase (maximum period 100 for 2000 collected values, after a 10000 transient). Parameters that result in periodicity in \mathcal{M} but not in the phase are outlined in this figure. For clarity only parameters that result in up to 6 bands are outlined. The period of \mathcal{M} found in each of these outlined zones is constant throughout the zone. The relative placement of these zones in the (B, τ) parameter space is the same as that seen for Eq. (2.6), Fig. 2.5.

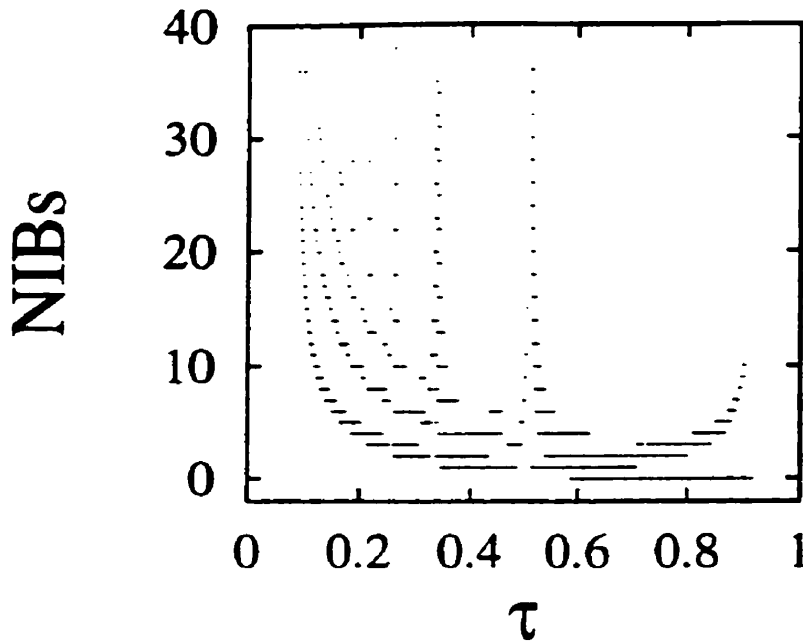


Figure 2.11: Different NIB values found in Eq. (2.7) for $B = 0.5$, $\theta = 0.3$. NIBs are counted by determining the number of successive iterates before $0 < \phi < (\tau - \frac{\theta}{T_E})$. The equation was iterated 20000 times for each value value of τ .

In contrast to the relatively simple situation found in Eq. (2.6), the parasystole map has a slope that is less than one over a range of ϕ_i , which allows for periodic and chaotic dynamics [143]. Here we investigate the relationship between rotation interval, Lyapunov number and periodicity for Eq. (2.7). Figure 2.10 summarizes

the results obtained by determining the Lyapunov number and the rotation number for τ from 0 to 1 (400 steps using multiples of an irrational number) for a constant weak stimulation strength ($B = 0.5$), for a range of initial conditions. Figure 2.10a shows the bifurcation diagram, Fig. 2.10b shows the Lyapunov number vs τ , Fig. 2.10c shows the rotation number vs τ , and Fig. 2.10d shows the rotation interval obtained from calculating bounding maps G_+ and G_- as described in Sec. 3.3.

Equation (2.7) is monotonic increasing for $\frac{1}{2(1-\theta)} < \tau < 1$ ($\tau > 0.71$). The dynamics are periodic [143] for discontinuous maps of this class (ρ is irrational on a set of measure zero). Periodic dynamics is detected in the bifurcation diagram (Fig. 2.10a) and by a negative Lyapunov exponent (Fig. 2.10b) for τ in this range. Another region of periodicity can be seen between $\tau = 0.45$ and 0.55. Regions in the bifurcation diagram that correspond to the chaotic banding zones seen in Fig. 2.5 are recognizable by the formation of distinct bands in this figure (for example, the 3:1 region can be located at $\tau = 0.3$).

The Lyapunov number is positive for a large range of τ , indicating chaotic dynamics. For most values of τ where the Lyapunov number is positive, the rotation number is sensitive to initial conditions (Fig. 2.10d), resulting in a range of rotation numbers for different initial conditions. The rotation number (Fig. 2.10c) is constant over ranges of τ that correspond to local decreases in the Lyapunov exponent (Fig. 2.10b). Local decreases in the Lyapunov exponent also correspond with a reduction in the rotation interval to a point (Fig. 10d). The rotation interval can have zero width even where the Lyapunov exponent remains above zero, which is characteristic of banding zones as described in Sec. 3.

In Fig. 2.11 we plot the different NIB values (expressed sinus beats between successive expressed ectopic beats) found from iterating Eq. (2.7) against τ for the same stimulation strength and refractory period used in Fig 2.10. Ectopic beats are concealed for $\tau < 0.08$ and $\tau > 0.92$. Values of τ in the banding zones give rise a large number of possible NIB values. NIB values of greater than 1000 have been found in these regions. In between these regions, the number of different NIB values for a given τ decreases.

We can make the following statements about possible NIB sequences for parameters within the banding zones. If there is a N banded chaotic trajectory, then ϕ returns every N iterates to a region centered around the discontinuity at ϕ_δ , but moves chaotically in this region. As the trajectory can return to $[0, \phi_\delta)$ at most every N iterates, and as the first sinus beat after an ectopic is blocked, NIB values must be in the set $Nn - 1$, where n is a positive integer. The NIB sequence will be aperiodic, as the trajectory moves in a chaotic fashion between the branches on either side of the discontinuity. Also, a banded chaotic trajectory will be associated with a relatively constant sinus-ectopic coupling interval, as ϕ is restricted to narrow regions on $[0, 1)$.

Figure 2.12 shows the dynamics of Eq. (2.7) for 4 values of τ stepping through the 3:1 banding zone. NIB values are plotted against the phase that the ectopic beat falls in the sinus cycle (ϕ_s) in the right column and ϕ_{i+3} plotted against ϕ_i in the left column. For $\tau = 0.32$ (Fig 2.12b) the conditions in Eq. (2.4) are satisfied and banding occurs; ϕ_s is restricted to a narrow region on $[0, 1)$ and NIB values are part of the set $3n - 1$. For τ outside of the banding zone ectopic beats cover $[\theta, 1)$, and NIB values are not restricted to $3n - 1$.

The dynamics associated with a banded chaotic behavior in Eq. (2.7) have been observed in clinical situations. Concealed bigeminy and concealed trigeminy, where NIBs conform to the formula $2n - 1$ and $3n - 1$ respectively, are frequently observed[247, 205]. Concealed quadrigeminy ($4n - 1$)[8] and concealed pentagemy ($5n - 1$)[9] have also been documented. These rhythms can be seen in Fig. 11 for τ between 0.2 and 0.21 ($5n - 1$), τ between 0.24 and 0.25 ($4n - 1$) and τ between 0.29 to 0.31 ($3n - 1$). There is a large bigeminy zone associated with the periodic region (τ between 0.48 and 0.5). Variant rhythms exist for parameters close to the banding zones of Eq. (2.7). For example, for τ between 0.52 and 0.56, all NIBs equal one or are even ($2n$), which has also been observed clinically[171].

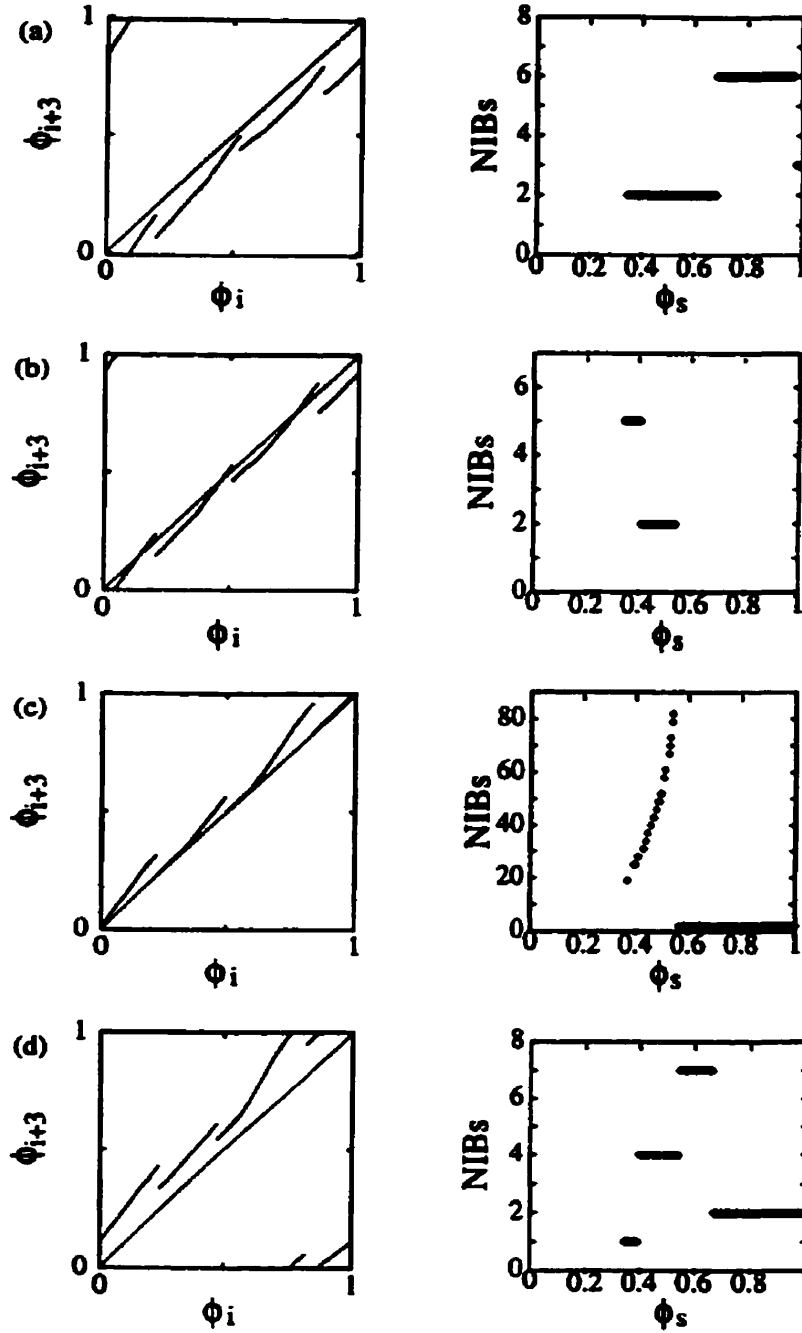


Figure 2.12: The dynamics associated with transition through the $1/3$ banding zone in Eq. (2.7) for $B = 0.5$, $\theta = 0.34$. ϕ_{i+3} is plotted against ϕ_i in the left column. NIBs are plotted against the phase in the sinus cycle (ϕ_s) where the ectopic beat occurred. Ectopic beats cannot occur during the sinus cycle's refractory time. (a) $\tau = 0.3$, (b) $\tau = 0.32$, (c) $\tau = 0.34$, (d) $\tau = 0.36$.

2.7 Discussion

We have analysed the bifurcations of a simple noninvertible discontinuous circle map, and applied these results to understanding the bifurcations of a general model for modulated parasystole. In section 3 of this paper, we found that piecewise monotonic discontinuous noninvertible maps with no fixed points can display banded chaos: the trajectory is restricted to narrow regions in the phase space. Banded chaos in these maps is associated with a positive Lyapunov exponent and a rotation interval of zero width. This is in contrast with results from similar maps with fixed points; these maps will have a rotation interval of zero width on a set of measure zero[143]. The bifurcations in parameter space associated with banded chaotic behavior share some characteristics associated with Arnold tongues in invertible circle maps (Eq. (2.1))[7, 6, 10]. However the dynamics in the zones for maps in class \mathcal{F} are chaotic, not periodic as in the original Arnold tongues.

The above behavior was demonstrated for a family of noninvertible discontinuous maps where the slope is always greater than one (Eq. (2.6)). The map associated with a model for modulated parasystole can have slope less than one and can be invertible or noninvertible, depending on the parameters used. Despite these differences, the modulated parasystole map displays banded chaotic behavior, over a large range of parameters. The organization of parameters in the parameter space that result in banded chaos is analogous to that seen in Eq. (2.6). However, the conditions for banded chaos for maps with slope sometimes less than one is still an open question.

An N -banded chaotic map will give rise to observed NIB values that are part of the set $(Nn - 1)$, n a positive integer. NIB sequences associated with banded chaos can have long uninterrupted trains of sinus beats, a large range of possible NIB values, and a relatively constant coupling interval. These characteristics are also observed in clinical settings; $(Nn - 1)$ rhythms are frequently encountered[247, 205], and are often associated with constant coupling intervals[195, 247], and long trains of sinus beats[205]. Other theoretical models display similar behaviors[43, 45, 125,

134. 195].

In summary, we have shown that the unusual mathematical properties of discontinuous circle maps shed insight into irregular cardiac arrhythmias observed clinically.

Chapter 3

Activation Mapping

The present chapter details the methods used for optical mapping, and outlines the various criteria that were evaluated in the design of the experimental system used in obtaining the experimental results in the final chapter of this thesis. The primary experimental protocol used is optical recording of propagation in monolayers of embryonic cardiac cells using calcium sensitive dyes. Section 3.1 outlines the basic theory of optical recording in the context of designing a system for mapping activation patterns on cultured cardiac monolayers. Section 3.2 details the construction of the macroscope. Section 3.3 gives details on the camera as well as general considerations involved in the choice of the CCD (charged coupled device). Section 3.4 outlines programs used to analyze camera data. Section 3.5 details photodiode array construction. Section 3.5.2 describes design and construction of the second stage (conditioning) circuitry. Results from optical mapping studies are presented in Chapter 4 and Chapter 5.

3.1 Introduction to Optical Recording

Recording complex patterns of activity in excitable media requires development of mapping techniques that record spatial as well as temporal information. There are many detailed reviews on optical mapping that outline theory and practice of various techniques[66, 51, 112, 111, 127, 117]. In the present section I detail mapping techniques in the context of choosing the appropriate method for detecting activity

on embryonic chick monolayers over a 1 cm^2 area.

In general, all mapping systems consist of a number of sensitive detecting elements which have their signals amplified, processed, displayed, and stored for later analysis. Monolayers are very thin (1-5 cells thick, depending on plating density) but can span a relatively large area (1.4 cm^2 in this study). This poses a challenge as signal strength is typically low for thin preparations and the light collecting power of conventional optical devices decreases with increasing field of view. In addition the type of experiments planned required long recording times (10-20 minutes) at high temporal and spatial resolution, putting additional demands on recording and storage apparatus.

3.1.1 Activation Mapping: Electrodes vs. Optical Techniques

Activity can be mapped using extracellular electrodes or optical techniques. There are advantages and disadvantages in both systems. Extracellular electrodes have been used to map activation in whole heart[117, 70] and in cultured tissue samples[127, 77]. This system used on cultured preparations involves plating monolayers on electrodes which have been etched on glass using photolithographic techniques. Optical techniques use changes in fluoresced or transmitted light from samples to map activity.

A major advantage to using electrode arrays is that the preparation is not subjected to potentially phototoxic effects of photosensitive dyes. Also, electrode arrays are both sensitive and fast, allowing detection of upstrokes at 0.1 ms temporal resolution[127]. These techniques seem to be the only viable ones for looking at fast activity in thin cell preparations where phototoxicity would affect the results. One drawback is that electrode arrays measure change in membrane voltage as opposed to DC voltage levels. Optical mapping techniques can give direct information on action potential shape.

Extracellular electrode arrays are less flexible than optical techniques because the spacing and number of detection sites is fixed once the array is constructed.

Optical techniques allow the user to ‘zoom’ in on interesting areas without affecting the number of spatial points collected. In addition, a constructed electrode array would have to be replaced after relatively few experiments as electrodes are sensitive to the saline cell bathing media (personal communication with Dr. Israel). Construction of the array involves specialized lithographic equipment, as well as sonic welding equipment not locally available. Construction of the array as well as welding to external amplifiers would have to have been done by an external company. Finally, the number of extracellular electrodes is limited by space constraints on the substrate, as present fabrication techniques place electrodes and the wires leading to them on the same plane. The low number of detection sites makes extracellular arrays a poor choice for mapping spatially complex activation patterns.

As the appropriate spatial resolution for mapping activation patterns in monolayer cultures was unknown, designing an extracellular array would have been impractical. We decided to use optical techniques as they provide a more general approach to mapping activity from an uncharacterised system.

3.1.2 Extrinsic vs. Intrinsic Signals

Optical activity can be recorded by using intrinsic or extrinsic signals. Extrinsic signals are generated when a dye added to the preparation changes its optical characteristics in response to changes in the preparation. Intrinsic signals are activity dependent changes in the optical character of the tissue itself.

Extrinsic signals are generated by dyes which are loaded into the preparation prior to mapping. Hundreds of dyes have been developed which use a variety of mechanisms to respond to dynamic changes in the preparation. Their mechanisms of action will be discussed in more detail in sections below.

Intrinsic signals are generated by three mechanisms: light scattering at the cell level, changes in fluorescence or absorption of intrinsic chromophores, or changes in local blood flow at the anatomic level. The light scattering characteristics[66] of cells are affected by changes in cell volume, rapid changes in the membrane dipoles, or morphological changes associated with mechanisms of secretion. An example of

measurement of scattering changes caused by cell shrinkage is demonstrated in studies by Mamose and colleagues[179] and by Kreisman and colleagues[159]. Intrinsic chromophores such as hemoglobin and cytochromes can change their fluorescent and absorptive characteristics during cellular activity. Intrinsic chromophores have been used to map activation in whole brain by Grinvald and associates[111]. Signals from changes in blood flow and oxygen delivery in *in vivo* preparations can also change light scattering and reflectance. Examples of these techniques are seen in publications by Grinvald and colleagues[111] and Bonhoeffer and colleagues[22].

Dyes can produce phototoxic effects: Di-4-ANEPPS, a popular voltage sensitive dye, is not toxic at low concentrations in the absence of light, but degrades membranes in the presence of even low levels of light[246]. An advantage associated with intrinsic signal measurement is that it avoids potentially phototoxic effects of dyes. However, the time course of intrinsic signals is relatively slow (1 - 3 seconds depending on wavelength[111]), and often relies on metabolic effects secondary to those being studied. Intrinsic signal measurements are not appropriate for mapping activity in cultures of embryonic cells. The lack of vasculature prevents blood flow measurements, and movement artifacts are not large enough to be detected reliably at low magnification¹.

3.1.3 Fluorescence vs. Absorption Dyes

Fluorescence and absorption dyes are available to measure extrinsic signals. Absorption dyes change the absolute level of light that reflects off or passes through a sample. Fluorescent dyes produce light when excited by light at a lower wavelength. In general, changes in the property being measured (voltage across the membrane, or concentration of a particular ion) cause a small change in light intensity (ΔI) that is accompanied by a large offset signal (I). The signal to noise ratio increases as the square root of total signal (see photodiode discussion following, and [110]), and is directly proportional to the fractional change in detected light caused by changes

¹Contraction in the monolayer is visually detectable at magnifications of 20x or greater. It is not observable at low magnification.

in the measured quantity [110]:

$$\text{signal to noise ratio} \propto \frac{\sqrt{I}(\Delta I)}{I} \quad (3.1)$$

There are advantages and disadvantages associated with absorption and fluorescent measurements. Absorption dyes change their absolute level by a very small fraction (0.01 -0.1 %) and fluorescent dyes change by a much greater amount (5% for some voltage sensitive dyes to 100% for calcium sensitive dyes). However as the absolute light level of absorption signals is 3-4 orders of magnitude higher, the signal to noise ratio can be better for these dyes. In addition, absorption dyes differ from fluorescent dyes in respect to their sensitivity to nonspecific binding and sample thickness. Absorption dyes are less sensitive to the amount of nonspecific binding in the sample because background fluorescence (I) increases with nonspecific binding (thereby decreasing the signal to noise ratio), but transmitted light does not. Also, background fluorescence increases with increased sample thickness, but background transmitted light does not. Therefore the signal to noise ratio of a transmission experiment increases linearly with sample thickness (as ΔI increases), but increases only as the square root of thickness in a fluorescence experiment[110].

The advantages that absorption dyes have in regard to staining thick preparations with nonspecific binding do not apply to monolayer cultures, as they are relatively thin and are relatively homogeneous compared to whole tissue². In addition, the small percentage change in absorption signals requires a method for subtracting off a large light offset. This can easily be done with specialized circuitry that subtracts off a constant voltage offset, but it is not available in any commercially available camera technology. Absorption dyes therefore are better suited for photodiodes (to be apparatus discussed in detail later) but are not appropriate choices for charge coupled devices (CCDs) where the offset would be stored and digitized along with the signal³. Fluorescent dyes offer more flexibility in experimental design by

²The monolayers are homogeneous in the sense that they do not contain connective tissue. They contain heterogeneities in the form of uneven cell spacing and fibroblasts.

³It is noteworthy that recently a camera has been developed by Fuji that stores only the change in light for each pixel.

allowing use of conventional camera technology. However, fluorescent signals can be very weak and are often at the noise floor of conventional camera equipment. The low light level necessitates design of specialized optical apparatus to capture the maximum amount of light as well as special care in selecting recording equipment. These issues are discussed in the following section.

3.1.4 Slow vs. Fast Fluorescent Dyes

Fluorescent dyes can be divided into slow and fast acting dyes. Slow dyes change their spatial distribution in cells with changes in cell potential or pH. As these dyes move through cell membranes in response to activity, the dyes' time course is affected by the permeability of the dye, its aggregation characteristics and its tendency to bind cell constituents. Studies that use such dyes are reviewed by Ebner and Chen[66]. Slow dyes have time constants on the order of 1 - 20 seconds and therefore are not useful for mapping fast activation changes. Fast dyes do not rely on dye movement, but change their optical characteristics by changing their conformation. Conformation changes occur when the dye binds to ion species released during metabolic activity or when the dye changes due to local changes in voltage. The time constant of such dyes is on the order of one millisecond. The mechanism responsible for the optical changes in these dyes has not been fully elucidated[66].

Fast voltage sensitive dyes are divided into four categories based on their chemistry: merocyanine-oxazolone, merocyanine-rhodanine, oxonol and styryl. There are several mechanisms that account for a given dye's voltage sensitivity. The dye molecule can change its shape (molecular motion) or change its charge distribution (electrochromism). Changes in the molecule's shape can change the depth of implantation, its orientation within, and its tendency to move on or off the membrane[85]. A variant on molecular motion is the rotation-dimer mechanism[87]. Here the dye switches from a monomeric form oriented perpendicular to the membrane to a dimer orientated parallel to the membrane with changes in voltage. Also, Fromherz and Lambacher[87] have suggested a molecular motion mechanism for styryl dyes where

the ‘twist’ of the molecule effects charge movement within the molecule. In contrast, electrochromism refers to the direct displacement of charges within a molecule by external electric fields. As there is no molecular movement involved, electrochromism effects have a nanosecond time scale. Dyes are designed to incorporate one or more of the above effects to optimize fluorescent and absorption characteristics[66, 85].

3.1.5 Ion Sensitive Dyes

Ion sensitive dyes change their conformation by reversibly binding with ion species. Dyes sensitive to sodium, pH, chloride, and calcium have been developed. Ion sensitive dyes can be broadly classified as ratiometric or non ratiometric. Nonratiometric dyes change their absolute level of fluorescence at a given wavelength. Examples of nonratiometric dyes are Fluo-3 used for Ca^{++} and SPQ for Cl^- . Ratiometric dyes are either dual emission, which fluoresce at two different wavelengths, or dual excitation, which are excited by two different wavelengths. Examples of dual emission dyes are Indo-1 (for Ca^{++} and Mg^{++}), DCH (for H^+) and FCORYP-2 (for Na^+). Common dual excitation dyes are Fura-2 (for Ca^{++} and Mg^{++}), SBFI (for Na^+), and BCECF (for pH).

Non-ratiometric dyes must be calibrated against known stock concentrations and controlled for light level variations between experiments if quantitative measurements are required. Ratiometric dyes give information on the absolute level of ion present without calibration. For example, Fura-2 increases fluorescence intensity in the presence of Ca^{++} when excited at 350 nm, but the intensity decreases when excited at 380 nm. Because the individual measurements are equally affected by variations in light levels and dye concentration, the ratio of fluorescence depends only on the Ca^{++} concentration.

Ratiometric measurements use more equipment than non-ratiometric measures and can be problematic when measuring rapid events. Dual excitation dyes must be stimulated at two wavelengths (at separate times) and sequential frames must be divided by each other for each measurement. Data collection rates are therefore half the acquisition rate of the imaging device. In addition, fast biological events

can cause discrepancies between ratioed frames, resulting in blurring artifacts. Dual emission measurements can avoid these problems by splitting the image onto two detectors. However this greatly increases the cost of the measuring system. As we were interested more in measuring activation times, not absolute ion levels, and cost and complexity of the mapping system was a concern, nonratiometric dyes were considered.

3.1.6 Dye Choice

The above considerations were used to choose two dye candidates for detection of signals in monolayers. The choice of dye also depends on tissue specific uptake: certain dyes are absorbed more easily by different cell types[66]. Di-4-ANEPPS, a fast voltage sensitive styryl dye and Fluo3, a non ratiometric calcium sensitive dye, were used. Di-4-ANEPPS was chosen as it had been successfully used in single cell and aggregate cultures of chick myocytes by other researchers[282]. Experiments using Fluo3 were initiated in Dr. Nelson Publicover's laboratory, where the correct cell densities and dye concentration were determined.

3.1.7 Detection Systems

Fluorescent activity can be detected using a variety of different systems. In general, all transform light energy to an electrical signal which is displayed and stored in some fashion. Light detection systems considered are photomultiplier tubes, photodiodes, photocathode tubes, and CCDs. The choice of detector depends on application.

All detection systems are governed by fundamental limitations that govern spatial and temporal resolution in relation to signal to noise ratios. For example, given a constant level of system noise and illumination, increasing spatial resolution decreases signal to noise ratio by decreasing the amount of light hitting the detector. If spatial resolution is increased by dividing up the detector area into more elements, then signal strength decreases by the inverse square of element width [100]. Increasing temporal resolution can decrease signal levels by decreasing integration time (in the case of CCDs, see sections below) or by necessitating an increase in bandwidth

which increases noise (as is the case with photodiodes, see below).

3.1.8 Photomultiplier Tubes

Photomultiplier tubes (PMT's) are single element detectors that are well suited for very low light level applications. The photomultiplier works by converting light energy to electrons via a phosphor screen. The resulting charge is amplified within the tube as electrons are cascaded off charged plates. Through this amplification process the PMT can detect light levels as low as a single photon. Due to their sensitivity, PMTs are ideal choices when only a single spatial point needs to be detected. PMTs are too bulky to practically mount more than one or two on an imaging setup. A multiple site mapping method using a single PMT was devised by Dillon and Morad[62, 196], where a laser is used to scan the surface of the sample, and the signal detected by PMT is later decoded into individual channels. This system is powerful and flexible, but we decided against it as building a laser scanning device was beyond our technological means. In addition, a primary advantage for laser systems is for scanning irregular or curved surfaces as no light collecting optics are involved. This allows scanning without consideration of the focal plane of the object or the depth of focus of the collecting optics. This is not a consideration when recording off flat monolayers of tissue.

3.1.9 Photodiodes

Photodiodes are individual photosensing elements constructed from a layer of silicon mounted on a substrate that acts as an electron well. When light hits silicon, it causes the release of electrons, providing current. The current is small, and has to be carefully amplified for low light level applications. Arrays of photodiodes can be constructed (either by placing individual elements in a grid or other pattern, or by purchasing an array of elements with leads coming out the back and sides). Photodiode arrays have been used for many years to detect activation patterns in a variety of preparations [37, 239, 241, 50, 110, 112, 99, 77]. The primary advantage offered by photodiodes is that each element is amplified individually and in parallel

so the signal degrades minimally after it has been transduced from light to electricity (as opposed to charge coupled devices, discussed below). Also, as each signal is treated individually, the experimenter can signal process each channel before storing the signal. The main difficulty in implementing a photodiode system is that amplification circuitry is associated with each diode, necessitating significant space and construction time for even small arrays. This makes construction of large arrays impractical. The electronic back end for such arrays is not commercially available.⁴

3.1.10 Video tubes

Video tubes are a common type of imaging device used for imaging applications[270]. Video tubes (also called Vidicon tubes) consist of an electron gun and a photoconductive faceplate housed in a cylindrical glass envelope. The photoconductive faceplate consists of a positively charged, transparent metal film. The image is focussed on the faceplate. The intensity of light on the metal film alters the charge carrying capacity of the film: dark areas on the faceplate retain a greater charge than light areas. A beam of electrons from the electron gun scans the faceplate at a certain resolution and frequency.⁵ A current proportional to the intensity of light on the faceplate is produced as electrons from the beam replace electrons in light areas of the faceplate. The resulting analog video signal can be displayed on a monitor or stored on tape. The video signal must be digitized using a frame-grabber board if quantitative measurements are required.

The characteristics of a video tube depend on the metal used as the photoconductor in the faceplate. The photoconductor effects dynamic range, spectral sensitivity and the speed and linearity of response to changes in the image. The dynamic range of video tubes is typically low, but can be increased if the gain (the strength of the electron beam) is varied using an automatic gain circuit. Varying gain allows for

⁴Hamamatsu has recently released a photodiode array with amplification circuitry, however the gain of the system is too low for measurements of low light levels and is not customizable.

⁵The rate and resolution depends on what convention is used. For example, a typical video system (using the Radio Electronics Television Manufacturing Association scanning convention) scans in 525 lines per frame at 30 frames per second for a scan rate of 15750 Hz.

adjustment in signal strength between frames (allowing the camera to compensate for a gradual decrease in overall signal intensity, for example), but cannot increase the dynamic range within one frame[261]. The dynamic range within a frame for video cameras is at most 50 fold[268]. This value is low compared to individual photodiodes or CCDs (charge coupled devices, discussed below) which are resolvable to 12 bits (4096 levels) or greater.

Although video tubes have been designed with greater sensitivity and lower lag (by using different photoconductive substrates), the poor dynamic range within each frame is a concern. If large variations in signal levels exist over one frame (due to uneven lighting, patchiness in the monolayer, or heterogeneous dye loading) certain regions within a frame may be unmeasurable even if they are generating adequate signal. CCDs are a better choice if the appropriate dynamic range over a frame is not known.

3.1.11 Charged Coupled Devices

Charged coupled devices (CCDs) are arrays of photosensitive elements. CCDs have underlying circuitry allowing the information from each element to be read off the array serially to be amplified and digitized. CCDs will be discussed in detail in Section 3.3.

3.1.12 Detector Choice

As the proposed experiments demanded both the capacity to have high spatial and temporal resolution, it was decided to develop both photodiode array techniques and to purchase a CCD imaging system. Imaging with a CCD offers high spatial resolution but low temporal resolution. A photodiode array offers the opposite. High speed and high temporal resolution CCDs and photodiode arrays exist but were too expensive. The system I will discuss involves using photodiodes and a CCD to provide high temporal and spatial resolution.

3.1.13 Light Collection and Data Acquisition

Fluorescent signals are relatively weak, necessitating the use of special optical apparatus to obtain enough light at low magnifications. Although microscopes are efficient light collectors at high magnification, they can be two orders of magnitude less efficient at low magnifications. Cultured monolayers of embryonic cardiac cells have previously been imaged by Rhor and colleagues[231, 232] and Fast and colleagues[77]. These researchers were interested in small areas ($250\text{ }\mu\text{m}$ squared) and could take advantage of high numerical aperture(NA) microscope objectives.

The macroscope used in this thesis work is based on designs outlined by Ratzlaff and associates[228] with some modifications. The macroscope is discussed in detail in Section 3.2.

Large amounts of data can be collected with imaging studies. Previously researchers relied on bulk storage media such as VCR tape or large scale RAM storage devices[282]. We used recordable CD ROM.

3.2 Optical Mapping System Design and Construction

3.2.1 Theory

Microscopes are optimized for collecting bright images from a small field of view by using high magnification lenses mounted close to the sample. Microscopes are not ideal for low magnification applications where long working distances are desirable. In general, the light collection efficiency of microscope objectives increases with increased magnification. For example, a typical $40\times$ lens collects 100 times more light than a $1\times$ objective. In addition, the distance between the lens and sample (working distance) is a few millimeters or less for microscope objectives. Commercial low magnification microscopes (called macrosopes) with long working distances are available, but are typically less efficient light collectors than microscopes [228]. Low

magnification, long working distance imagers can be constructed from conventional camera equipment with relative ease. These macroscopes collect light as efficiently as high powered microscopes while allowing for a large (1 cm^2) field of view [228].

In general, image brightness in a conventional microscope imaging application is a function of the size of the field being imaged, the diameter of the lens and the distance between the lens and the sample. The constructed macroscope has a similar light path to a microscope, but increases image brightness by increasing the diameter of the lens relative to sample size. I will briefly review the microscope light path and go over some essential concepts related to macroscope construction. Background information on optics can be found in several basic texts[86].

The most familiar way of imaging an object is using a single lens, as shown in Figure 3.1. Here the object (O) sits past the focal point of the lens (L1) and a real image (I) is created on the opposite side. Magnification is given by:

$$M = \frac{D_i}{D_o} \quad (3.2)$$

where D_o is the distance from the object to L1 and D_i is the distance from the image to L1. Although simple, the above scheme is not used in microscopes because different magnifications require changing object and image distances.

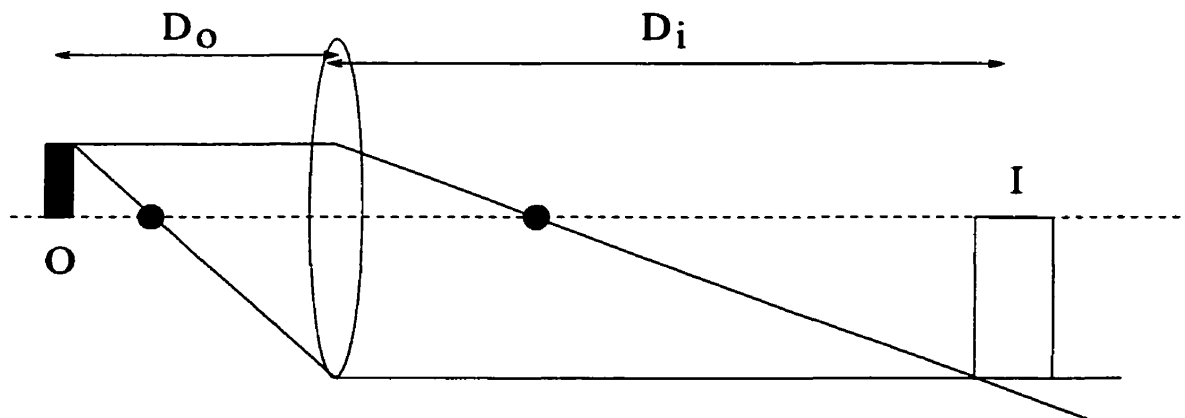


Figure 3.1: Use of a single lens to magnify an image.

Microscopes typically use a tandem lens scheme, as shown in Figure 3.2. Here two lenses are used. The object is placed at the focal plane of the objective lens

(L1). Collected light is projected to infinity and is focussed by an imaging lens, or ocular (L2), to form an image at its focal plane. The magnification is given by the ratio of focal lengths:

$$M = \frac{F(L1)}{F(L2)} \quad (3.3)$$

where $F(L1)$ is the focal length of the objective lens L1 and $F(L2)$ is the focal length of the imaging lens L2. The tandem lens design allows changing magnifications by changing L1 without affecting the location of the magnified image.

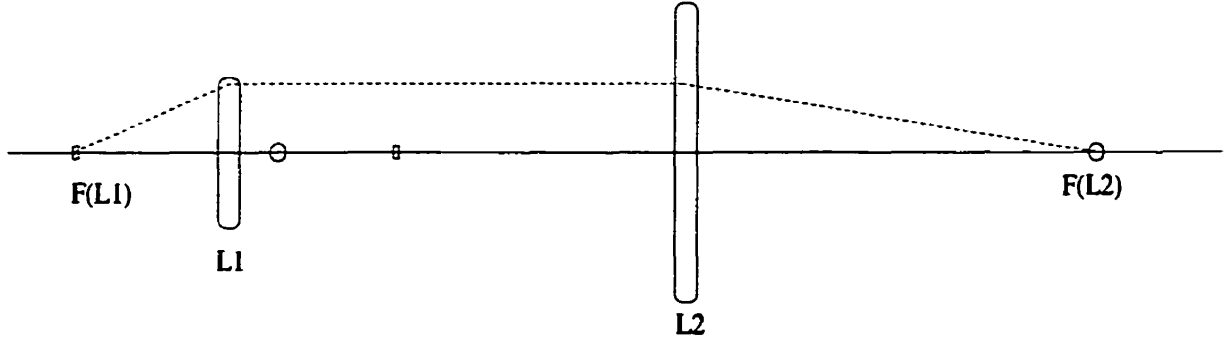


Figure 3.2: The tandem lens design is used to image items while maintaining focal distance. Objective lens (L1) and imaging lens (L2).

In both the single and tandem lens imagers, brightness of the image is a function of the numerical aperture (NA) of L1. The NA is defined as:

$$NA = I \sin(\alpha/2) \quad (3.4)$$

where α is the maximum accepted light angle from the object at the optical axis, and I is the refractive index of the medium in which the lens is working (in our case I always equals 1). NA can be approximated in simple lenses as:

$$NA = \frac{\text{Diameter}}{\text{Focal Length}} \quad (3.5)$$

Light collected from L1 can be limited by the diameter of L2 and the distance between L1 and L2 in the tandem lens design. These points will be addressed below. Image brightness is also a function of the distance between L1 and the object in the single lens design (as that is a variable controlling magnification). In general, image

brightness decreases as the square of the distance to the object in the single lens scheme.

Fluorescence imaging using a single lens scheme would be implemented as shown in Figure 3.3. Monochromatic light is directed at the sample (by use of additional lenses or fiber optic light guides). Fluorescent and reflected light from the sample is collected by the lens and passes through a barrier filter(B) prior to forming an image.

Fluorescence imaging is implemented in the tandem lens scheme by adding a light source, excitation(E) and barrier(B) filters, as shown in Figure 3.3. A dichroic mirror (D) acts as a wavelength sensitive reflector. Excitation light passes to the dichroic mirror and is reflected to the sample. Fluorescent light (at a longer wavelength) passes through the dichroic mirror to a barrier filter, and is imaged by L2. The use of illumination in this configuration is referred to as epi-illumination.

Both tandem and single lens imaging schemes have been used for imaging fluorescence at low magnification. Single lens imaging is achieved by using a single macro camera lens, or by using a standard lens with macro adapters (which change the camera/image distance). Single lenses have been used by Witkowski and colleagues[294] and Rosenbaum and colleagues[237]. Tandem lens designs have been implemented using camera lenses[228] or high NA aspheric lenses[50] to image cardiac and neural preparations. Single lens design is easier to implement as all components are commercially available without using specialized holders and mounts. However, the tandem lens design has two advantages. Consider a $1\times$ magnification imaging application. The single lens design has the object at $2\times$ the focal length of the objective, while the tandem lens always has the object at the focal plane. The doubling in distance results in a $4\times$ reduction in image brightness. More importantly, the barrier filter(B) may not function optimally as shown in Figure 3.3. Optical filters are designed to filter light when they are perpendicular to the light path. Some optical coatings block different wavelengths at even small (5%) angles. The choice of (B) in the single lens scheme is limited to coloured glass as light is not collimated. The above considerations led to the adoption of a tandem lens scheme.

3.2.2 Design

The following design considerations are summarized from reference number [228]. Lenses L1, L2 and L3 in Figure 3.3 are standard compound 35 mm camera lenses. Two lenses set to focus at infinity are placed face to face so the object and image conjugates are located at the back focal planes of the lenses. There are several advantages to using camera lenses as opposed to single lenses. All lens aberration concerns (spherical aberration, coma, astigmatism, distortion, chromatic aberration) have been accounted for by the lens manufacturer. Camera lenses come premounted with standard adapters and have focusing sleeves. Camera lenses are high quality and have antireflection coatings on them as a matter of course.

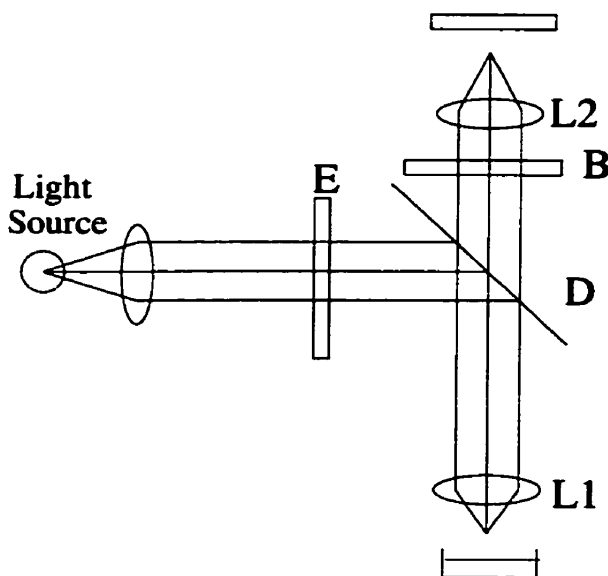


Figure 3.3: A schematic of a macroscope imaging system. Light source (L), excitation filter (E), barrier filter (B), dichroic mirror (D), objective lens (L1) and imaging lens (L2).

As light is collimated after L1, the distance between L1 and L2 does not affect the location of the image or its magnification. This allows flexibility in mounting the dichroic mirror(D). As shown, the light path suggests that the distance between L1 and L2 is not a factor. However, this distance affects image brightness due to vignetting.

Vignetting refers to light loss at image points off the central axis due to obstructions near the periphery of the light path[228]. Ratzlaff and colleagues explain that the collimated beam is “somewhat divergent”[228], and that L2 should have a slightly larger entrance pupil than the exit pupil of L1 to reduce vignetting. This is an oversimplification of the vignetting problem in this design. Part of the design strategy outlined by Ratzlaff and associates[228] suggests that an additional imaging stage for focusing should be added by putting a beam splitter between L1 and L2. Ignoring losses due to reflection, this results in a reduction of image brightness at L2 for two reasons. First, a certain amount of light is diverted from L2 by the beam splitter. Second, adding a beam splitter increases the distance between L1 and L2 a minimum of $\sqrt{2} \times$ beam width, which results in light loss due to vignetting. Figure 3.4 demonstrates the effect of vignetting on the tandem lens imager. In order to prevent excessive vignetting (here defined as light loss greater than 50 percent for off-axis points), the image lens (L2) radius $L2_r$ must increase proportionally to the distance between the lenses,

$$L2_r \propto d \frac{x}{f} \quad (3.6)$$

where x is the diameter of the object, f is the focal length of the objective lens, and d is the distance between L1 and L2. If the radius of the image lens is not increased, the brightness of the image falls off as a function of d .

Despite vignetting, it is often desirable to have a second imaging stage. Extending d and splitting the light path is the only option if fluorescent signals are required (for example, data can be collected from a photodiode array and a photomultiplier simultaneously.) A better alternative is available if collecting fluorescent light with the second stage is not essential. For example, an ocular or simple camera used for focusing the microscope can use non fluorescent light to monitor the object. This could be implemented as shown in Figure 3.5. An image is collected using light discarded by the dichroic mirror. The use of a beam splitter in this configuration does not increase d or split the fluorescent light path. The disadvantage of this

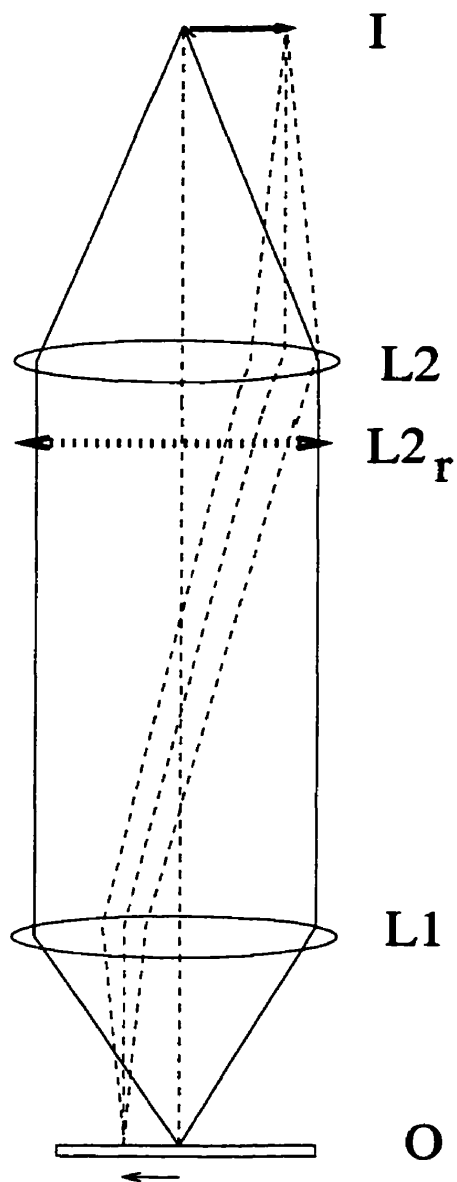


Figure 3.4: Vignetting occurs if the distance between the two lenses in the tandem lens macroscope is too great. Objective lens (L1) to image lens (L2) distance along with image lens radius ($L2_r$) play roles in controlling vignetting. See text.

system is that illumination brightness is reduced by the beamsplitter (R2), and L1 - L3 distance must be increased which would also effect illumination brightness. The beamsplitter can be removed after focusing if more illumination is required. The disadvantage incurred by reduced illumination strength may not be a significant factor if a strong light source is available. The minimum amount of light required is lowered by reducing d , which is an advantage if phototoxicity is a concern.

3.2.3 Macroscope Construction

The macroscope was constructed by mounting lenses and filters on Spindler and Hoyer MacroBench (Spindler and Hoyer GmbH, 37070 Cottingen, Germany) optical components. The macroscope itself (Figure 3.5) was placed on horizontal rails, which allowed it to be slid over different preparations. The macroscope is mounted over an inverted microscope, allowing simultaneous monitoring of the sample from the top and bottom sides at different magnifications. Alternatively, it can be placed over a moving stage and heated bath for monitoring larger preparations. The illuminator can also be moved in the horizontal plane. The frame of the macroscope can be lowered by adjusting the height of specially machined legs. This allows for gross focusing of the macroscope. Fine focus is achieved by manipulating the focusing sleeve on the objective lens.

3.2.4 Optical Components

The objective lens is a Nikon 80 mm F 2.0 lens. The imaging lens is a Sun Cosmicar videography lens with zoom. The variable focal length of the imaging lens allowed convenient change in magnification and field of view without changing the objective lens. Light from the epi-illuminator was collimated using an Oriel one Lens collimator and focusing sleeve (Oriel, Stratford,CT,USA), and focused using a Canon 50 mm lens. Filters and dichroic mirrors were purchased from Omega Optical (Omega Optical, Battleboro, VT, USA). Filters for monitoring Di-4-ANEPPS were a 1 inch emission filter centered at 530 ± 20 nm, a dichroic mirror at 560 nm and a bandpass barrier filter set at 630 ± 20 nm. Calcium-sensitive Fluo-3 measurements

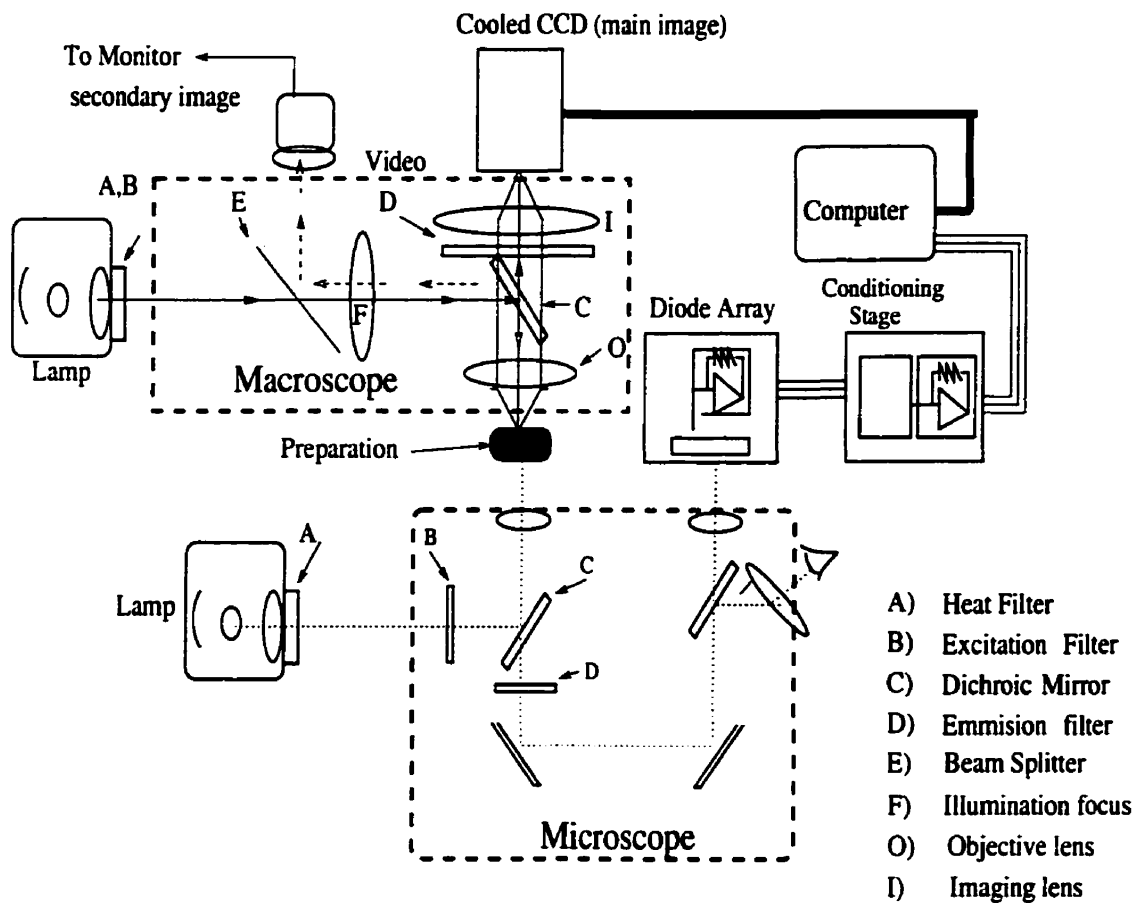


Figure 3.5: The macroscope as constructed. The macroscope itself is mounted above an inverted microscope or over a heated bath for larger preparations. The macroscope slides along rails to either configuration. A second imaging camera could use discarded light instead of increasing L1,L2 distance. The camera captures light reflected back from the dichroic mirror.

were performed using 490 ± 20 nm emission filter, 515 nm dichroic, and a 530 nm high pass filter. Dichroic mirrors and barrier filters were custom made to order, as the size required is greater than those used in conventional microscopes. Standard 1 inch filters were used for generating monochromatic light from the the light source. Additional filters for Di-4-ANEPPS and Fluo-3 were obtained as stock components for the Zeiss microscope (Axiovert 135m, Carl Ziess Inc, Thornwood, NY, USA).

3.2.5 Mechanical Components

Specialised parts were machined at the McGill Physics Department machine shop. Special parts were made to interface the camera lenses to the Spindler and Hoyer components. These were simple plates with a threaded hole in the center designed for use with different camera lenses. Nikon lenses were mounted using a bayonet mount taken from a camera body and attached directly to an adapter plate.

3.2.6 Illumination

According to researchers in Dr.Jalife's laboratory in SUNY (State University of New York, Syracuse NY), conventional lamp housings have too much interior space, which allow convective air currents to be created as the housing heats up. We elected to purchase a specially designed 250 Watt lamp, 24 Volt housing from Dr.Jalife's laboratory.

A tungsten halogen lamp is used for illumination. Different light sources (xenon, mercury arc, and laser) are relatively unstable and can add noise to measurements. Other labs have used different sources; however specific noise reduction circuitry was required[36] in some cases. Tungsten halogen is lower noise (in general, the output of the bulb fluctuates on the order of 10^{-5} [36], while arc lamps typically have fluctuations $20\times$ as large).

Most of the energy produced by tungsten lamps is in the UV range. This requires high power lamps for moderate illumination at the desired wavelengths. In addition, the lamp housing can become very hot, and stray UV light can be dangerous if care is not taken. The lamp housing was powered by two Eltech 12 V power supplies.

Power supply stability is controlled by running a feedback controller to the lamp leads within the housing.

Illumination intensity was measured to be roughly $100\mu\text{W}/\text{cm}^2$ for the calcium and voltage imaging experiments. A light meter was not available in our laboratory. Estimation of illumination intensity was carried out using a MRD500 photodiode coupled to a AD645 operational amplifier in the current to voltage configuration (see Section 3.5 for details on this type of circuit). The MRD500 photodiode is rated at $6.6\text{ mA}/\text{W}$, or $3.3\text{ }\mu\text{A}/\text{W}/\text{cm}^2$. The current output of the illuminated photodiode was determined by dividing the voltage of the circuit by the feedback resistance. Illumination intensity was determined by dividing the current by the quantum efficiency (see Section 3.3 for definition) of a typical silicon diode at the illumination wavelengths used[86], and converting the current to watts based on the conversion factors above.

3.2.7 Performance

The light collecting capacity of the microscope was estimated by using a scientific grade CCD camera (Princeton Instruments EEV 576×384 frame transfer CCD, see Section 3.3 for details). The camera was focussed on an image using a Zeiss microscope ($2.5\times$ objective, NA 0.075). An identical image was obtained using the microscope, where the microscope's optics were adjusted so that the field of view was identical. The light collection capacity of the microscope and macroscope were compared by changing the integration time of the camera. The camera had to integrate the microscope's image 20 times longer than the macroscope image to achieve equivalent intensity. I therefore estimate that the macroscope collects 20 times more light than the microscope for similar fields of view.

3.3 Camera Theory

Commercial video rate CCD cameras have been used to acquire fluorescence data from cardiac preparations. These CCDs are constructed to output analog video

rate signals (charge is not digitized after it is shifted off the array). Davidenko and colleagues[50, 51] at SUNY used a Cohu camera to acquire images from a Di-4-ANEPPS stained epicardial sheet at 60 frames per second (fps). Such video rate cameras are usable for some applications. The experiments performed were at the limit of the detection capabilities of this technology. Researchers at SUNY generously gave our group an opportunity to use their system on a embryonic chick monolayer preparation. Monolayers were stained with voltage sensitive dye Di-4-ANEPPS as described in Section 5.2.1. Although the camera is mounted on a high light throughput microscope (see Section 3.2), no usable signal was detected despite repeated attempts. This negative result is not surprising considering the relative thickness of the monolayer in comparison with the epicardial sheet successfully imaged by Jalife's laboratory. The signal to noise ratio for the epicardial sheet experiment was approximately 1:1. Because the monolayer is expected to give a lower magnitude signal (as there are fewer dye loaded cells at any given point), the signal is hidden by noise.

Video cameras in general have a dynamic range of only 8 bits (due to noise generated by the camera) and have low light collection efficiency (due to dead space between light collecting elements). The majority of noise in the camera's output signal is generated by the process of converting data stored on large numbers of storage elements (on the order of 700×400) to an analog video signal at high rates. Data collected from conventional video can be averaged to reduce noise, however this results in a loss of temporal resolution.

Scientific grade CCDs are an improvement on the design of conventional video chips in several ways. CCDs are programmable, allowing the user to use several processing techniques on the data while it is still on the CCD chip, to significantly lower noise. CCDs are designed to have good light collection characteristics and have a small dead space between light sensing elements. Individual light sensing elements are frequently relatively large, which improves dynamic range. A negative aspect of this technology is that users can no longer use conventional storage and viewing apparatus. Conventional video signals can be stored on VCR tape and viewed real-

time on monitors. Storage and display of scientific CCD information is frequently done on a frame by frame basis, which complicates long term recording and analysis of signals. In addition CCD imaging systems differ greatly in acquisition speed, spatial resolution, noise levels, sensitivity, data storage and display characteristics. An understanding of how a CCD functions is essential for choosing a system for demanding applications. The following overview of scientific CCD characteristics is relevant to recording low light signals at high rates.

A CCD consists of an array of light gathering elements with support circuitry. Each element in the array is called a *pixel*. Light energy is transduced to electrical energy with a certain *quantum efficiency*, which varies for different CCDs. The *well capacity* is a measure of how much charge each pixel can hold before saturating. Electrical energy is transferred between pixels with a certain loss determined by the *charge transfer efficiency* of the CCD. Basic CCDs collect images in the following way: light hits a CCD, which collects charge in individual pixels. After a certain amount of time (*the integration time*) the charge is shifted, pixel by pixel, to horizontal shift registers. After the charge is collected in the shift registers, it is collected at an *output node*, preamplified, and eventually digitized. The output node is a capacitor where the charge is stored prior to amplification. This process is repeated for every frame collected.

The above sequence is associated with several noise sources. *Shot noise* is a random noise due to the particulate nature of light. It is proportional to the square root of the number of electrons gathered. As the signal increases proportionately to charge, the signal to noise ratio increases as the square root of charge. *Dark current* is a source of noise that is caused by thermal interactions at each pixel, and is a function of the temperature of the chip, integration time and the CCD architecture. *Frame read out noise* is generated as accumulated charge in each pixel is shifted to the output node for digitization. It is proportional to the square root of the pixel read-out rate. Electron shot noise and dark noise are generated at each pixel, and are generic properties of any light detector. Frame read-out noise is created in the process of moving information from a large number of pixels to a single amplifier

and digitiser, and is specific to CCDs.

The signal to noise ratio can be increased by functional and structural changes to the CCD. Structural changes can include cooling, use of multi-phased pinned (MPP) architecture, or back lighting the CCD. Cooling reduces read noise and dark current at the expense of charge transfer efficiency (the amount of charge transferred between pixels during readout.) MPP pixel architecture reduces dark current at the expense of the light collecting capacity of each pixel in the CCD. Back lit CCDs decrease noise by increasing the quantum efficiency (the percentage of photons falling on the pixel surface that generate electrons). Normally, some of the light hitting each pixel is absorbed by circuitry associated with each pixel. The back lit CCD architecture is a means of avoiding this problem but at considerable financial expense. Functional changes involve on chip binning and sub-array read-out (to be discussed below) which reduce noise by lowering read-out rate at the expense of spatial information.

In general, faster read-out rates contribute to noise in the following ways:

Higher read-out rates result in lower integration times, which reduce the signal levels in each pixel. This increases the relative contribution of shot noise (decreasing signal to noise ratio). Dark current contribution is actually lowered at high read out rates, as the amount of current collected is time dependent. High readout rates also increase read out noise, which originates at the processing end of the CCD. Importantly, both spatial and temporal resolution of the CCD affect read out noise levels. Higher spatial resolution require more pixels to be digitized per frame. As read noise is a function of the readout rate of individual pixels, increasing spatial resolution increases read noise at a fixed frame rate.

Another structural feature that must be considered is well capacity. The well size of an electronic component controls the number of electrons it can store before it saturates. Charge is accumulated at various points in the CCD prior to preamplification. The well size of these critical points in the CCD puts an upper limit on the dynamic range of the system. There are three areas of a CCD which are affected by well capacity. The pixel size is proportional to well capacity: large pixels can store more charge. The shift register capacity must be proportional to the well

capacity of individual pixels. The output node of the CCD must be large enough to store the charge. Shift registers and output nodes typically hold more charge than a single pixel, but are often not much larger. As pixel binning increases the amount of charge moved to the shift registers and output node: intelligent CCD selection requires knowledge of these parameters.

Binning is a process in which adjacent pixels are summed. Binning can increase the dynamic range and reduce noise of a CCD at the expense of spatial resolution. Binned pixels are dumped to the shift register. The well capacity of the shift register is typically only 4 times that of a pixel. Therefore the dynamic range for certain CCDs is not increased for greater than 2×2 pixel binning. The greatest advantage of binning is that increased frame rates are possible (at the same read out rates) at the expense of spatial resolution. Also, the read noise for a binned vs. non binned image (at the same frame rate) is lower for the binned image (as there are less pixels to process.) Binning also collects more light per (binned) pixel, however this effect can be achieved by summing pixels offline. Offline summation is preferable to on chip binning as it does not permanently discard spatial information.

Sub-array processing is a process in which only a small set of pixels is used. This increases frame rate without increasing the read noise but it lowers the size of the field of view. Because there is a certain amount of time and noise associated with moving pixels to the shift registers, a 64×64 pixel array will have lower noise and faster readout than a 64×64 sub-array on a 512×512 CCD.

Shifting information across the surface of the CCD to the output node takes a certain amount of time. Pixels are still light-sensitive as charges are being shifted to the output node. Charge accumulated during the shifting process causes blurring, which becomes more noticeable as integration time is reduced as the charge collected during shifting increases relative to the measured signal. Three strategies can be used to reduce blurring. The most common method is using a shutter to cut light as the image is being shifted. This is not ideal as information is lost while the shutter is closed, and shutter movement is a potential source of noise. Another method is using *line transfer* CCDs. In these CCDs, every second pixel column is covered

by opaque material. Charge can be transferred very quickly to these columns as charge moves only one pixel as opposed to being shifted across the whole array. The charge is then transferred without degradation to the output node. The main disadvantage with this system is that each CCD consists of 50% dead space, making low light measurements difficult. The final method, called *frame transfer*, shifts the entire image to a masked section of the CCD. The image is then read out as the next frame is collected. Information is shifted relatively quickly to the masked region as it is shifted row by row not pixel by pixel. The speed of the charge shift operation reduces blurring significantly. Shifting the image to the output node for amplification and digitization can occur over a relatively long period of time (the integration time of the CCD), reducing read noise. Even though half the array is used for storage, there is no dead space on the section of the CCD used for imaging, making this architecture ideal for low light, high frame rate applications.

Finally, commercially available CCD solutions come with appropriate control software that dictates display and storage of data while the information is being gathered. As a large amount of information can be collected by a CCD in a short period of time (512×512 CCD digitized at 12 bits comes to over 400Kb per frame), display and storage can be rate limiting steps in an experiment.

Scientific grade CCDs do not output video signals but transfer digitized frames to computers for storage and display. Camera manufacturers offer different storage options. The simplest, if least effective, storage technique is to move the information to a frame grabber board while the camera is collecting data. Information is later moved off the board to computer memory for offline display and storage. The main disadvantage of this system is that recording time is severely limited by the amount of RAM on the frame grabber board. A preferable method is moving the information directly to computer memory. This allows online viewing of the data and more rapid transfer to permanent storage. This is also a less expensive option, as frame grabber memory is more expensive than conventional computer RAM. Finally, the data can also be streamed to hard disk. Modern hard disk systems can accept 20-30 megabytes of data per second, which easily accommodates demanding camera

applications. However, no camera manufacturer has implemented data streaming in this way. All cameras offered within a reasonable price range are designed to collect a few seconds worth of data at a time. Most are specifically designed for long integration time applications, where the CCD collects an image from a low light source for several seconds prior to digitization. Software as well as CCD choices reflect this bias: CCDs often have low dark current but poor well size or read noise characteristics.

3.3.1 Choosing an Appropriate System:

A large number of CCD chips are available and many are ideal for high speed imaging applications. However, very few companies offer cameras which are optimized for low light, high speed recording. For example, Dalsa (Dalsa Inc. Waterloo, Ontario, Canada) offers a range of low resolution high speed camera systems. These cameras come with no software or support hardware, and are not cooled for low noise applications. Dalsa (personal communication) warned that these cameras are 8 bit resolution devices as sold. Very recently, Frank Witowski and colleagues[294] modified a Dalsa 64×64 array camera by adding a cooling stage and recorded potentials from intact heart preparations with millisecond resolution. The modifications involved were beyond the capabilities of our laboratory. Commercial options designed for optical mapping are available but at a prohibitively high price. Fuji Electric (Japan), makes a cooled 128×128 800 fps camera system that outputs differential measurements allowing offset subtraction prior to digitization. Kodak has intensified CCD systems that record more than 1000 fps at 128×128 . Both systems cost in excess of \$100,000. Furthermore, these systems output digitized frames to special memory buffers, which limits continuous recording time to periods of a few seconds. Microphotronics Inc. offers a cooled 64×64 CCD array at lower cost (about \$40,000). The camera operates with a frame grabber board, limiting recording time to 4000 frames. The company offers a S-bus model for continuous streaming. This option would have required the use of a Sun workstation for downloading, which was unavailable at the time.

Additional options were not considered due to cost. Various thin film coatings increase quantum efficiency of CCDs. Uncoated CCDs have peak sensitivity at around 800nm, and are light sensitive into the UV range. Thin coatings with various substances can shift peak responsivity to lower wavelengths, improving detection of some dyes. Also, thinned, back lit CCDs show a 70% increase in quantum efficiency over front lit CCDs. Finally, CCDs with several readout nodes are available. These decrease read noise by decreasing the bandwidth at each node. However, cameras have to be designed with additional amplification circuitry, and this increases cost.

Most systems offered at a moderate price (lower than \$40,000) are general purpose devices that are optimized primarily for long integration time applications. Long integration time devices are useful for observing low light level phenomena that remain unchanged over long periods of time. These devices use CCDs with high spatial resolution (frames are read out every few seconds, reducing read noise and allowing higher resolution, see Section 3.5) and low dark current. Dark current optimized systems use an architecture that limits dynamic range (see Section 3.3), and are therefore not desirable. Finally, manufacturers sell general purpose software that is not optimized for high speed continuous recording.

Several CCD systems were evaluated, and three camera systems were tested with monolayers loaded with Ca^{++} sensitive dye Fluo3. None of the systems available at reasonable cost were optimized to continuously stream information to a storage device for long periods. In all cases, the rate limiting step in the storage and display process was the software as opposed to camera or computer hardware. In particular, camera control software is designed to be used with inappropriate operating systems: all cameras in a moderate price range operate under Microsoft Windows. Aside from placing unnecessary overhead on computer resources, the operating system caches memory prior to streaming to disk. As a result, the operating system tries to transfer cached RAM to disk in one operation. As the camera continues to download information to the computers direct memory access buffers, overload results and the camera stops recording.

The configuration chosen was the Princeton Instruments (Trenton, NJ, USA)

camera with the EEV 576×384 frame transfer CCD. The choice involved software considerations (it was one of two cameras tested that could stream data to disk as described above) and CCD options. Princeton Camera offered the EEV 576×384 frame transfer CCD which has several advantages over those offered by other companies. The CCD has larger than average pixels, and doesn't use AGP architecture (a common CCD configuration which limits dark current at the expense of well size.) Noise associated with frame transfer is comparable to more modern CCDs. The camera is cooled, lowering shot noise and dark current. The camera transfers information directly to computer memory via an interface board mounted on an EISA bus (an extended computer bus architecture designed for fast throughput). Each pixel is digitized at 12 bits, and the image is displayed in a window on the computer screen. The software (Winview, Princeton Instruments, Trenton, NJ, USA) has a mode of operation in which screen display is updated after all essential storage and camera operation are complete. This allows continuous storage with no skipped frames while still permitting intermittent screen display for visual feedback during experimental runs. Images are stored directly on hard drive (Micropolis model 4AV) and then permanently stored on recordable CD ROM.

The camera can transfer a maximum of 1.4 megabytes per second to the computer due to limitations in the serial cable connecting the camera to the control board. This limits the camera to 8 frames per second at full resolution. By binning the image extensively, high temporal resolution was achieved (200 fps, using 5×5 binning on a 100×100 subarray). Even at 8 frames per second, the software cannot store and display this information for more than a few frames without crashing due to direct memory access (DMA) overruns as described above. The operating system's interaction with the program limits the bandwidth of the camera system to 75 Kb/s. However, as experiments at low light required extensive binning, 75 Kb/s proved to be sufficient for some applications. Typical experiments used 3×3 binning from a sub array on the chip for a final spatial resolution of 50×50 pixels. Frame read out rate was set at 20 fps to limit throughput to 75 Kb/s. Although temporal resolution is low, continuous records of up to 30,000 frames (the upper limit allowed by the

software) were collected. Records at different temporal and spatial resolution were acquired within the described throughput limits.

3.4 Data Analysis

The software sold with the Princeton Instruments camera was not capable of playing back the data files collected during experimental runs. The camera control software (Winview, Princeton Instruments) saves data from the camera in a proprietary format. Princeton Instruments provided details of the SPE format. Custom software was written that allowed playback, image processing, and data analysis.

The software (called gview.exe) runs under a 256 color DOS window in Windows 95. The interface allows mouse control and keyboard control of a variety of functions. The following sections summarize image processing and data analysis methods in gview.

3.4.1 Pixel and Frame Transformations

Data from each pixel in the camera is saved as a 12 bit number, corresponding to 4096 gray levels. The human eye, however is comfortable resolving 5 bits of colour[214], necessitating massive data compression prior to display. In practice, the graphics drivers available use 16 gray levels, and color data display (although implemented as an option) was frequently distracting. The software therefore has to perform a large amount of compression on the data while preserving interesting features for display.

Each pixel undergoes the following transformation prior to display:

$$Final\ Value[x, y] = Offset + \frac{(Pixel[x, y])}{Stretch} \quad (3.7)$$

where *Offset* and *Pixel Value* are global variables (variables applied to each pixel regardless of spatial location) that can be adjusted by the user while the program runs. *Offset* functions as a brightness control, and *Stretch* controls contrast. The above transformation would be adequate if each pixel requires the same brightness

and contrast adjustment, but this is rarely the case. For example one pixel can be changing its value between 1000 and 2000 in response to changes in the preparation, while another can be changing between 300 and 305. A single choice of *Offset* and *Stretch* would display appropriate information for only one of the pixels.

Pixel-specific transformations allow automatic setting of offset and stretch parameters for each pixel over the whole frame. A background frame and a pixel normalization frame can be calculated and applied to the raw data prior to display. The user can determine which frame or frames are used to calculate background or normalization frames and update them as required while viewing the data. Background frames are obtained by averaging each pixel in 20 successive frames and storing the result as an array of offset values. A normalization value for a pixel is determined by finding the maximum and minimum data values that the pixel must display over a certain time range (set at a default of 50 frames). The range (maximum - minimum value) for each pixel is stored in a array, which is then used to scale the data for each pixel in the display frame. Background subtract is a common feature found in most image processing packages. However, pixel normalization is specific to this application.

In addition to the above transformations, adjacent pixel averaging was implemented. Data values from 8 nearest neighbours are averaged and used instead of the raw pixel data. When this is done the background frame has to be spatially averaged in the same way to ensure that the spatial frequency of the background and displayed frame are the same. Spatial averaging is a common transformation used to reduce noise. Temporal averaging, where pixels are averaged over a number of subsequent frames, is implemented when calculating background frames. Temporal averaging is not applied on raw data continuously as this transformation tended to blur travelling wavefronts.

The final value at each pixel given the above transformations (background subtract, pixel normalization, and spatial averaging) is:

$$Final\ Value[x, y] = Offset - Background[x, y] \quad (3.8)$$

$$+ \sum_{n=-I}^I \sum_{m=-J}^J \frac{pixel[x + I, y + J]}{n(Stretch \times normalization[x + I, y + J])}. \quad (3.9)$$

where $I = J$ is 1 if eight adjacent pixels are averaged.

Offset and *Stretch* parameters still operate as brightness and contrast that operate over the whole image.

Examples using the transformations in Equation (3.8) are shown in Figure 3.6. Data was obtained from a spontaneously beating monolayer preparation (see section 5.2.1). Figure 3.6A shows a frame of data with minimal processing, as only the *Offset* and *Stretch* are adjusted. Figure 3.6B shows the same frames with background subtraction. Figure 3.6C shows the effect of averaging, and Figure 3.6D shows the effect of pixel normalization. Details in the data become progressively more clear; pixel normalization brings out details hidden by uneven lighting in the lower half of the frame, as well as low dye loading and response in the top left corner.

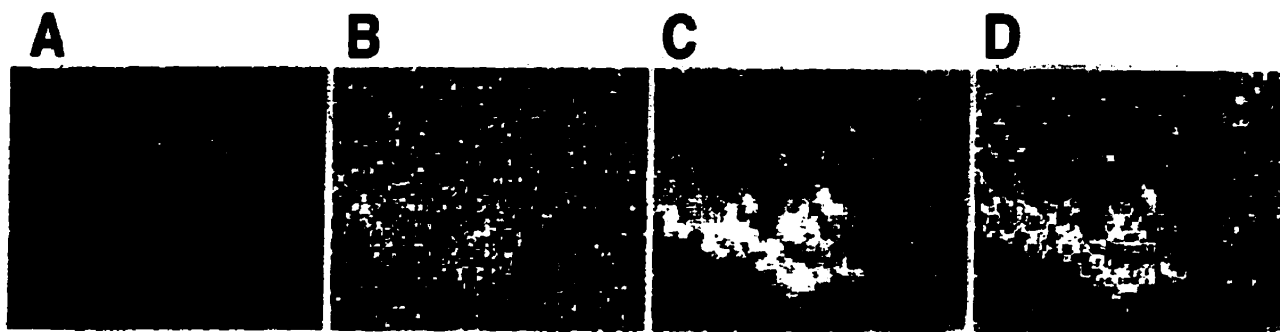


Figure 3.6: Software data processing. A) raw data. B) background subtraction. C) spatial averaging. D) pixel normalization.

3.4.2 Data Analysis within Gview.exe

Relative timing of events is important when mapping activation patterns. Two techniques for determining the timing of events at different points in the frame were

developed. The first involves selection of pixels of interest within the frame using the cursor or the mouse. Pixel intensity within the selected area is summed over the area, and the result plotted in a separate window and saved to disk as a separate file. The second technique involves detecting wavefront location automatically and generating isochronal maps (see [124]) from the transformed data.

Plotting pixel intensity over time gives a measure of the fluorescent signal at one point in the frame over time. As data is noisy, it is useful to average a number of adjacent pixels to reconstruct the underlying fluorescent signal. The user can select any number of rectangular areas with the mouse or cursor and the resulting intensity vs. time plots are displayed. The location of the boxes can be adjusted, and additional regions can be selected and deselected as needed. The resulting intensity vs. frame number plots are stored in separate files with a header giving frame number and the dimensions and location of the bounding rectangle for later analysis. The summed pixel values are obtained from raw data and are not affected by the transformations in the above equations.

Frequently, useful timing information can be obtained from within gview by manipulating the intensity plots on the screen as they are generated. The user can move and scale traces within the display window. This allows traces to be lined up over each other in order to better resolve timing between events. This technique has been useful for rapid analysis between experimental runs enabling change of protocols if needed.

Figure 3.7 shows traces generated from the spiral shown in Figure 3.6. The location of the rectangles used is shown in Figure 3.7A. Spikes can be observed as the wave travels through individual boxes. This diagram indicates that the wave front travels in a roughly circular path.

Data can also be exported from gview in the form of isochronal maps. Isochronal maps are contour maps in which each contour gives the location of the wave front at constant time intervals. Isochronal maps have been used for displaying data from optical[51, 35, 68, 69] and electrode mapping[210] experiments. Gview generates

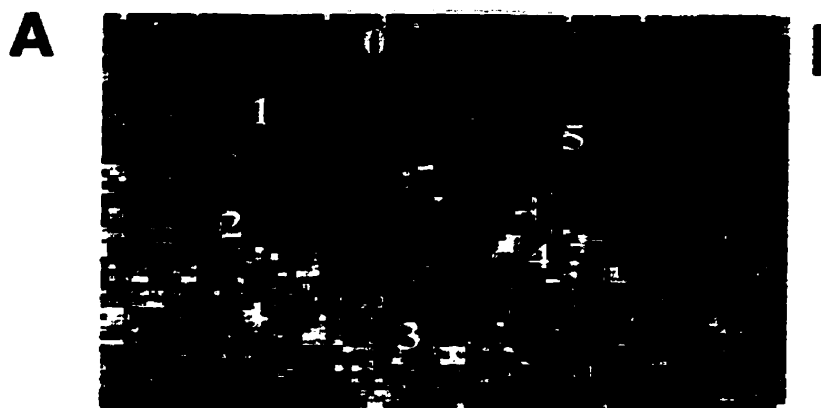


Figure 3.7: Use of pixel summation to obtain fluorescence vs time plots. A) location and size of summed rectangles.

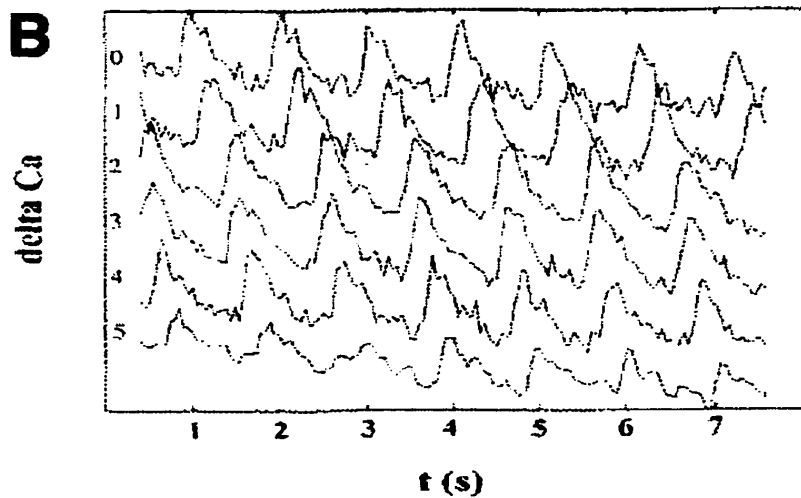


Figure 3.8: Use of pixel summation to obtain fluorescence vs time plots. B) output from the software generates traces as shown. Reentry is confirmed using this technique.

isochronal map files from image data directly ⁶.

Maps are generated as follows. Gview is operated in 2 colour mode, and the user manipulates parameters in Equation (3.8) to remove noise and enhance the signal. The user has direct access to the background and normalization frames. Noisy areas can be selected with a mouse and blacked out, or especially faint regions can be enhanced. These manipulations are sometimes necessary as compression of data from 12 to 1 bit can result in artifacts. Also, regions of the frame that are not of interest can be removed from the final calculation. Parameters in Equation (3.8) cannot be changed once the isochron mapping routine is initiated, as this could generate false data.

Isochron generation starts once the user has a reasonably clear travelling wavefront on screen. The algorithm used removes high frequency temporal events using a heuristic approach without resorting to temporal averaging. Temporal averaging tended to blur the location of the wavefront. The user can change parameters that control how the algorithm calculates the location of the wave front. For example, noise in the signal can create small transient 'holes' in the recorded traveling wave. Holes in the wave can be filled depending on the size of the hole, the number of frames that the hole persists, and the intensity of the surrounding wave. Isolated large events (a region becomes active but persists for one or two frames only) can be also ignored. As the algorithm assumes the presence of smoothly travelling waves and tries to ignore isolated events, care must be taken to make sure that the resulting isochrons represents actual data.

The location of the wave is stored in an array which stacks the wave location over a user controlled number of frames prior to outputting the result to a file. Many sequential isochron files can be generated; for example a five second sequence consists of a 100 frames of raw data at 20 fps. Outputting an isochron file every second generates 5 isochron files, each containing the location of the wave over 20 frames.

⁶Software has previously been developed for generating isochronal maps from electrode arrays[210]

A separate program (`isoview.exe`) is used to view the isochron files. It reads in consecutive isochrone map files, and displays them as a movie by hi-lighting the location of the wave over time. The user can then select a frame from this movie and output it as a portable greymap file. This allows the user to choose the time window over which the final isochron map is generated. An example of an isochronal map generated from the same data set shown in Figure 3.6 is given in Figure 3.9.

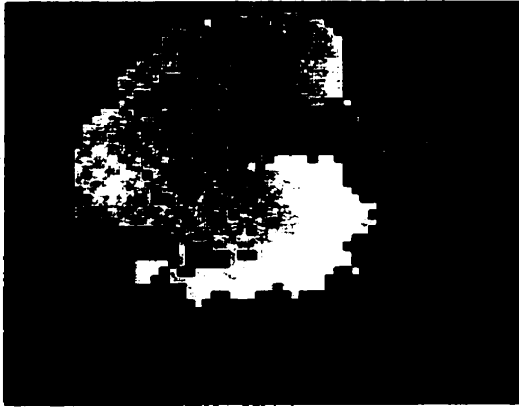


Figure 3.9: Isochronal map generated as discussed in text.

3.4.3 Additional Output Modes

Gview also can output files as a frame stack. This output mode is useful for compressing large amounts of data to a single file. Pixel values are summed over each column in a frame and the resulting row of summed values are outputted instead of the whole frame. An example of a spiral wave displayed as a frame stack is shown in Figure 3.10.

Gview outputs all graphics as portable greymap files⁷. Portable greymap (PGM) is an open graphics standard which can be read and converted by several commercially available graphics programs.

⁷The portable greymap (PGM) format is part of the Extended Portable Bitmap format. Information on this format can be obtained by viewing the manual pages on PGMs on all Unix (and Unix-like) systems.

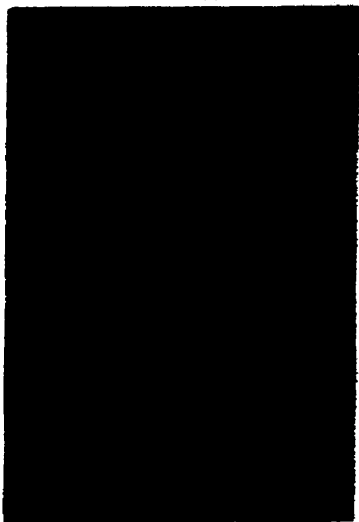


Figure 3.10: Framestack image of spiral wave generated as discussed in text.

3.5 Photodiode Array Construction

This section discusses construction of a photodiode array with second stage amplification. Photodiodes were used in pilot studies of monolayer preparations stained with voltage- and calcium-sensitive dyes (see Chapter 5.3.1). Photodiode measurements were largely abandoned as the camera system (Section 3.3) was better suited for high spatial resolution mapping of the monolayer preparation. Photodiodes will be used in future studies in which millisecond temporal resolution is required.

Equations governing noise and gain of photodiodes and operational amplifiers can be found in basic textbooks[25, 123] and technical publications[24]. The photodiode array constructed in our lab is similar to those used by several researchers[36, 66, 75, 112, 239, 241, 246]. Some distinguishing features of the photodiode array used here are very high value feedback resistors and individual photodiode elements. The second stage unit introduces a novel circuit design to implement computer controlled gain and offset adjustments. Design and construction of the photodiode and second stage are discussed in Sections 3.5.1 and 3.5.2 below.

3.5.1 The Photodiode Array

Photodiodes are individual light sensitive elements that transduce photons to electrons. As the signal from a photodiode can be very low, amplification circuitry is required. The energy transmitted from a photodiode can be measured as a voltage or a current output. Voltage measurements can be obtained by putting the photodiode in series with the operational amplifier input, which ideally draws no current. As the sensitivity of the diode varies with voltage across it, output voltage varies logarithmically with light. A more desirable linear relationship between light and voltage requires a current to voltage conversion circuit (Figure 3.11). This circuit represents the most common way of amplifying photodiode output[24, 123]. The voltage across the pins of the photodiode are held at zero as the amplifier gain keeps the voltage at the inverting input at virtual ground. The input resistance at the non-inverting input is R_{gain}/A , where R is the resistance of the feedback resistor, and A is the open-loop gain of the operational amplifier. Although R_{gain} is large, the high amplifier open loop gain causes the input resistance to be negligible in comparison to the output resistance of the photodiode. Current from the photodiode does not pass through the input of the operational amplifier but causes the amplifier gain to match the current by creating a voltage drop across R_{gain} . The output voltage developed is equal to the diode current times R_{gain} . For maximum sensitivity the feedback resistor should be as high as other factors, such as frequency response and noise, permit. Noise from the photodiode and operational amplifier in the IV conformation come from two sources. Noise is generated from the feedback resistor itself and has a spectral density of $\sqrt{4kTR}$, where k is Boltzman's constant, and T is absolute temperature. This noise appears at the output of the IV converter without amplification. A common measure of the performance of a circuit is the signal-to-noise ratio[25],

$$\text{signal to noise ratio} = \frac{\text{RMS voltage of the signal}}{\text{RMS voltage of the noise}} \quad (3.10)$$

where RMS voltage is the root mean square (the square root of a mean of a set of squared values) of the voltage⁸. The signal increases in direct proportion to R , so signal to noise ratio increases as the square root of R . For low light signals, R_{gain} is typically in the gigaohm range[24].

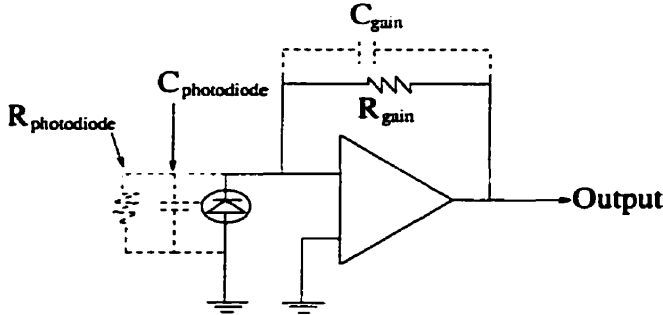


Figure 3.11: Basic operational amplifier current to voltage circuit schematic.

Noise from the operational amplifier that arises from the shot noise of the input bias current also influences the output, and is amplified the same amount as the signal current. The noise shows a characteristic frequency dependence known as *gain peaking*. Under DC conditions, the noise is amplified as $1 + R_{gain}/R_{photodiode}$ [24]. Although R_{gain} is in the gigaohm range, $R_{photodiode}$ is larger, minimizing noise gain. However, the capacitance of the photodiode passes noise current at higher frequencies which effectively decreasing $R_{photodiode}$, adding significant noise. This noise can result in destabilizing oscillations as it is amplified by high R_{gain} . The amplification of gain peaking noise is given by $1 + C_{photodiode}/C_{gain}$ [24], where $C_{photodiode}$ and C_{gain} are capacitance of the photodiode and feedback resistor respectively. Gain peaking noise is attenuated by stray capacitances across the feedback resistor. As $C_{photodiode}$ is usually in the hundreds of picofarads, and C_{gain} is low, noise is amplified by a factor of several hundred. To minimize this effect, low input bias operational amplifiers, and low capacitance, high resistance photodiodes are required[24]. Also, as gain peaking occurs at higher frequencies, it can be reduced by putting a capacitor across the feedback resistor. As picofarad capacitances can decrease bandwidth

⁸A conceptually simpler way to think of RMS is that the probability is 68% that the voltage signal will be between -RMS and +RMS.

below 10 Hz if R_{gain} is large, this approach is limited by bandwidth requirements.

Another source of error is a DC offset current, created from high R_{gain} as it develops significant thermal DC voltage drift from the small current from the inverting input[24]. If the offset error is large, it can saturate the operational amplifier. To compensate for this error, an equal resistance can be put across the operational amplifier, noninverting input and ground. The remaining DC error is caused by mismatches between the two resistors and the amplifier input currents at the two inputs. However this approach causes a voltage drop across the photodiode as the noninverting input is no longer held at ground. This results in a leakage current from the photodiode, which can be as large as the original offset. In addition, matched gigaohm resistors are costly. The original problem is best avoided by using an operational amplifier with low input current specifications.

Finally, a major source of noise is interference from external noise sources. A current to voltage converter is sensitive to noise coupling from electrostatic, magnetic and radio frequency sources. Electrostatic coupling supplies noise signals through the mutual capacitances that exist between any two objects[24]. To minimize this error signal, shielding is used to intercept that current and shunt it to ground. A potential problem with shielding is that it can create parasitic capacitances which can add to gain peaking noise. Electrostatic noise can come from sources independent of the circuit, such as power lines, but can also come from neighbouring operational amplifier outputs such as operational amplifiers placed in an array. External noise sources are easily identified and shielding can be added until the noise disappears. However signal pick up from neighbouring amplifiers is more difficult to isolate. Amplifiers are in close proximity to each other as they must be mounted as close as possible to the photodiodes they monitor (long wires leading from the photodiodes would pick up external interference, and shielding these wires to decrease noise would add capacitance to the signal, increasing the gain peaking effects). As a result, the output of one amplifier may be close enough to the input of others to be detected and amplified. Special attention must be made to avoid this possibility by keeping the outputs of the operational amplifiers as far as possible from the inputs of other

amplifiers. One approach to minimizing this problem is using fiberoptic cables to carry the signal from different points in the image to the photodiodes. Photodiodes can then be placed farther apart. The sensitivity of the current-to-voltage circuit to noise makes careful wiring and soldering very important. It is necessary to keep the circuit as simple as possible around the amplifier inputs to avoid unnecessary interference and capacitance effects.

Design of a photodiode array involves defining the required performance of individual sensing elements, as well as taking into account noise sources outlined above. In general, increasing gain of a circuit decreases the frequency response, or bandwidth, of the circuit. Therefore, one has to consider the circuits expected input levels and required output levels as well as bandwidth requirements.

The circuit should be as sensitive to light as possible, so that excitation light levels can be kept low. If the circuit saturates for a given input level, excitation light can be lowered with the added benefit of lowered phototoxicity. Therefore sensitivity should be maximized given bandwidth constraints.

Resolving the upstroke of the action potential requires millisecond temporal resolution, which at first suggests a circuit with kiloHertz bandwidth. Such a high bandwidth is not required, as action potentials have durations of hundreds of milliseconds. Action potential shape is distorted in a predictable way by low frequency filtering, and can be reconstructed if necessary. It is also possible to determine with millisecond resolution the action potential start time as the circuit responds at the start of a stimulus even though the amplitude of the response is attenuated. As cardiac action potentials are 100 ms in duration or more, 10 Hz bandwidth can be sufficient. As a decreased minimum bandwidth allows use of higher gain, circuit design should take advantage of this expected signal shape in order to optimize performance. It should be noted that since neural action potentials have durations of only a few milliseconds, detection of neural action potentials would require circuits with higher bandwidth.

The Motorola MRD500 photodiode was chosen as the detector element in the array because of its low capacitance[299]. This minimizes the effects of gain peaking.

Its small photosensitive area (the capacitance of a photodiode is proportional to its size) is compensated for by a collecting lens built onto the photodiode. The resistance of the photodiode is large enough to minimize noise for low frequency signals. The wavelength is typical of most silicon photodiodes, and peaks at 800 nm. Although it is possible to get diodes with sensitivities in other ranges, this frequency is close to the ideal range needed for Di-4-ANEPPS (630 nm) measurements. The feedback resistor chosen was a 10 gigaohm Eltec glass resistor. The resistor is very small, allowing it to be mounted directly across the inverting input and operational amplifier output, minimizing interference noise caused by longer leads. In addition it is expected to have small stray capacitance due to its size, preserving bandwidth.

The amplifier used is an Analog Devices AD645. It was chosen because it has very low offset voltage[299], which allows shunting the noninverting input directly to ground. Offset correction circuitry would have added an additional resistor and bypass capacitor to the inputs, which would increase the circuit's tendency to pick up noise. The operational amplifier also has low input bias current, which minimizes the effects gain peaking.

Amplifiers are glued on their backs to bread-board. This allows attachment of the feedback resistors across the underside of the operational amplifiers. This arrangement minimizes the amount of wire attached to the input pin. The inverting input is attached to a photodiode, and the noninverting input is attached directly to a groundplane surrounding the breadboard. The photodiode is then attached to the groundplane in close proximity to the noninverting input. The output of each amplifier is as far away from the photodiode as its package allows. The output signal moves off the board and up through a shielded printer cable for further processing. This configuration allows 8 operational amplifiers to be mounted (on either side of the board) in close proximity to the photodiodes while minimizing electrostatic coupling effects from the operational amplifier inputs and outputs.

The response of one diode in the array is shown in Figure 3.12. A square pulse of light lasting 200 ms is generated from a LED powered by a signal generator (Wavetec80, San Diego, CA, USA). The resulting signal is shown. Dis-

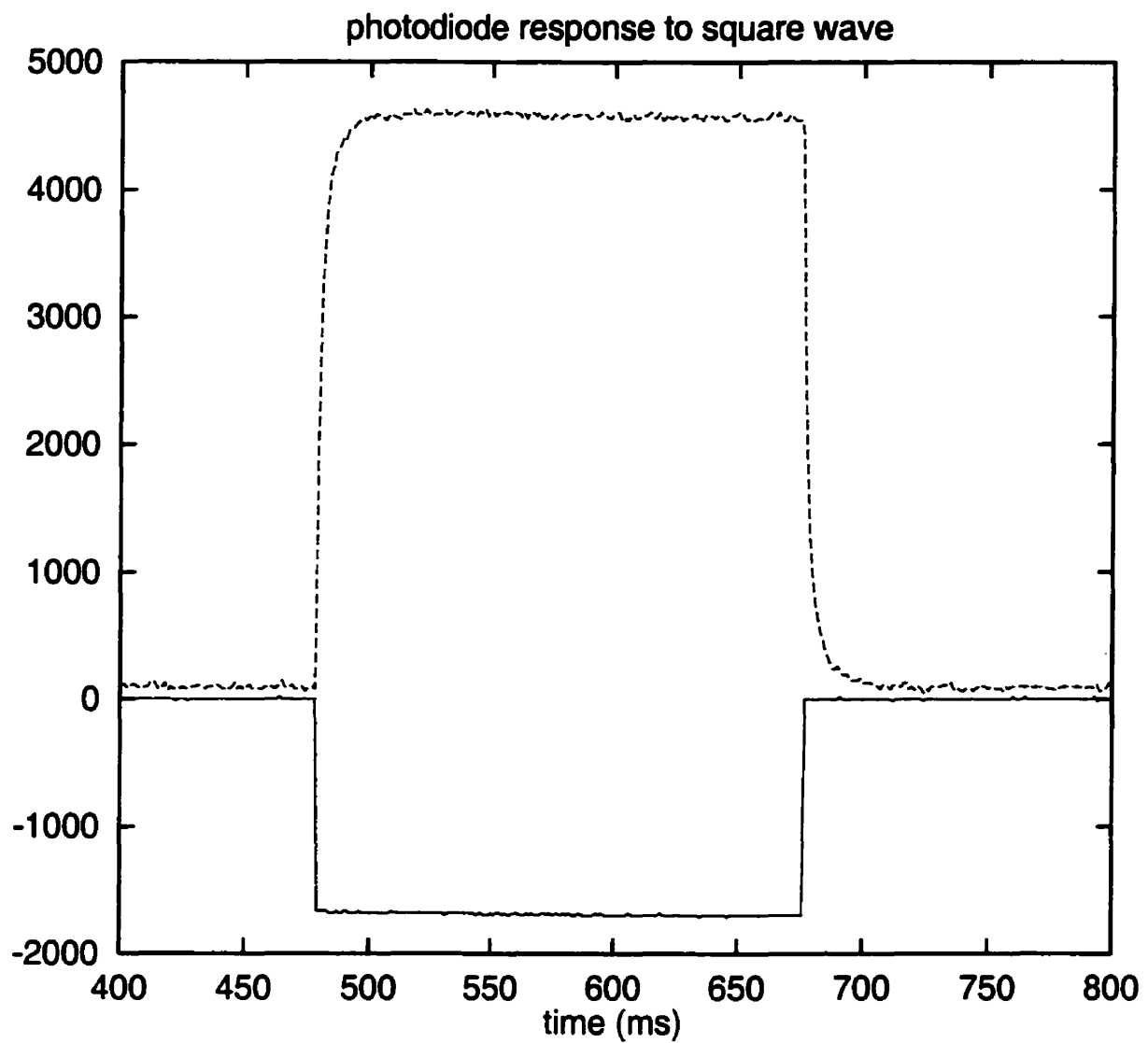


Figure 3.12: Output from the photodiode from a square test pulse of light. The pulse is 200 ms in duration.

tortion due to low bandwidth is visible near the top of the pulse. Frequency response can be estimated from this figure by obtaining a time constant τ , where Photodiode Output $\propto 1 - \exp\frac{-T}{\tau}$, where T is the time. The time constant τ is roughly 0.01 s. If we assume that the dominant limit on frequency is due to stray capacitance across the photodiode, and we assume a one pole roll-off, we can estimate the stray capacitance to be 1 picofarad⁹. The response of the diode to shorter signals is also shown. A plot of output size vs. input repetition rate is given in Figure 3.13. The range of the circuit is ± 10 V, approximately (rail to rail). The noise level is roughly 5 mV. There is negligible interference with shielding. However, a large 60 cycle (100 mV peak to peak) signal is observed if the shielding is removed.

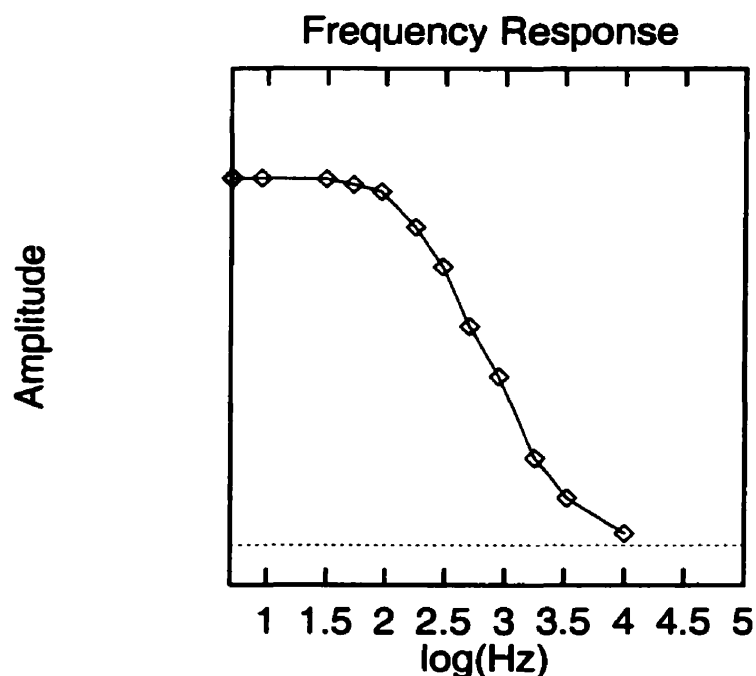


Figure 3.13: A plot of output signal amplitude vs. input signal repetition rate. Square light pulses of different frequencies were detected by the photodiode array. The magnitude of the signal decreases with decreases in signal repetition rate.

⁹ $\tau = CR$, where C is capacitance and R is resistance. Here $R=10$ gigaohm and $\tau=0.01$ s

3.5.2 Second Stage Circuitry

Useful optical signals often are small signals that are summed with a large offset. For example, voltage sensitive dye Di-4-ANEPPS gives a large fluorescent signal which only changes 5-10% with membrane potential changes of 100mV[87]. Ideally the offset should be subtracted and the useful signal amplified before the signal is recorded¹⁰.

Initial experiments with a small 3 element array demonstrated that this approach does not work. Offset signals vary greatly from point to point within the Di-4-ANEPPS stained monolayer. Offsets could vary from 300 mV to more than 2 V depending on location, presumably due to differential staining and irregularities in the surface of the monolayer. There is also a significant signal drift associated with dye bleaching (which acts to reduce offset)[246]. More importantly, the system is very sensitive to light noise. It was difficult to isolate the array so that movement from the operator or output from computer screens did not affect the output. Also, the quality of the signal varied from point to point in the monolayer. Typical signals were 4-8% of total offset. However, useful signals were sometimes as low as 2% of total offset. The above considerations resulted in signals that were not recordable. As the signals vary by as much as 10× and the range of the digitizing equipment has to be set to encompass the largest signal, digitizing equipment cannot record unconditioned signals reliably. For example, a 8% signal riding on a 300 mV offset would result in a useful signal of 24 mV, which would be digitized with 32 point resolution. Even though this may be sufficient for some purposes, interference noise make it impossible to move a 24 mV signal from detector to digitizer without loss.

The amount of noise inherent in the system makes AC coupling impossible. Preliminary experiments showed that action potentials are not easily resolvable with an AC coupled signal. This is not surprising considering the signal to noise ratio is sometimes as low as 3/1.

¹⁰If a high resolution digitization scheme is used, offset and signal can be recorded without loss of data. For example, a 12 bit digitization scheme could potentially record a useful signal with 400 (4096 x 10 %) point resolution.

A simple three element second stage was constructed that incorporates hand tunable offset voltage controls and variable amplification (Figure 3.14). The circuit allowed the offset to be removed and the signal amplified by as much as $500\times$ prior to digitization. However, slowly changing offsets, as well as room light noise, required frequent operator adjustment. Manual adjustments are impractical for larger arrays.

Automatic offset control circuits have been developed for use with photodiode arrays[241]. These circuits use a large resettable capacitor to store the DC level which is then subtracted off the incoming signal. The operator can hit a switch to reset the capacitors in the second stage. Although this technique is simple and effective, it requires a large capacitor and an analog switch for each channel. The number and size of components make laying out a large number of automatic offset circuits impractical. In addition, capacitors drift over time. Automatic gain circuits have also been developed[239, 241] which allow the operator to switch between a few preset gain levels. This approach requires digital logic for each channel. Even though signals are eventually digitized, the above circuits do not take advantage of the recording computer's ability to monitor and change incoming signal.

A circuit was developed that allowed computer controlled offset and gain control for each photodiode. The second stage circuit takes advantage of the fact that information on each channel is available to computer algorithms in real time. The computer outputs control signals to the second stage circuit, adjusting gain and offset automatically.

As every channel is eventually digitized by computer, this system was designed to allow automatic monitoring of levels with a computer program which outputs signals to second stage circuitry to optimize the voltage levels prior to digitization.

Offset and gain control are accomplished by the circuits shown in Figure 3.15. A digital signal is outputted from the computer and changed to an analog signal by multichannel 8 bit digital to analog converters(D-As). D-As can be arranged in parallel so that a single 12 bit word can control 32 D-A channels. As the D-As generate analog signals from a preset reference signal, one D-A in the chain is used to provide reference signals to the other channels, increasing the D-A's resolution

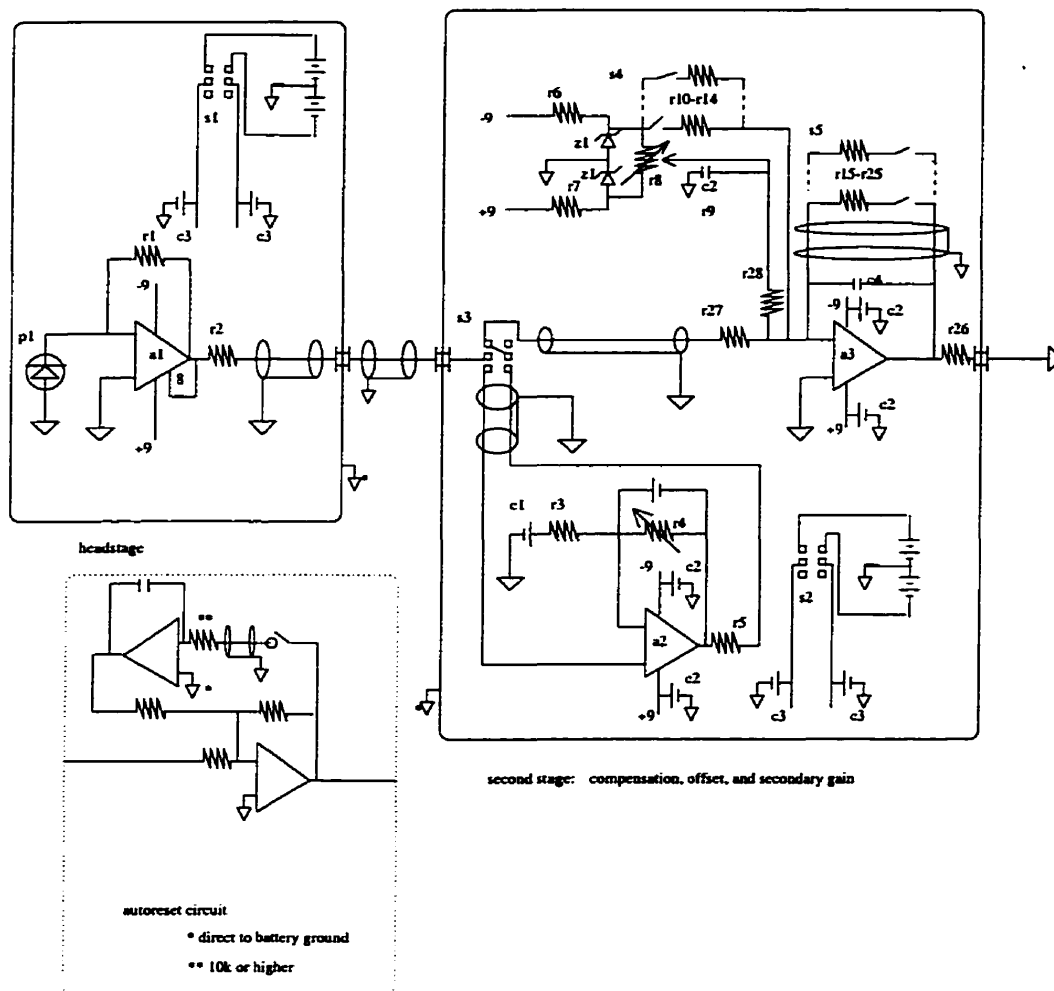


Figure 3.14: A simple second stage circuit. The circuit is shown connected to the a photodiode output (right) and a automatic reset control switch (inset). The circuit itself consists of an offset control, which is an operational amplifier (a2) with variable gain controlled via r4, summed with the input signal. The variable gain circuit is operational amplifier a3 with a 10 element switch to toggle between different resistors (r15-r25). The automatic reset control switch was included as a test circuit in this design, and was later abandoned in favour of the computer controlled gain and offset described in sections below.

to 10 bits[123, 299]. The circuit uses one analog channel to control the offset and one channel to control the gain. As there are 8 D-As per chip in the AD7064 package used, one chip is required to condition 4 channels. Automatic gain control is accomplished by the circuit shown in Figure 3.15A. The circuit uses an analog offset line from the D-A's to control gain, and sums another analog line with the output of the photodiode. The circuit uses an original design that allows use of very inexpensive audio circuitry and a small number of components to control gain over a large range with very little noise.

Voltage controlled amplifiers for low noise applications exist but are often expensive and come in large package sizes, making them impractical for multichannel applications. Lower cost VCAs in quad chips are available. A typical unit is Analog Devices SSM2024. These units function as current attenuators: an applied control voltage can decrease the current output of the circuit, not increase it. The resulting current has to be amplified by second amplifier. In addition, these circuits function optimally over a very narrow current input range requiring an input voltage less than 50 mV. Using these circuits as suggested by the manufacturer has three disadvantages. The weak incoming signal from the photodiode stage has to be scaled down before entering the VCA, which will increase the relative noise contribution from the second stage. The level of the signal is not known before entering the VCA, so optimal performance from the VCA is not possible. Finally the signal is attenuated by the VCA before being amplified, further increasing the contribution of noise.

The following circuit was designed to remove these disadvantages of the SSM2024¹¹. The VCA is placed in the feedback loop of an amplifier in a non inverting gain configuration (see Figure 3.5.2A). Unlike conventional gain circuits, the level of the input signal is not known, but the desired output level is. The output level of the circuit should fill the A-D range of the digitizing board. As the output peak-to-peak signal is known, it is possible to scale the input to the VCA so that its input is

¹¹Recently, the SSM2024 has been discontinued. Analog Devices supplies a replacement part with better specifications.

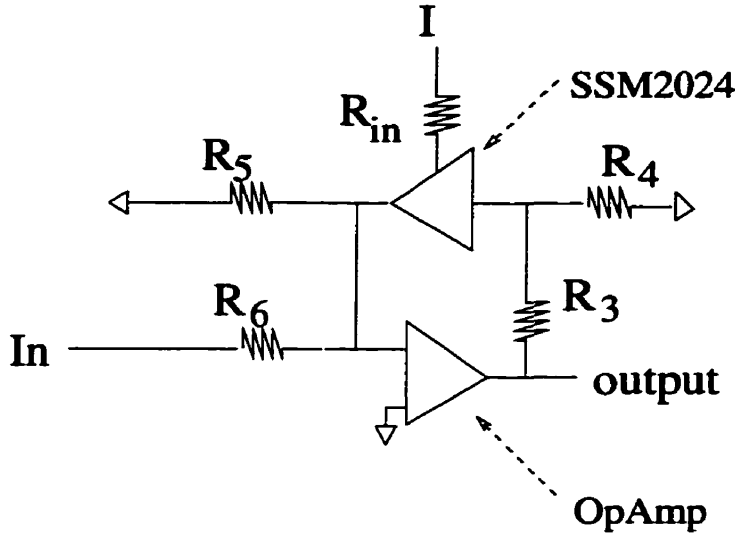


Figure 3.15: The computer controlled second stage circuit. See text.

optimal. The VCA output acts as a resistor in the feedback loop of the operational amplifier. The signal from the photodiode stage inputs directly into the operational amplifier, protecting the signal.

The circuit shown is laid out so that the VCA replaces the feedback resistor R_{gain} in a typical noninverting operational amplifier application (Figure 3.15). The gain of the circuit shown is inversely proportional to the current supplied to the VCA input. The VCA itself outputs a current that is proportional to V_{in} [299]:

$$I_{VCA} = 8.17 I_{control} (200 / (R_{in} + 200) V_{in}), \quad (3.11)$$

where $I_{control}$ must be no more than $500 \mu A$. The SSM2024 attenuates the signal it receives. The feedback resistor in a typical noninverting operational amplifier circuit essentially performs the same task. The VCA is used in the second stage circuit as a voltage controlled variable resistor.

The VCAs total harmonic distortion (THD) performance and signal to noise ratio are determined by the peak-to-peak input signal level. There is an inverse relationship between the signal to noise ratio and THD. The SSM2024 can give a signal to noise ratio of 80dB with a THD of 1% for a 50mV peak-to-peak signal[299]. Increasing the signal size degrades THD to as much as 10% which is unacceptable,

while decreasing signal size decreases the signal to noise ratio to as low as 60 dB.

Resistor R_4 's value of 200 ohms is recommended by the manufacturer as offering the best offset and control rejection[299]. R_3 scales the input to the VCA. As the input to R_3 is the operational amplifier output, and we know that that equals the 10 V peak-to-peak, R_3 can be calculated to be

$$50mV = (200/R_3 + 200)10V, R_3 \approx 40K\Omega \quad (3.12)$$

The output signal from the SSM2024's pin 4 is given by Equation (3.11). For a 500 μA control current, the output of the VCA $I(VCA)$ is 0.0002A, for a 100 μA control current, the output is 0.00005A. The circuit is expected to deal with signals as low as 50 mV peak-to-peak, but as high as 1 V peak-to-peak. For the maximum input control current of 500 μA we desire a gain

$$V_{out}/V_{in} = 10, \text{ so } V_{in} = 10V. \quad (3.13)$$

and for the minimum control current we require a gain of 200.

As the inverting pin accepts minimal current (input resistance is ideally infinite for operational amplifiers), the current leaving the VCA must pass through R_5 . If the voltage drop across R_5 is 1V, and the output current is 0.0002A,

$$R_5 = V/I = 1V/0.0002A = 5K\Omega \quad (3.14)$$

For example, if the input was 100 mV p-p, then a gain of 100 is required. For the values of resistances calculated above, the control current is

$$0.1V = R_5 I_{VCA}, I_{VCA} = 0.1V/5K\Omega = 2e^{-5}A \quad (3.15)$$

from Equation (3.11),

$$\begin{aligned} I_{control} &= I_{VCA}/(8.17(200/(R_{in} + 200)V_{in}), \\ I_{control} &= 2e^{-5}A/(8.17(200/40200)10, \\ I_{control} &= 50\mu A. \end{aligned} \quad (3.16)$$

If a 0-10V variable voltage is applied to the VCA, 10V gets scaled by R_6 to be 500 μA , so $R_6 = 20K\Omega$. The VCA passes no current if less than 200 mV is applied

to the control input (this information comes from the SSM2024 data sheet), which corresponds to an input current of $10\ \mu\text{A}$. This gives a maximum bound to the gain at $500\times$.

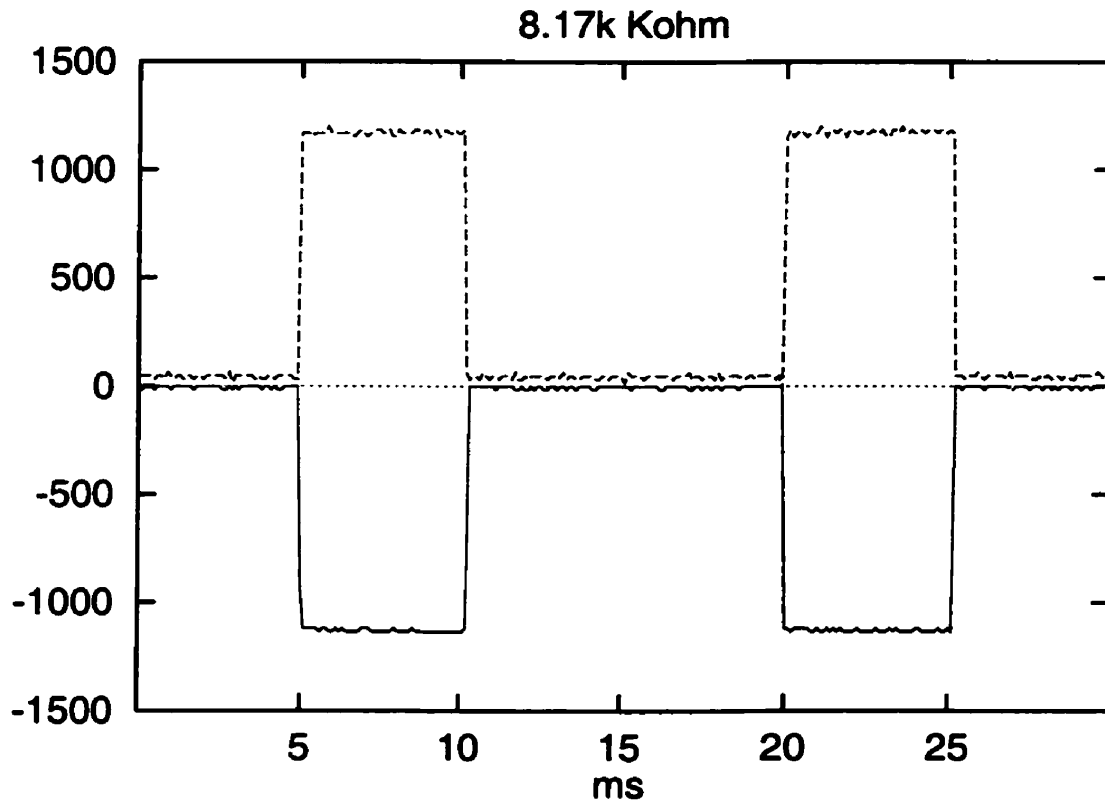


Figure 3.16: Square wave applied to second stage circuit, with low gain. The solid line is the input signal and the dashed line is the output signal. See text for details.

Performance of the circuit for different levels of $V_{control}$ and V_{in} are shown in Figures 3.16 and 3.17. The test voltage being inputted is a sine wave generated from a Wavetec signal generator. The output is digitized across $\pm 5\text{V}$ range at 12 bits. The resultant square wave is not distorted at either the high or low input ranges (20mV -1V). In comparison, if operated outside of a feedback loop, the VCA would not tolerate such a large ($50\times$) swing in input levels without having unacceptably large shifts in THD and signal to noise ratio.

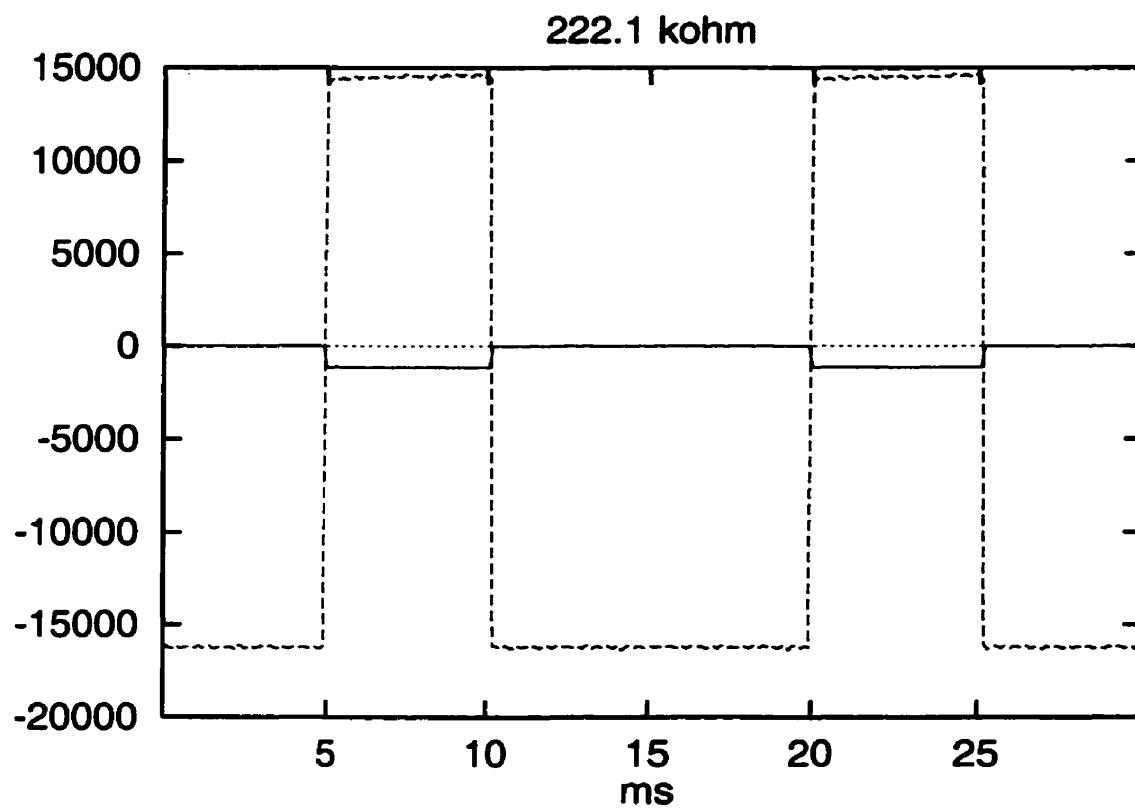


Figure 3.17: Square wave applied to second stage circuit, with high gain. The solid line is the input signal and the dashed line is the output signal. See text for details.

Chapter 4

Optical Mapping of the Atrioventricular Node.

4.1 Introduction

The apparatus described in Chapter 3 was designed to map signals from cultured monolayers of cardiac cells. However, similar optical mapping systems have been used to map potential waves from intact sections of the heart and whole heart preparations[35, 50, 62, 68, 69, 168, 189, 196, 240, 294, 295]. Our optical mapping system was modified to record waves of excitation from the atrioventricular (AV) node in sectioned rabbit heart. Conventional microelectrode techniques have been used to map conduction pathways through the AV node[4, 17, 18, 19, 136, 185, 207]. However limited spatial resolution of these techniques left the location of delays and activation sequences a matter of debate[35, 185, 186]. Optical mapping techniques had not been applied to the AV node at the time the experiments in this chapter were performed. A preliminary study using voltage mapping techniques on three rabbit hearts was conducted using the optical mapping system. The results were presented as an abstract and poster at the Noble Symposium[200]. Since that time other groups have optically mapped conduction through the AV node[35, 68, 69].

My contribution to this study includes the design¹ of a stage and perfusable, heated bath for large preparations, dye loading and optical mapping the AV node,

¹machining was done by S. Kekani, Physics Department, McGill University

and presenting and analyzing the data with the software described in Chapter 3. Dissection of the AV node, calibration of the bath, design of stimulation protocols and subsequent interpretation of the data were carried out by Dr. Andrew Munk and Kevin Petrecca. Additional immunohistochemical studies which related the sites of delay to the concentration of sodium channels were conducted on the preparations by Kevin Petrecca *et al.*[209]. As the immunohistochemical results do not relate to optical mapping they are not presented here.

4.1.1 Background

The atrioventricular (AV) node is the sole conduction pathway between the atria and ventricles in healthy hearts[185, 267]. The AV node causes a delay between atrial and ventricular contractions allowing optimal filling of the ventricle's chambers. It also acts as a low frequency filter by not conducting premature atrial beats[172]. Rapid atrial activity (atrial tachycardia) does not result in dangerous rates of ventricular contraction. Finally the AV node is a backup pacemaker if the sinus node fails to fire[186]. Despite its many important functions, the conduction pathway, site of delays and regions where automaticity originates are still not well known[35, 185, 186].

Ablation techniques (where a section of the AV node is surgically destroyed by a pulse from a catheter) have been successful in treatment of atrioventricular nodal reentrant tachycardia (AVNRT)[213]. The theoretical basis underlying these techniques is the concept of dual AV nodal pathways, hypothesized by Moe *et al.*[187, 193]. This early work showed that the recovery curve in dogs can show a distinct discontinuity, suggesting a switch in conduction between two pathways. Mapping studies[5, 132, 187] suggest that the slow pathway activates the node from the posterior direction while the fast pathway activates the node anteriorly. AVNRT supposedly occurs when an impulse travels down one pathway and up the other, forming a reentrant circuit[265]. Cardiologists target one of the pathways in order to break this circuit. Remarkably, despite extensive investigation over the last 50 years[68, 136, 276], the location and existence of the pathways is a subject of

continued debate.

There are two competing views of conduction through the AV nodal region[35]. One hypothesis is that conduction is slowed decrementally[121] due to high coupling resistance across the nodal region. The competing view is that delay is localized in a region of the node[207]. The discontinuous gap in conduction was inferred from intracellular electrode studies[18, 207]. The cause of the discontinuity in conduction is likely due to an anatomical inexcitable gap[35, 54] which causes the impulse to conduct electrotonically.

Optical mapping techniques are better suited than single electrodes for constructing activation maps of the AV node[69, 185]. Conventional electrode mapping studies require replicating experimental protocols while changing electrode placement. The AV node has numerous cell types and a complex three dimensional morphology[18, 185, 199]. Extracellular recording cannot resolve activation times of different cell types at appropriate space scales. Accurate mapping of activation times using intracellular electrodes is difficult as electrodes impale at unknown depths, resulting in measurement of different activation times at similar electrode positions[35, 18, 19].

Choi and Salama[35] and Efimov *et al.*[68, 69] have used optical mapping methods to record from the rabbit AV node. Both groups used photodiode arrays to record optical signals from Di-4-ANEPPS stained rabbit hearts. Choi and Salama[35] found that the location of the primary conduction delay within the AV nodal region is between atrium and AV node. Propagation is discontinuous in the sense that the atria, AV node, and ventricles activate with periods of electrical silence between them. Efimov *et al.*[68] mapped activation patterns to the node, and concluded that activation occurs through the posterior slow pathway during normal sinus rhythm. The discontinuous conduction observed in Choi and Salama's work[35] was not obvious in Efimov's records.

4.2 Atrioventricular Node Preparation

New Zealand White rabbits (2.5 kg) were anaesthetized with an intramuscular injection containing ketamine (75 mg per kg weight) and xylazine (5 mg per kg weight). Heparin was injected as an anticoagulant. The rabbit was killed by a blow to the neck. A mid-line thoracotomy was performed and the heart removed. The heart was pinned to a custom made stage which allows the preparation to be held at any angle relative to the optical axis of the macroscope. The wall of the right ventricle and atrium were dissected open to reveal the AV node, and the preparation was pinned in such a way as to avoid stretching the tissue. The heart was superfused with gassed (5%CO₂ balance O₂) Tyrode solution at a rate of 10 ml/min. The Tyrode solution contained NaCl 121.0 mM, NaHCO₃ 15.0 mM, KCl 5.0 mM, CaCl₂ 2.2 mM, MgCl₂ 1.0 mM, NaH₂PO₄ 1.0 mM, glucose 5.5 mM, and pH was adjusted to 7.3 with 2M NaOH.

The preparation was stained with 20 μ M Di-4-ANEPPS (4-[β -[2-(di-*n*-butylamino)-6-naphthyl]vinyl]pyridinium, Molecular Probes, Eugene OR) for 20 minutes. The Di-4-ANEPPS was prepared as a stock solution in dimethyl sulfoxide (DMSO) and Pluronic acid (1:1 ratio). After staining the preparation was rinsed with fresh oxygenated Tyrode to remove excess dye.

A high resolution image of the node is shown in Figure 4.1A. The image lines up with the labelled diagram shown in Figure 4.1B.

4.3 AV Node Results

Optical signals were captured with the CCD camera and signal processed as described in previous sections. Images were collected every 10 ms. Figure 4.2 shows an application of the signal summation technique discussed in Section 3.4. Boxes used for signal reconstruction are shown in Figure 4.2A. As fluorescence in Di-4-ANEPPS stained preparations decreases as cells depolarize, downward spikes represent peak activity as the wave passes through the node. Boxes 0 and 1 are excited simultaneously under conditions of spontaneous activity. A 20 ms delay occurs between boxes

1 and 2. This corresponds to an area near the compact node. This site of delay corresponds well with those elucidated from microelectrode studies[18, 19].

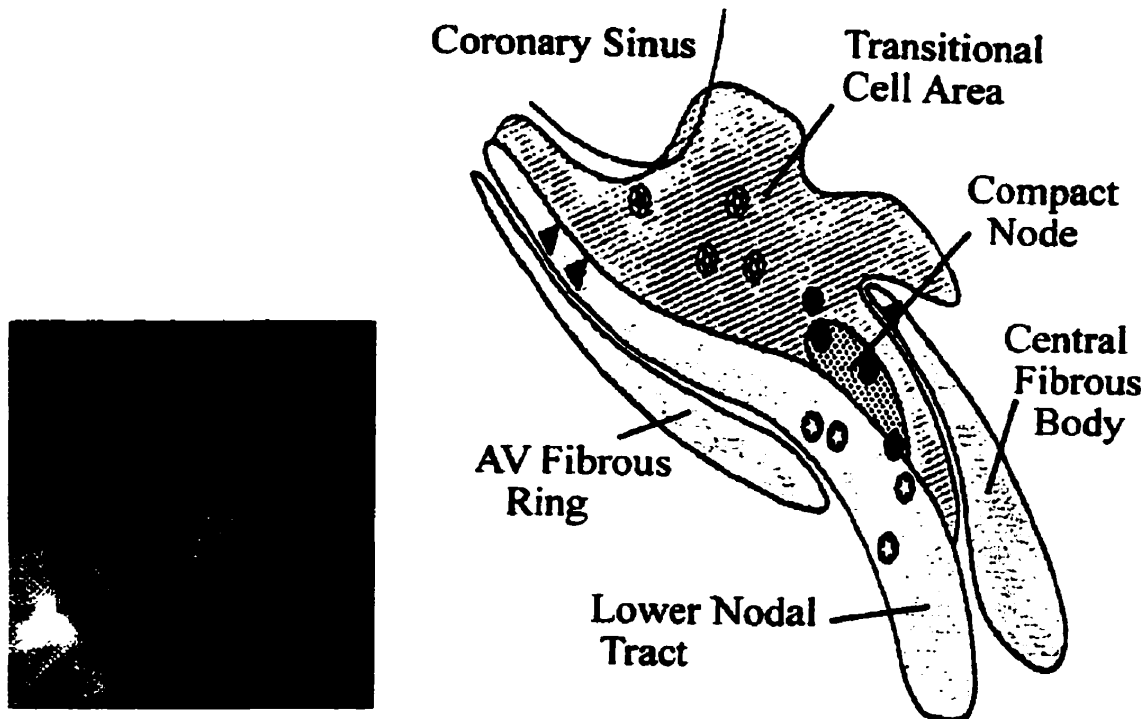


Figure 4.1: The left panel is a high resolution image of the node as imaged. The image width is 2 cm. The right panel is a sketch of the AV node where the landmarks of the node are labelled. The coronary sinus (dark indentation in the top left region of the left panel) and AV fibrous ring (area immediately to the right of the bright area at the bottom left of the left panel) are identifiable in the high resolution image. The sketch was modified from [4]

Panels showing the progression of a impulse triggered in the right atrium are shown in Figure 4.2C. The images presented are shown in reverse video (low fluorescence is shown as brighter pixels.) Images were collected every 10 ms (7x7 pixels binned.) Spontaneous impulses originating from the sinoatrial node approached the nodal region as a broad wavefront oriented parallel to the AV ring. The wave front became narrower and curved posteriorly towards a region below the coronary sinus. The wave front then paused before the central region of the node. The final part of nodal activation was characterized by a rapid and synchronous activation of an

anterior strip of cells along the AV ring.

Figure 4.3 shows a spontaneous escape beat from the AV node. Impulses progress in a reverse direction from that shown in Figure 4.2. Here the impulse originates in a more posterior portion of the node instead of the anterior strip of cells observed in the previous figure. A delay analogous to that seen in Figure 4.2 exists between activation of the central node (Panels 2-5) and the region above the coronary sinus (Panels 6-8).

4.4 Discussion

The data shows that the delay is concentrated in a narrow region of the AV node. This favours the inexcitable gap hypothesis of conduction; here the excitation has to pass over an electrically dead region in the AV node, which introduces delay. An alternate hypothesis, that delay is spread evenly over the whole node, is not supported by this study.

Figure 4.2 is similar in activation pattern and timing to Figure 6 in Choi and Salama[35]. Based on the data in Figure 6, Choi and Salama concluded that the delay occurs between atrial and AV node tissue. They also concluded that spread of activation within the AV node (the compact node) occurs over 10 ms. These conclusions are confirmed by our recordings. The records of Efimov *et al.* (Reference [68], Figures 5 and 6) display what appears to be a different activation pattern. The activation passes from the posterior side of the node, and does not display a distinct delay. This apparent difference may be partially artifactual as the scale, location, and format of the record are dissimilar. The difference may also be due to differences in experimental protocol. Both groups used contraction blockers (diacetyl monoxime (DAM) or butanedione monoxime (BDM)) at low concentrations. However Choi and Salama washed the contraction blocker out of the preparation after 10-12 minutes, while Efimov *et al.* maintained constant concentrations of contraction blocker in the bath. Prolonged (>45 minutes [35]) exposure to contraction blockers is known to cause changes in action potential shape and duration. We used DAM at constant

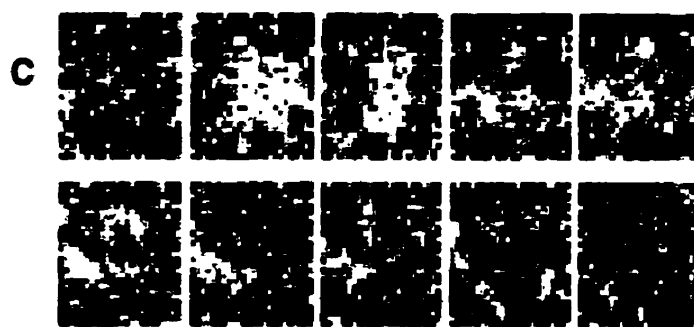
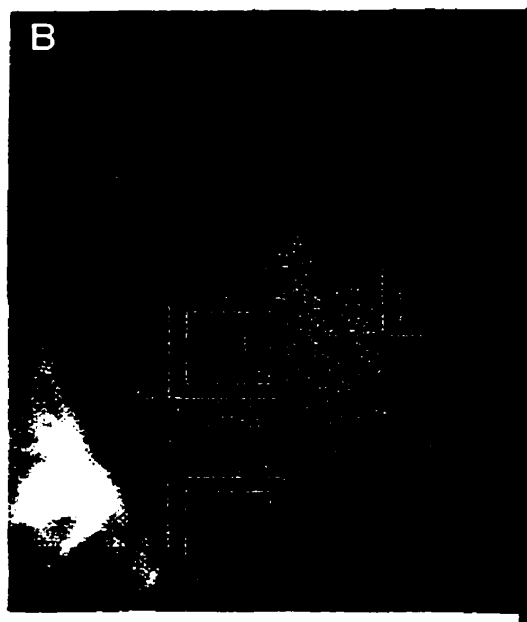
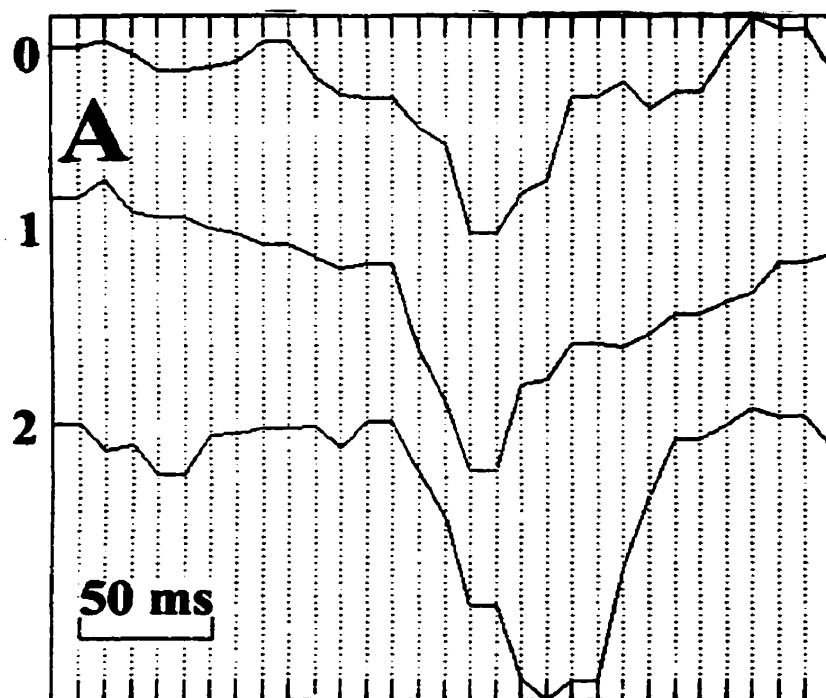


Figure 4.2: Potential wave mapped in the AV node. Boxes sum total fluorescence as shown in (B). A sequence of activation maps are shown in (C). See text.

concentration for the duration of the experiments. The data presented in this Chapter was collected within 30 minutes of loading with contraction blocker. Efimov *et al.* performed experiments on tissue for one to three hours[68].

Interpretation of optical records is complicated by overlapping action potentials within one recorded optical signal. This effect is pronounced in optical records of the AV node because of its complex three dimensional structure. Both Efimov *et al.* and Choi *et al.* recorded distinct spikes from cells at different depths. This allowed construction of activation maps in the x, y and z axes. The CCD system used in our study does not have sufficient temporal resolution to resolve spikes from different layers in this fashion. This limitation could be addressed in future studies by using a small photodiode array in conjunction with the CCD.

The CCD based system successfully measured conduction through the AV node in several preparations. These experiments were not pursued due to time constraints. Optical mapping experiments of the AV node are presently underway in our laboratory, with the goal of resolving the presence of different conduction pathways at different pacing rates.

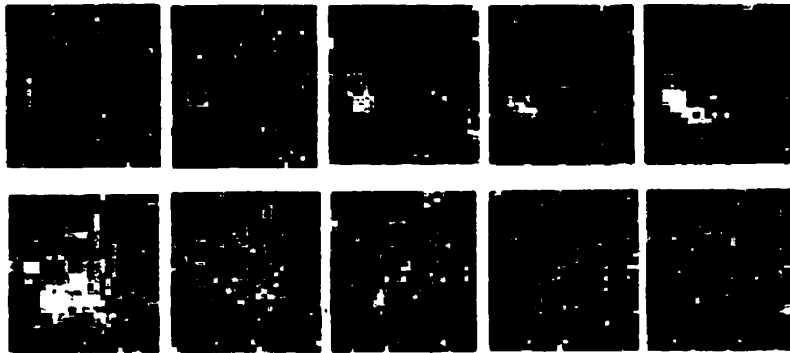


Figure 4.3: Potential waves mapped in AV node. Spontaneous activity indicates an escape beat. The impulse travels in a reverse direction.

Chapter 5

Bursting Behaviour in Cardiac Monolayer Preparations

5.1 Introduction

Bursting behaviour, where cells rapidly fire followed by periods of silence, is observed in single neurons[74, 233] and networks of cells such as pancreatic β -cells[32, 53, 252], cortical slices[253] and cultured monolayers of neurons[198]. Similar types of behaviour are seen in disease states such as paroxysmal (reoccurring) reentrant tachycardias[224] and epilepsy[63].

Since early studies demonstrated that bursting rhythms could originate from single cells[74], theoretical analyses of bursting have focused on cellular ionic mechanisms[29, 41, 274, 251], or small network models[38, 250]. The current work demonstrates that bursting also occurs in dispersed monolayer cultures of embryonic heart cells.

5.2 Methods

This section summarizes methods used in experiments presented in subsequent chapters. Apparatus and theory for optical mapping experiments are detailed in Chapter 3.

5.2.1 Monolayer Cell Culture

Cells were isolated using techniques described previously[40, 55, 57, 157, 114]. White Leghorn chick embryos were incubated for seven days at 37°C and at a relative humidity of 85%. They were decapitated and their hearts removed. Ventricles were isolated, diced into small chunks, and dissociated into single cells in DNase and trypsin containing dissociation medium[55]. The dissociation medium contained 5.25×10^{-5} g/ml crystalline lyophilized trypsin (Worthington Biochemical, 245 U/mg) and 5×10^{-6} g/ml deoxyribonuclease I (Worthington Biochemical, 91000 U/mg) in a Ca^{++} and Mg^{++} free, phosphate buffered, balanced salt solution. A pH of 7.3 was obtained by adding HCl or NaOH. The solution had the the following concentrations: NaCl 116.0 mM, KCl 51.4 mM, NaH_2PO_4 0.44mM, NaHPO_4 0.95 mM, and dextrose 5.6 mM. Enzyme inactivating medium was added to stop cell digestion. The enzyme inactivating medium was similar to maintenance medium (below) but with horse serum 10% instead of fetal calf serum, and KCl at 4 mM. The resulting cell suspension was filtered through a filter with 12 μm diameter pore size to remove large cell clumps. The single cell suspension was centrifuged for 15 minutes at 170 g. The cells were resuspended in maintenance medium. The maintenance medium (called 818a) contained 20% medium 199 (Grand Island Biological (GIBCO)), and 4% fetal bovine serum (Kansas City Biological) in a bicarbonate buffered balanced salt solution. The 818a media had the following concentrations: NaCl 116.0 mM, KCl 1.3 M, CaCl_2 1.8 mM, MgSO_4 0.8 mM, NaH_2PO_4 0.9mM, NaHCO_3 20.0 mM, and dextrose 5.5 mM. Gentamicin sulfate (Schering, Garamycin, 10 mg/ml) was added to a final concentration of 5×10^{-5} g/ml.

Cells were plated at just under confluent densities of $7.0\text{-}14.0 \times 10^3$ cells/cm² within 12mm diameter glass retaining rings on lysine coated plastic cell culture dishes. Cells were kept in maintenance medium 818a at 5% CO₂, 15% O₂, ballance N₂, at 36°C for one to two days before experiments.

All solutions were filtered through a sterile 0.22 μm pore size filter prior to use to remove impurities.

5.2.2 Electrophysiology

Electrical activity was recorded using borosilicate microelectrodes filled with 3M KCL. The microelectrode resistance was typically between 30 and 60 M Ω . Transmembrane potential was recorded using an electrophysiology amplifier (Axoclamp, Axon Corporation). The bathing medium was kept at virtual ground by coupling to the amplifier through an agar salt bridge and chlorided silver wire. All data was digitized by a Microstar 3200e A-D board for storage and analysis. Data storage and viewing software was custom made to allow simultaneous recording from photodiode and electrode sources.

5.2.3 Optical Mapping

Optical mapping experiments were conducted using the apparatus described in Chapter 3.

Monolayers were loaded with calcium sensitive dye Fluo-3 (5 μ M) (Molecular Probes, Eugene, OR) or with Di-4-ANEPPS (20 μ M)(Molecular Probes, Eugene OR) for 20 minutes. The Di-4-ANEPPS was prepared as a stock solution in dimethyl sulfoxide (DMSO) and pluronic acid (1:1 ratio). After staining the preparation was rinsed with fresh Tyrode to remove excess dye. The Tyrode solution contained NaCl 124.0 mM, NaHCO₃ 15.0 mM, KCl 1.3 mM, CaCl₂ 2.2 mM, MgCl₂ 1.0 mM, NaH₂PO₄ 1.0 mM, glucose 5.5 mM, and pH was adjusted to 7.3 with 2M NaOH. The monolayers were then transferred to the imaging setup. All experiments were conducted at 36°C.

5.3 Preliminary Experiments

Mapping activation by imaging fluorescent activity from living tissue is technically challenging. Commercially available imaging systems are expensive and require significant technical ability to operate. In addition, commercially available solutions are not optimized for different experimental preparations. Researchers often resort to using custom-built apparatus. Differences in dye choice, image field size, preparation

thickness, image resolution and recording duration can make techniques appropriate for one preparation not optimal in another. In addition, design and construction of imaging solutions requires familiarity with optics, electronics, and computer programming. Due to these constraints, there are relatively few laboratories that perform high speed optical imaging.

Several pilot studies using voltage sensitive dyes and photodiodes were carried out using the photodiode array described in Chapter 3. These experiments are outlined below. Although the photodiodes produced high quality signals, technical difficulties associated with building a large array prompted us to investigate other options. Several researchers were approached for advice. I visited the laboratories of Dr. Grinvald, Dr. Windisch, Dr. Jalife, and Dr. Publicover. Ratslaff and Grinvald's macroscope design was used as a template for the macroscope built in our laboratory. Dr. Windisch's laboratory provided technical help on monolayer staining and photodiode amplifier construction. Complete pilot studies using the monolayer preparation were performed at Dr. Jalife's laboratory and Dr. Publicover's laboratory. Voltage sensitive dye measurements using the setup at Dr. Jalife's laboratory did not yield measurable signals. The lack of signal was not surprising: Dr. Jalife's system was optimized for measuring signals from preparations several millimeters thick. Voltage sensitive dye experiments at Dr. Publicover's laboratory also failed to produce results. Dr. Publicover suggested using the calcium sensitive dye Fluo-3. The success of these measurements (described below) prompted us to change our experimental focus from photodiode measurement of voltage sensitive dyes to CCD based measurements of calcium sensitive dye. Data from calcium imaging experiments in our laboratory are presented in Section 5.4.1.

5.3.1 Potential Mapping

Monolayers stained with Di-4-ANEPPS were monitored using photodiodes. Monolayers used for Di-4-ANEPPS studies were plated at high densities to maximize signal. The following photodiode records were obtained using a $10\times$ lens, with a NA of 0.15. Signal levels from the Di-4-ANEPPS monolayers were too low to record

using microscopic objectives less powerful than 10 \times .

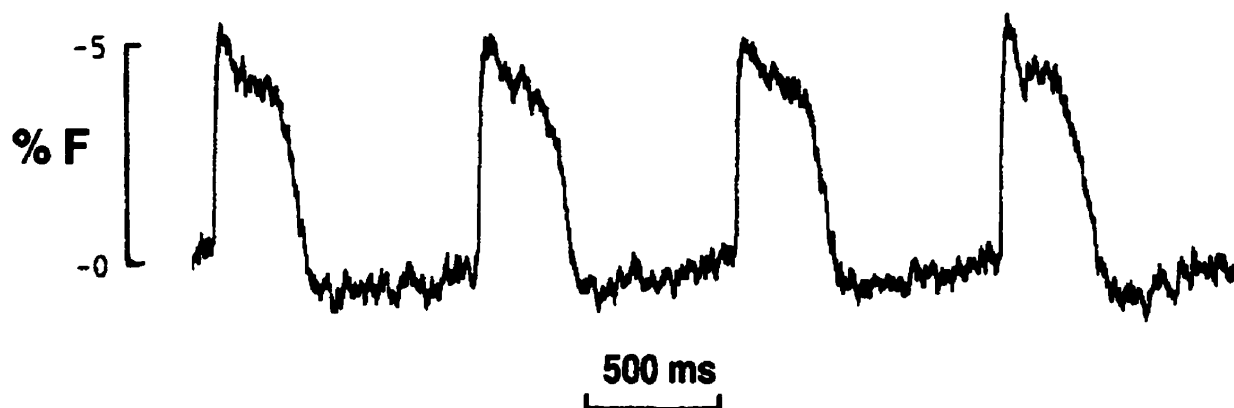


Figure 5.1: Photodiode recording from monolayer preparation. See text.

Figure 5.1 shows the output of a single photodiode recording spontaneous activity from a monolayer preparation. As discussed before, the signal is distorted due to the low frequency response of the circuit. Signal quality still allows clear estimation of key action potential characteristics. An estimate of action potential duration (200 ms) and the presence of phase 4 (the slow depolarization to threshold) can be resolved using this technique. Upstroke velocity should not be estimated from the raw signal however, for three reasons. Voltage signals do not give an absolute measure of voltage, so dV/dt would have to be made using estimates of V_{min} and V_{max} . The circuit used to obtain the signal has a time constant of 10 ms which should be accounted for in a measurement. Finally, the photodiode is obtaining a measure of potentials from multiple cells. At 10 \times magnification, the MRD500 photodiode detects light from a 0.3 mm diameter region of the monolayer. If the cells within this region fired simultaneously, the resulting signal would give an average of the rise times of the individual cells. However, if we assume the cells fire in succession (a wave of excitation travels across the monolayer) then the rise time from individual cells is distorted. A estimate of this distortion (called spatial blurring) as a function of spatial resolution was carried out in guinea pig hearts by Girouard *et al.*[99]. Rise time from a single cell (RT_{cell}) can be estimated from the optical signal (RT_{op}) as

follows[100]:

$$RT_{cell} = RT_{op} - r/\theta. \quad (5.1)$$

where θ is conduction velocity and r is spatial resolution.

The rise time of the optical signal is roughly 30 ms. If we account for the time constant of the measuring circuit, the rise time of the tissue culture is 24 ms¹. Using Equation 5.1, with a conduction velocity of 20 mm/s (see below for estimates of conduction velocity) the rise time can be estimated to be 9 ms. The rise time from Figure 5.1 can now be given as 1 ms. If we assume that the action potential covers 80 mV over this time, Dv/Dt is approximately 8.9 mV/ms.

Figure 5.2 shows a simultaneous recording from a monolayer preparation impaled with a microelectrode. The signal obtained shows that the optical signal corresponds closely to the signal obtained from the electrode.

Figure 5.3 shows optical signals from 2 photodiodes simultaneously. The photodiodes were positioned to maximize the delay between them (as a travelling wave could potentially pass under both diodes simultaneously, giving a measured wave speed of zero). The image was collected using a 10x lens. The photodiodes are measuring points approximately 0.5 mm apart and the signals from the photodiodes are 25 ms apart in time. If we assume that the wave of activity passed parallel to the plane of the photodiodes, we can estimate that the conduction velocity is 20 mm/s.

5.3.2 Calcium Mapping

Initial wide area mapping experiments were carried out with the help of Dr. Nelson Publicover in the University of Nevada School of Medicine. Young, sparse cultures were stained with calcium sensitive dye and mapped at low magnification using a

¹The response of a simple RC circuit is $V(t) = RC^{-1} \int_{-\infty}^t V_i(\tau) e^{-(t-\tau)/RC} d\tau$ [123]. An RC circuit driven by a ramp signal $S_{ramp}(t)$ was integrated with a computer program that simulated a compensating circuit. The output of the simulated compensatory reached $S_{ramp}(30ms)$ (the value the ramp signal had at 30 ms) at 24 ms.

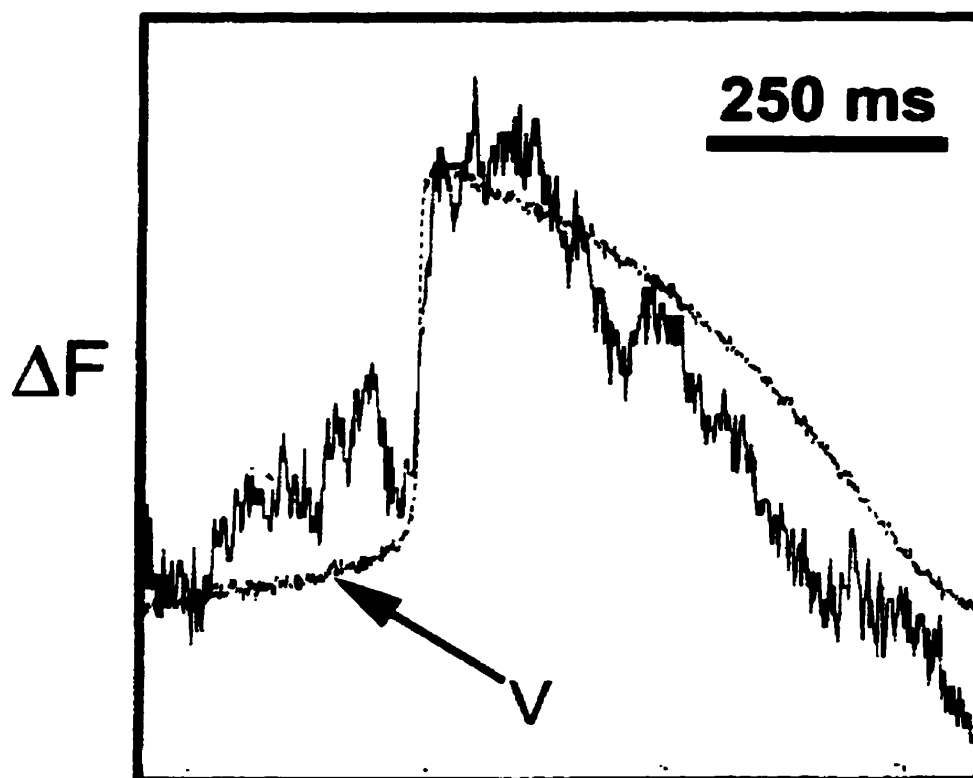


Figure 5.2: Output from the photodiode and an electrode. The electrode impaled a high density region (an aggregate) of the monolayer, and the photodiode recorded from a point directly adjacent to the impalement site. The tracing from the electrode spans 80 mV.

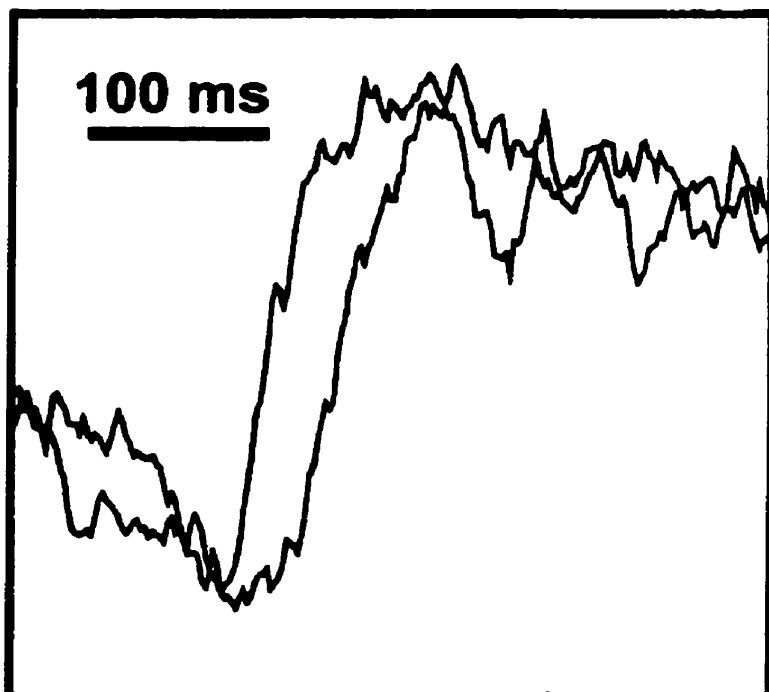


Figure 5.3: Output from two photodiodes monitoring a 3 day old monolayer preparation.

very sensitive commercially available optical mapping system². The results from one experiment are shown in Figure 5.4. The optical system was not able to map propagation but did capture periodic increases in activity that spanned the monolayer preparation. The results suggested that weakly coupled cardiac cells are able to periodically synchronize over an area many orders of magnitude larger than the range of local cell interaction. The monolayer displayed *bursting* behaviour (see Chapter 1.4).

The bursting behaviour was interesting on several levels. Bursting is usually modeled by the local dynamics of single cells[29, 41, 274] or small networks of cells[38, 250], not the group activity of many thousands of cells. Although there are models of bursting in clusters of cells[251, 256], these models rely the intrinsic capacity of each unit to burst under appropriate low noise or parametric conditions(Chapter 1.4.5). Since cardiac cells do not burst in isolation³ or have ionic currents or the cellular interconnections normally associated with bursting behaviour, the monolayer may be a novel model for bursting in large groups of coupled non bursting units.

The low spatial resolution of the data in Figure 5.4 provided little insight into the mechanisms of the synchronized bursting activity. The optical system described in Chapter 3 was designed to elucidate bursting mechanisms in the monolayer preparation.

5.4 Optical Mapping of Bursting Behaviour

Optical mapping experiments demonstrate that bursting in the monolayer system is driven by spatial patterns of activation in the form of repeated initiation and termination of rotors (Section 5.4.1). Rotors are observed in such diverse systems as chemical reactions[147], slime mold cultures[90], slices of brain tissue[253] and the developing retina[106]. Rotors are common to two dimensional excitable media:

²The system used a $1\times$ Zeiss microscope objective on a inverted microscope with a Hamamatsu intensified high speed imaging system. See [226] for system details.

³This may not always be true. Michael Guevara (personal communication) has on rare occasions observed bursting dynamics in aggregates. Bursting in aggregates is characterized by a short period of rapid beating within the normal rhythm.

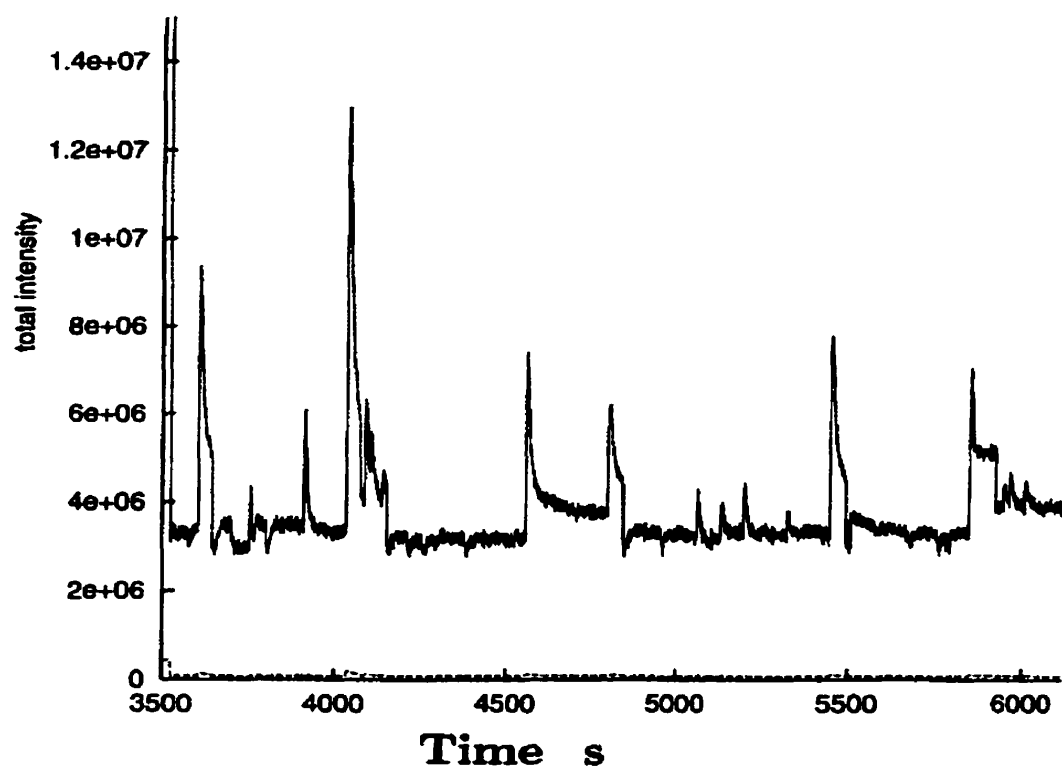


Figure 5.4: Optical mapping data. The plot shows intensity of calcium fluorescence vs time from all the pixels (512x720) of intensified imager.

any sufficiently large continuous system of coupled excitable cells is thought to be able to generate rotors of excitation under the right conditions[290].

Rotors do not form spontaneously in homogeneous systems[287], but rather are induced by special initial conditions such as cross field stimulation[50], or physically induced wave breaks[194, 221]. Rotors can also form when a well timed pulse is initiated in the wake of a passing wave[217, 288]. More recently, attention was focussed on the role of heterogeneity[221] and geometrical boundaries[1, 107] in the creation of rotors. Rotor initiation in the monolayer appears qualitatively different: unidirectional propagation evolves directly to a rotor without the interaction of other waves or obstacles.

The observed dynamics are simulated with modified two dimensional excitable media models. Excitable cells are modeled by mathematical constructs that have trajectories that undergo an excursion from a resting state if stimulated, and become refractory to stimulation for a finite time after being activated. Excitable cells are coupled to their neighbours allowing excited cells to trigger unrefractory cells to activate. Existing excitable media models support rotors but do not display bursting behaviour observed in the monolayer preparation. The membrane potential of embryonic chick myocytes in culture displays intrinsic spontaneous oscillation[157, 115]. In addition, in many cardiac preparations[206, 19], including cultured cardiac myocytes[164] there is a decrease in excitability, or fatigue[19], due to rapid stimulation. Excitable media models are modified by adding spontaneous activity and fatigue seen in the monolayer.

Excitable media are modeled using cellular automata or coupled differential equation models. Cellular automata use discrete time and space and simple update rules to simulate an excitable medium. The simplicity of cellular automata make them popular as models for physical and biological systems[34, 108, 109, 194, 275, 277, 298], but they fail to adequately model effects of wave front geometry (the curvature effect) or recent activation history (dispersion) on wave speed. Coupled systems of partial differential equations have also been used extensively to model excitable media[28, 46, 65, 80, 83, 84, 142, 188, 234, 272, 289]. Coupled differential equation

models are generally better at modeling dispersion and curvature effects, but are less easily manipulated and are more computationally expensive[97].

Bursting is modeled using two cellular automata models and a coupled partial differential equation model. The purpose of presenting different model types to simulate the same behaviour is twofold. First, the minimal set of assumptions used in the modified cellular automaton models generates behaviour that is easily understood. The differential equation model is then used to simulate the behaviour in a more realistic setting. Second, different models with similar behaviours suggest the mechanism of initiation and termination of spirals are not artifacts of the modeling environment. The minimal set of assumptions necessary to generate bursting in these simple models suggests that spatially driven bursting may be seen in other physical or biological systems.

Results from optical mapping of cultured cardiac monolayers are reported in Section 5.4.1. Section 5.4.2 reports results from computer simulations of bursting in spatially extended systems. The results are discussed in Section 5.5.

5.4.1 Bursting Dynamics: Experimental Results

Rotors in Cardiac Monolayer Preparations.

Cardiac monolayers support rotors. Clear rotors are frequently observed in monolayers after 24 to 48 hours in culture. Figure 5.5 shows a representative example. Frames are taken 50 ms apart. The double armed spiral persisted for the duration of the experiment (20 minutes). The spiral has a period that varies between 600 and 700 ms. Figure 5.6 shows isochronal maps from the same preparation. Isochrons (see Methods, Chapter 2) represent location of the activation front at 50 ms intervals, where time is represented by progressively darker shades of gray. Figure 5.7 shows a different stable spiral configuration. Here, the spiral wave is single armed. The spiral has a period of approximately 700 ms. Figure 5.8 shows the evolution of the same spiral over approximately 16 minutes. Although the geometry and period of the spiral are similar in both sets of frames, the spiral core has moved approximately 3 mm (from center to left) during this time. Although the change in this preparation

is pronounced, the core in several preparations demonstrated some motion (called *meander drift*) over the time course of the experiment. This observation indicates that spirals are not anchored to a anatomical obstacle (although anchoring cannot be ruled out in cases where no meander is observed).

a3.5pe
110

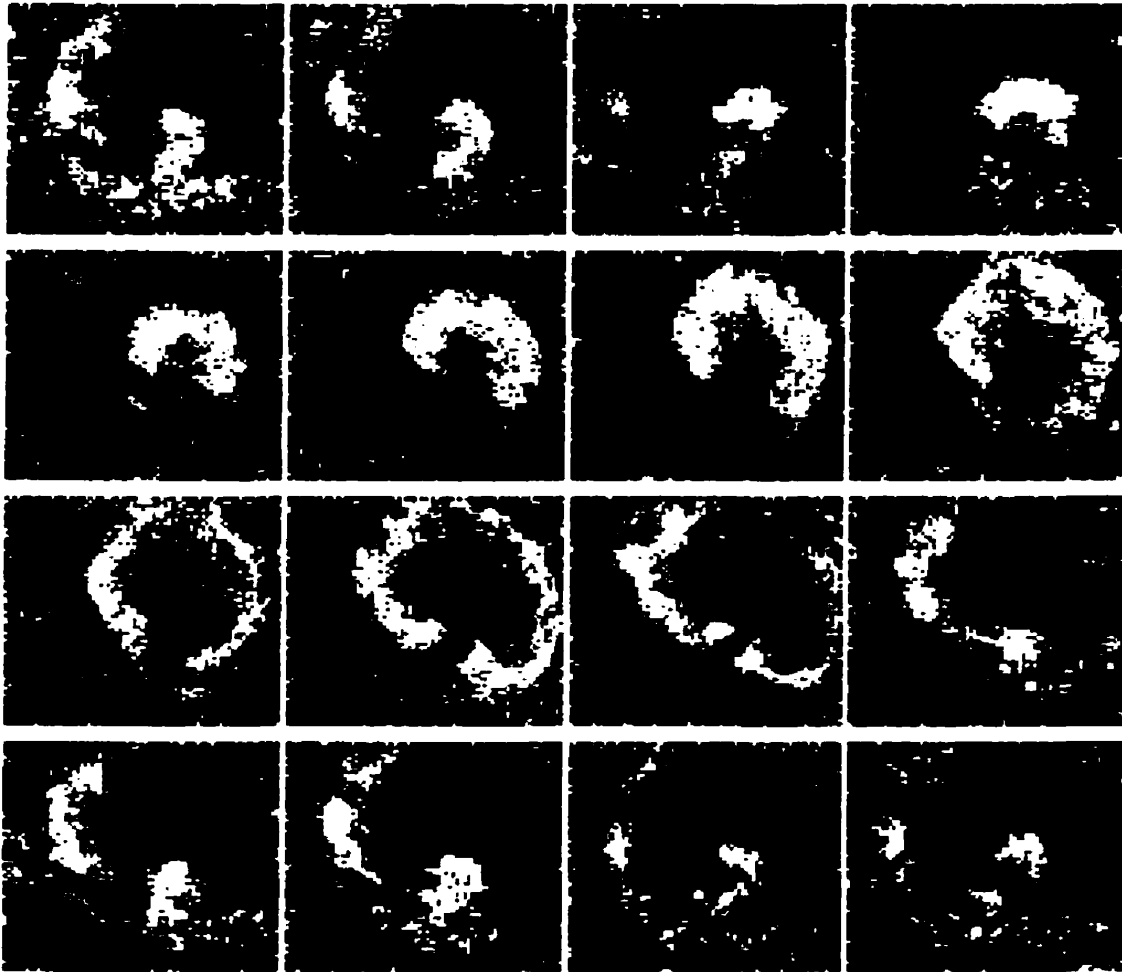


Figure 5.5: Persistent double armed rotor. Successive frames are ordered left to right and top down. Bright shades represent high calcium fluorescence. The top of each panel is 13 mm.

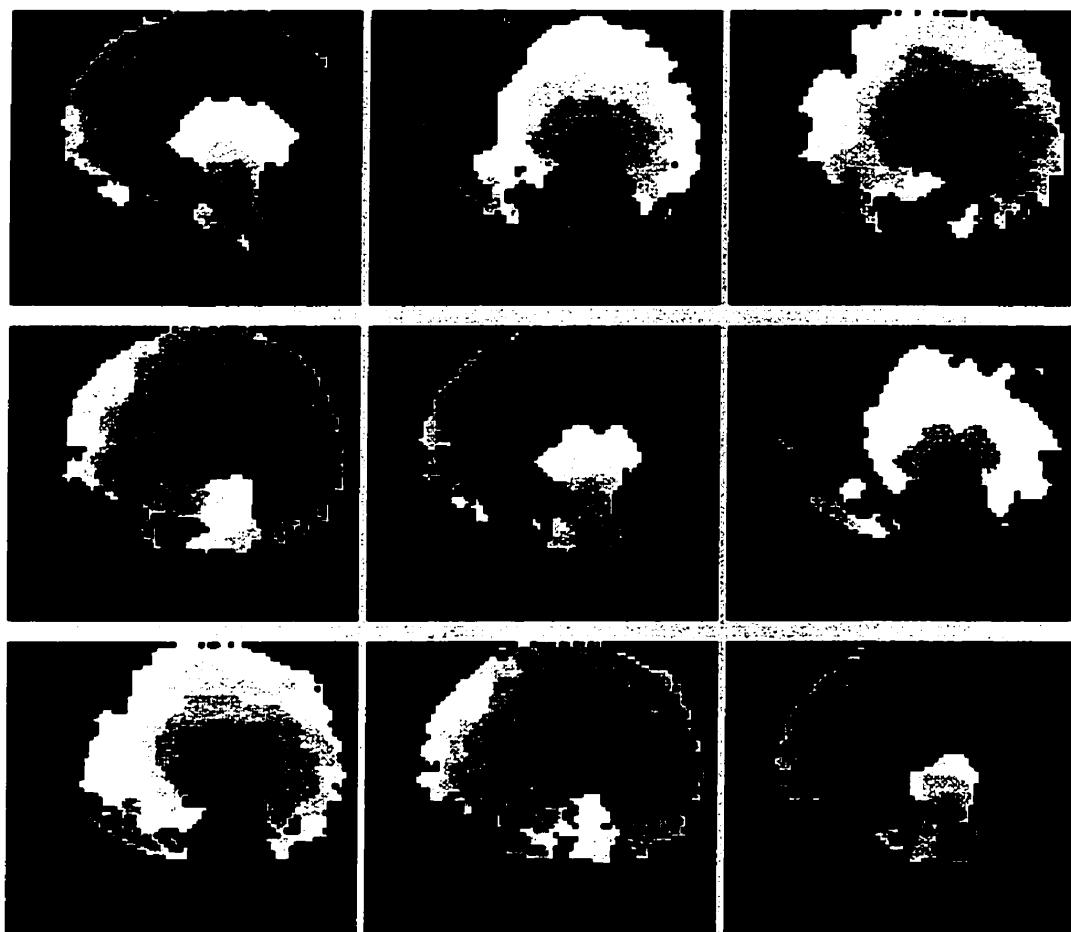


Figure 5.6: Isochronal map of data in Figure 5.5. Isochrons are drawn where the activation front is detected every 50 milliseconds. Isochrons lie on the boundaries of shaded regions, where brightest shades of grey represent the most recent activity.

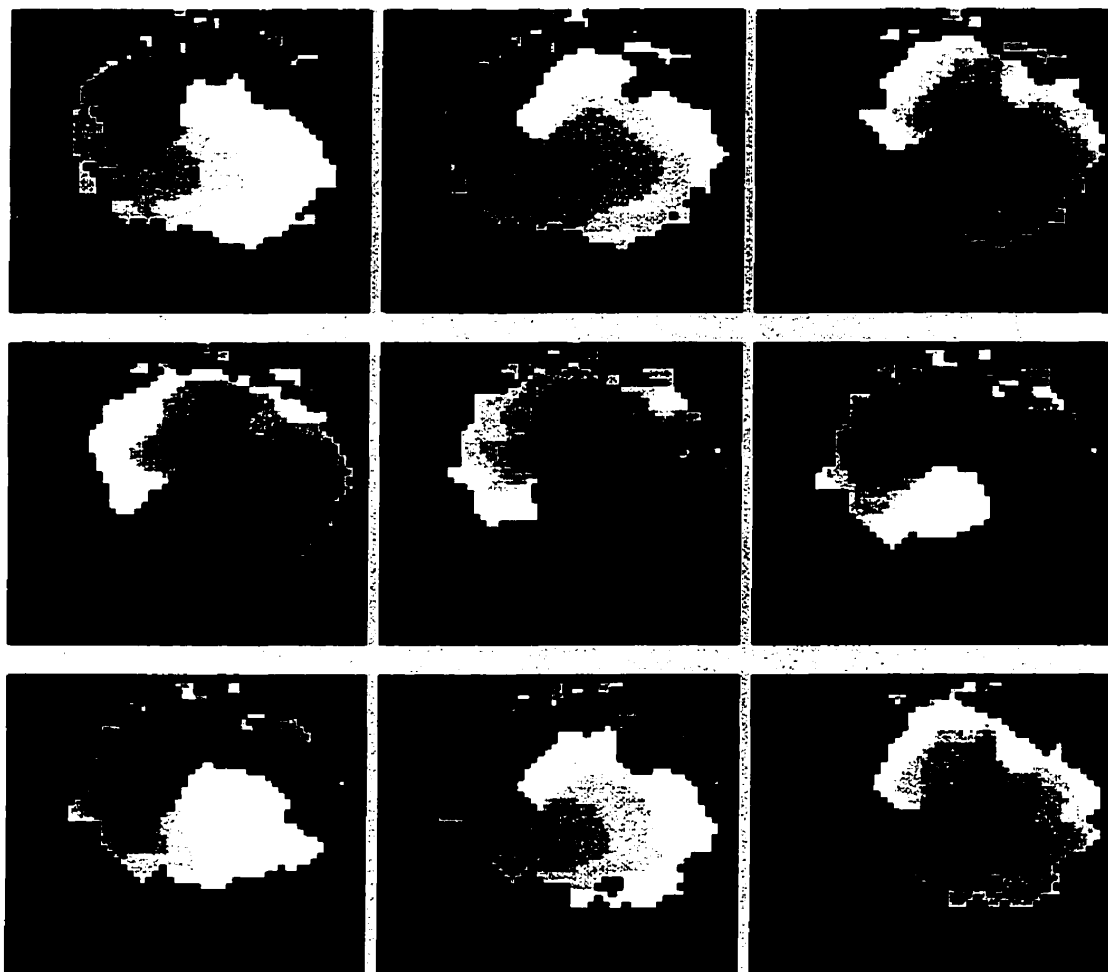
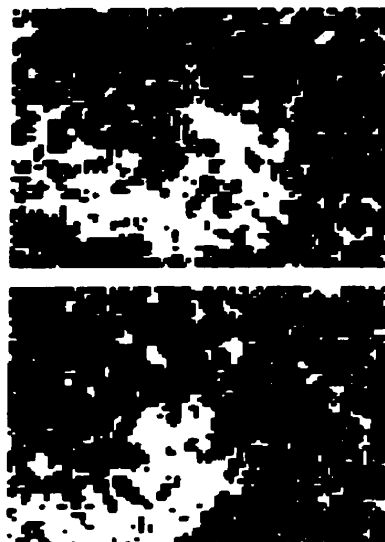


Figure 5.7: Isochronal map of a single armed spiral. Isochrons are drawn where the activation front is detected every 50 milliseconds. Isochrons lie on the boundaries of shaded regions, where brightest shades of grey represent the most recent activity.

A



B

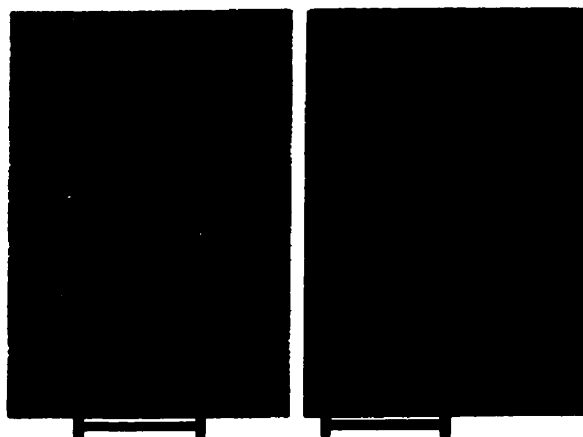


Figure 5.8: A. Frames of raw data of single armed spiral taken 16 minutes apart. The spiral tip is displaced leftward during this time. B. Framestack view of the single armed spiral 50 frames after the two snapshots in A. The core of the spiral is indicated by a bar at the bottom of each stacked frame view.

Spontaneously Bursting Preparations

Bursting dynamics were observed in 14/17 different preparations. Figure 5.9A shows fluorescent intensity over a duration of 6 minutes recorded from an area of 1 mm^2 in a single preparation. Six bursts of fluorescence were recorded. During each burst, there were distinct fluorescent peaks. The period between the peaks increased from 450 ms to 700 ms during a single burst. Figure 5.9B shows the period recorded over six consecutive bursts plotted against time utilizing the data in Figure 5.9A. The time between bursts remained relatively constant ($40 \pm 15 \text{ s}$). Figure 5.9C summarizes data from 30 bursts recorded in 6 different preparations. The mean period for the first 5 peaks of each burst is given at time 0. Each dashed line represents a single burst, where the abscissa and ordinate of the right end point give the burst duration and mean period of the last 5 peaks, respectively. In six preparations the mean period within a single burst increases by 20–80%.

In order to determine the spatio-temporal patterns of activity underlying the burst, fluorescent activity was recorded from a 1 cm^2 area. These recordings demonstrated the presence of a spontaneously initiated rotor associated with the burst (Figure 5.10). The top trace in Figure 5.10 shows a 25 s burst of increased Ca^{++} recorded from a 1 mm^2 region. A peak in activity is created every time the activation front passes through the 1 mm^2 recording region. In order to study the activation sequences leading to the initiation and the termination of the burst, contour plots of activation times were constructed. A wave of activity was spontaneously initiated (Figure 5.10A) but did not propagate uniformly. The wave was blocked at a point near the site of initiation leading to unidirectional propagation to the left. After the wave propagated about 2 mm (Figure 5.10B) it doubled back, invading the previously blocked regions leading to two mirror-image rotors, with a common pathway in between them. For the initial 14 rotations, the top rotor excites the common pathway first (Figure 5.10C). Then the top and bottom rotors simultaneously excited the common pathway (Figure 5.10D). After 44 rotations, the top rotor was blocked, after which there remained only a single rotor (Figure 5.10E). This wave

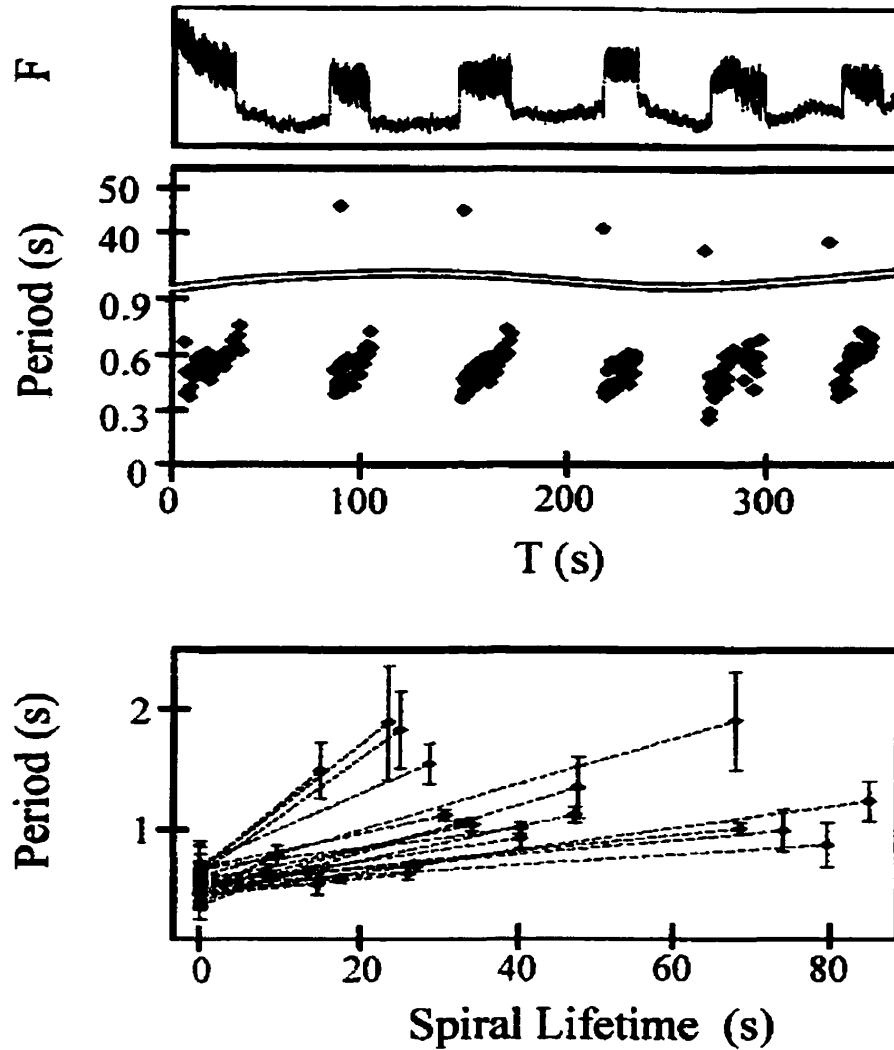


Figure 5.9: A) Calcium fluorescence for 5 consecutive bursts from a 1 mm^2 area. B) The interbeat period measured from calcium fluorescence during rotor bursting as a function of time. During each burst duration increases from about 0.4 s to 0.8 s. The interburst duration ranges from 36 s to 44 s. C) Average period of rotor rotation for 24 representative rotor bursts taken from 6 different preparations. The average period, calculated for the first and last 5 rotations of each rotor during a burst, is plotted as a function of burst duration. The error bars show the standard deviation of the period over the 5 averaged periods.

was eventually blocked leading to termination of the burst (Figure 5.10F).

The sequence shown in Figure 5.10 was observed in 72/120 bursts. In 24/120 cases there was a similar initiation to a pair of mirror-image rotors, but there was no evolution to a single rotor before termination. In 24/120 rotor bursts, unidirectional propagation evolved directly to a single rotor and then terminated. An example of unidirectional propagation resulting in a single armed rotor is shown in 5.11.

Monolayers do not necessarily display bursting dynamics. Bursting rhythms occur in cultures incubated for relatively short times, while regular periodic beating is observed after about 3 days in culture. The effect of incubation time on dynamics was systematically explored in 3 culture preparations. Fluorescence data was collected at different incubation times from spontaneously beating and extracellularly paced monolayers. The results from representative experiments are shown in Figures 5.12 and 5.13.

The spontaneous rhythms from 6 monolayers plated at identical densities from the same culture with varying incubation times are shown in Figure 5.12. Infrequent bursting is observed after 24h in culture. Bursting frequency and duration increases from 36 to 48 hours. By 54h activity becomes regular, with infrequent short breaks. At 68h the dynamics are periodic. Rotors were clearly observed at every time point except the one measured at 68h. In this case the periodic rhythm was generated by a regularly beating focus. At 54h, the regular beating was generated by a stable rotor.

The effect of periodic stimulation on rhythm is shown in Figure 5.13. The preparations are paced every 800 ms at 2x the minimum stimulation current necessary to illicit a pulse. Waves of excitation are observed travelling from the electrode to entrain the monolayer. After 24 hours incubation time, the monolayer is able to follow every beat for 23 stimuli before skipping 3 beats, at which point it follows the pacing electrode for 14 beats before failing completely. After 42 hours, pacing is able to maintain a 1:1 rhythm for 40 beats prior to skipping one beat. At this point the dynamics follow a 3:2 rhythm for 6 beats, then a 2:1 rhythm for 5 beats, and then go to a regular 3:1 rhythm for the duration of the protocol. After 68 hours

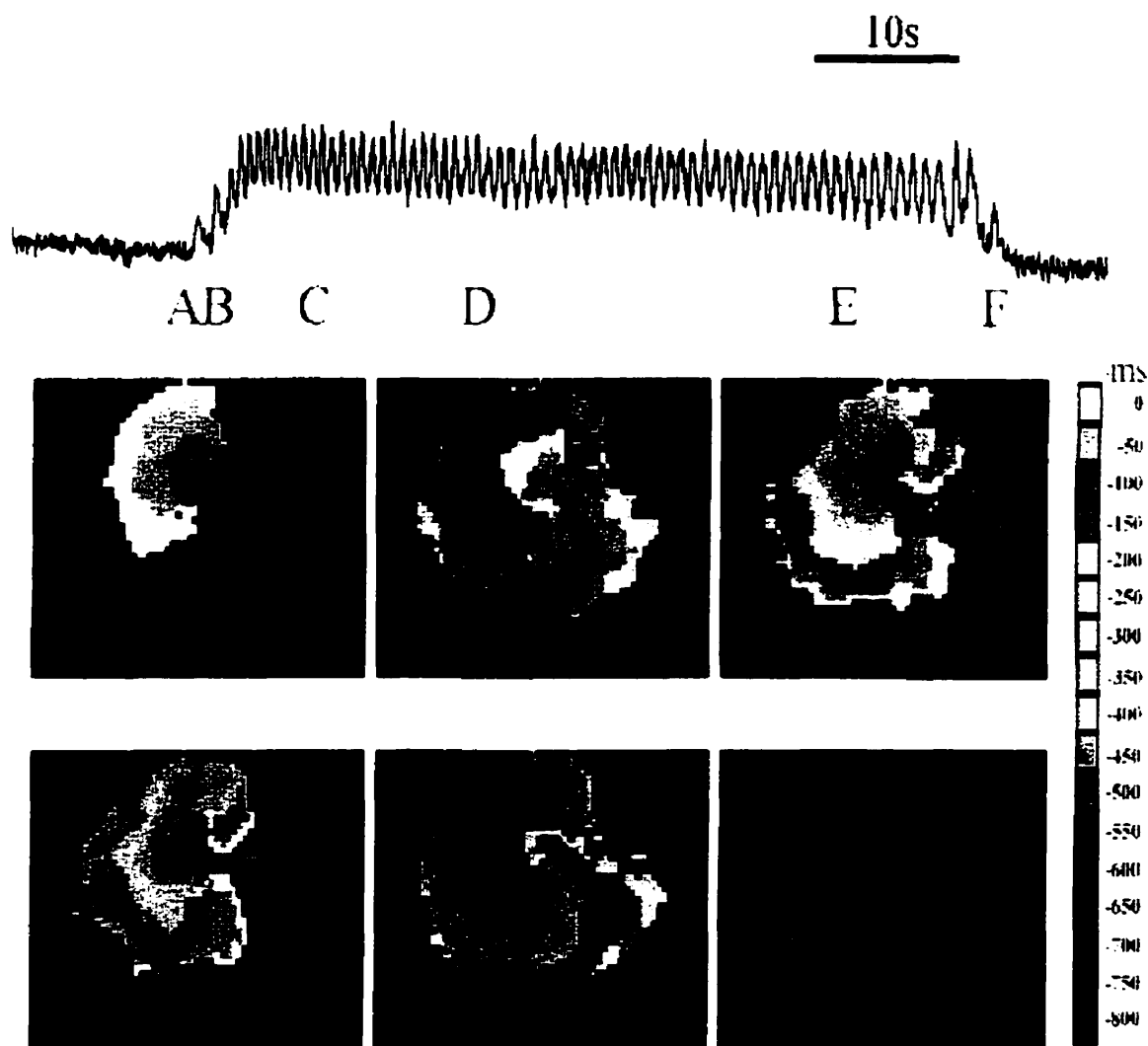


Figure 5.10: Anatomy of a typical burst. The upper trace shows fluorescence intensity during a single burst. The width of each panel is 1 cm. The coloured images show contour plots of activation times at several different times during the burst indicated by the labels. Contour maps are constructed by determining the location of the activation front at 50 ms intervals. The location of the activation front at a given time is plotted in a colour given by the key. This format allows for the representation of a number of consecutive raw data frames onto a single composite image. Activation front detection is determined by a threshold set at half maximum fluorescence. A. Unidirectional block. The wave is initiated at a single site and propagates only to the left. B. Formation of two mirror-image rotor waves. The excitation doubles back, to invade the tissue forming a mirror-image pair or rotors. C and D. Contour plots of the mirror-image pair of rotors. E. Destruction of one of the rotors leaves a single rotor. F. Termination of the remaining rotor.

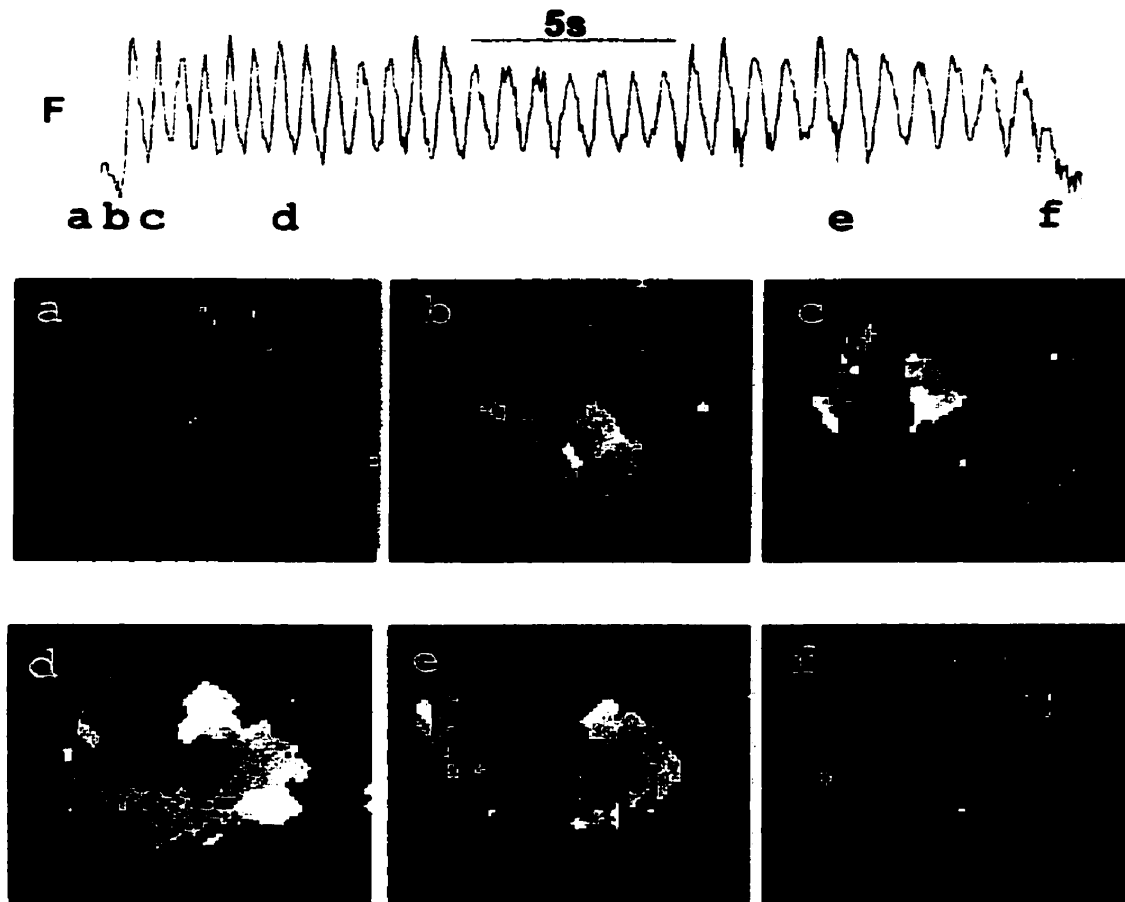


Figure 5.11: Anatomy of an atypical burst. The rotor wave in this case evolves directly to a single armed rotor. See 5.10 for details. a. Unidirectional block. The wave is initiated at a single site and propagates unidirectionally. b. Formation of a single rotor wave. The excitation doubles back, to invade the tissue to form a single rotor. c and d. Contour plots of the evolving rotor e. and f. Termination of the rotor.

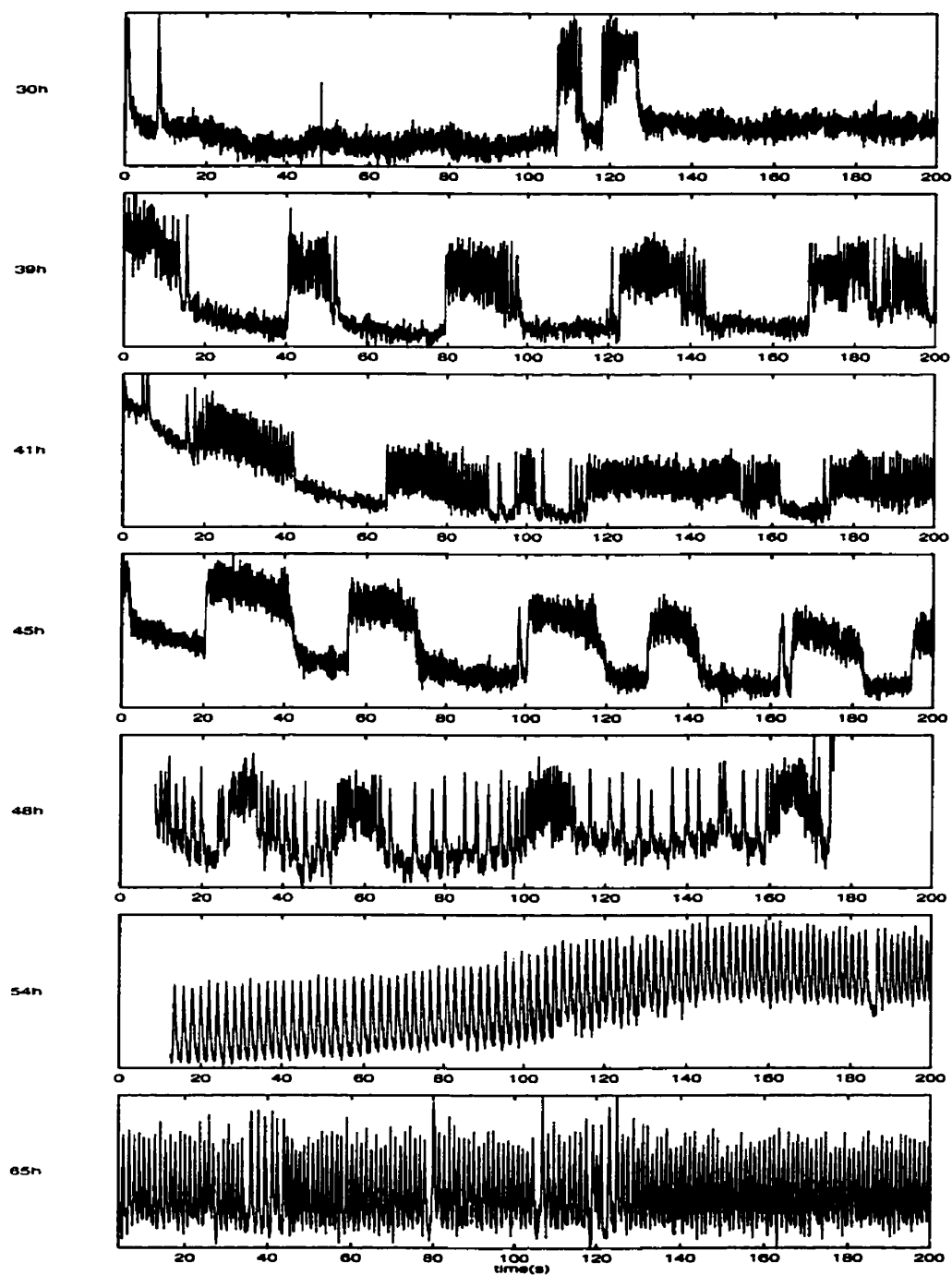


Figure 5.12: Fluorescence intensity from cultures of differing ages under non pacing (spontaneous) conditions. Details in text.

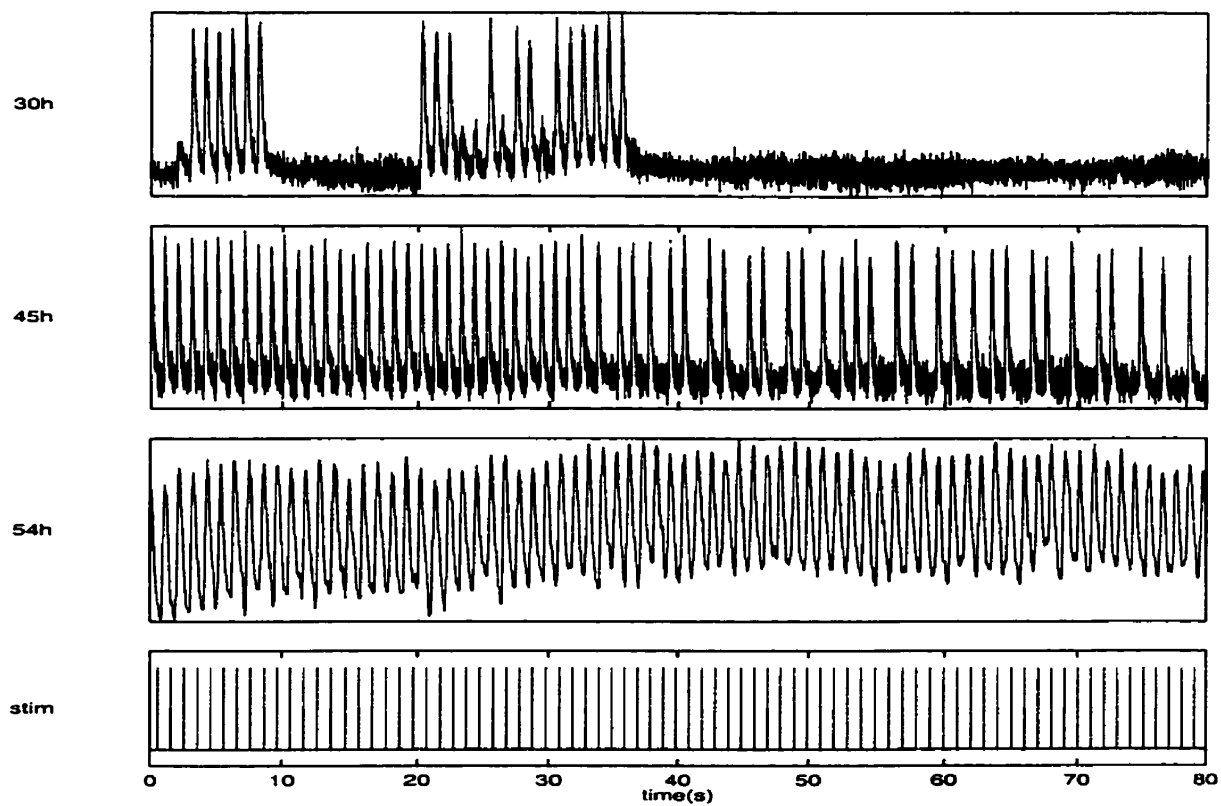


Figure 5.13: Fluorescence intensity from cultures of different ages under pacing conditions. The monolayers in the top three panels were stimulated every 800 ms. The trace in the bottom panel give stimulation times. Details in text.

incubation time, the preparation beat with a 1:1 rhythm for the duration of the protocol.

The dynamics in Figure 5.12 indicates that developmental changes occur as the culture matures. It is possible that individual cells change from aperiodic, to bursting, to periodic dynamics as they mature in culture, and cell-cell interconnectivity does not play a role. The experiment in Figure 5.13 attempts to partially address this issue. The protocol determines the monolayers ability to conduct impulses as a function of time in culture. Increased propagation capacity is consistent with increased cell-cell coupling, and gap junction coupling increases with time in contact[235]. Increased propagation is also consistent with changes in the excitability of individual cells.

Figure 5.14 details calculations of curvature vs wave front velocity for several preparations. The dependence of wave speed on wave curvature is roughly linear for this preparation. Five different preparations were tested, with over 30 points taken from each. The diffusion coefficient averaged $0.07 \text{ cm}^2/\text{s}$ and planar wave speed was estimated to be 20 mm/s .

The above determination of diffusion coefficient and planar wave speed depend on certain continuum conditions being met. These are discussed in Section 5.5.4.

5.4.2 Bursting Dynamics: Modeling

Bursting phenomena are modeled using a cellular automaton and continuous differential equation models. Existing models of excitable media are modified so that they display bursting behaviour as seen in the experimental preparation. Although optical mapping of the monolayer revealed that the bursting is associated with the presence of rotors, there is relatively little information on what individual cells or groups of cells are doing during and between bursts. For example, it is not known if cells are electrically active between bursts, or whether all cells fire during a wave of activity, or even what fraction of cells are spontaneously active prior to initiation of the burst. It is also impossible to rule out the possibility that groups of cells under these experimental conditions endogenously burst, in which case rotors are a

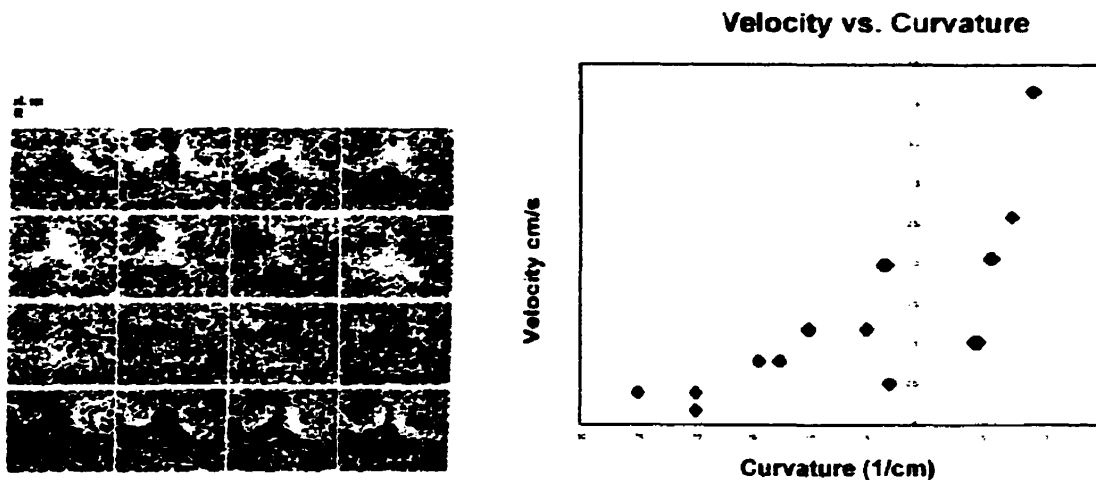


Figure 5.14: Curvature and velocity were measured at several points for six different preparations. Wave fronts from successive frames were fitted with computer drawn circles. The difference in radii from successive frames were used to calculate speed, and the result was plotted against the average radii between successive frames. A least squares method was used to determine the slope and y intercept of the line (Microsoft Excel). The coefficient of determination r^2 is 0.89, the $F(\text{observed})$ value is 48.1, and the $F(\text{critical})$ value is 5.78.

secondary behaviour.

A simple cellular automaton model was developed which demonstrates that the addition of certain assumptions can result in bursting behaviour in groups of spontaneously active, excitable, but nonendogenously bursting cells. An intermediate cellular automata model (see Section 1.3.2), and a continuous differential equation model were developed to incorporate measurements of D (see Figure 5.14) and to confirm that the behaviour is not an artifact of discrete cellular automata. The intermediate cellular automaton model and the continuous differential equation model simulate propagation in continuous excitable media. There are difficulties with treating the bursting monolayer as a continuum. These are discussed in Section 5.5.4. Due to these difficulties and to the complexity of the parameter space of these models, simulation results from the two continuum models are presented primarily as demonstrations of bursting in continuous excitable media models. A detailed investigation of the parameter space for these models is beyond the scope of this work.

We modify two cellular automata models and coupled differential equation model to simulate bursting dynamics. The Greenberg-Hastings (GH) model [108, 81] is a simple cellular automaton model. The Gehrhardt-Shuster-Tyson (GST) [95, 96] model is an intermediate cellular automaton that simulates properties of continuous excitable media. The FitzHugh-Nagumo (FHN) [84] model is a coupled differential equation model that is a phenomenological model of excitable media. The models are modified to account for the physiological properties of spontaneous activity and fatigue.

Spontaneous activity is simulated either by giving each grid point a different intrinsic periodicity, or giving all grid points a probability of firing when excitable. A mechanism for fatigue in the monolayer preparation may involve the influence of Ca^{++} on gap junctional conductance. For rapid firing, we hypothesize Ca^{++} builds up to levels which decrease gap junctional conductance. The decrease in gap junctional conductance occurs over many seconds allowing for gradual buildup of fatigue [64, 206]. Changes in gap junctional conductance affects the diffusion

coefficient D . The diffusion coefficient in cardiac preparations can be given by $D = \frac{S_v \rho}{(C_m(1\mu F/cm^2))}$ [139, 291], where S_v is cell surface to volume ratio, C_m is membrane capacitance, and ρ is resistivity of the interstitial fluid, cytoplasm and gap junctions. This is modeled in the modified FitzHugh-Nagumo equations by decreasing the diffusion coefficient under conditions of rapid cell firing or by lowering the excitability of each grid point. Lowered gap junctional conductance is simulated in the cellular automaton models by decreasing a fatigued grid point's ability to stimulate its neighbours.

Waves are initiated by the chance random activation of a sufficient number of sites in a given neighborhood. Once initiated, a wave can be blocked from propagating in all directions, it can propagate as a broken wave in one direction, or it can propagate symmetrically to generate a target pattern. Waves of high curvature are blocked more easily by refractory sites than waves of low curvature. As high curvature activation fronts advance, they become less curved and less vulnerable to block. The relationship between curvature and stability allow stable rotors to be generated from broken activation fronts created at initiation sites.

Greenberg-Hasting Model

Each site of a two-dimensional grid at time (t) is assigned a state, $u_{ij}(t)$ and a level of fatigue $\phi_{ij}(t)$, where the subscripts refer to the location in the grid. The neighborhood of a given site corresponds to its N nearest neighbors. The state is an integer: 0 is a rest state; states 1, 2, ..., E are excited states; states $E + 1$, $E + 2$, ..., $E + R$ are refractory states; state $(E + R + 1)$ is identified with the rest state 0.

The update rule for the state of a site is as follows: if $1 \leq u_{ij}(t) \leq (E + R)$, then $u_{ij}(t + 1) = u_{ij}(t) + 1$. If $u_{ij}(t) = 0$, then $u_{ij}(t + 1) = 0$, unless one of two conditions hold: (i) the number of sites with an excited state at time (t) in the neighborhood of a site at (ij) is greater than $\theta_{ij}(t) = \theta + \phi_{ij}(t)$, where K_{exci} is a positive number indicating the threshold for excitation in the absence of fatigue and $\phi_{ij}(t)$ is a fatigue term defined below; or (ii) $\xi_{ij}(t) < p$, where $\xi_{ij}(t)$ is a random number uniformly distributed on the interval $[0,1]$, and p is a positive

number representing the probability for spontaneous activation of a site.

The update rule for $\phi_{ij}(t)$ is as follows: if $u_{ij}(t) = 0$ and $u_{ij}(t + 1) = 1$, then $\phi_{ij}(t + 1) = \phi_{ij}(t) + \delta$; otherwise $\phi_{ij}(t + 1) = \gamma\phi_{ij}(t)$ where γ is a positive constant, $0 < \gamma < 1$. Thus, there is an increment of the fatigue term associated with excitation of a site, and exponential decay of the fatigue at other times.

By setting p , ϕ and δ equal to 0 we recover the Greenberg-Hastings model[108, 81] of excitable systems.

To carry out the simulations we need to set E , R , K_{exci} , δ , γ and p and the neighbourhood size. This is a rich array of parameters, and we have not systematically investigated behaviors throughout parameter space. For simplicity, we assume the neighbourhood consists of the eight nearest neighbours of a given site. For this neighbourhood planar wave propagation requires that $K_{exci} \leq 2$, and we set $\theta = 2$. By choosing K_{exci} at the maximum value that allows planar wave propagation, we increase the likelihood for block and the initiation of rotors. We require that broken wave fronts curve to generate rotors as observed in the experiments. With $K_{exci} = 2$, rotors will form if $E \geq 5$ and we select $E = 5$. R is set equal to $E + 1 = 6$ to prevent a wave from exciting sites directly in its refractory wake. Simulations with the above parameters with no fatigue give a rotor with a period of about 36 iterations. If $\phi_{ij} > 1$, then site (ij) will not be excited by a planar wave. For these parameters, a rotor of period N will not persist if $(1 + \delta)\gamma^N > 1$. To obtain long burst we need a slow buildup of fatigue. We arbitrarily set $\delta = .05$ and $\gamma = 0.999$ based on the above equation. The probability of random firing at a site is 7.5×10^{-4} per iteration. The mean burst time and time between bursts increases as p decreases.

The model shows initiation and annihilation of bursting rotors similar to experimental observations. Impulses are initiated by the chance simultaneous firing of several sites in close proximity to each other, so that additional sites in the neighbourhood fire. In the example shown (Figure 5.15) local heterogeneity prevents spread of excitation in all directions, resulting in unidirectional propagation upwards (Figure 5.15A). The wave advances and doubles back to excite the region previously blocked (Figure 5.15B), resulting in reentrant excitation in the form of

two mirror-image rotors (Figure 5.15C). Heterogeneity, induced by random firing in the model, breaks the symmetry (Figs. 5.15D) leading to a single rotor (Figure 5.15E). The buildup of fatigue eventually makes propagation impossible and the rotor is annihilated (Figure 5.15F). These features are similar to experimental observations (Figure 5.10).

In the cellular automaton model each site corresponds to approximately 0.1 mm^2 , or 7-14 cells in the biological preparation. During the burst the period of rotation of the rotor is approximately 36 iterations, so each iteration step corresponds to approximately 20 ms. With this scaling, the time interval between bursts in the cellular automaton model is about 1000 iterations or 20 seconds, which is comparable to experimental observations (Figure 5.9).

Simulations were carried out for models with neighbourhood sizes greater than one. Table 1 summarizes the results. Parameter values are set to allow planar wave propagation from an initiation site proportional to neighbourhood size. K_{exci} is set to the maximum possible for propagation from an activated planar wave segment of size r grid points times $(2r + 1)$ grid points. The value in brackets is the largest value of K_{exci} that allows planar wave propagation. E is set to the minimum value that allows the broken wave front to curve inward and R is set to $1 + E$. P is the measured rotor period for the parameter values used. V is wave front velocity measured at the initiation site. Wave speed is measured in the direction of planar wave propagation. For these simulations, planar wave propagation is measured parallel⁴ to the orientation of the grid. Propagation speeds in directions diagonal to the grid orientation is lower[275]. Planar wave speed for these K_{exci} values is 1 grid point per time step for unbroken wave segments.

⁴Distances measured in either the x or y directions from a given grid point are measured parallel to the orientation of the grid, while distances measured in both the x and y directions are measured diagonal to the orientation of the grid.

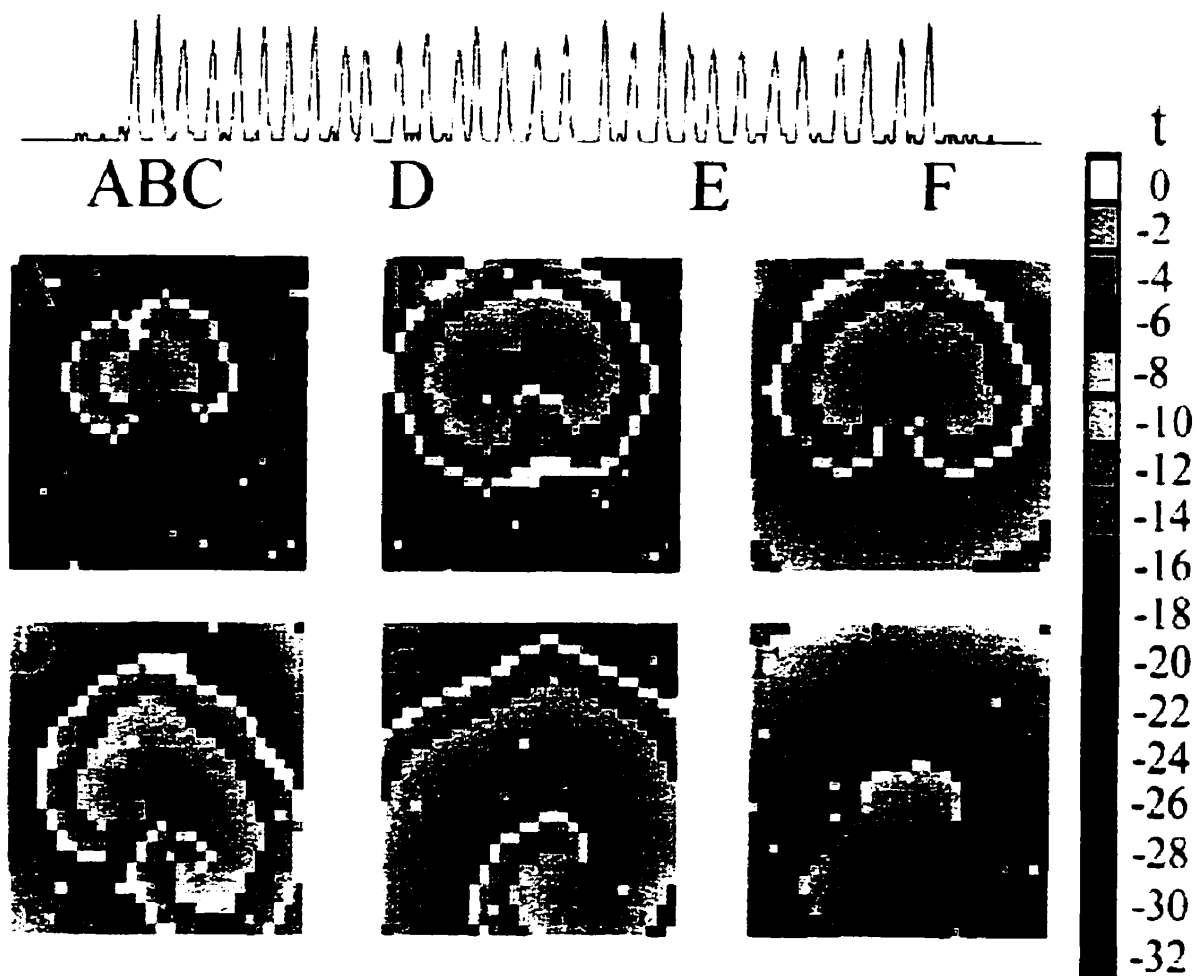


Figure 5.15: Simulation of a single burst in a 30×30 array. Contour maps of activation times for the cellular automata model during a rotor burst. A. Unidirectional block. The wave is initiated from the random firing of more than 2 neighbouring sites. Heterogeneity results in unidirectional propagation upwards. B and C. Formation of two mirror-image rotors. The excitation doubles back and, invades the site of block to form a rotor. D and E. Rotation of the mirror-image pair of rotors. The rightmost rotor dominates and the leftmost rotor dies out first. F. Termination of the remaining rotor.

r	k	E	R	P	dx/dt
1	3 (3)	5	6	36	1/5
2	8 (10)	6	7	56	2/5
3	17 (21)	9	10	76	3/7
4	29 (36)	18	19	47	4/13
5	43 (55)	16	17	61	5/12

Table 1

The rotor periods for four different values of K_{exci} is given for neighbourhood sizes 1 through 5 in table 2. The same values of E and R for the corresponding neighbourhood sizes are used as in the previous table. For each neighbourhood size, K_{exci} is varied between the values shown in the second column. Values of K_{exci} that do not result in a stable rotor are denoted with an 'x'. The simulations indicate how rotor period is expected to change under the influence of fatigue for different neighbourhood sizes.

r	K_{exci}	Rotor Period (P)			
1	0 \rightarrow 3	x	12	12	36
2	5 \rightarrow 8	14	14	19	56
3	14 \rightarrow 17	20	27	42	76
4	26 \rightarrow 29	x	x	43	47
5	40 \rightarrow 43	30	41	45	61

Table 2

Rotor Initiation in Simple Cellular Automata Models

Rotor initiation in cellular automata is a simple process. Initiation of a wave occurs when a number of grid points greater than or equal to K_{exci} are active within a neighbourhood. As the probability of initiation is low, we assume for this discussion that at any initiation site only K_{exci} grid points are active, and that there are no grid points close to the initiation site that are refractory. If this is the case, unidirectional propagation can only occur if one or more of the initiating grid points

becomes refractory. Furthermore, the grid point must become refractory before the target wave advances past the immediate neighbourhood of the refractory grid point.

Consider a GH model with a Moore neighbourhood of size 1, $K_{exci} = 3$, $E = 5$, and $R = 6$. There are 56 ($\frac{8 \cdot 7 \cdot 6}{6!}$) different positions that three active grid points can have in a given 3×3 neighbourhood. Cells can have activation states ranging from 1 to 5 in each of these configurations. At least one grid point has a value of 1 at the moment of initiation. There are three possible locations for this grid point, giving $3 \times 5 \times 5 - 14 = 61$ different permutations (where 14 is the number of identical repeats) for the 56 spatial configurations at the initiation site. Of these 3416 (56×61) different configurations, a certain portion give rise to unidirectional propagation and rotor waves, while the rest result in target patterns.

The probability that wave initiation results in a rotor can be determined by iterating the model for each of the 3416 possible configurations. One of these spatial configurations (with 61 different configurations of activation state) is analysed in detail. The representative spatial configuration is chosen so that the results can be generalized to the remaining 55.

The two examples presented below demonstrate that different spatial configurations generate different patterns of activation even when the state of each grid point at wave initiation is similar. The numbers give the activation state (1 to 5) of each grid point. The symbol '+' denotes the extent of the neighbourhood at $t = 0$. Refractory grid points are represented as 0 and excitable grid points are left blank.

Example 1.

t=0	t=5	t=10
		1
		12321
		2345432
	121	135000531
+++	13431	240000042
141	25052	13500 00531
+++	13431	240000042
	121	135000531
		2345432
		12321
		1

Example 2.

t=0	t=5	t=10
•4•	303	1350 0531
1+1	15451	240000042
+++	232	135000531
	1	2450542
		1234321
		121

The first configuration gives rise to a target. The second results in unidirectional propagation that eventually evolves to a double armed rotor.

Once initiated, the advancing wave is vulnerable to the effects of grid points becoming refractory only while the wave is close to (within one neighbourhood distance of) the initiating grid points. The configuration that results in the fastest propagating wave is more stable than others because the wave is in the neighbourhood of the initiating grid points for the least amount of time.

The configuration where three grid points are activated in a row (as is shown in the first example) is more stable than other configurations as it gives rise to more rapidly propagating wave fronts than other configurations. Other configurations activate grid points in the center of the neighbourhood before the wave is able to advance outward. An example of this behaviour is seen by comparing the two activation patterns above. By $t = 5$, the propagating wave from the 'three in a row' activation pattern has advanced farther (in all directions) than the second disjoint configuration.

Analysis of the 'three in a row' configuration gives an upper bound on the number of targets for all possible spatial configurations as it is least susceptible to the effects of its initiating grid points becoming refractory. Of the 61 different state configurations, 47 gave rise to propagating waves, 24 of which were targets, and 23 of which gave rise to unidirectional propagation and rotors. Therefore, slightly less than half of all propagating waves seen in this system will give rise to rotors. The actual number is higher as other configurations generate proportionately more rotors than targets. For example, the configuration

++x
 +++
 xx+

where x can be any activation state 1 through 5, generates only 35 propagating wavefronts (from a total of 61 different configurations) of which 31 give rise to rotors. Only one true target is generated (when all grid points fire at the same time), the remaining three start out as unidirectional propagating wavefronts, but collapse into targets.

Bursting in Other Models

The Gerhardt-Shuster-Tyson (GST) Model

The modified Greenberg-Hastings model described in the last section has several drawbacks. The most serious flaw is that rotor initiation depends critically on the pattern of active grid points in the initial configuration. Furthermore, the simple cellular automaton lacks two important features. First, the cellular automaton does not display dispersion effects associated with physical excitable media[95]. Second, the cellular automaton model's space and time units can only be scaled to physical systems in an arbitrary way[97]. It would be preferable to scale space and time to measured characteristics of the monolayer preparation.

The GST model[95, 96] is formulated as a cellular automaton, but addresses the issues raised above. Excitation spreads to a grid point if more than a critical number (K_{exci}) of neighbours within a Moore neighbourhood of radius R_n centered at the grid point are excited at the previous time.

The GST model displays important physiological properties commonly observed in excitable media: dispersion and curvature effects. Dispersion refers to the decrease in propagation velocity as the time elapsed since the passage of a previous wave decreases. Curvature effects refer to the slowing of propagation velocity for waves with a high curvature[95, 287, 292]. Although the GST model does support propagating rotor waves[95, 97] it does not show the spontaneous bursting observed in our experiments.

We extend the GST model by incorporating spontaneous oscillation and fatigue. The spontaneous activity was generated by assigning a random probability for non refractory grid points to fire. Fatigue is modelled by increasing K_{exci} as a consequence of rapid activity.

The GST model has an excitation variable U , which has the values 0 (unexcited) and 1 (excited), and a recovery variable V . Transition between excited and unexcited states is controlled by V . V increases by G_{up} every time step when U is 1 to a V_{max} , at which point U is set to 0; V is decreased by G_{down} to 0. A grid point is excitable if $U = 0$ and V is less than variable V_{exci} . A grid point will become excited in the next time step ($U(t + 1) = 1$) if $U(t) = 0$, $V(t) < V_{exci}$ and more than K_{exci} neighbours are excited. Similarly an excited grid point can become prematurely unexcited if $V(t)$ is less than V_{rec} and more than K_{rec} neighbours are unexcited. Dispersion effects are included in the model by making K_{exci} an increasing function of V , $K_{exci}(V) = K_{exci}^0 + [r(2r + 1) - K_{exci}^0](V/V_{exci})$. Similarly, K_{rec} is made a decreasing function of V ($K_{rec}(V) = K_{rec}^0 + [r(2r + 1) - K_{rec}^0](V - V_{max})/(V_{rec} - V_{max})$).

Spontaneous firing of cells was incorporated into the GST model by assigning a probability that each grid point will spontaneously fire once V drops to 0. Fatigue is modelled by adding a fatigue term F to K_{exci} . A large constant F_{add} is added to F every time the grid point fires and F decays exponentially by multiplying it by F_{sub} ($F_{sub} < 1$) every time step of the simulation. F_{add} and F_{sub} are set so the rapid firing resulting from rotor wave activity causes a gradual buildup of fatigue.

Space and time units for the GST model are set by scaling the model to known values of planar wave speed (c) and diffusion coefficient (D). Gerhardt and coworkers[97, 96] show that the normal velocity (V) of the wave front in the GST model is a linear function of wave front curvature (See Chapter 1.2.) For the GST model, the slope and intercept of the curvature relation are functions of K_{exci} and r [95] only. Plane waves (c) propagate at a speed equal to the radius of the extended Moore neighbourhood for values of K_{exci} used in these simulations[97] (we use K_{exci} less than or

equal to $2r + 1$, the value necessary for plane wave propagation):

$$c = r \frac{l}{\text{time step}} \quad (5.2)$$

Gerhardt and colleagues[97] found that D depends primarily on r , and has the following approximate relationship:

$$D(r) = 0.032(2r + 1)^2 \frac{l^2}{\text{time step}} \quad (5.3)$$

where l is the distance between adjacent grid points. Following the method employed in reference[96], we solve the equations for D and c simultaneously setting D and c to known values. D and c for the monolayer preparation were approximated in Figure 5.14 to be $0.07 \text{ cm}^2/\text{s}$ and 2 cm/s respectively.

$$t = \frac{0.546875r^2}{(2r + 1)^2} \quad (5.4)$$

$$l = \frac{1.0937r}{(2r + 1)^2} \quad (5.5)$$

G_{up} and G_{down} are chosen to give a maximum action potential duration of 400 ms and a maximum refractory period of 200 ms.

Two versions of the GST model were developed. The first version uses a Moore neighbourhood with cells positioned evenly on a grid. The second version assigns a random location to each cell by displacing each cell a random angle and distance from its original grid point location. The neighbours of each cell are then determined by checking which cells fall within a circular radius R_c of each other. Both versions gave nearly identical results for rotor initiation and annihilation. The second version gave rise to smoother wave fronts. The original model (with Moore neighbourhood and a rigid grid) is presented here, as the scaling relation determined above applies strictly only to cells on a grid as used in Ref.[96].

Parameters were set to reasonable estimates for embryonic heart cells. We assume $V_{max} = 1000$, $g_{up} = 250$, $g_{down} = 95$, $K_{exci} = 5$, $K_{reco} = 25$, $V_{exci} = 625$ and $V_{reco} = 900$. Parameters that control spiral wave break-up[95], (V_{reco} and K_{reco}), by allowing for waves of inexcitation are set to have negligible effect ($K_{reco} > \text{total}$

neighbours), since termination of spiral wave activity in our experiments does not involve spiral wave break up[95]. The probability of a grid point spontaneously firing is 0.005 per iteration. F_{add} and F_{sub} are set so that F increases during spiral wave activity and decreases during spontaneous activity, $F_{add} = 0.16$, $F_{sub} = 0.008$. With $Rc = 3$, the time units are 100 ms. per time step and the space unit is 0.67 mm for the Moore neighbourhood simulation. Results are shown in Figure 5.17. Figure 5.17 models the data shown in Figure 5.12 for the maturing culture preparation. Different values of K_{exci} simulate differences in excitability or connectivity between cells. For $K_{exci} = 11$, broken wave fronts do not easily curve inward to form stable rotors. The models activity is sporadic as it is dominated by random activation of groups of cells. For $K_{exci} = 10$, broken wavefronts can more easily turn inward to form rotors. The model displays bursts of activity with interspersed with individual spikes. Spike frequency increases because the threshold for activation decreased. For $K_{exci} = 9$, activation is common, with numerous spiral waves and targes.

The FitzHugh-Nagumo (FHN) Model

The GST model corrects an inadequacy apparent with the simple modified GH simulation. The model can be appropriately scaled to known values of D and c . The final concern is whether initiation is an artifact caused by the discrete nature of grid point firing. It can be argued that individual grid points in a excitable media would not fire independently; rather they are continuously influenced by the state of their neighbours by diffusion. The simulations in this section attempt to broadly address this issue by using a continuous time, continuous space approximation to an excitable medium.

In general, excitable media can be described simply by two partial differential equations[95]. One equation describes an excitation variable (u) and the other describes a recovery variable (v):

$$\frac{\partial u}{\partial t} = \frac{f(u, v)}{E} + D_1 \frac{\partial^2 u}{\partial x^2} \quad (5.6)$$

$$\frac{\partial v}{\partial t} = Eg(u, v) + D_2 \frac{\partial^2 v}{\partial x^2} \quad (5.7)$$

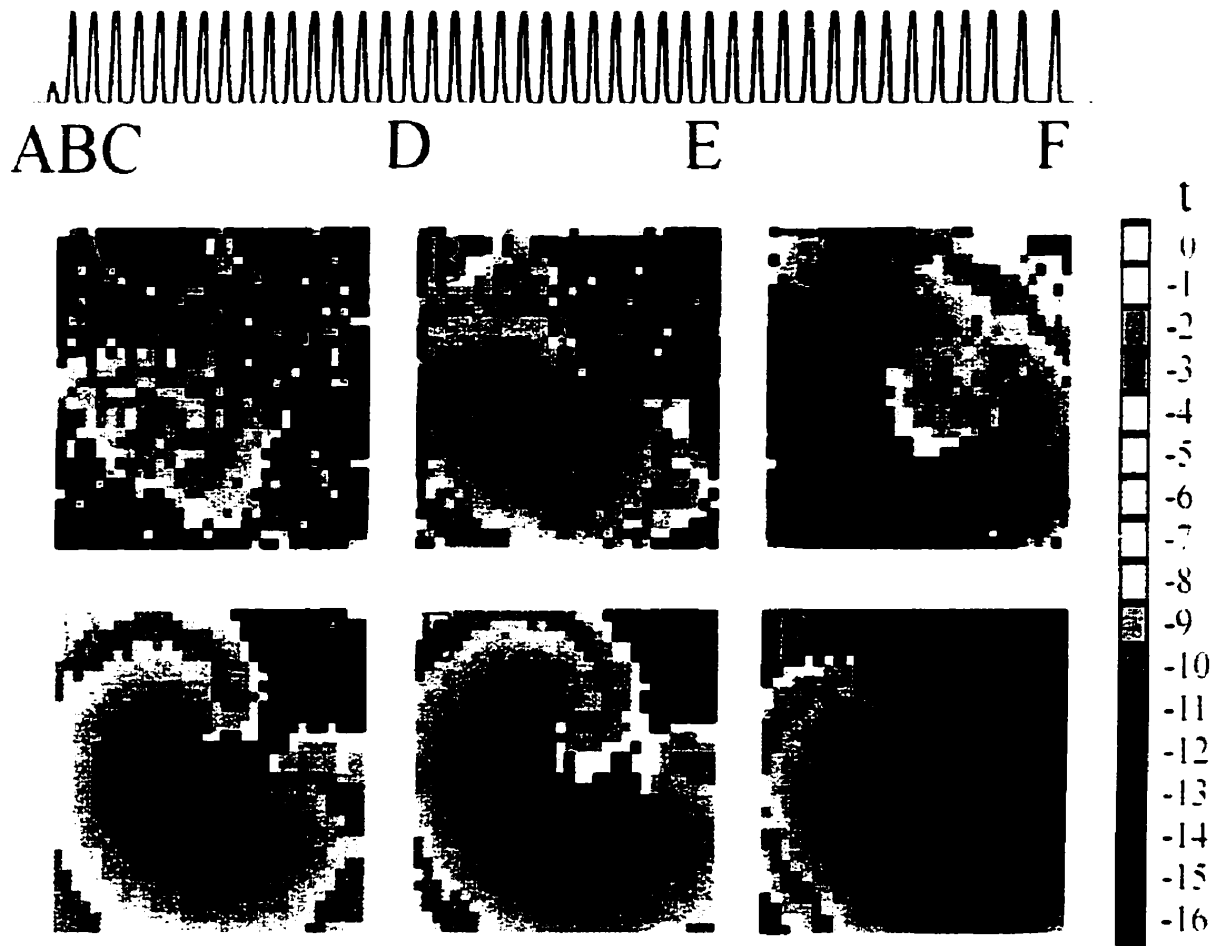


Figure 5.16: Simulation of a single burst in a 30×30 array. Contour maps of activation times for the GST model during a rotor burst. A. Unidirectional block. The wave is initiated from the random firing of more than 2 neighbouring sites. Heterogeneity results in unidirectional propagation upwards. B and C. Formation of two mirror-image rotors. The excitation doubles back and, invades the site of block to form a rotor. D and E. Rotation of the mirror-image pair of rotors. The rightmost rotor dominates and the leftmost rotor dies out first. F. Termination of the remaining rotor.

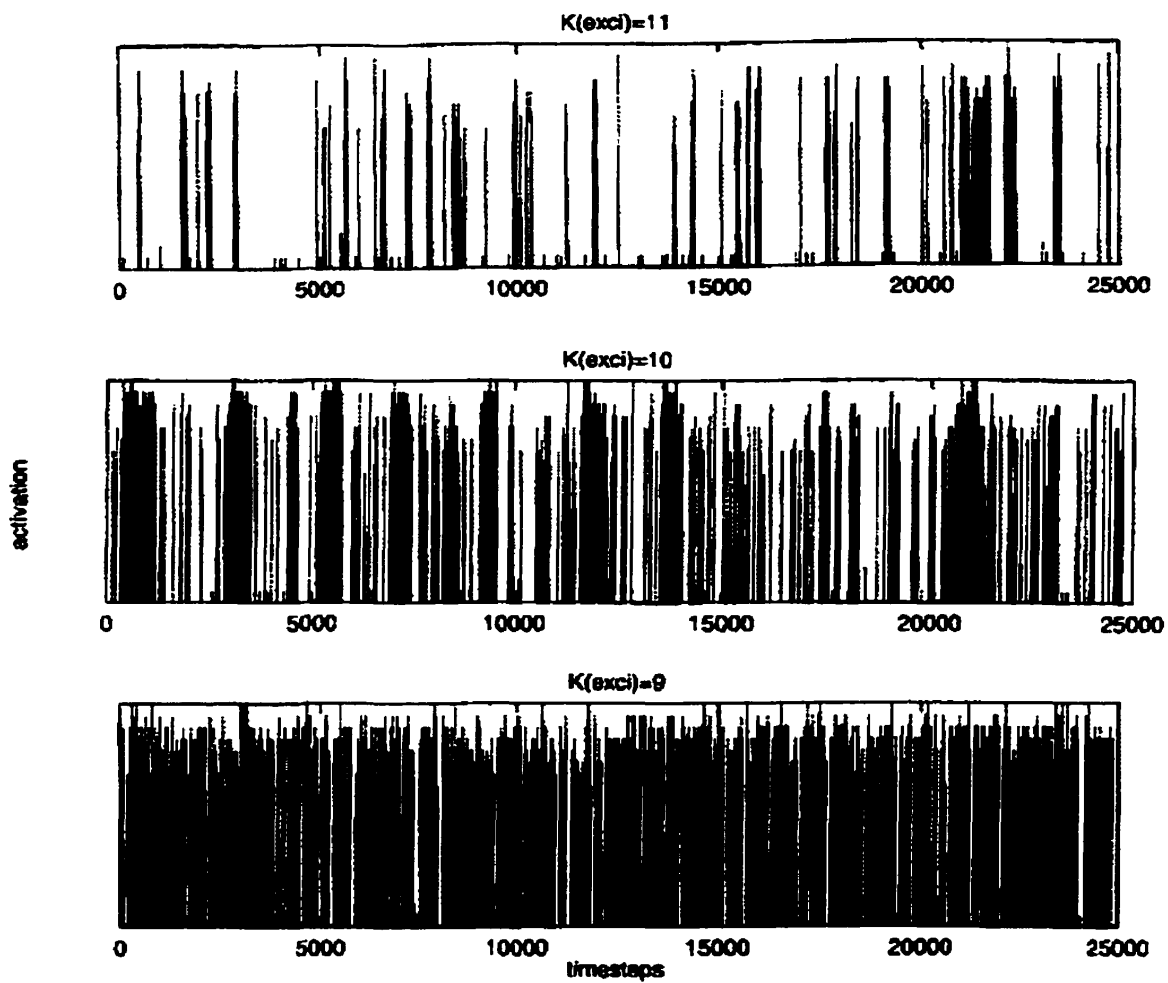


Figure 5.17: The model used for Figure 5.16 was run for different values of K_{exci}

In cardiac preparations, u represents electrical potential and v represents membrane recovery. D_1 and D_2 are diffusion coefficients expressed in space units² over time units. In most excitable media, the excitation variable changes on a faster time scale than the recovery variable, so E is set to a (small) fraction less than one.

The FitzHugh-Nagumo model[83, 202] of an excitable medium are:

$$f(u, v) = u - u^3/3 - v \quad (5.8)$$

$$g(u, v) = u + \beta - \gamma v \quad (5.9)$$

In cardiac simulations, v represents permeability of ion channels and does not diffuse, so $D_2=0$. Computations with D_2 set to 1 display similar qualitative features but have some quantitative differences (see [289] and references within). The local behaviour of the FitzHugh-Nagumo equations depend on parameters E , β and γ , whereas the diffusion coefficient D is closely tied to time and space scales of the excitable media. Parameter β controls threshold, larger values of β cause the FitzHugh-Nagumo equations to require larger stimuli before they undergo an excursion from steady state (a simulated action potential). Low values of β cause the FitzHugh-Nagumo equations to oscillate spontaneously (the exact ranges for these behaviours depend on the other two parameters). Parameter E controls the ratio of excitation to recovery rates. Higher values give slower rise time kinetics and allow faster recovery. Lower values give sharper rise times (as are seen in physical excitable media such as heart and nerve tissue) and longer refractory times. Parameter γ does not have a critical effect on the overall dynamics for small E [289]; increasing γ increases excursion speed of the trajectories for both recovery and excitation.

Computations of the FHN equations are carried out by constructing a two dimensional grid of points which calculate the FHN equations at small time steps (dt). Diffusion is simulated by summing the difference in u at each grid point with the value of its four nearest neighbours times a factor $\frac{D}{h^2}$. The term $\frac{D}{h^2}$ is proportional to the number of samples per space unit. Here we use $h = 0.5$, sampling 2 times every space unit. The first set of computations were carried out at $\beta = 0.7$, $E = 0.3$ and

$\gamma = 0.5$. For this parameter range, rotor waves have a period of 11.4 time units, and a plane wave propagates at a maximum (fully recovered) speed of two grid points per time unit[289]. As rotors in the monolayer preparation have an initial period of approximately 400ms and a planar wave speed of 2 cm/s, the time and space units are scaled to be 40 ms per time unit, and 0.4 mm per space unit. Using these values, the diffusion coefficient is (space unit² / time unit) 0.04 cm²/s⁵, which is half the value determined in Figure 5.14.

Spontaneous activity was added to the FHN model in two ways. For the first set of simulations, any grid point can spontaneously fire with a probability P_f if it is sufficiently recovered (recovery is defined as any grid point with $u < -1$ and $v > 0.6$). This method is similar to the technique used in the simple cellular automaton described in the previous sections. Although random activation is not realistic, it maintains the scaling calculations defined above.

For the second set of simulations, spontaneous activity was generated by assigning random values (within a range) to parameters β and E . The fatigue term was modified to decrease the spontaneous activity as well as increase E ; simulations with fatigue only added E resulted in transient phase waves in the simulation, which are not evident in the monolayer preparation. E was varied evenly between 0.27 and 0.37, and β was varied evenly between 0.49 and 0.69. By randomly setting E and β , the model represents an assortment of coupled cells with a range of excitability and intrinsic periodicities, which we may expect to find in recently plated monolayer preparations. The main difficulty with this approach is that is harder to generalize these results to other homogeneous models of excitable media.

Both approaches resulted in the generation of rotors. The result from one representative simulation is shown in Figure 5.18 and Figure 5.19. The parameter values for the simulation are $E = 0.3$, $\beta = 0.7$, $\gamma = 0.5$, $D = 1$, $P_f = 0.00005$. Fatigue ϕ is increased by $0.000001 \times dt$ if $u > 1$, and decays by a factor of 0.99995 each time step. An isochronal map of a typical burst is shown in Figure 5.18. Figure 5.19

⁵Although a factor of two appears large as a comparison between experimental and theoretical values, it is in good agreement when compared to similar scalings for cardiac muscle, which are up to a factor of six too high.

shows a series of bursts, with a close view of one of them.

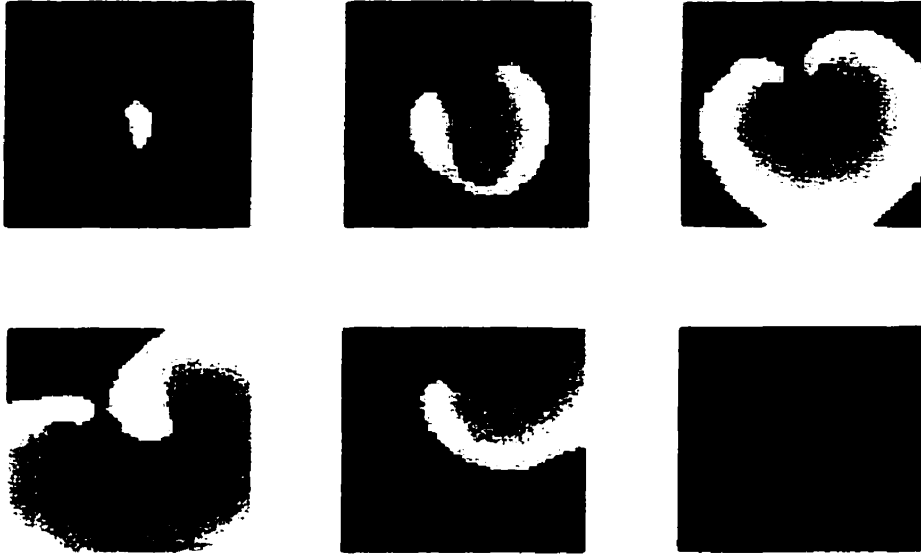


Figure 5.18: Simulation of a single burst in a 75×75 array. Contour maps of activation times for the FHN model during a rotor burst. Top left panel: Unidirectional block. The wave is initiated from the random firing of more than 2 neighbouring sites. The wave propagates downwards. Top middle and top right panels: Formation of two mirror-image rotors. The excitation doubles back and invades the site of block to form a rotor. Bottom left panel: Rightmost rotor dominates prior to meandering off the simulation grid. The remaining rotor (bottom middle panel) eventually collides with the simulation boundary.

The model shows initiation and annihilation of bursting rotors. Impulses are initiated by the chance simultaneous firing of several sites in close proximity to each other, so that additional sites in the neighbourhood fire. In the example shown (Figure 5.18) local heterogeneity prevents spread of excitation in all directions, resulting in unidirectional propagation downward. The wave advances and doubles back to excite the region previously blocked, resulting in reentrant excitation in the form of two mirror-image rotors. There is a break in the symmetry leading to a single rotor rotating clockwise. The buildup of fatigue appears to cause the tip of the spiral to drift to the boundary of the simulation and annihilates.

The top panel of Figure 5.19 shows 5 bursts from the FHN model simulated

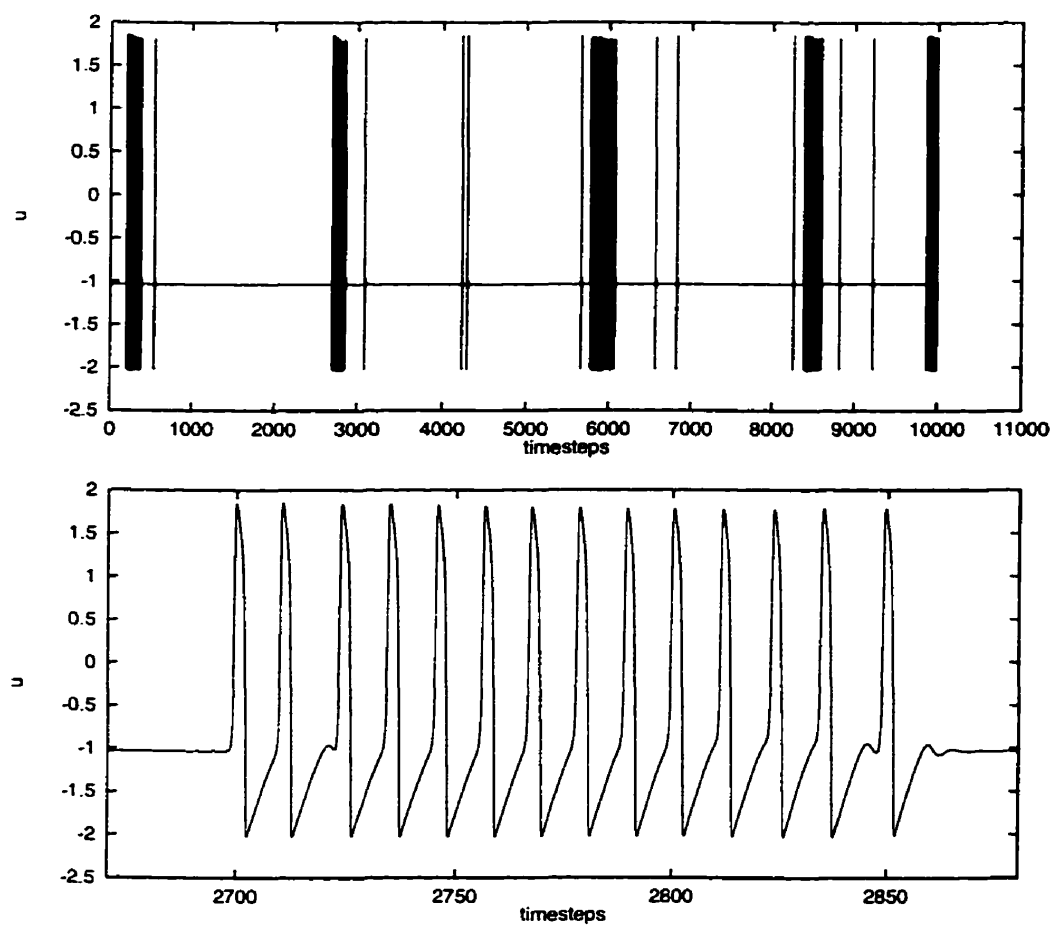


Figure 5.19: The activity from a single cell (at position [30,30]) from the simulation shown in Figure 5.18. Top panel: Bursting activity over 10000 timesteps. Bottom panel: A closer view of one of the bursts.

for 10000 time steps. The remaining 11 isolated spikes in the top panel are caused by circular wavefronts. The interburst interval is on average approximately 2200 timesteps, or 88 s. The bottom panel of Figure 5.19 shows a single burst. Even though the interspike interval increases at the end of the burst, the increase is not monotonic. The third action potential in the burst has the same period as the last. It is possible that the variation is due to meander of the spiral.

Initiation of the FHN spiral appears similar to what is seen in the GH and GST models. However, termination of the spiral has a different character, as the spiral arm collides with the boundary of the simulation instead of blocking. Spiral waves are not observed to annihilate in this way in experiments. The mechanism of initiation is also less transparent than it is in the GH or GST models. It is not obvious that a set of conditions for spiral wave initiation as simple as was found for the discrete case (Section 5.4.2) exists.

5.5 Discussion

The monolayer preparation generates bursts of activity as it matures. The mechanism generating bursts is spontaneous initiation and annihilation of rotors. Both bursting dynamics and rotor activity have been extensively studied in isolation; the cardiac monolayer preparation is the first description of a system where bursting dynamics are linked to the presence of rotors of activity.

5.5.1 Mechanisms for Bursting in Other Systems

Bursting in the cultured monolayer system is associated with the onset and offset of rotors of activity. Although experiments do not rule out the possibility that rotors are a secondary effect, simulations suggest that bursting dynamics are directly caused by spontaneous initiation and termination of rotors.

Several mechanisms have been proposed to explain bursting dynamics in diverse biological systems (see Chapter 1.4). These mechanisms include interacting slow and fast ionic currents within a single cell or averaged over many cells (Chapter

1.4.2), networks of different cell types (Chapter 1.4.6), and fixed delay reentry of a pacemaker (Chapter 1.4.7). The above mechanisms are qualitatively different from those described in this chapter.

Simulations demonstrate that bursting can occur in nonendogenously bursting cells if they are spontaneously active, exist in weakly coupled groups, and display fatigue. It is interesting to speculate that bursting in other biological system may be driven by spatial patterns of activation. For example, bursting in β -cells may be caused by a mechanism similar to that observed in the monolayer. The possibility that bursting in β -cells is driven by patterns of excitation is suggested by the following: First, β -cells only burst in groups and show irregular spontaneous activity in isolation[254]. It is possible that individual β -cells do not have the capacity to endogenously burst even under low noise conditions. Irregular spiking could trigger spiral waves as demonstrated in the cellular automaton and differential equation models. Eddlestone and colleagues[67] recorded potential from two sites within an islet. They discovered that bursting within each islet is synchronized, although the spikes are not. More recently waves of electrical activity have been observed in Islets of Langerhans[208] using optical recording techniques. These observations indicate the islets are not isopotential and raise the possibility that spiral or scroll waves exist in the islet. Finally, gap junction conductance decreases significantly during bursts in β -cell clusters, which may reduce fatigue like effects and heterogeneity in gap junctional conductance exists in the islet[184], which can give rise to unidirectional propagation.

5.5.2 Rotor Initiation in Other Systems

Rotors are well known from experimental[2, 50, 169, 249, 284] and theoretical studies[161, 194, 95, 287]. There are several known mechanisms for rotor formation in excitable media. Mechanisms for generating spirals in homogeneous excitable media using external manipulation are reviewed in Chapter 1.3.3.

Rotors form spontaneously in a variety of different excitable media. Unlike spirals initiated by external manipulation, heterogeneity of some form is thought to be

necessary for spontaneous spiral formation. The primary mechanism proposed for the creation of these waves was that spiral wave formation was due to heterogeneity of refractoriness[1, 194]. Two waves (from a distant source) propagate toward a finite region of enhanced refractoriness. If the time between the waves is sufficiently short, the second wave cannot penetrate into the refractory region. A wave break is then formed at the boundary of the heterogeneity. The broken wave moves along the heterogeneity boundary until the tissue becomes excitable, at which point the break propagates into the previously refractory region forming a rotor. Another mechanism for wave generation involves chance initiation of a wave during the vulnerable period of an excitable media. Pacemakers at arbitrary sites in the excitable media results in initiation of multiple circular wave fronts at different locations. When wave is initiated by chance in the wake of a previous wave, a wave break occurs which can result in a rotor. This mechanism has been observed directly in slime mold cultures[217]. A third mechanism of rotor formation in heterogeneous systems involves the presence of obstacles in the path of rapidly propagating waves[1, 107, 262]. When the period between travelling waves is long, the medium at the obstacle is well recovered and the wave splits at the obstacle and rejoin at the other side. When the wave period is shorter, the medium at the obstacle is not sufficiently recovered. Due to dispersion and curvature effects, wave speed is slowed at the broken tips so that they travel outward from the obstacle some distance before rejoining. If the obstacle is sufficiently large, the wave tips can curl inward before having the chance to rejoin, and form two rotors.

Rotor formation in the above examples involve the breakup of established stable waves (as in the pinwheel and crossfield stimulation protocols[283, 289] and the obstacle experiments[1]) or the creation of a broken wavefront in the wake of an established wave (as occurs premature pulse protocol[217]). In the experiments and models of the bursting monolayer, the focus is on initiation of a broken wave front in media with heterogeneities created by local refractory cells or patches of lower excitability. The media is heterogeneous on small space scale. Unlike the mechanisms discussed above, a travelling plane wave propagates easily through these

obstacles without breaking. However, an initiating pulse is going to be affected by the heterogeneity; if we assume that the distance between adjacent grid points is smaller than the critical radius of excitation for the medium then a wave will only be triggered if a certain number of those grid points fire in near synchrony. It is most likely that close to the minimum number of grid points will fire synchronously (unless these points are already entrained). If this is the case then the initiation site will be equal to or only slightly greater than the critical radius of the media and therefore maximally sensitive to heterogeneity. The degree of heterogeneity in the monolayer is unknown. In the simulations, the media is designed to be heterogeneous ‘enough’: planar and slightly curved waves travel easily, and only waves of high curvature break.

5.5.3 Rotor Annihilation in Other Systems.

Rotor breakup has been extensively studied in mathematical models of excitable media[48, 95, 129, 142, 219]. One of the motivations for the study of rotor breakup is that it is thought to play a critical role in the transition from tachycardia to fibrillation in the heart[48, 135, 292]. Rotor breakup involves a complex set of behaviours that are not well defined and are often model dependent. All models of rotor behaviour can break-up if the activation front collides with its own refractory wake. This is caused by slow recovery fronts (SRFs)[48]. Most models give rise to SRFs if the action potential duration in the model is sensitive to recovery time[48, 142, 219].

Spirals in the monolayer preparation are not observed to break up as observed in the model systems discussed above. Spiral break-up in these models give rise to many small spirals: it is this condition that is associated with fibrillation in the heart[48, 135, 292]. A typical annihilation sequence for the monolayer spiral is that its period slows, followed by wave front propagation failure. Present modeling assumes that a parameter in the biological system changes in a way that slows and eventually prevents conduction. However, it is possible that the core simply increases to a size greater than the diameter of the monolayer and that propagation

would have continued if the medium was larger. Alternatively, the spiral tip could have undergone meander and collided with the edge of the preparation. This latter possibility is unlikely, as in most cases the core was stationary or only meandered slightly before annihilating.

5.5.4 Continuum Considerations

An important issue that must be addressed is whether the monolayer preparation can be modeled as a anisotropic continuous medium. Most excitable media models of cardiac conduction assume that conduction is continuous. Continuous excitable media models of cardiac conduction are known as *cable equations* and have the following form[291]:

$$\frac{\partial V_m}{\partial t} = -\frac{J_m}{C_m} + D_x \frac{\partial^2 V_m}{\partial x^2} + D_y \frac{\partial^2 V_m}{\partial y^2} + D_z \frac{\partial^2 V_m}{\partial z^2} \quad (5.10)$$

V_m is local membrane potential, J_m is the sum of local ion-channel current densities, C_m is membrane capacitance, and D_x , D_y and D_z are diffusion coefficients that control the relative contribution of voltage from neighbouring regions (in the x, y and z axes) have on the local membrane potential. Models which employ the diffusion coefficient (such as the models presented in Section 5.4.2) assume continuum conditions. An underlying assumption in continuous cable theory is that the effect of discrete intercellular connections can be averaged out over the space scales important for conduction.

Although it is likely that propagation in the healthy heart can be treated as continuous[291], propagation in certain cardiac preparations is saltatory[259]; that is waves of excitation propagate more rapidly through individual cells than between them. Israel and colleagues[127, 128] recorded electrical potentials from chick cardiac monolayers cultured on a microelectrode array. The elements in the array were spaced to allow simultaneous recording from points within individual cells and between adjacent cells. Conduction delays of up to 0.41 ms were observed between electrodes recording from adjacent cells under some experimental conditions. Similar results were obtained using a photodiode array recording from cultured monolayers

of rat cardiac cells[77]. Rhor and colleagues[232] lowered connectivity in strands of cultured neonatal rat ventricular myocytes using gap junction uncouplers. They were able to lower conduction velocity from 47 cm/s to under 1 cm/s. At high levels of cellular uncoupling, conduction jumped between adjacent patches of simultaneously activated cells instead of propagating smoothly. Rhor's measurements of discontinuous conduction is similar to visual observations of young chick monolayers loaded with calcium sensitive dye. Observations under high power (20× or 40×) reveal that conduction occasionally progresses as a rapid series of jumps, while at other times conduction progresses smoothly. The slow propagation velocities in the chick monolayer after one day in culture suggests that these cells are coupled to the same extent as Rhor's 3-8 day old rat cultures treated with gap junction uncoupling agents.

Winfree[289, 290, 291, 292] collected several 'rules of thumb' based on cable theory, continuum conditions and observations of rotor behaviour in different continuous media. Some of these rules are applied below to measured values from the monolayer preparation in order to test whether its behaviours are consistent with continuous cable theory.

One definition for D provided by Winfree is $D = \frac{\lambda^2}{\tau}$. Here λ is the space constant defined as the distance where effects of potential drop off exponentially, and τ is the rise time of space clamped excitation. If we take our measured value of D as the known quantity, and use $\tau = 0.001\text{s}$ we get $\lambda = 0.00837\text{cm}$. If we assume that τ can be a factor of 5 larger (due to slow upstroke velocity) then we have $\lambda = 0.01878\text{cm}$. From an estimation of planar wave speed c_0 being approximated by $\sqrt{(\frac{D}{\tau})}$, we get $\tau = 0.018\text{s}$. This value is twice as high as estimates from photodiode measurements (Chapter 5.3.1) and is higher than measurements obtained from microelectrodes. Several electrophysiological measurements of monolayer preparations were conducted by myself and Dr. Arkady Kunysz (unpublished results) and upstroke velocities were on the order of several millivolts per millisecond. The electrophysiological trace in Figure 5.2 is representative of action potential shapes observed over many preparations. However, I cannot rule out the possibility that the monolayers

used in the calcium mapping studies displayed slower upstroke velocities.

One criterion for treating an excitable medium as continuous is if λ is greater than 10 cell lengths[234]. Clearly, this is not the case for the monolayer as λ is on the order of one cell length. Another criterion is that observations should be made at a scale greater than wavefront thickness[259]. Wavefront thickness can be approximated by $\tau \times c_0$ [291] which in our case is $0.001 - 0.005\text{s} \times 2\text{cm/s} = 0.002 - 0.01\text{ cm}$. If we apply this criteria, the bursting monolayer preparation can be treated as continuous for the observations made using the optical setup, but may be discontinuous at scales important for rotor initiation.

Another criterion applied by Winfree to the monolayer preparation (personal communication) is that $D > 1/(\tau \times \text{cell density})$. In our case, monolayer density is $7 - 14 \times 10^3$ cells per cm^2 , resulting in a value that ranges between $1/7$ and $1/14$ for $\tau = 0.001\text{ms}$ and $5/7$ and $5/14$ for $\tau = 0.005\text{ms}$. The value of D calculated in Figure 5.14 only exceeds the smallest of these values.

Winfree presents several equations that relate rotor core diameter (d) and period (P) to planar wave speed, diffusion coefficient and length and space scales. The observed diameter of spiral cores in different monolayer preparations was approximately 1-2 mm, however a reliable estimate is difficult as some records are of poor quality. We consider the maximum diameter of the core to be $d = \frac{c_r \rho}{\pi} = 3\text{ mm}$ where c_r is wavespeed at curvature present at the spiral core (taken here to be roughly equal to planar wave speed). Winfree states that the expressions $\sqrt{(c_0 \pi d / D)}$ and $\sqrt{(c_0^2 P / D)}$ are equivalent and approximately equal to 9, and reports that minimum and maximum values for different continuous excitable media are 4 and 11, respectively[291]. The value of the expression based on rotor diameter is 5.2 for $d = 3\text{ mm}$ and 3 for $d = 1\text{ mm}$ for the bursting monolayer preparation. Using the expression based on rotor period, we get 4.8 for $P = 0.4$ and 7.4 for $P = 1$. Depending on the criteria used, the bursting monolayer is either slightly out of or comfortably within the limits of rotor behaviour in continuous media.

A final concern is the relationship between curvature and wave speed (see Equation 1.2). To the best of my knowledge, all derivations of the curvature relation

are based on continuum assumptions. The curvature relation was used to calculate D for the monolayer preparation (see figure 5.14). The linear dependence of wave speed on curvature could be taken as an indication that the monolayer is best represented as a continuum. However, cellular automata display curvature dependent wave speed effects when their threshold (K_{exci}) is greater than one. Gerhardt and colleagues[95] calculated the relationship between curvature effects in their cellular automaton model and the continuous curvature relation based on diffusion (see Section 5.4.2). Even though the dependence of wave speed on curvature in Gerhardt's model is due to discontinuous threshold parameter K_{exci} , the relationship between wave speed and curvature is linear. If the monolayer is best described as a discontinuous system, the value of D calculated in Figure 5.14 should be treated as an abstract measure of slope rather than a true diffusion coefficient.

Cable theory also has implications for rotor block under the influence of fatigue. The cable equations have wave speed decrease proportional to the square root of D , where D is proportional to the resistivity of the media. Therefore conduction velocity falls proportional to the square root of resistance, but only is zero for infinite resistance. This implies that rotors would slow but not block in response to increases in gap junctional resistance. Rotor annihilation would then depend on the core diameter increasing to a point where it exceeds the diameter of the monolayer, which is not seen in the present experiments. James Keener modified versions of the cable equations to account for the discontinuous nature of conduction between cells[148, 150]. These modified cable equations predict that conduction blocks at finite gap junctional resistances, which is observed in experiments where resistance is increased using blocking agents[58, 232, 259].

In conclusion, use of continuous differential equation models based on cable theory to model the monolayer preparation requires more thought. The estimation of D in Figure 5.14 depends on Equation 1.2, which is strictly valid for waves of low curvature (although it has been shown to hold for highly curved waves in experiments[89, 90]). Different estimates of D may confirm continuum conditions in the monolayer preparation. Use of discontinuous cellular automata models that

do not depend on continuum conditions for interpretation is the most reasonable modeling choice until these issues are resolved. Another safe approach would be to develop models similar to those used in reference [150].

5.5.5 Conclusion

The current work demonstrates bursting rotors and provides a novel mechanism for bursting behavior in diverse settings. Bursting arises due to local interactions of non-bursting elements. An alternative mechanism is that the individual cells display bursting dynamics and that the rotors are a secondary phenomenon. However, previous studies of cultured embryonic chick cardiac myocytes failed to display spontaneous bursting[157, 164]. Moreover, by changing the parameters in the theoretical model, other types of non-bursting dynamics could be observed including localized activity with no macroscopic wave propagation and wave propagation in plane waves or target patterns. Similar dynamics were observed in the cultured myocytes as the plating densities and media conditions were modified. The current parameters in the model were selected to demonstrate the feasibility of obtaining bursting dynamics in a model with elements that do not burst themselves.

Studies of excised slices of cardiac tissue demonstrate that sustained spirals can be initiated by electrical stimulation, and proposed that spirals might be a mechanism for abnormally rapid cardiac arrhythmias (tachycardias)[3, 50]. Although tachycardias in people can be initiated by electrical stimulation, the more usual circumstance is that they start spontaneously. In most instances the rhythms also terminate spontaneously. On occasion there is a repeated spontaneous paroxysmal initiation and termination of tachycardias[42]. Although it is likely that the tachycardia are caused by reentrant activity and possibly by rotors of activation, the mechanism of initiation and termination of the tachycardia is unclear. The paroxysmal onset and offset of reentrant cardiac arrhythmias presents significant clinical management problems[42]. The monolayer preparation may be a model system for this class of arrhythmia. The monolayer preparation may also be a model system for bursting in neural systems[192, 60] and in pancreatic β cells[184], but more work

is needed to determine the actual patterns of spatio-temporal activation in these systems.

Chapter 6

Conclusions

This thesis describes theoretical and experimental studies of pacemaker initiation and interaction. Mathematical models of two pacemaker and multiple coupled pacemaker systems are investigated in Chapter 2 and the last section of Chapter 5. Experimental results from optical mapping experiments of whole heart preparations and cultured monolayer preparations are detailed in Chapters 4 and 5. A large portion of this thesis deals with construction of an optical mapping system. A description of the system used for getting mapping results is detailed in Chapter 3.

Chapter 2 is a study of an arrhythmia called modulated parasystole. The arrhythmia is generated by the interaction between the sinus pacemaker and an ectopic pacemaking focus. A mathematical model was developed to study the dynamics of modulated parasystole. The model is formulated as a discontinuous circle map with no fixed points. In Chapter 2 we consider the possible dynamics of a general class of discontinuous maps with no fixed points and apply these findings to a mathematical model for modulated parasystole.

The family of discontinuous circle maps investigated in Chapter 2 display banded chaos for some parameters. Banded chaotic behaviour is characterized by zero rotation interval width in the presence of a positive Lyapunov exponent. The conditions for banded chaos in these maps are determined analytically. Methods are developed for determining the bifurcation structure and the location of banded chaotic zones in parameter space. The bifurcations in parameter space associated with banded

chaotic behavior share characteristics associated with entrainment zones (Arnold tongues) characterized for mathematical oscillators. There are zones in the parameter space where all initial conditions result in the same rotation number, and these zones are organized such that between any two zones with rotation number $N:M$ and $N':M'$, there is a third zone with rotation number $(N+N')/(M+M')$. Unlike Arnold tongues, the trajectory for maps within the zones is not periodic. In addition, the zones cannot overlap, in contrast to Arnold tongues which overlap as parameters cross the critical line.

The general form of the modulated parasystole model was first used by Courtemanche *et al.*[43]. Phase resetting curves for the ectopic focus in Courtemanche *et al.*[43] were elucidated from clinical data. In Chapter 2 phase resetting is modelled by the Poincaré oscillator which has been studied as a model for biological oscillators. Use of the Poincaré oscillator facilitated mapping the model's behaviour in parameter space as it allowed continuous changes in stimulation amplitude. The modulated parasystole model displayed banded chaos over a large range of parameters. The organization in parameter space of parameters that result in banded chaos is analogous to that seen in the general family of discontinuous circle maps.

The parasystole map produces rhythms characteristic of those found clinically. The dynamics of the parasystole map can be expressed as a sequence that corresponds to the number of expressed sinus beats between successive expressed ectopic beats. The number of intervening sinus beats (NIBs) have been used to classify parasystolic rhythms both in theoretical models and in clinical situations. Concealed bigeminy and trigeminy, where NIBs conform to the formula $2n - 1$ and $3n - 1$ respectively, are frequently observed in clinical situations[247, 205]. Concealed quadrigeminy ($4n - 1$) and concealed pentagemy ($5n - 1$) have also been documented[247, 205]. These NIB patterns are associated with banding zones in the modulated parasystole model.

The relevance of this work to understanding clinical data is not clear. It is interesting to speculate that a banded chaotic trajectory produced by a parasystolic mechanism could cause parasystole to be mistaken for other arrhythmias. A banded

chaotic trajectory produces a relatively constant sinus to ectopic timing interval, which is a hallmark of reentry. A careful analysis concerning the relation of NIB sequences to banded chaos would help in the comparison of our results to clinical data and the results of other theoretical models.

Chapter 5 describes experiments on oscillators coupled by an excitable substrate. These experiments are performed using monolayer cultures of embryonic chick cardiac cells. The pacemaking behaviour of embryonic chick cells has been extensively documented. Aggregates of embryonic chick cardiac cells spontaneously beat and their dynamics under periodic forcing have been extensively studied and are relatively well understood. Aggregates are considered to be isopotential systems and therefore do not incorporate effects of conduction into their dynamics. However, conduction can be observed in spatially extended cultured monolayers of cardiac cells.

Monolayers are used to investigate the interaction of many oscillators dispersed in space. Monolayers of coupled pacemaking cells can potentially provide insight into fundamental issues related to initiation and conduction in spontaneously active media. The behaviour of the model system may be applicable to the study of diseased cardiac tissue, which displays spontaneous oscillations when ischemic.

Cultured cells couple to each other by forming gap junctions after they are plated. Microscopic examination of cultured cells suggests that functional connectivity increases over time. Older cultures (2-3 days) fire in relative synchrony. Younger cultures (1 day old) display complex dynamics. Cells occasionally synchronize, but often beat in a disorganized fashion. The dynamics of the entire system are impossible to characterize by eye as the field of view (where movement artifacts are visible) is only a few tenths of a millimeter in diameter. An optical mapping system was developed to study the behaviour of cardiac monolayer cultures. The macroscopic mapping techniques are described in Chapter 3.

Optical mapping techniques demonstrate that cells in the monolayer display bursting behaviour characterized by rapid cell firing followed by periods of silence. Conceptual models of bursting are based on cellular ionic mechanisms or the inter-

actions of a small number of functionally different cells in a network[29, 38, 41, 250, 251, 274]. The results presented in Chapter 5 show that bursting activity occurs prior to the onset of regular beating in cardiac monolayer cultures. This observation is unexpected as mechanisms responsible for bursting in single and network systems are not present in cardiac monolayers.

Bursting dynamics were observed in roughly 80% of the preparations tested. Bursting in these preparations is characterized by an increase in period of 20–80% from the beginning to the end of the burst. Timing between bursts varied between preparations. In some preparations interburst intervals were relatively constant (Figure 5.9). Bursting dynamics are also a function of time in culture. Infrequent bursting is observed after 24h in culture. Bursting frequency and duration increases from 36 to 48 hours. By 54h activity becomes regular, with infrequent short breaks. At 68h the dynamics are periodic (Figure 5.12).

Optical mapping experiments demonstrate that local dynamics are associated with large scale patterns of activation in the form of target patterns or spiral waves. Targets and spiral waves are commonly observed in two dimensional excitable media[287]. The results presented in Chapter 5 are the first demonstration of spiral waves in monolayers of cardiac tissue. Both target patterns and spiral waves are associated with regular periodic beating in culture. Bursting behaviour is associated with spontaneous initiation and termination of spiral waves. Rapid beating during bursts is associated with the presence of a single or figure of eight spiral wave. The spiral wave in the bursting cell culture repeatedly blocks and restarts, causing the long periods of silence between bursts (Figure 5.10).

Onset and offset of spirals in the monolayer system is not similar to what is seen in other systems. Other studied mechanisms for spiral wave initiation include wavefront initiation in the wake of a traveling wave or break up of an existing planar wave (Section 5.5.2). In contrast, small broken wavefronts arise spontaneously in the cardiac monolayer preparation (Figure 5.10). The broken wave fronts evolve into spiral waves. The spiral wave in the monolayer preparation slows and eventually blocks (Figure 5.10). In contrast, spirals in other systems terminate by breaking up

into smaller spirals(Section 5.5.3).

Simulations demonstrate that bursting can occur in cells that do not burst in isolation if they are spontaneously active, exist in weakly coupled groups and display fatigue (Figure 5.15). Unidirectionally propagating wavefronts are generated when asynchronously beating cells fire in close proximity to each other. Waves are initiated by the chance random activation of a sufficient number of sites in a given neighbourhood. Once initiated, the wave is frequently blocked in one direction as the initiating cells become refractory. As high curvature activation fronts advance, they become less curved and less vulnerable to block. Spiral termination is caused by simulating fatigue in the models. This is modeled by decreasing excitability of cells as a function of rapid cell firing. Spiral wave activity causes a gradual decrease in excitability, which eventually results in block. Both simple cellular automaton models (Figures 5.15 and 5.16) and coupled differential equation models (Figure 5.18) generate bursting for some parameters.

The current work underscores the delicate factors that lead to the stabilisation and destabilization of rotating waves of activity independent of external interventions. Moreover, since biological systems are spatially extended, patterns of spatial activation must necessarily be investigated before the mechanism of bursting behavior can be assessed.

Bibliography

- [1] Agladze K, Keener J P, Müller S C, Panfilov A. Rotating spiral waves created by geometry. *Science*, 264:1746-1748, 1994.
- [2] Allesie M A, Bonke F I M, Schopman F J G. Circus movement in rabbit atrial muscle as a mechanism of tachycardia: I. *Circ. Res.*, 33:54-62, 1973.
- [3] Allesie M A, Bonke F I M, Schopman F J G. Circus movement in rabbit atrial muscle as a mechanism of tachycardia: III The leading circle. *Circ. Res.*, 41:9-18, 1977.
- [4] Anderson R H, Janse M J, van Capelle F J L, Billette J, Becker A E, Durrer D. A combined morphological and electrophysiological study of the atrioventricular node of the rabbit heart. *Circ. Res.*, 35:909-922, 1974.
- [5] Anselme F, Hook B, Monahan K, Frederiks J, Callans D, Zardini M, Epstein L M, Zebede J, Josephson M E. Heterogeneity of retrograde fast-pathway conduction pattern in patients with atrioventricular nodal reentry tachycardia: Observations by simultaneous multisite catheter mapping of Koch's triangle. *Circulation*, 93:960-968, 1996.
- [6] Anosov D V, Arnold V I. *Dynamical Systems I: Ordinary Differential Equations and Smooth Dynamical Systems*. Springer-Verlag, Berlin 1980.
- [7] Arnold V I. Small denominators I: mapping the circumference onto itself. *AMS. Trans. Ser. 2*, 46:213-284, 1965.

- [8] Aygen M M, Dean H, Almog H. Concealed quadrigeminy. *Cardiology*, 68:42-48, 1981.
- [9] Aygen M M, Melamed R. Concealed pentageminy. *Cardiology*, 69:297-300, 1982.
- [10] Bak P. The devils staircase. *Physics Today*, Dec, 38-45, 1986.
- [11] Bak P, Chen K, Tang C. *Phys. Lett. A.*, 147:297-300, 1990.
- [12] Bär M, Eiswirth M. Turbulence due to spiral breakup in continuous excitable media *Phys. Rev. E*. 48 R1635-R1637, 1993.
- [13] Barkley D, Kress M, Turchman S Spiral-wave dynamics in a simple model of excitable media: transition from simple to compound rotation. *Phys. Rev. A.*, 42:2489-2491, 1990.
- [14] Beeler G W, Reuter H. Reconstruction of the action potential of ventricular myocardial fibres. *J. Physiol. (Lond.)*, 268:177-210, 1977.
- [15] Bélair J, Glass L. Self-similarity in periodically forced oscillators. *Phys. Lett. A*, 96:113-116, 1983.
- [16] J. Bélair, L. Glass Universality and self similarity in the bifurcations of circle maps *Physica* 16D, 143-154, 1985.
- [17] Billette J, Janse M J, van Capelle F J L, Anderson R H, Touboul P, Durrer D. Cycle-length-dependent properties of AV nodal activation in rabbit hearts. *Am. J. Physiol.*, 231:1129-1139, 1976.
- [18] Billette J. Atrioventricular nodal activation during premature stimulation of the atrium. *Am. J. Physiol.*, 252:H163-H177, 1987.
- [19] Billette J, Metayer R, St-Vincent M. Selective functional characteristics of rate-induced fatigue in rabbit atrioventricular node. *Circ. Res.*, 68:790-799, 1988.

- [20] Bernstein R C, Frame L H. Ventricular reentry around a fixed barrier: resetting with advancement in an in vitro model. *Circulation*, 81:267-280 1990.
- [21] Boyd C. On the structure of the family of cherry fields on the torus. *Ergod. Th. Dynam. Sys.*, 5:27-36,1985.
- [22] Bonhoeffer T, Grinvald A. Iso-orientation domains in cat visual cortex are arranged in pinwheel-like patterns. *Nature*, 353:429-431, 1991.
- [23] Bressloff P C , Stark J. Neuronal dynamics based on discontinuous circle maps. *Phys. Lett. A*, 150(3,4) 1990.
- [24] Photodiode monitoring with op amps. *Burr-Brown Application Bulletin AB075*, Burr-Brown Corporation, Tuscon, AZ, USA. 1994.
- [25] Brown P, Maxfield B, Moraff H. *Electronics for Neurobiologists*. MIT Press, Boston, USA, 1973.
- [26] Bub G, Glass L. Bifurcations in a discontinuous circle map: A theory for a chaotic cardiac arrhythmia. *Int. J. Bifurc. Chaos*, 5:359-371, 1995.
- [27] Bub G, Glass L, Publicover N G, Shrier A. Bursting calcium rotors in cultured cardiac myocyte monolayers. *Proc. Natl. Acad. Sci. USA*, 95:10283-10287, 1998.
- [28] Cabo C, Pertsov A M, Baxter W T, Davidenko J M, Gray R A, Jalife J. Wave-front curvature as a cause of slow conduction and block in isolated cardiac muscle. *Circ. Res.*, 75:1014-1028, 1994.
- [29] Canavier C C, Clark J W, Byrne J H. Simulation of the bursting activity of neuron R15 in Aplysia: role of ionic currents, calcium balance, and modulatory transmitters. *J. Neurophys.* 66:2107-2124, 1991.
- [30] Carpenter A. Bursting phenomena in excitable membranes. *SIAM J. Appl. Math.*, 36:334-372, 1979.

- [31] Casdagli M. Rotational chaos in dissipative systems. *Physica D*, 29:365-386, 1988.
- [32] Chay T R, Keizer J. A minimal model for membrane oscillations in the pancreatic β cell. *Biophys. J.*, 42: 181-190, 1983.
- [33] Chay T R, Kang H S. Role of single channel stochastic noise on bursting clusters of pancreatic β -cells. *Biophys. J.*, 54:427-435, 1988.
- [34] Chen K, Bak P, Jensen M H. A deterministic critical forest fire model. *Phys. Lett. A.*, 149:207-210, 1990.
- [35] Choi B R, Salama G. Optical mapping of atrioventricular node reveals a conduction barrier between atrial and nodal cells. *Am. J. Physiol.*, 273:H829-H845, 1998.
- [36] Cohen L B, Leshner S. *Optical monitoring of membrane potential: methods of multisite optical measurement*. Optical Methods in Cell Physiology, P. de Weer and B. Salzberg eds., Wiley-Interscience, New York, 1986.
- [37] Cohen A H. Effects of oscillator frequency on phase-locking in the lamprey central pattern generator. *J. Neurosci. Methods*, 21:113-125, 1987.
- [38] Cohen A H, Dobrov T A, Li G, Kiemel T, Baker M T. The development of the Lamprey pattern generator for locomotion. *J. Neurobiol.*, 21:958-969, 1990.
- [39] Cohen J, Fozzard H, Shue S S. Increase in intracellular sodium ion activity during stimulation in mammalian cardiac muscle. *Circ. Res.*, 50:651-662, 1982.
- [40] Colizza D, Guevara M R, Shrier A. A comparative study of collagenase- and trypsin- dissociated embryonic heart cells: reaggregation, electrophysiology, and pharmacology. *Can. J. Physiol. Pharmacol.*, 61:408-419, 1983.
- [41] Cook D L, Satin L S, Hopkins W F. Pancreatic B cells are bursting, but how? *TINS* 14:411-414, 1991.

- [42] Coumel P, Leclercq J F, Slama R. Chapter 50, *Cardiac Electrophysiology and Arrhythmias* eds. Zipes, D. P, Jalife, J. (Grune & Stratton, Orlando), 1985.
- [43] Courtemanche M, Glass L, Rosengarten M D, et. al. Beyond pure parasystole: promises and problems in modelling complex arrhythmias. *Am. J. Physiol.*, 257:693-706, 1989.
- [44] Courtemanche M, Glass L, Belair J, Scagliotti D, Gordon D. A circle map in a human heart. *Physica D*, 40:299-310, 1989.
- [45] Courtemanche M, Glass L, Rosengarten M D. Modelling ventricular parasystole. Mathematical approaches to cardiac arrhythmias *Ann. N.Y. Acad. Sci.*, vol 591 1990.
- [46] Courtemanche M, Winfree A T. Re-entrant rotating waves in a Beeler-Reuter based model of two dimensional cardiac conduction. *Int. J. Bifurc. and Chaos*, 1:431-444, 1991.
- [47] Courtemanche M, Glass L, Keener J P. Instabilities of a propagating pulse in a ring of excitable media. *Phys. Rev. Lett.*, 70:2182-2185, 1993.
- [48] Courtemanche M. Complex spiral wave dynamics in a spatially distributed ionic model of cardiac electrical activity. *Chaos*, 6:579-600, 1996.
- [49] Daniel E E, Bardakjian B L, Huizinga J D, Diamant N E. Relaxation oscillator and core conductor models are needed for understanding of GI electrical activities. *Am. J. Physiol.*, 266:G339-G349, 1994.
- [50] Davidenko J M, Kent P F, Chialvo D R, Michales D C, Jalife J. Sustained vortex-like waves in normal isolated ventricular muscle. *Proc. Natl. Acad. Sci. USA*, 87:8785-8789, 1990.
- [51] Davidenko J M. Spiral wave activity: a possible common mechanism for polymorphic and monomorphic ventricular tachycardias. *J. Cardiovasc. Electrophysiol.*, 4:730-746, 1993.

- [52] Davila H V, Salzberg B M, Cohen L B, Waggoner A S. A large change in axon fluorescence that provides a promising method for measuring membrane potential. *Nature New Biol.*, 241:159-160, 1973.
- [53] Dean P M, Matthews E K. Electrical activity in pancreatic islet cells: effect of ions. *J. Physiol.*, 210:265-275, 1970.
- [54] DeFelice L J, Chalice C E. Anatomical and ultrastructural study of the electrophysiological atrioventricular region of the rabbit. *Circ. Res.*, 24:457-474, 1969.
- [55] DeHaan R L. Regulation of spontaneous activity and growth of embryonic chick heart cells in tissue culture. *Developmental Biol.*, 16:216-249, 1967.
- [56] DeHaan R L, Sachs H G. Cell coupling in developing systems: the heart-cell paradigm. *Curr. Top. Dev. Biol.*, 7:193-228, 1972.
- [57] DeHaan R L, Fozzard H A. Membrane response to current pulses in spheroidal aggregates of embryonic heart cells. *J. Gen. Physiol.*, 65:207-222, 1975.
- [58] Delmar M, Michaels D C, Johnson T, Jalife J. Effects of increasing intercellular resistance on transverse and longitudinal propagation in sheep epicardial muscle. *Circ. Res.*, 60:780-785, 1987.
- [59] De Paola R, Wang H X, Norwood W I. Fractal structure underlying patterns of premature heart beats. *Am. J. Physiol.*, 265:H1603-H1613, 1993.
- [60] Destexhe A, Contreras D, Sejnowski T J, Steriade M. A model of spindle rhythmicity in the isolated thalamic reticular nucleus. *J. Neurophys.*, 72:803-818, 1994.
- [61] Diaz P J, Rudy Y, Plonsey R. Intercalated discs as a cause for discontinuous propagation in cardiac muscle: A theoretical simulation. *Ann. Biomed. Eng.*, 11:177-189, 1983.

- [62] Dillon S, Morad M. A new laser scanning system for measuring action potential propagation in the heart. *Science*, 214:453-456, 1981.
- [63] Dudec F E, Snow R W, Taylor C. Role of electrical interactions in synchronization of epileptiform bursts. *Advances in Neurology*, 44:593-617, 1986.
- [64] De Mello W C. Effect of intracellular injection of calcium and strontium on cell communication in heart. *J. Physiol.*, 250:231-245, 1975.
- [65] DiFrancesco D, Noble D. A model of cardiac electrical activity incorporating ionic pumps and concentration changes. *Phil. Trans. R. Soc. Lond.*, B307:353-376, 1985.
- [66] Ebner T J, Chen G. Use of voltage-sensitive dyes and optical recordings in the central nervous system. *Prog Neurobiol.*, 46:463-506, 1995.
- [67] Eddlestone G T, Goncalves A, Bangham J A, Rojas E. Electrical coupling between cells in Islets of Langerhans in mouse. *J. Memb. Biol.*, 77:1-14, 1984.
- [68] Efimov I R, Fahy G J, Yuanna C, van Wagoner D R, Tchou P J, Mazgalev T N. High-resolution fluorescent imaging does not reveal a distinct atrioventricular nodal anterior input channel (fast pathway) in the rabbit heart during sinus rhythm. *J. Cardiovasc. Electrophysiol.*, 8:295-306, 1997.
- [69] Efimov I R, Mazgalev T N. High-resolution, three dimensional fluorescent imaging reveals multilayer conduction pattern in the atrioventricular node. *Circulation*, 98:54-57, 1998.
- [70] El-Sherif N, Smith A, Evans K. Canine ventricular arrhythmias in the late myocardial infarction period. 8. Epicardial mapping of reentrant circuits. *Circ. Res.*, 49:255-265, 1981.
- [71] Endresen B. Chaos in weakly-coupled pacemaker cells. *J. Theor. Biol.*, 184:41-50, 1997.

- [72] Fabiato A. Fluorescence and differential light absorption recordings with calcium probes and potential-sensitive dyes in skinned cardiac cells. *Can. J. Physiol. Pharmac.*, 60:556-567, 1982.
- [73] Fabiato A. Calcium-induced release of calcium from the sarcoplasmic reticulum. *J. Gen. Physiol.*, 85:247-320, 1985.
- [74] Farber DS, Klee MR. Membrane characteristics of bursting pacemaker neurones in Aplysia. *Nature New Biol.* 240:29-31. 1972.
- [75] Fast V G, Kleber A G. Anisotropic conduction in monolayers of neonatal rat heart cells cultured on collagen substrate. *Circ. Res.*, 75:591-595, 1994.
- [76] Fast V G, Kleber A G. Block of impulse propagation at an abrupt tissue expansion: Evaluation of the critical strand diameter in 2- and 3- dimensional computer models. *Cardiovasc. Res.*, 30:449-459, 1995.
- [77] Fast V G, Darrow B J, Saffitz J E, Kleber A G. Anisotropic activation spread in heart cell monolayers assessed by high-resolution optical mapping. *Circ. Res.*, 79:115-127, 1996.
- [78] Fast V G, Efimov I R. Stability of vortex rotation in an excitable cellular medium. *Physica D*, 49:75-81, 1991.
- [79] Feely O, Chua L. Nonlinear dynamics of a class of analog to digital converters. *Int. J. Bifurc. Chaos*, 2:325-340, 1992.
- [80] Field R J, Koros E, Noyes R M. Oscillations in chemical systems II, Thorough analysis of temporal oscillations in the bromate-cerium-malonic acid system. *J. Am. Chem. Soc.*, 94:8649-8664, 1972.
- [81] Fisch R, Gravner J, Griffeath D. *Statistics and Computing*, 1:23-29, 1991.
- [82] FitzHugh R. Mathematical models of threshold phenomena in the nerve membrane. *Bull. Math. Biophys.*, 17:257-278, 1955.

- [83] FitzHugh R. Pulses and physiological states in theoretical models of nerve membrane. *Biophys. J.*, 1:445, 1961.
- [84] FitzHugh R. *Mathematical models of excitation and propagation in nerve*. ed. H.P. Schwan, Biological Engineering. McGraw-Hill, New York, 1969.
- [85] Fluhler E, Burnham V G, Loew L M. Spectra, membrane binding and potentiometric responses of new charge shift probes. *Biochemistry*, 24:5749-5755, 1985.
- [86] Fowles G. *Introduction to Modern Optics*. Dover Publications, 328 pgs, (1989)
- [87] Fromherz P, Lambacher A., Spectra of voltage sensitive fluorescence of styryl-dye in neuron membrane. *Biochimica et Biophysica Acta*, 1068:149-156, 1991.
- [88] Foerster P, Müller S C, Hess B. Curvature and propagation velocity of chemical waves. *Science*, 241:685-687, 1991.
- [89] Foerster P, Müller S C, Hess B. Critical size and curvature of wave formation in an excitable chemical medium. *Proc. Natl. Acad. Sci. USA.*, 86:6831-6834, 1989.
- [90] Foerster P, Müller S C, Hess B. Curvature and spiral geometry in aggregation patterns of *Dictyostelium discoideum*. *Development*, 109:11-17, 1990.
- [91] Frame L H, Simson M B. Oscillations of conduction, action potential duration, and refractoriness: A mechanism for spontaneous termination of reentrant tachycardias. *Circulation*, 78:1277-1287, 1988.
- [92] Frazier D F, Wolf P D, Wharton J M, Tang A S L, Smith W M, Ideker R E. Mechanism for electrical initiation of reentry in normal canine myocardium. *J. Clin. Invest.*, 83:1039-1047, 1989.
- [93] Gambaudo J M, Glendinning P, Tresser C. The rotation interval as a computable measure of chaos. *Phys. Lett. A*, 105:97-100, 1984.

- [94] Gerhardt M, Schuster H. A cellular automaton describing the formation of spatially ordered structures in chemical systems. *Physica D.*, 36:209-221, 1989.
- [95] Gerhardt M, Schuster H, Tyson J J. A cellular automaton model of excitable media including curvature and dispersion. *Science*, 247:1563-1566 1990.
- [96] Gerhardt M, Schuster H, Tyson J J. cellular automaton model of excitable media II. Curvature, dispersion, rotating waves and meandering waves. *A Phys. D*, 46:392-415, 1990.
- [97] Gerhardt M, Schuster H, Tyson J J. A cellular automaton model of excitable media III. Fitting the Belousov-Zhaboinski reaction. *Phys. D*, 46:416-426, 1990.
- [98] Gerisch, G. Chapter 6. in *Current Topics in Developmental Biology, Vol. 3*, eds. Moscona, A. Monroy, A. (Academic Press, New York), 1986.
- [99] Girouard S D, Laurita K R, Rosenbaum D S. Unique properties of cardiac action potentials recorded with voltage-sensitive dyes. *J. Cardiovasc. Electrophysiol.*, 7:1024-1038, 1996.
- [100] Girouard S D, Pastore J M, Laurita K R, Gregory K W, Rosenbaum D S. Optical mapping in a new guinea pig model of ventricular tachycardia reveals mechanisms for multiple wavelengths in a single reentrant circuit. *Circulation*, 93:603-613, 1996.B
- [101] Glass L, Goldberger A, Belair J. Dynamics of pure parasystole. *Am. J. Physiol.*, 251:H941-H847, 1986.
- [102] Glass L, Mackey M C. *From Clocks to Chaos: The Rhythms of Life*. Princeton U.P, Princeton NJ, 1988.
- [103] Glass L, Zeng W Z. Complex bifurcations and chaos in simple theoretical models of cardiac oscillations. *Mathematical Approaches to Cardiac Arrhythmias, Ann. N. Y. Acad. Sci.*, 591:316-327, 1990.

- [104] Glass L, Josephson M E. Resetting and annihilation of reentrant abnormally rapid heart beat. *Phys. Rev. Lett.*, 2059-2063, 1995.
- [105] Gonzalez C, Rodriguez M. A flexible perforated microelectrode array probe for action potential recording in nerve and muscle tissues. *J. Neurosci. Meth.*, 72:189-195, 1997.
- [106] Gorelova N A, Bures J. Spiral waves of spreading depression in the isolated chicken retina. *J. Neurobiol.*, 14:353-363, 1983.
- [107] Graham M D, Kevrekidis I G, Asakura K, Lauterbach J, Krischer K, Rotermund H H, Ertl G. Effects of boundaries on pattern formation: Catalytic oxidation of CO on platinum. *Science*, 264:80-82, 1994.
- [108] Greenberg J M, Hastings S P. Pattern formation and periodic structures in systems modeled by reaction diffusion equations. *Bull. Amer. Math. Soc.*, 6:84-92, 1978.
- [109] Greenberg J M, Hassard B, Hastings S P. Spatial patterns for discrete models of diffusion in excitable cells. *SIAM J. Appl. Math.*, 34:515-523, 1978.
- [110] Grinvald A. Real-time optical mapping of neuronal activity from single growth cones to the intact mammalian brain. *Ann. Rev. Neurosci.*, 8:263-305, 1985.
- [111] Grinvald A, Bonhoeffer T, Malenk D, Shoham D, Bartfield E, Arieli A, Hildesheim R, Ratzlaff E. *Optical imaging of architecture and function in the living brain. in Memory: Organization and Locus of Change.* editors Squire L R, Weinberger N M, Lynch G, McGaugh J L Oxford University Press, 1991.
- [112] Grinvald A, Frostig R D, Lieke E, Hildesheim R. Optical imaging of neuronal activity. *Physiol. Rev.*, 68:1285-1366, 1988.
- [113] Guckenhiemer J, Holmes P. *Nonlinear Oscillations, Dynamical Systems, and Bifurcations of Vector Fields.*, Springer-Verlag, New York, 1983.

- [114] Guevara M R, Glass L, Shrier A. Phase locking, period-doubling bifurcations, and irregular dynamics in periodically stimulated cardiac cells. *Science*, 214:1350-1353, 1981.
- [115] Guevara M R, Glass L. Phase locking, period doubling bifurcations, and chaos in a mathematical model of a periodically driven oscillator: a theory for the entrainment of biological oscillators and the generation of cardiac dysrhythmias. *J. Math. Biol.*, 15:339-349, 1982.
- [116] Hao B.-L. *Elementary Symbolic Dynamics and Chaos in Dissipative Systems*. World Scientific, Singapore, 1989.
- [117] Harrison L, Ideker R E, Smith W M, Klein G J, Kasell J, Wallace A G, Gallagher J J. The sock electrode array: a tool for determining global epicardial activation during unstable arrhythmias. *Pacing Clin. Electrophysiol.*, 3:531-540, 1980.
- [118] He Y, Chi R, He N. Lyapunov exponents of the circle map in human hearts. *Phys. Lett. A.*, 170:29-32, 1992.
- [119] M. R. Herman in *Geometry and Topology*, edited by J. Palis, Lecture Notes in Mathematics Vol 597.
- [120] Hodgkin A L, Huxley A F. A quantitative description of membrane currents and its application to conduction and excitation in nerve. *J. Physiol.*, (Lond.) 117:500-544, 1952.
- [121] Hoffman B F, Cranefield P F. *Electrophysiology of the Heart*. New York, McGraw-Hill, 1960.
- [122] Honerkamp J, Mutschler G, Seitz R. Coupling of a slow and a fast oscillator can generate bursting. *Bull. Math. Biol.*, 47:1-21, 1985.
- [123] Horowitz P, Hill W. *The art of electronics*. Cambridge University Press, 1989.

- [124] Ideker RE, Smith WM, Blanchard SM, Reiser SL, Simpson EV, Wolf PD, Danieleley ND. The assumptions of isochronal cardiac mapping. *Pacing Clin. Electrophysiol.*, 12:456-478, 1989.
- [125] Ikeda N, Yoshizawa S, Sato T. Difference equation model of ventricular parasystole as an interaction between cardiac pacemakers based on the phase response curve. *J. theor. Biol.*, 103:439-465, 1983.
- [126] Ikeda T, Uchida T, Hough D, Lee J J, Fishbein M C, Mandel W J, Chen P S, Karagueuzian H S. Mechanism for spontaneous termination of functional reentry in isolated canine right atrium. *Circulation*, 94:1962-1973 1996.
- [127] Israel D A, Barrey W, Edell D, Mark R. An array of microelectrodes to stimulate and record from cardiac cells in culture. *Am. J. Physiol.*, 247:H669-H674, 1984.
- [128] Israel D A, Edell D J, Mark R G. Time delays in propagation of cardiac action potentials. *Am. J. Physiol.*, 258:H1906-H1917, 1990.
- [129] Ito H, Glass L. Spiral breakup in a new model of discrete excitable media. *Phys. Rev. Lett.*, 66:671-674, 1991.
- [130] Ito H. Mesoscopic modeling of wave propagation in excitable media. *Physica D.*, 79:16-40, 1994.
- [131] Jacklet J, Barnes S, Bulloch A, Lukowiak K, Syed N Rhythmic activities of isolated and clustered pacemaker neurons and photoreceptors of *Aplasia* retina in culture. *J. Neurobiol.*, 31:16-28, 1996.
- [132] Jackman W M, Beckman K J, McClelland J H , Wang X, Friday K J, Roman C A, Moulton K P, Twidale N, Hazlitt H A, Prior M I et al. Treatment of supraventricular tachycardia due to atrioventricular nodal reentry, by radiofrequency catheter ablation of slow-pathway conduction. *N. Engl. J. Med.*, 327:313-318, 1992.

- [133] Jalife J, Moe G J. Excitation, conduction and reflection of impulses in isolated bovine and canine cardiac fibers. *Circ. Res.*, 49:233-247, 1981.
- [134] Jalife J, Antzelevitch C, Moe G. The case for modulated parasystole. *PACE* 5:911-926, 1982.
- [135] Janse M J, Kleber A G, Capucci A. Electrophysiological basis for arrhythmias caused by acute ischemia. *J. Mol. Cell Cardiol.*, 18:339-355, 1986.
- [136] Janse M J, McGuire M A, Loh P, Thibault B, Hocini M, de Bakker J M. Electrophysiology of the A-V node in relation to A-V nodal reentry. *Jpn. Heart J.*, 37:785-791, 1996.
- [137] Jensen M H, Bak P, Bohr T. Complete devils staircase, fractal dimension, and universality of mode-locking structure in the circle map. *Phys. Rev. Lett.*, 50:1637-1639, 1983.
- [138] Jongsma H J. Interactions between neonatal rat heart cells in tissue culture. *J. Physiol. (Paris)*. 65:Suppl:327A 1972.
- [139] Joyner R W, Veenstra R, Rawling D, Chorro A. Propagation through electrically coupled cells: Effects of a resistive barrier. *Biophys. J.*, 45:1017-1025, 1984.
- [140] Kaneko K. Pattern dynamics and spatiotemporal chaos. Pattern selection, diffusion of defect and pattern competition intermittency. *Physica D.*, 34:1-41, 1989.
- [141] Kaneko K. Overview of coupled map lattices. *Chaos*, 2:279-282, 1992.
- [142] Karma A. Spiral breakup in model equations of action potential propagation in cardiac tissue. *Phys. Rev. Lett.*, 71:1103-1106, 1993.
- [143] Keener J P, Chaotic behavior in piecewise continuous difference equations. *Trans. Amer. Math. Soc.*, 261:589-603, 1980.

- [144] Keener J P, Glass L. Global bifurcations of a periodically forced oscillator *J. Math. Biol.*, 21:175-190, 1984.
- [145] Keizer J, Smolen P. Bursting electrical activity in pancreatic β -cells caused by Ca^{2+} and voltage inactivated Ca^{2+} channels. *Proc. Natl. Acad. Sci. USA* 88:3897-3901, 1991.
- [146] Keener J P. Chaotic behaviour in piecewise continuous difference equations. *Trans. Amer. Math. Soc.*, 261:589-603, 1980.
- [147] Keener J P, Tyson J J. Spiral waves in the Belusov-Zhabotinskii reaction. *Physica D*. 21:269-324, 1986.
- [148] Keener J P. Propagation and its failure in coupled systems of discrete excitable cells. *SIAM J. Appl. Math.*, 47:556-572, 1987.
- [149] Keener J P. The dynamics of three-dimensional scroll waves in excitable media. *Physica D*, 31:269-276, 1988.
- [150] Keener J P. *Wave propagation in myocardium*. Theory of Heart: Biomechanics, Biophysics, and Nonlinear Dynamics of Cardiac Function. eds. L Glass, P Hunter and A McCulloch. Springer-Verlag New York, 1991.
- [151] Kimura H, Oyamada Y, Ohshika H, Mori M, Oyamada M. Reversible inhibition of gap junctional intercellular communication, synchronous contraction, and synchronism of intracellular Ca^{2+} fluctuation in cultured neonatal rat cardiac myocytes by heptanol. *Exp. Cell Res.*, 220:348-356, 1995.
- [152] Knisley S B, Hill B C. Effects of bipolar point and line stimulation in anisotropic rabbit epicardium: assessment of the critical radius of curvature for longitudinal block. *IEEE Trans. Biomed. Eng.*, 42:957-966, 1995.
- [153] Kleber A G. Mechanisms of ventricular arrhythmias: A perspective. *J. Cardiovasc. Pharmacol.*, 17:S1-S8, 1991.

- [154] Kleber A G, Janse M J, Wilms-Schopman F J G, Wilde A A M, Coronel R. Changes in conduction velocity during acute ischemia in ventricular myocardium of the isolated porcine heart. *Circulation*, 73:189-198, 1986.
- [155] Kleber A G, Riegger C B, Janse M J. Electrical uncoupling and increase of extracellular resistance after induction of ischemia in isolated, arterially perfused rabbit papillary muscle. *Circ. Res.*, 61:271-279, 1987.
- [156] Fast V G, Kleber A G. Role of wavefront curvature in propagation of cardiac impulse. *Cardiovasc. Res.*, 33:258-271, 1997.
- [157] Koidl B, Tritthart H A, Erkingen S. The effects of ouabain on the electrical and mechanical activities of embryonic chick heart cells in culture. *J. Molec. Cell. Cardiol.*, 12:165-178, 1980.
- [158] Kopell N, Ermentrout G B. Symmetry and phaselocking in chains of weakly coupled oscillators. *Commun. Pure. Appl. Math.*, 39:623-660, 1986.
- [159] Kreisman NR, LaManna JC, Liao SC, Yeh ER, Alcala JR. Light transmittance as an index of cell volume in hippocampal slices: optical differences of interfaced and submerged positions. *Brain Res.*, 25:179-186, 1995.
- [160] Krinsky V I. Systems Theory Research (translation of Problems in Cybernetics) *Problem. Kibern.*, 20:59-80, 1968.
- [161] Kopell N, Howard L N. Target patterns and spiral solutions to reaction-diffusion equations with more than one space dimension. *Adv. Appl. Math.*, 2:417-449, 1981.
- [162] Kukuljan M, Goncalves A, Atwater I. Charybdotoxin-sensitive K-Ca channel is not involved in glucose-induced electrical activity of pancreatic β cells. *J. Memb. Biol.*, 119:187-195, 1991.

- [163] Kunysz A, Glass L, A. Overdrive suppression of spontaneously beating chick heart cell aggregates: experiment and theory. *Am. J. Physiol.*, 269:H1153-H1164, 1995.
- [164] Kunysz A, Shrier A, Glass L. Bursting behaviour during fixed delay stimulation of spontaneously beating chick heart cell aggregates. *Am. J. Physiol.*, 42:C331-C346, 1997.
- [165] Kurrer C, Schulten K. *Propagation of chemical waves in discrete excitable media: anisotropic and isotropic wave fronts*. Nonlinear Wave Processes in Excitable Media, eds. Holden A V, Markus M, Othmar H G. Plenum Press, New York, 489-500, 1991.
- [166] Lasota A, Yorke J A. On the existence of invariant measures for piecewise monotonic transformations. *Trans. Amer. Math. Soc.* 186:481-488, 1973.
- [167] Lasota A, Mackey M C. Chaos, Fractals and Noise: Stochastic Aspects of Dynamics. in *Applied Mathematical Sciences* 97, Springer Verlag, New York, 1994.
- [168] Laurita K R, Girouard S D, Rosenbaum D S. Modulation of ventricular repolarization by a premature stimulus. Role of epicardial dispersion of repolarization kinetics demonstrated by optical mapping of the intact guinea pig heart. *Circ. Res.*, 79:493-503, 1996.
- [169] Lechleiter J, Girard S, Peralta E, Clapham D. Spiral calcium wave propagation and annihilation in *Xenopus laevis* oocytes. *Science*, 252:123-126, 1991.
- [170] Leon L J, Roberge F A, Vinet A. Simulation of two-dimensional anisotropic cardiac reentry: Effects of wavelength on the reentry characteristics. *Ann. Biomed. Eng.*, 22:592-609, 1994.
- [171] Levy M N, Kerin N, Eisenstein I. A subvariant of concealed bigeminy. *J. Electrocardiol.*, 10:225-32, 1977.

- [172] Lewis T, Masters A M. Observations upon conduction in the mammalian heart. A-V conduction. *Heart*, 12:209-269, 1925.
- [173] Lieberman M, Roggeveen A, Purdy J E, Johnson E A. Synthetic strands of cardiac muscle: growth and physiological implication. *Science*, 175:909-911, 1972.
- [174] Lieberman M, Horres C R, Shigeto N, Ebihara L, Aiton J F, Johnson E A. Cardiac muscle with controlled geometry: application to electrophysiological and ion transport studies. Nelson P G, Lieberman M, eds. *Excitable Cells in Tissue Culture*. Plenum, New York, 1981.
- [175] Lipp P, Niggli E. Modulation of Ca^{2+} release in cultured neonatal rat cardiac myocytes. Insight from subcellular release patterns revealed by confocal microscopy. *Circ. Res.*, 74:979-990, 1994.
- [176] Lipson M J, Naimi S. Multifocal atrial tachycardia: Clinical associations and significance. *Circulation*, 67:397-407, 1970.
- [177] Lloyd D. Circadian and ultradian clock-controlled rhythms in unicellular microorganisms. *Adv. Microb. Physiol.*, 39:291-338, 1998.
- [178] Lorenz E N. *Noisy periodicity and reverse bifurcations*. in Nonlinear Dynamics, Vol 357 of the Annals of the New York Academy of Sciences, 1980.
- [179] Momose-Sato Y, Sato K, Hirota A, Kamino K. GABA-Induced intrinsic light-scattering changes associated with voltage-sensitive dye signals in embryonic brain stem slices: coupling of depolarization and cell shrinkage. *Neurophysiol.*, 79:2208-2217, 1998.
- [180] Marban E, Kitikaze M, Koretsune Y, Yue D T, Chacks T, Pike M M. Quantification of $[\text{Ca}^{2+}]_i$ in perfused hearts; Evaluation of the 5F-BAPTA/NMR method as applied to the study of ischemia and reperfusion. *Circ. Res.*, 66:1255-1287, 1990.

- [181] Marcus M, Hess B. Isotropic cellular automaton for modelling excitable media. *Science*, 347:56-58, 1990.
- [182] McClintock M K. Menstrual synchrony and suppression. *Nature*, 229:244-246, 1971.
- [183] Martiel J L, Goldbeter A. A model based on receptor desensitization for cyclic AMP signaling in *Dictyostelium* cells. *Biophys. J.*, 52:807-828, 1987.
- [184] Mears D, Sheppard N F, Atwater I, Rojas E. Magnitude and modulation of pancreatic beta-cell gap junction electrical conductance in situ. *J. Memb. Biol.*, 146:163-176, 1995.
- [185] Meijler F L, Janse M J. Morphology and electrophysiology of the mammalian atrioventricular node. *Physiol. Rev.*, 68:608-647, 1988.
- [186] Meijler F L, Fisch C. Does the atrioventricular node conduct? *Br. Heart J.*, 61:309-315, 1989.
- [187] Mendez C, Moe G K. Demonstration of a dual A-V nodal conduction system in the isolated rabbit heart. *Circ. Res.*, 19:378-393, 1966.
- [188] Mercader M A, Michaels D C, Jalife J. *Reentrant activity in the form of spiral waves in mathematical models of the sinoatrial node*. Cardiac Electrophysiology: From Cell to Bedside, 2nd Edition. eds. Zipes D P, Jalife J., W. B Saunders, Philadelphia PA, 1995.
- [189] Minamikawa T, Cody S H, Williams D A. In situ visualization of spontaneous calcium waves within perfused rat heart by confocal imaging. *Am. J. Physiol.*, 272:H236-H234, 1997.
- [190] Mines G R, On the dynamic equilibrium of the heart. *J. Physiol. (Lond.)*, 46:349-383, 1913.
- [191] Mironov S L. Theoretical model of slow-wave membrane potential oscillations in molluscan neurons. *Neuroscience*, 10:899-905, 1983.

- [192] Misgeld U, Swandulla D. Development of spontaneous synaptic activity in a hypothalamic network grown in culture. *J. Basic Clin. Physiol. Pharmacol.*, 1:57-63, 1990.
- [193] Moe G K, Preston J B, Burlington H. Physiological evidence for a dual A-V transmission system. *Circ. Res.*, 4:357-375, 1956.
- [194] Moe G K, Rheinbolt W C, Abildskov J A A computer model of atrial fibrillation. *Am. Heart. J.*, 67:200-220, 1964.
- [195] Moe G K, Jalife J, Mueller W J, Moe B. A mathematical model of parasystole and its application to clinical arrhythmias. *Circulation*, 56:968-979, 1977.
- [196] Morad M, Dillon S, Weiss X. *An acousto-optically steered laser scanning system for measurment of action potential spread in intact heart.* in Optical Methods in Cell Physiology, eds. De Weer P and Salzberg B M, 1986.
- [197] Morad M, Trautwein W. The effect of duration of the action potential on contraction in the mammalian heart tissue. *Pflugers Arch. ges. Physiol.*, 299:66-82, 1969.
- [198] Müller T H, Misgeld U, Swandulla D. Ionic currents in cultured rat hypothalamic neurons. *J. Physiol. (Lond.)*, 450:341-362, 1991.
- [199] Munk A A, Adjemian R A, Zhao J, Ogbaghebriel A, Shrier A. Electrophysiological properties of morphologically distinct cells isolated from the rabbit atrioventricular node. *J. Physiol.* 493:801-18, 1996.
- [200] Munk A A, Bub G, Petrecca K, Shrier A. Imaging the spread of excitation on the atrioventricular node of the rabbit heart. *Noble Symposium*. 1996.
- [201] von Neuman J. Theory of self-reproducing automata. *University of Illinois Press.*, Urbana, 1966.
- [202] Nagumo J, Yoshizawa S, Arimoto S. *IEEE Trans. Commun. Technol.*, 12:400-, 1965.

- [203] Nakagawa N, Kuramoto Y. From collective oscillations to collective chaos in a globally coupled oscillator system. *Physica D*, 75:74-80, 1994.
- [204] Nakamura Y, Tominaga F, Munakata T. Clustering behavior in time-delayed nearest neighbor coupled oscillators. *Phys. Rev. E.*, 49:4849-4856, 1994.
- [205] Nilsson G, Ahlfeldt H, Ahren T, Jonasson T. Distribution patterns of ventricular premature complexes in long-term electrocardiographic recordings and their usefulness in disclosing modulated parasystole. *Am. J. Cardiol.*, 68:1045-1048, 1991
- [206] Noma A, Tsuboi A N. Dependence of junctional conductance on proton, calcium and magnesium ions in cardiac paired cells. *J. Physiol.*, 382:193-211, 1987.
- [207] Paes de Carvalho A, De Almeida D F. Spread of activity through the atrioventricular node. *Circ. Res.*, 8:801-809, 1960.
- [208] Palti Y, Ben David G, Lachov E, Mika Y H, Omri G, Schatzberger R. Islets of Langerhans generate wavelike electrical activity modulated by glucose concentration. *Diabetes*, 45:595-601 1996.
- [209] Petrecca K, Amellal F, Laird D W, Cohen S A, Shrier A. Sodium channel distribution within the rabbit atrioventricular node as analysed by confocal microscopy. *J. Physiol.*, 501:263-74, 1997.
- [210] Pieper CF, Parsons D, Lawrie GM, Lacy J, Roberts R, Pacifico A Design and implementation of a new computerized system for intraoperative cardiac mapping. *J. Appl. Physiol.*, 71:1529-1539 1991.
- [211] Plant R E, Kim M. On the mechanism underlying bursting in the Aplasia abdominal ganglion R-15 cell. *Math. Biosci.*, 26:357-375, 1975.

- [212] Plant R E, Kim M. Mathematical description of a bursting pacemaker neuron by modification of the Hodgkin-Huxley equations. *Biophys. J.*, 16:227-244, 1976.
- [213] Prystowsky EN. Atrioventricular node reentry: physiology and radiofrequency ablation. *Pacing Clin. Electrophysiol.*, 20:552-571, 1997.
- [214] Oberholzer M, Ostreicher M, Christen H, Bruhmann M. Methods in quantitative image analysis. *Histochem. Cell Biol.*, 105:333-355, 1996.
- [215] Orbach H S, Cohen L B. Optical monitoring of activity from many areas of the in vitro and in vivo salamander olfactory bulb: a new method for studying functional organization in the vertebrate central nervous system. *J. Neurosci.*, 3:2251-2262, 1983.
- [216] Onimaru H, Arata A, Homma I. Neuronal mechanisms of respiratory rhythm generation. An approach using *in vitro* preparation. *Jpn. J. Physiol.*, 47:385-403, 1997.
- [217] Palsson E, Cox E C. Origin and evolution of circular waves and spirals in *Dictyostelium discoideum* territories. *Proc. Natl. Acad. Sci. USA.*, 93:1151-1155, 1996.
- [218] Panfilov A V, Holden A V. Self-generation of turbulent vortices in a two-dimensional model of cardiac tissue. *Phys. Lett. A.*, 151:23-26, 1990.
- [219] Panfilov A V, Holden A V. Computer simulation of re-entry sources in myocardium in two and three dimensions. *J. Theor. Biol.*, 161:271-285, 1993.
- [220] Panfilov A V, Hogeweg P. Spiral breakup in a modified FitzHugh-Nagumo model. *Phys. Lett. A.*, 176:295-299, 1993.
- [221] Panfilov A V, Vasiev B N. Vortex initiation in a heterogeneous excitable medium. *Physica D*, 49:107-113, 1991.

- [222] Pertsov A M, Ermakova E A. Mechanism of drift of a spiral wave in an inhomogeneous medium. *Biofizika*, 33:338-342, 1988.
- [223] Pizarro G, Cleemann L, Morad M. Optical measurement of voltage-dependent Ca^{2+} influx in frog heart. *Proc. Natl. Acad. Sci. USA.*, 82:1864-1868, 1985.
- [224] Pritchett E L C, McCarthy E A, Lee K L, Wilkinson W E. *Cardiac Electrophysiology: From Cell to Bedside*, 703-707, eds. D. P. Zipes, J. Jalife, Philadelphia, W. B. Saunders Co., 1990.
- [225] Provatas N, Mackey M C. Asymptotic periodicity and banded chaos. *Physica D* 53:295-318, 1991.
- [226] Publicover N. Calcium oscillations in freshly dispersed and cultured interstitial cells from canine colon. *Am. J. Physiol.*, 262:C589-C597, 1992.
- [227] Quan W, Rudy Y. Unidirectional block and reentry of cardiac excitation: A model study *Circ. Res.*, 66:367-382, 1990.
- [228] Ratzlaff E H, Grinvald A. A tandem-lens epifluorescence macroscope: hundred-fold brightness advantage for wide-field imaging. *J. Neurosci. Meth.*, 36:127-137, 1991.
- [229] Rhodes F, Thompson C L. Topologies and rotation numbers for families of monotone functions of the circle. *J. London Math. Soc.* 43:156-170, 1991.
- [230] Rhor S, Scholly D M, Kleber A G. Patterned growth of neonatal rat heart cells in culture: Morphological and electrophysiological characterization. *Circ. Res.* 68:114-130, 1991.
- [231] Rhor S, Salzberg B M. Characterization of impulse propagation at the microscopic level across geometrically defined expansions of excitable tissue: multiple site recording of transmembrane voltage (MSORTV) in patterned growth heart cell cultures. *J. Gen. Physiol.*, 104:287-309, 1994.

- [232] Rhor S, Kucera J P, Kleber A G. Slow conduction in cardiac tissue, I: Effects of reduction of excitability versus a reduction of electrical coupling on microconduction. *Circ. Res.*, 83:781-794, 1998.
- [233] Rinzel J, Lee Y S. Dissection of a model for neural parabolic bursting. *J. Math. Biol.*, 25m:653-675, 1987.
- [234] Roberge F A, Vinet A, Victorri B. Reconstruction of propagated electrical activity with a two-dimensional model of anisotropic heart muscle. *Circ. Res.*, 58:461-475, 1986.
- [235] Rook M B, de Jonge B, Jongsma H J, Masson-Pevet M A. Gap junction formation and functional interaction between neonatal rat cardiocytes in culture: a correlative physiological and ultrastructural study. *J. Memb. Biol.*, 118:179-92, 1990.
- [236] Rosario L M, Barbosa R M, Antunes C M, Silva A M, Abrunhosa A J, Santos R M. Bursting electrical activity in pancreatic β cells: evidence that the channel underlying the burst is sensitive to Ca^{2+} influx through L-type Ca^{2+} channels. *Pfluegers Arch.*, 424:439-447, 1993.
- [237] Rosenbaum D S, Kaplan D T, Kanai A, Jackson L, Garan H, Cohen R J, Salama G. Repolarization inhomogeneities in ventricular myocardium change dynamically with abrupt cycle length shortening. *Circulation*, 84:1333-1345, 1991.
- [238] Rudy Y, Quan W. A model study of the effects of the discrete cellular structure on electrical propagation in cardiac tissue. *Circ. Res.*, 61:815-823, 1987.
- [239] Salama G, Morad M. Merocyanine 540 as an optical probe of transmembrane electrical activity in the heart. *Science*, 191:485-487, 1976.
- [240] Salama G, Lombardi R, Elson J. Maps of optical action potentials and NADH fluorescence in intact working hearts. *Am. J. Physiol.*, 252:H384-394, 1987.

- [241] Salzberg B M, Grinvald A, Cohen L B, Davila H, Ross W N. Optical recording of neuronal activity in an invertebrate central nervous system: simultaneous monitoring of several neurons. *J. Neurophysiol.*, 40:1281-1291, 1977.
- [242] Salzberg B M, Davila H V, Cohen L B. Optical records of impulses in individual neurons of an invertebrate central nervous system. *Nature*, 246:508-509, 1973.
- [243] Sano T, Takayama N, Shimamoto T. Directional difference in conduction velocity in cardiac ventricular syncytium studied by microelectrodes. *Circ. Res.*, 7:262-267, 1959.
- [244] Satin L, Cook D. Calcium current inactivation in insulin-secreting cells is mediated by calcium influx and membrane depolarization. *Pfluegers Arch.*, 418:417-422, 1989.
- [245] Saxberg B E H, Cohen R J. *Cellular automata models of cardiac conduction*. in Theory of Heart: Biomechanics, Biophysics, and Nonlinear Dynamics of Cardiac Function. eds. L Glass, P Hunter and A McCulloch, Springer-Verlag New York, 1991.
- [246] Schaffer P, Ahammer H, Müller W, Koidl B, Windisch H Di-4-ANEPPS causes photodynamic damage to isolated cardiomyocytes. *Pflugers Arch.*, 426:548-551, 1994.
- [247] Schamroth L, Mariott H J L. Intermittent ventricular parasystole with observations on its relationship to extrasystolic bigeminy. *Am. J. Cardiol.*, 7:99-809, 1961.
- [248] Schamroth L, Martin D H, Pachter M. The extrasystolic mechanism as the entrainment of an oscillator. *Am. Heart J.*, 115:1363 - 1368, 1988.
- [249] Schoels W, Gough W B, Restivo M, El-Sherif, N. Circus movement atrial flutter in the canine sterile pericarditis model. Activation patterns during initiation, termination, and sustained reentry in vivo. *Circ. Res.*, 67:35-50, 1990.

- [250] Selverston A I, Moulins M. Oscillatory neural networks. *Ann. Rec. Physiol.*, 47:29-48 1985.
- [251] Sherman A, Rinzel J, Keizer J. Emergence of organized bursting in clusters of pancreatic β cells by channel sharing. *Biophys. J.*, 54:411-425, 1988.
- [252] Sherman A. Contributions of modeling to understanding stimulus-secretion coupling in pancreatic β cells. *Am. J. Physiol.*, 271:E362-E372, 1996.
- [253] Shibata J, Bures J. Optimum topographical conditions for reverberating cortical spreading depression in rats. *J. Neurobiol.*, 5:107-118, 1974.
- [254] Smith P A, Ashcroft F M, Rorsman P Simultaneous recordings of glucose dependent electrical activity and ATP-regulated K^+ - currents in isolated mouse pancreatic β cells. *FEBS Lett.*, 261:187-190, 1990.
- [255] Smolen P, Keizer J. Slow voltage inactivation of Ca^{2+} currents and bursting mechanisms for the mouse pancreatic β cell. *J. Memb. Biol.*, 127:9-19, 1992.
- [256] Smolen P, Rinzel J, Sherman A. Why pancreatic islets burst but single β cells do not: the heterogeneity hypothesis. *Biophys. J.*, 64:1668-1680, 1993.
- [257] Sole R V, Vallis J Spiral waves, chaos and multiple attractors in lattices models of interacting populations. *Phys. Lett. A*, 166:123-128, 1992.
- [258] Spach M A, Dolber P C, Chapter 50, in *Cardiac Electrophysiology and Arrhythmias* eds. Zipes, D. P, Jalife, J. (Grune & Stratton, Orlando), p 241, 1985.
- [259] Spach M S, Miller W T, Geselowitz D B, Barr R C, Kootsey J M, Johnson E A. The discontinuous nature of propagation in normal canine cardiac muscle. *Circ. Res.*, 48:39-54, 1981.
- [260] Spach M S, Heidlage J F. The stochastic nature of cardiac propagation at a microscopic level: electrical description of myocardial architecture and its application to conduction. *Circ. Res.*, 76:366-380, 1995.

- [261] Spring K R. Detectors for fluorescent microscopy. *Scanning Microsc.*, 5:63-69, 1991.
- [262] Starobin J M, Zilbeiter Y I, Rusnak E M, Starmer C F. Wavelet formation in excitable cardiac tissue: the role of wavefront-obstacle interactions in initiating high-frequency fibrillatory-like arrhythmias. *Biophys. J.*, 70:581-594, 1996.
- [263] Strogatz S H, Mirollo R E. Collective synchronization in lattices of non-linear oscillators with randomness. *J. Phys. A: Math. Gen.*, 21:L699-L705, 1988.
- [264] Strogatz S H, Stewart I. Coupled oscillators and biological synchronization. *Scientific American*, 269:102-109, 1993.
- [265] Sung RJ, Lauer MR, Chun H Atrioventricular node reentry: current concepts and new perspectives. *Pacing Clin. Electrophysiol.*, 17:1413-1430, 1994.
- [266] Tasaki I, Watanabe A, Sandlin R, Carnay L. Changes in fluorescence, turbidity, and birefringence associated with nerve excitation. *Proc. Natl. Acad. Sci. USA.*, 61:883-888, 1968.
- [267] Tawara S. *Das Reizleitungs System des herzens*. Jena, Germany: Fischer, 1906.
- [268] Tsay T, Inman R, Wray B, Herman B, Jacobson K. *Characterization of low light level video cameras for fluorescence microscopy*. Optical Microscopy for Biology, eds. Herman B, Jacobson K, Wiley-Liss, New York, 219-233. 1990.
- [269] Tyson J J, Keener J P. Singular perturbation theory of travelling waves in excitable media (a review). *Physica D*, 32:327-361, 1988.
- [270] Valaskovic G A, Morrison G H. Quantitative imaging ion microscopy: a short review. *Scanning Microsc.*, 6:305-318, 1992.
- [271] Vasalle M. The relationship among cardiac pacemakers: Overdrive suppression. *Circ. Res.*, 41:269-277, 1977.

- [272] Vinet A, Roberge F A. The dynamics of sustained reentry in a ring model of cardiac tissue. *Ann. Biomed. Eng.*, 22:568-591, 1994.
- [273] Wang H X, de Paola R, Norwood W I, Dynamics underlying the patterning of cardiac dysrhythmias. *Phys. Rev. Lett.*, 70:3671-3674, 1993.
- [274] Wang X -J, Rinzel J. in *The Handbook of Brain Theory and Neural Networks* ed. Arbib, M. A., MIT Press, Cambridge MA, 686-691, 1995.
- [275] Weimar J, Tyson J J, Watson L T. Diffusion and wave propagation in cellular automaton models of excitable media. *Physica D.*, 55:309-327, 1992.
- [276] Weiss J, Cabeen W R Jr, Roberts N K. Nodoventricular accessory atrioventricular connection associated with dual atrioventricular pathways: a case report and review of the literature. *J. Electrocardiol.*, 14:185-190, 1981.
- [277] Wiener N, Rosenblueth A. The mathematical formulation of the problem of conduction of impulses in a network of connected excitable elements, specifically in cardiac muscle. *Arch. Inst. Cardiol. Mex.*, 16:205-265, 1946.
- [278] Wilders R, Jongsma H, Ginneken A. Pacemaker activity of the rabbit sinoatrial node. A comparison of mathematical models. *Biophys. J.*, 60:1202-1215, 1991.
- [279] Williams T L, Sigvart K A, Kopell N, Ermentrout G B, Remyer M P. Forcing of coupled nonlinear oscillators: studies of intersegmental coordination in the lamprey locomotor central pattern generator. *J. Neurophysiol.*, 64:862-871, 1990.
- [280] Willows A O D. Behavioral acts elicited by stimulation of single, identifiable brain cells. *Science*, 157:570-574, 1967.
- [281] Wilson W A, Wachtel H. Negative resistance characteristics essential for the maintenance of slow oscillations in bursting neurons. *Science*, 186:932-934, 1974.

- [282] Windisch H, Ahammer H, Schaffer P, Müller W, Platzter D. Optical multisite monitoring of cell excitation phenomena in isolated cardiomyocytes. *Pflügers Arch.*, 430:508-518, 1995.
- [283] Winfree A T. An integrated view of the resetting of a circadian clock. *J. Theor. Biol.*, 28:327-352, 1970.
- [284] Winfree A T. Spiral waves of activity. *Science*, 175:634-636, 1972.
- [285] Winfree A T. Scroll-shaped waves of chemical activity in three dimensions. *Science*, 181:937-939, 1973.
- [286] Winfree A T, Strogatz S H. Singular filaments organize chemical waves in three dimensions. I. Geometrically simple waves. *Physica D*, 8:35-49, 1983.
- [287] Winfree A T. *When Time Breaks Down: The Three-Dimensional Dynamics of Electrochemical Waves and Cardiac Arrhythmias*, Princeton University Press, Princeton, NJ, 1987.
- [288] Winfree A T. Electrical instability in cardiac muscle: Phase singularities and rotors. *J. Theor. Biol.*, 138:353-405, 1989.
- [289] Winfree A T. Varieties of spiral wave behavior: an experimentalists approach to the theory of excitable media. *Chaos*, 1:303-334, 1991.
- [290] Winfree A T. Alternative stable rotors in an excitable medium. *Physica D*, 49:125-140, 1991.
- [291] Winfree A T. *Estimating the ventricular fibrillation threshold*. in Theory of Heart: Biomechanics, Biophysics, and Nonlinear Dynamics of Cardiac Function. L Glass, P Hunter and A McCulloch eds. Springer-Verlag New York, 1991.
- [292] Winfree A T. Heart muscle as a reaction-diffusion medium: the roles of electric potential diffusion, activation front curvature, and anisotropy. *Int. J. Bifurc. Chaos*, 7:487-526, 1997.

- [293] Wit A L, Cranefield P F, Hoffman B F. Slow conduction and reentry in the ventricular conducting system. *Circ. Res.*, 30:304-322, 1972.
- [294] Witkowski F X, Leon L, Penkoske P, Giles W, Spano M, Ditto W, Winfree A. Spatiotemporal evolution of ventricular fibrillation. *Nature*, 392:78-82, 1998.
- [295] Witkowski F X, Leon L J, Penkoske P A, Clark R B, Spano M L, Ditto W L, Giles W R. A method for visualization of ventricular fibrillation: design of a cooled fiberoptically coupled image intensified CCD data acquisition system incorporating wavelet shrinkage based on adaptive filtering. *Chaos*, 8:1054-1500, 1998.
- [296] Zeng W Z, Glass L, Shrier A. Evolution of rhythms during periodic stimulation of embryonic chick heart cell aggregates. *Circ. Res.*, 69:1022-1033, 1991.
- [297] Zykov V S. Analytical evaluation of the dependence of the speed of an excitation wave in a two-dimensional excitable medium on the curvature of it's front. *Biophysics*, 25:906-911, 1980.
- [298] Zykov V S. Spiral waves in two-dimensional excitable media. *Ann N Y Acad Sci.* 591:75-85, 1990.
- [299] The technical specification for the AD645 amplifier and the SSM2024 VCA units are available from <http://www.analogdevices.com>. The technical specification for the MRD500 are available from <http://www.motorola.com>, and are also listed in the Electrosonic electronics catalogue.